Mitigating Scarring and Inflammation during Corneal Wound Healing using Nanofiber-Hydrogel Scaffolds

Thesis by

Amy Fu

In Partial Fulfillment of the Requirements

for the Degree of

Doctor of Philosophy

CALIFORNIA INSTITUTE OF TECHNOLOGY

Pasadena, California

2015

(Defended May 19, 2015)

Acknowledgements

"We must find time to stop and thank the people who make a difference in our lives"

-- John F. Kennedy

To my advisor Julie Kornfield: Thank you. Thank you for teaching me to avoid "icky" people; thank you for telling me after practice talks that my "fonts were too small"; thank you for encouraging me during tough times that "obstacles were part of my training as a graduate student." Because of you, I am a better scientist, a better presenter, a better listener, and most importantly, a better person.

To my committee members (Prof. Mark Davis, Mikhail Shapiro and David Tirrell): Thank you for finding the time to read and evaluate my dissertation.

To my collaborators (Dr. Bala Ambati, Moran Eye Center, U. Utah and Prof. Giyoong Tae, GIST, S. Korea): Thank you for allowing me to work in your laboratories; thank you for your hospitality while I was in your cities; and thank you for your guidance throughout the years.

To my labmates, past and present: I DID IT! Thank you for listening to my (endless) complaints; thank you for never saying anything about my messy desk; thank you for understanding the emotions that come with being in graduate school (and in Julie's group).

To my “army” of undergraduates (Amy Proctor, Jackie Chan, Eric Li, Jacqueline Masehi-Lano, Lauren Li): Thank you for allowing me to be your mentor, and giving me a chance to teach you (a little bit) about science and life.

To some “unsung heroes” at Caltech (Marcy Fowler, Andrea Arias and Sarah Mojared of the Kornfield lab; Kathy Bubash, Mike Vicic, Elisa Brink, Steve Gould of the CCE Division; Joe Drew, Memo Correa and Art Larenas of the Chemistry stockroom; Gwen Williams of the Animal Facility; Michael Chuah of the EH&S office): Thank you for making my life at Caltech so much easier and always being available for me to ask questions.

To the Chemical Engineering class of 2009 (Brett Babin, Jeff Bosco, Tristan Day, Joseph Ensberg, and honorable member, Clint Regan): Thank you for the laughs and the tears; thank you for the wonderful memories (rushing to finish Transport homework, going to Las Vegas after qualification exam, burning old study notes in a bonfire, drinking mind erasers at Amigos!).

To my family (the Fus, the Maks, the Chans, the Chows and the Yuets) and friends (Danielle, Yung-Chi, Fiona, Mary, Maren, M.G.R., V.B.L., S.G., L.L., B.G.Y., G.T.Y., C.R.K.): Thank you for your continuous support and encouragement, and thank you for helping maintain my sanity throughout the years. I could not have done this without you. Special shout-out to my dear cousins, Jeff, Stef, Henry and Ed, for replying my late-night

text messages, making sure that I am always “drinking enough water” and “wearing enough layers of clothes”, and reassuring me that I am “unique”.

To my parents: Thank you for allowing me to choose my own path; thank you for not complaining (that much) that I am physically so far away; thank you for trying to understand what “graduate school” and “chemical engineering” actually means. Thank you, mom, for taking me to school every day when I was a little girl and thank you, dad, for all the life lessons you have taught me. I am proud to call you my parents; and I hope I have made you proud.

And finally, to my husband Kai: Thank you. It is hard to describe in words the journey that we have been on, but what an incredible journey it has been. Thank you for giving me a place to vent my frustrations and escape from the craziness that is graduate school. WE DID IT!

Amy (May 2015)

Abstract

Due to the universal lack of donor tissue, there has been emerging interest in engineering materials to stimulate living cells to restore the features and functions of injured organs. We are particularly interested in developing materials for corneal use, where the necessity to maintain the tissue's transparency presents an additional challenge. Every year, there are 1.5 – 2 million new cases of monocular blindness due to irregular healing of corneal injuries, dwarfing the approximately 150,000 corneal transplants performed. The large gap between the need and availability of cornea transplantation motivates us to develop a wound-healing scaffold that can *prevent* corneal blindness.

To develop such a scaffold, it is necessary to regulate the cells responsible for repairing the damaged cornea, namely myofibroblasts, which are responsible for the disordered and non-refractive index matched scar that leads to corneal blindness. Using *in vitro* assays, we identified that protein nanofibers of certain orientation can promote cell migration and modulate the myofibroblast phenotype. The nanofibers are also transparent, easy to handle and non-cytotoxic. To adhere the nanofibers to a wound bed, we examined the use of two different *in situ* forming hydrogels: an artificial extracellular matrix protein (aECM)-based gel and a photo-crosslinkable heparin-based gel. Both hydrogels can be formed within minutes, are transparent upon gelation and are easily tunable.

Using an *in vivo* mouse model for epithelial defects, we show that our corneal scaffolds (nanofibers together with hydrogel) are well-tolerated (no inflammatory response or turbidity) and support epithelium regrowth. We developed an *ex vivo* corneal tissue culture

model where corneas that are wounded and treated with our scaffold can be cultured while retaining their ability to repair wounds for up to 21 days. Using this technique, we found that the aECM-based treatment induced a more favorable wound response than the heparin-based treatment, prompting us to further examine the efficacy of the aECM-based treatment *in vivo* using a rabbit model for stromal wounds. Results show that treated corneas have fewer myofibroblasts and immune cells than untreated ones, indicating that our corneal scaffold shows promise in promoting a calmer wound response and preventing corneal haze formation.

Table of Contents

Acknowledgements iii
Abstract vi
Table of Contents viii
List of Figures x
List of Tables xiii

Chapter 1: Introduction
1.1 Tissue Regeneration 1-1
1.2 Corneal Blindness 1-2
1.3 Structure of the Cornea 1-4
1.4 Corneal Injury 1-5
1.5 Tissue-Engineered Corneal Scaffolds 1-6
1.6 Objectives and Organization 1-7
1.7 References 1-8

Chapter 2: Effects of nanofiber diameter and orientation on corneal epithelial cells, fibroblasts and myofibroblasts
2.1 Introduction 2-1
2.2 Methods 2-3
2.3 Results 2-9
2.4 Discussion 2-13
2.5 Conclusion 2-20
2.6 References 2-20
2.7 Figures and Tables 2-25
2.8 Additional Information 2-34

Chapter 3: Effects of growth factors on corneal myofibroblast phenotype
3.1 Introduction 3-1
3.2 Methods 3-2
3.3 Results 3-6
3.4 Discussion 3-8
3.5 Conclusion 3-16
3.6 References 3-16

Chapter 4: Development of a heparin-based hydrogel for corneal injury
4.1 Introduction 4-1
4.2 Methods 4-4
4.3 Results 4-9
4.4 Discussion 4-13
4.5 Conclusion 4-21
4.6 References 4-21
4.7 Figures and Tables 4-27
4.8 Additional Information 4-36

Chapter 5: *In vivo* study of corneal scaffold in a mouse epithelial defect model
5.1 Introduction 5-1
5.2 Methods 5-3
5.3 Results 5-9
5.4 Discussion 5-12
5.5 Conclusion 5-16
5.6 References 5-17
5.7 Figures and Tables 5-19

Chapter 6: Development of an *ex vivo* tissue culture model system
6.1 Introduction 6-1
6.2 Methods 6-3
6.3 Results 6-6
6.4 Discussion 6-9
6.5 Conclusion 6-12
6.6 References 6-13
6.7 Figures and Tables 6-15

Chapter 7: *In vivo* study of corneal scaffold in a rabbit model
7.1 Introduction 7-1
7.2 Methods 7-2
7.3 Results 7-6
7.4 Discussion 7-8
7.5 Conclusion 7-12
7.6 References 7-13
7.7 Figures and Tables 7-15

List of Figures

Chapter 1: Introduction
Figure 1. Structure of the eye and cornea 1-12
Figure 2. SEM of the stroma from wounded and healthy corneas 1-13

Chapter 2: Effects of nanofiber diameter and orientation on corneal epithelial cells, fibroblasts and myofibroblasts
Figure 1. SEM of electrospun gelatin nanofibers 2-25
Figure 2. Schematic of electrospinning setup and different grounded collectors 2-26
Figure 3. Nanofiber orientation influences cell shape and orientation 2-27
Figure 4. Nanofiber orientation affects the rate of cell migration 2-28
Figure 5. Myofibroblasts seeded on nanofibers of different orientation 2-30
Figure 6. Nanofiber orientation modulates myofibroblast phenotype 2-31
Figure 7. siRNA transfected myofibroblasts on uniaxially aligned nanofibers 2-33
Figure S-1. Electrostatic interaction of electrospun nanofibers and split electrodes . 2-35
Figure S-2. Relative αSMA mRNA expression of myofibroblasts on nanofibers 2-37
Figure S-3. Relative αSMA protein expression of myofibroblasts on nanofibers 2-38
Figure S-4. Optical transmittance of nanofiber mats on explanted porcine corneas.. 2-39
Figure S-5. LIVE/DEAD cell viability assay on fibroblasts on nanofibers 2-40
Figure S-6. Rate of cell migration on nanofibers as a function of time 2-41
Figure S-7. Validation of knockdown protein expression of siRNA treated cells 2-42

Chapter 3: Effects of growth factors (GFs) on corneal myofibroblast phenotype
Figure 1. Myofibroblast response to EGF at different concentrations 3-21
Figure 2. Myofibroblast response to FGF at different concentrations 3-22
Figure 3. Myofibroblast response to PDGF at different concentrations 3-23
Figure 4. Relative αSMA mRNA expression of myofibroblasts treated with GFs.... 3-24
Figure 5. Relative αSMA protein expression of myofibroblasts treated with GFs ... 3-25
Figure 6. αSMA expression of GF treated myofibroblasts cultured on nanofibers .. 3-26
Figure 7. Response of siRNA transfected myofibroblasts treated with GFs..... 3-27
Figure 8. Possible mechanisms by which GFs regulate αSMA expression 3-28

Chapter 4: Development of a heparin-based hydrogel for corneal injury
Figure 1. Schematic representation of heparin-based hydrogel formation 4-27
Figure 2. Effect of concentration on gelation kinetics and micropatterning time..... 4-28
Figure 3. Effect of formulation on gelation kinetics and micropatterning time..... 4-29
Figure 4. Effect of crosslinker on gelation kinetics and micropatterning time 4-30
Figure 5. *In vitro* release profiles of EGF from heparin-based hydrogels 4-31
Figure 6. Effect of released EGF on cell migration in a wound healing assay 4-32
Figure S-1. Photo-rheology appartus 4-37
Figure S-2. Stress sweep and strain sweep of heparin-based hydrogels 4-38
Figure S-3. Schematic representation of the micropatterning process..... 4-39
Figure S-4. Light intensity profiles for heparin-based hydrogels 4-41
Figure S-5. Computational eye model using ZEMAX ray-tracing software 4-42

Figure S-6. Gelation kinetics of hydrogels prepared at different temperatures 4-43
Figure S-7. Cell viability of encapsulated fibroblasts in hydrogels 4-44

Chapter 5: *In vivo* study of corneal scaffold in a mouse epithelial defect model
Figure 1. Schematic of *in vivo* mouse epithelial defect model..... 5-19
Figure 2. aECM-PEG treatment is transparent and non-toxic 5-20
Figure 3. Epithelial regrowth in aECM-PEG treated corneas 5-21
Figure 4. aECM-PEG treatment remains in the wound bed..... 5-22
Figure 5. Heparin-based treatment is transparent and remains in the wound bed..... 5-23
Figure 6. Epithelial regrowth in heparin-based treated corneas 5-24
Figure S-1. Nanofiber substrates used in study..... 5-25
Figure S-2. aECM-PEG hydrogel used in study 5-26
Figure S-3. aECM-PEG treatment remains in the wound bed (flat mount)..... 5-27
Figure S-4. H&E staining of unwounded and wounded but untreated corneas 5-28
Figure S-5. Oscillatory rheology results of aECM-PEG hydrogels..... 5-29
Figure S-6. Light device used for photo-crosslinking heparin-based hydrogels..... 5-30

Chapter 6: Development of an *ex vivo* tissue culture model system
Figure 1. Schematic of *ex vivo* corneal tissue culture 6-15
Figure 2. Photographs of preparing a porcine cornea for *ex vivo* culture 6-16
Figure 3. Photographs of an epithelial defect and a stromal wound 6-17
Figure 4. Representative images of a bovine cornea recovering from a wound 6-18
Figure 5. Representative images of *ex vivo* culture in different animal eyes..... 6-19
Figure 6. Wound closure of aECM-PEG treated corneas 6-20
Figure 7. TEM of aECM-PEG treated and untreated corneas..... 6-21
Figure 8. Wound closure of heparin-based hydrogel treated corneas 6-22
Figure 9. Wound closure of heparin-based hydrogel (with GFs) treated corneas 6-23
Figure 10. H&E staining of tissue sections from treated and untreated corneas 6-24
Figure 11. Higher magnification pictures of those shown in Figure 10..... 6-25

Chapter 7: *In vivo* study of corneal scaffold in a rabbit model
Figure 1. Schematic of *in vivo* rabbit model for stromal wounds 7-15
Figure 2. Wound closure of aECM-PEG treated rabbit corneas 7-16
Figure 3. Immunolabeling of myofibroblasts in treated and untreated corneas..... 7-17
Figure 4. Immunolabeling of immune cells in treated and untreated corneas 7-18
Figure 5. Masson's trichrome staining in treated and untreated corneas 7-19
Figure S-1. SEM of gelatin nanofibers used in the study..... 7-20
Figure S-2. Quantification of epithelial closure from fluorescein staining..... 7-21
Figure S-3. H&E staining of all rabbits used in aECM-PEG group 7-22
Figure S-4. H&E staining of all rabbits used in aECM-PEG-F127 group 7-23
Figure S-5. H&E staining of unwounded and wounded but untreated corneas 7-24
Figure S-6. Immunostaining of myofibroblasts of all rabbits sacrificed on day 13... 7-25
Figure S-7. Immunostaining of macrophages of all rabbits sacrificed on day 13..... 7-26
Figure S-8. Immunostaining of neutrophils of all rabbits sacrificed on day 13..... 7-27
Figure S-9. SEM of cross-sections of aECM-PEG hydrogels 7-28

Figure S-10. Live/dead staining of encapsulated cells in aECM-PEG hydrogels..... 7-29
Figure S-11. Migration of cells into aECM-PEG hydrogels in scratch wound assay 7-30

List of Tables

Chapter 1: Introduction
Table 1. Number of donor and transplanted corneas in the US and UK 1-14
Table 2. Synthetic polymer-based corneal scaffolds 1-15
Table 3. Protein-based corneal scaffolds 1-16

Chapter 2: Effects of nanofiber diameter and orientation on corneal epithelial cells, fibroblasts and myofibroblasts
Table S-1. Average fiber diameter of nanofibers used in the study 2-43
Table S-2. P-values of cell migration on nanofibers of different orientation 2-44
Table S-3. P-values of cell migration on nanofibers of different diameter 2-45
Table S-4. Average fiber density in nanofiber mats of different orientation 2-46

Chapter 3: Effects of growth factors (GFs) on corneal myofibroblast phenotype
Table 1. Summary of prior literature on using GFs to influence corneal cells 3-29

Chapter 4: Development of a heparin-based hydrogel for corneal injury
Table 1. Effect of heparin concentration on gel properties 4-33
Table 2. Effect of gel formulation on gel properties 4-34
Table 3. Effects of crosslinking stoichiometry and architecture on gel properties 4-35
Table S-1. Comparison of visible and UV photo-gelation conditions to eye safety .. 4-45
Table S-2. Quantification of cell viability of encapsulated fibroblasts in hydrogels . 4-46

Chapter 5: *In vivo* study of corneal scaffold in a mouse epithelial defect model
Table 1. Experimental groups for mice receiving heparin-based treatment 5-31

Chapter 6: Development of an *ex vivo* tissue culture model system

Chapter 7: *In vivo* study of composite scaffold in a rabbit model

Chapter 1

Introduction

1.1 Tissue regeneration

The field of regenerative medicine or tissue engineering uses various scaffold materials to stimulate living cells to restore injured organs and/or tissues, in hopes of reducing the need for organ replacement. The first attempt at tissue engineering is widely recognized as the effort of Dr. W.T. Green in generating new cartilage using chondrocytes seeded onto small pieces of bone in the early 1970s.[1] In the 1980s, Drs. John Burke and Ioannis Yannas together developed the first commercially reproducible, synthetic human skin substitute using silicone and a matrix containing cow tendons and shark cartilage.[2] It was not until the mid 1980s - early 1990s that scientists started designing biomimetic scaffolds, in contrast to seeding cells onto naturally occurring ones.[3] Since then, the field of tissue engineering has grown exponentially, and it was estimated that $600 million was spent in tissue engineering research alone in 2001.[4]

Recently, with increasing knowledge that cells acting to repair damaged tissues *in vivo* are bombarded with a multitude of molecular signals, there has been emerging interest to develop scaffolds with specific biochemical, mechanical and topographical cues to *guide* the regeneration of new tissue by these repair cells. For example, in the context of bone tissue and cartilage engineering, osteoblasts that are seeded on nanofibrous scaffolds have increased rates of proliferation, differentiation and mineralization[5-7] and in nerve regeneration, controlled release of fibroblast growth factor enhances neurite extension of various types of neurons[8-10]. We are particularly interested in developing materials for the

cornea, which has a complex nanostructure that is necessary and essential for maintaining the transparency of the tissue (described below).

In developing a corneal scaffold, we will gain a deeper understanding on how native corneal cells respond to their microenvironment. We envision that accumulation of such knowledge will provide new insight on central processes responsible for tissue repair and regeneration that can be extended to other organs, as well as possibly aid in the development of *in vitro* models for cancer metastasis.

1.2 Corneal blindness

As stated above, our focus is in creating materials for corneal applications. We are motivated by the fact that corneal blindness is the fourth leading cause of blindness worldwide (after cataracts, glaucoma and age-related macular degeneration), and impairs the vision of more than 10 million people worldwide.[11] Currently, the only way to treat corneal blindness is by removing the injured tissue and replacing it with either a donor cornea or an artificial implant.

Worldwide, there are 1.5 - 2 million new cases of monocular blindness per year, dwarfing the approximately 150,000 corneal transplants performed every year.[11] According to the Eye Bank Association of America, there were approximately 68,000 donated corneas in the United States in 2012, of which only 38,496 (56%) were implanted into patients (**Table 1**).[12] Tissue suitability was the leading cause of tissue judged unsuitable for transplant. In addition, although the initial success rate of donor corneas can be quite high (~90% in the

first year post-transplant), this number decreases to around 75% after 5 years (i.e. 25% rejection rate).[13] It is also estimated that the average cost of a corneal transplantation surgery is $14,000,[14] not easily affordable for patients in developing countries.

Synthetic artificial corneas have been developed to alleviate the need for donor tissues. The Boston Keratoprosthesis (Boston KPro) was developed under Dr. Claes Dohlman in the 1960s, and was approved by the FDA in 1992.[15,16] Its most recent design consists of a front plate, a piece of medical grade polymethylmethacrylate (PMMA), and a back plate; during assembly, the front and back plates snap together with the PMMA piece sandwiched in-between to form a collar-button-like device. More recently, Chirila, Hicks and colleagues have developed the AlphaCor (approved by the FDA in 2003),[17,18] which is made of a central transparent region made of poly(2-hydroxyethyl methacrylate) and a peripheral region with interconnecting pores that allow integration with surrounding corneal tissue. Despite these efforts, artificial corneas have not yet expanded the availability of corneal replacement due to the high incidence of severe complications (e.g., a 2009 study of Boston KPro found that 65% of patients suffered from postoperative complications[19], while a 2011 study of AlphaCor found that 9 out of 15 patients suffered "corneal melt" after implantation[20]). There are only approximately 1000 Boston KPro devices implanted every year[21], and only ~300 AlphaCor devices have been implanted total (up to 2008)[22]. In addition, the AlphaCor implantation is a two-stage process over several months, and requires tremendous technical ability. Therefore, there still exists an urgent need to develop alternative approaches to treating corneal blindness that are not only effective, but easy for physicians to implement.

1.3 Structure of the cornea

The human cornea is a 500-μm-thick transparent, dome-shaped layer in the front of the eye that covers the iris and pupil (**Figure 1A**), and is responsible for two-thirds of the eye's total focusing power.[23] The cornea can be separated into three main layers (**Figure 1B**): the outer epithelium (made up of multi-layers of epithelial cells), the middle stromal layer, and the inner endothelium (made up of a single layer of endothelial cells). The epithelium is regenerative (every 7 days), and provides protection for the eye against foreign materials (e.g. dust, bacteria). The endothelial cells making up the endothelium contain many metabolic enzymes that work to pump water from the cornea, thereby keeping it clear. If the endothelial cells become damaged, they do not regenerate, and corneal edema will ensue.

The middle stromal layer makes up the bulk of the cornea (85-90% of the total corneal thickness) (**Figure 1C**).[24] Its highly-ordered network of extracellular matrix (ECM) proteins and keratocytes (specialized fibroblasts that reside in the stroma) are crucial to maintaining corneal transparency. The stromal ECM is made up of mainly collagen and proteoglycans. Collagen fibers (25 - 35 nm in diameter) align parallel to each other at uniform distances to form a lamellae sheet. Over 300 lamellae sheets stack on top of each other at varying angles from 0 to 90 degrees to form the full thickness of the stroma (**Figure 1D**). The proteoglycans in the stroma absorb and retain large amounts of water, therefore giving the stroma its hydrogel-like quality. They also act to regulate the uniform spacing between the collagen fibrils, thereby keeping the collagen fibrils at defined distances that

minimizes light scattering.[25] Corneal keratocytes reside between the collagen lamellae with a flattened morphology (**Figure 1E**). In a healthy cornea, the keratocytes usually display a quiescent phenotype, are largely immobile and incapable of rapid rates of migration. Keratocytes continuously synthesize corneal crystallins, which are water-soluble cytoplasmic proteins that unify the refractive index within the cells, thereby minimizing light scattering.

1.4 Corneal injury

When minor abrasions occur on the surface of the cornea, healthy epithelial cells migrate and close the wound quickly. However, for deeper injuries that penetrate into the stroma, the healing process is much more intensive, and takes much longer.[26] Keratocytes in the direct vicinity of the wound site undergo apoptosis, while adjacent keratocytes become activated and differentiate into repair phenotypes – fibroblasts and myofibroblasts. These repair cells migrate into the wound and actively secrete new ECM proteins. However, the newly synthesized collagen is disorganized and lacks the orderly structure that maintains corneal transparency (**Figure 2**).[27] In addition, there is a decreased production of keratan sulfate proteoglycans and an increased expression of hyaluronan, which disrupts the spacing between newly deposited collagen fibrils. The myofibroblasts express alpha-smooth muscle actin (αSMA), which organizes into stress fibers and generates high contractile forces that function to close wounds[28,29], but also contributes to disrupting the smooth refracting surface of the cornea. Also, myofibroblasts have a decreased expression of corneal crystallins[30], which renders them less transparent as quiescent keratocytes. To

prevent corneal blindness, it is essential to modulate the activation of myofibroblasts, thereby reducing the production of αSMA and disordered ECM proteins.

1.5 Tissue-engineered approaches

There have been significant efforts in developing a corneal scaffold, and they can be divided into two main categories: synthetic-polymer based scaffolds (**Table 2**) and protein-based materials (**Table 3**).

Synthetic polymers used include poly(ethylene glycol) (PEG), poly(acrylic acid) (PAA), polyvinyl alcohol (PVA) and poly(lactic-co-glycolic acid) (PLGA).[31-36] One of the more successful attempts was developed by Curtis Frank,[33,34] where he and his students created a hydrogel with an interpenetrating network of PEG and PAA, and demonstrated that the hydrogels are optically clear, highly permeable to glucose, and have high tensile strength despite having a high water content. However, they observed that epithelial wound closure over the hydrogel was not comparable to sham wounds in an organ culture model, possibly due to the lack of cell-binding domains in the hydrogel.

Protein-based scaffolds have also been investigated, with a majority of them using collagen as the main material.[37-45] Sheardown and colleagues developed a dendrimer-crosslinked collagen scaffold, which has favorable glucose permeability and mechanical properties, and also supported human corneal epithelial cell growth and adhesion.[45] However, they observed that the optical transparency of the crosslinked gels was variable and highly dependent on the crosslinker used.

The most promising efforts have come from May Griffith's work throughout the past 15 years. In 1999, she published a pivotal paper where she isolated cells from different corneal layers and successfully constructed an artificial cornea by culturing the cells around a cellular scaffolding structure.[46] More recently, she and her coworkers have developed a corneal substitute composed of 1-ethyl-3-(3-dimethylaminopropyl) carbodiimide (EDC) crosslinked recombinant human collagen and implanted the material into 10 patients using sutures to secure in place.[47] They reported that two years after implantation, all 10 patients improved their vision to levels comparable that of patients who received donor corneas, but only when the patients also wore contact lens (the sutures impaired vision and needed to be smoothed by a contact lens). In addition, they observed that epithelial cells did not fully migrate over the implant, and instead halted at the sutures, causing discrete areas of corneal haze in those areas.

1.6 Objectives and organization

While alternatives to donor corneas are being developed, the large gap between the need and availability of cornea transplantation motivates us to take a different approach. Specifically, our goal is to develop a wound-healing scaffold that can *prevent* corneal blindness. An ideal corneal scaffold should have several basic qualities: (1) appropriate topological and biochemical cues that modulate myofibroblast phenotype, (2) suitable architecture that directs cell infiltration, (3) optical and mechanical profiles that match those of the native cornea, and (4) ability to form *in situ* to prevent the need for sutures.

The present thesis details our efforts in developing such a corneal scaffold. Chapter 2 describes effects of electrospun gelatin nanofibers (different diameter and orientation) on corneal cell behavior (migration, phenotype). Chapter 3 describes effects of growth factors on myofibroblast phenotype. Chapter 4 details the development of a visible-light photo-crosslinkable heparin-based hydrogel that is within the safety limits of corneal and retinal light exposure. Our composite scaffold (nanofibers together with hydrogel) was tested *in vivo* using a mouse model (Chapter 5), *ex vivo* (Chapter 6), and *in vivo* using a rabbit model (Chapter 7).

1.7 References

1 Green, W.T. Articular cartilage repair. Behavior of rabbit chondrocytes during tissue culture and subsequent allografting. *Clin. Orthop. Relat. Res*. **1977**; 124:237-250.

2 Yannas, I.V.; Burke, J.F.; Gordon, P.L.; Huang, C.; Rubenstein, R.H. Design of an artificial skin. II. Control of chemical composition. *J. Biomed. Mater. Res*. **1980**; 14:107-132.

3 Langer, R.; Vacanti, J.P. Tissue engineering. *Science* **1993**; 260:920.

4 Lysaght, M.J.; Reyes, J. The growth of tissue engineering. *Tissue Engineering* **2001**; 7:485-493.

5 Chen, V.J.; Smith, L.A.; Ma, P.X. Bone regeneration on computer-designed nano-fibrous scaffolds. *Biomaterials* **2006**; 27:3973-3979.

6 Woo, K.M.; Jun, J.H.; Chen, V.J.; Seo, J.; Baek, J.H.; Ryoo, H.M. *et al.* Nano-fibrous scaffolding promotes osteoblast differentiation and biomineralization. *Biomaterials* **2007**; 28:335-343.

7 Venugopal, J.; Vadgama, P.; Sampath Kumar, T.S.; Ramakrishna, S. Biocomposite nanofibers and osteoblasts for bone tissue engineering. *Nanotechnology* **2007**;18:055101.

8 Aebischer, P.; Salessiotis, A.N.; Winn, S.R. Basic fibroblast growth factor released from synthetic guidance channels facilitates peripheral nerve regeneration across long nerve gaps. *J. Neurosci. Res.* **1989**; 23:282-289.

9 Grothe, C.; Nikkah, G. The role of basic fibroblast growth factor in peripheral nerve regeneration. *Anat. Embryol*. **2001**; 204:171-177.

10 Fujimoto, E.; Mizoguchi, A.; Hanada, K.; Yajima, M.; Ide, C. Basic fibroblast growth factor promotes extension of regenerating axons of peripheral nerve. In vivo experiments using a Schwann cell basal lamina tube model. *J. Neutrocytology* **1997**; 26:511-528.

11 Whitcher, J.P.; Srinivasan, M.; Upadhyay, M.P. Corneal blindness: a global perspective. *Bulletin of the World Health Organization* **2001**; 79:214-221.

12 Eye Bank Association of America (2012 Eye Banking Statistical Report) (Accessed April 20th 2015).

13 Haft P, Kymionis G, Goldman DA. Corneal transplant rejection. *Exp. Review Ophthalmol.* 2008;3:293-297.

14 2002 Organ and Tissue Transplant Costs and Discussion, Richard H. Hauboldt, Nickolas J. Ortner, Milliman, 2002 (Accessed April 20th, 2015).

15 Chang, H.Y.; Luo, Z.K.; Chodosh, J.; Dohlman, C.H.; Colby, K.A. Primary implantation of type I Boston keratoprosthesis in nonautoimmune corneal diseases. *Cornea* **2015**; 24:264-270.

16 Harissi-Dagher, M.; Dohlman, C.H. The Boston Keratoprosthesis in severe ocular trauma. *Can. J. Ophthalmol*. **2008**; 43:165-169.

17 Hicks, C.R.; Crawford, G.J.; Tan, D.T.; Snibson, G.R.; Sutton, G.L.; Gondhowiardjo, T.D. *et al.* Outcomes of implantation of an artificial cornea, AlphaCor: effects of prior ocular herpes simplex infection. *Cornea* **2002**; 21:685-690.

18 Hicks, C.R.; Chirila, T.V.; Vijayasekaran, S.; Crawford, G.J. PHEMA as a keratoprosthesis material. *Br. J. Ophthalmol*. **2006**; 90:124.

19 Chew, H.F.; Ayres, B.D.; Hammersmith, K.M.; Rapuano, C.J.; Laibson, P.R.; Myers, J.S. *et al.* Boston keratoprosthesis outcomes and complications. *Cornea* **2009**; 28:989-996.

20 Jiraskova, N.; Rozsival, P.; Burova, M.; Kalfertova, M. AlphaCor Artificial Cornea. *Eye* **2011**; 25:1138-1146.

21 Boston KPro Update 2013, Harvard Medical School/Mass. Eye and Ear Department of Ophthalmology (accessed April 20th 2015)

22 Liu, C.; Hille, K.; Tan, D.T.; Hicks, C.R.; Herold, J. Keratoprosthesis surgery. *Dev. Ophthalmol.* **2008**; 41: 171-186.

23 Ruberti, J.W.; Roy, A.S.; Roberts, C.J. Corneal biomechanics and biomaterials. *Annu. Rev. Biomed. Eng.* **2011**; 13: 269-295.

24 Oyster, C.W. The Human Eye: Structure and function; Chapter 8: The cornea and the sclera 1999. Sinauer Associates, Inc.

25 Lewis, P.N.; Pinali, C.; Young, R.D.; Meek, K.M.; Quantock, A.J.; Knupp, C. Structural interactions between collagen and proteoglycans are elucidated by three-dimensional electron tomography of bovine cornea. *Structure* **2010**; 18:239-245.

26 Wilson, S.E.; Mohan, R.R.; Mohan, R.R.; Ambriosio Jr., R.; Hong, J.; Lee, J. The corneal wound healing response: cytokine-mediated interaction of the epithelium, stroma and inflammatory cells. *Prog. Retin. Eye Res.* **2001**; 20:625-637.

27 Saika, S.; Yamanaka, O.; Sumioka, T. *et al*. Fibrotic disorders in the eye: targets of gene therapy. *Prog. Retin. Eye. Res.* 2008;27:177-196.

28 Jester, J.V.; Petroll, W.M.; Cavanagh, H.D. Corneal stromal wound healing in refractive surgery: the role of myofibroblasts. *Prog. Ret. Eye Res.* 1999;18:311-356.

29 Jester, J.V.; Petroll, W.M.; Barry, P.A.; Cavanagh, H.D. Expression of alpha-smooth muscle (alpha-SM) actin during corneal wound healing. *Invest. Ophthalmol. Vis. Sci.* 1995;36:809-819.

30 Jester, J.V.; Brown, D.; Pappa, A.; Vasiliou, V. Myofibroblast differentiation modulates keratocyte crystalline protein expression, concentration, and cellular light scattering. *Invest. Ophthalmol. Vis. Sci*. **2012**; 53:770-778.

31 Myung, D.; Koh, W.; Bakri, A.; Zhang, F.; Marshall, A.; Ko, Jungmin. *et al.* Design and fabrication of an artificial cornea based on a photolithographically patterned hydrogel construct. *Biomed. Microdevices* **2007**; 9:911-922.

32 Xu, F.; Li, Y.; Yao, X.; Liao, H.; Zhang, L. Preparation and in vivo investigation of artificial cornea made of nano-hydroxapatite/poly(vinyl alcohol) hydrogel composite. *J. Mater. Sci.: Mater. Med.* **2007**; 18:635-640

33 Hartmann, L.; Watanabe, K.; Zheng, L.L.; Kim, C.Y.; Beck, S.E.; Huie, P. *et al.* Toward the development of an artificial cornea: improved stability of interpenetrating polymer networks. *J. Biomed. Mater. Res. B Appl. Biomater.* **2011**; 98:8-17.

34 Myung, D.; Farooqui, N.; Zheng, L.L.; Koh, W.; Gupta, S. Bakri, A. *et al.* Bioactive interpenetrating polymer network hydrogels that support corneal epithelial wound healing. *J. Biomed. Mater. Res. A* **2009**; 90:70-81.

35 Ortega, I.; Ryan, A.J.; Deshpande, P.; MacNeil, S.; Claeyssens, F. Combined microfabrication and electrospinning to produce 3-D architectures for corneal repair. *Acta Biomaterialia* **2013**; 9:5511-5520.

36 Hu, X.; Lui, W.; Cui, L.; Wang, M.; Cao, Y. Tissue engineering of nearly transparent corneal stroma. *Tissue Eng*. **2005**;11:1710-1717.

37 Lawrence, B.D.; Marchant, J.K.; Pindrus, M.A.; Omenetto, F.G.; Kaplan, D.L. Silk film biomaterials for cornea tissue engineering. *Biomaterials* **2009**; 30:1299-1308.

38 Gil, E.S.; Park, S-H.; Marchant, J.; Omenetto, F.; Kaplan, D.L. Response of human corneal fibroblasts on silk film surface patterns. *Macromol. Biosci.* **2010**; 10:664-673.

39 Mimura, T.; Amano, S.; Yokoo, S.; Uchida, S.; Yamagami, S.; Usui, T. *et al.* Tissue engineering of corneal s troma with rabbit fibroblast precursors and gelatin hydrogels. *Mol. Vis.* **2008**; 14: 1819-1828.

40 Alaminos, M.; Del Carmen Sanchez-Quevedo, M.; Munoz-Avila, J.; Serrano, D.; Medialdea, S. *et al.* Construction of a complete rabbit cornea substitute using a fibrin-agarose scaffold. *Invest. Ophthalmol. Vis. Sci*. **2006**; 47:3311-3317.

41 Mi, S.; Connon, C.J. The formation of a tissue-engineered cornea using plastically compressed collagen scaffolds and limbal stem cells. *Methods Mol. Biol.* **2013**; 1014:143-155.

42 Crabb, R.A.; Hubel, A. Influence of matrix processing on the optical and biomechanical properties of a corneal stroma equivalent. *Tissue Eng. Part A* **2008**; 14: 173-182.

43 Wilson, S.L.; Wimpenny, I.; Ahearne, M.; Rauz, S.; El Haj, A.J.; Yang, Y. Chemical and topographical effects on cell differentiation and matrix elasticity in a corneal stromal layer model. *Adv. Funct. Mater*. **2012**; 22: 3641-3649.

44 Builles, N.; Janin-Manificat, H.; Malbouyres, M.; Justin, V.; Rovere, M-R.; Pellegrini, G. *et al.* Use of magnetically oriented orthogonal collagen scaffolds for hemi-corneal reconstruction and regeneration. *Biomaterials* **2010**; 31: 8313-8322.

45 Duan, X.; Sheardown, H. Dendrimer crosslinked collagen as a corneal tissue engineering scaffold: mechanical properties and corneal epithelial cell interactions. *Biomaterials* **2006**; 27: 4608-4617.

46 Griffith, M.; Osborne, R.; Munger, R.; Xiong, X.; Doillon, C.J.; Laycock, N.L. *et al.* Functional human corneal equivalents constructed from cell lines. *Science* **1999**; 286:2169-2172.

47 Fagerholm, P.; Lagali, N.S.; Merrett, K.; Jackson, W.B.; Munger, R.; Liu, Y. *et al.* A biosynthetic alternative to human donor tissue for inducing corneal regeneration: 24-month follow-up of a phase 1 clinical study. *Sci. Transl. Med.* **2010**; 2:p.46ra61.

48 Knupp, C.; Pinali, C.; Lewis, P.N.; Parfitt, G.J.; Young, R.D. Meek, K.M. *et al.* The architecture of the cornea and structural basis of its transparency. *Adv. Protein Chem. Struct. Biol.* **2009**; 78:25-49.

49 Komai, Y.; Ushiki, T. The three-dimensional organization of collagen fibrils in the human cornea and sclera. *Invest. Ophthamol. Vis. Sci*. **1991**; 32:2244-2258.

50 Connon, C.J.; Meek, K.M. Organization of corneal collagen fibrils during the healing of trephined wounds in rabbits. *Wound Repair Regen.* **2003**; 11:71-78.

51 NHS UK Transplant Registry (Annual Activity Report 2013-2014, Section 10: cornea activity) (Accessed April 20th 2015).

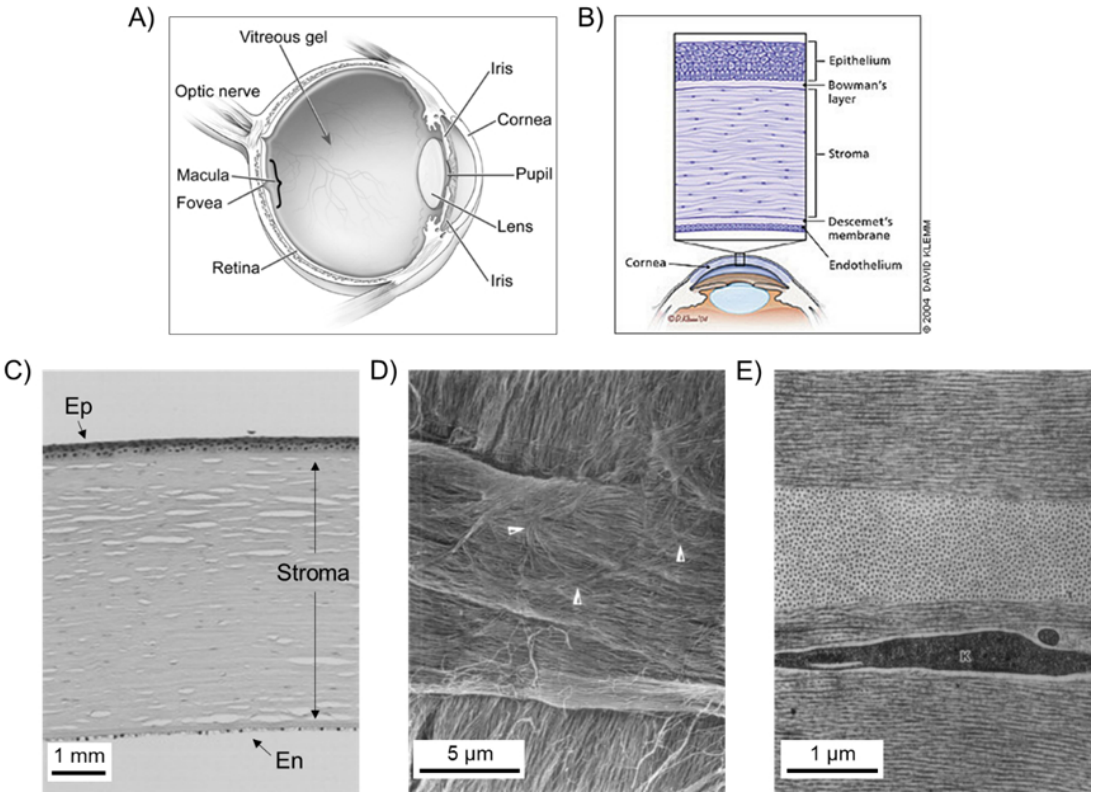

Figure 1. Structure of the eye and cornea. A) Schematic of the human eye. The cornea is the outermost part of the eye. B) The cornea can be separated into three main layers: epithelium, stroma and endothelium. C) Hematoxylin-and-eosin stained tissue section of a human cornea.[48] D) Top-down view of the stroma: lamellae of collagen fibrils stack on top of each other.[49] E) Cross-section of the stroma: keratocytes (K) are found in between layers of the collagen lamellae.[49]

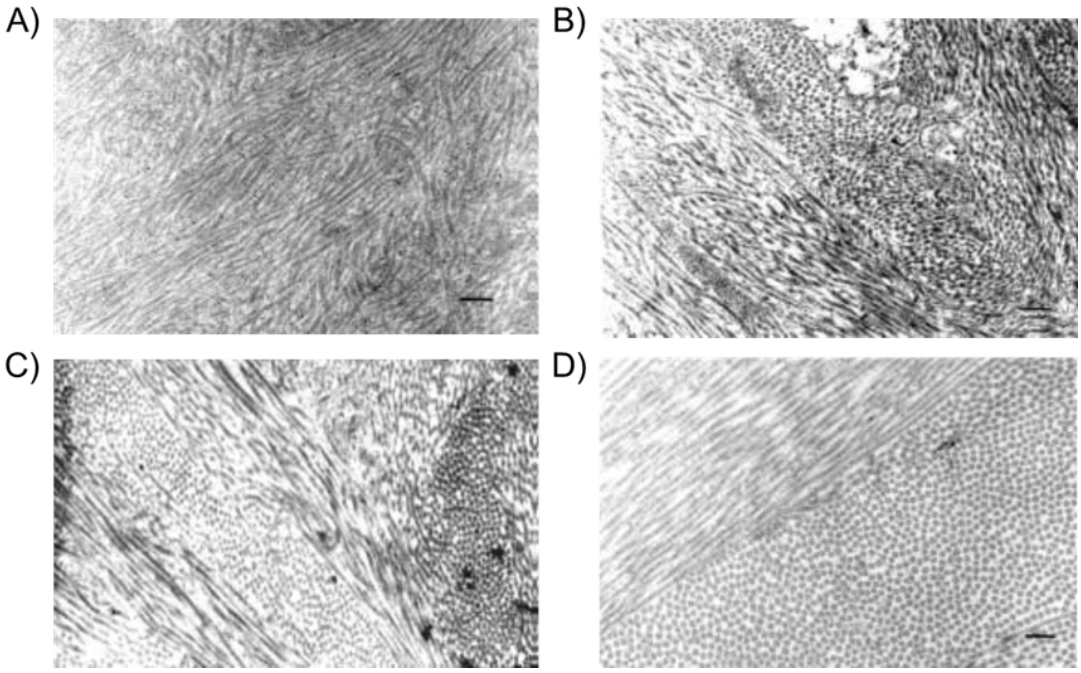

Figure 2. Scanning electron micrographs of the stroma from wounded and healthy corneas.[50] The collagen fibrils are disorganized at A) month 5, B) month 10, and C) month 16 after injury. D) In a normal cornea, the collagen fibrils are regularly spaced and uniaxially aligned inside the lamellae. Scale bar = 200 nm.

Table 1. Number of donor and transplanted corneas in the US and UK.

	US (2012)[12]	**UK (2013-2014)[51]**
Donated corneas	68,681	6,255
Transplanted corneas	38,502 (56%)	3,597 (66%)
Top reasons for tissue not being used	17% tissue quality	14% tissue quality
	13% contamination	11% medical contraindications
	12% medical record or autopsy findings	5% exceeded storage days
		4% bacterial/fungal contamination

Table 2. Synthetic polymer-based corneal scaffolds

Description	**Authors**	**Ref.**
Central core optical component made of a poly(ethylene) glycol, poly(acrylic acid) double network; peripheral skirt of poly(hydroxyethyl acetate) hydrogel; surface modified with collagen type I	Myung, D. *et al.*	31
Central core made of polyvinyl alcohol; skirt made of a nano-hydroxyapatite/polyvinyl alcohol hydrogel composite	Xu, F. *et al.*	32
Interpenetrating network of poly(ethylene glycol) and poly(acrylic acid)	Hartman, L. *et al.* Myung *et al.*	33 34
Electrospun poly(lactic-co-glycolic acid) scaffolds containing micropockets	Ortega, I. *et al.*	35
Corneal stromal cells mixed with non-woven polyglycolic acid fibers to form cell-scaffold construct	Hu, X. *et al.*	36

Table 3. Protein-based corneal scaffolds

Description	**Authors**	**Ref.**
Silk films	Lawrence, B.D. *et al.* Gil, E.S. *et al.*	37 38
Fibroblast precursor cells combined with gelatin hydrogels	Mimura, T. *et al.*	39
Corneal cells (epithelial cells, fibroblasts and endothelial cells) cultured on a fibrin-agarose scaffold to construct full-thickness corneal substitute	Alaminos, M. *et al.*	40
Compressed collagen scaffolds with embedded corneal keratocytes and limbal stem cells	Mi, S.; Connon, C.J.	41
Glucose-mediated UV crosslinkable collagen scaffolds	Crabb, R.A.; Hubel, A.	42
Aligned polylactic acid nanofibers within a collagen hydrogel	Wilson, S.L. *et al.*	43
Magnetically-oriented orthogonal collagen scaffolds	Builles, N. *et al.*	44
Dendrimer crosslinked collagen gels	Duan, X.; Sheardown, H.	45

Chapter 2

Effects of nanofiber diameter and orientation on corneal epithelial cells, fibroblasts and myofibroblasts

2.1 Introduction

In vivo, keratocytes in the corneal stroma reside between layers of lamellae, which have a distinctive nanometer scale morphology that includes aligned collagen fibrils. Thus, keratocytes are continuously exposed to a microenvironment containing oriented topological and biochemical signals. The present study builds upon recent advances in understanding how biophysical cues affect corneal cell behavior, especially by Murphy, Nealey and Russell, who have collectively demonstrated that topography can influence the corneal fibroblast-myofibroblast transformation *in vitro*.[1-3] Substrate anisotropy (aligned pitches 400 - 4000 nm compared to planar controls)[1-2] and compliance (polyacrylamine hydrogels 4-71 kPa compared to tissue culture plates >1GPa)[3] influence myofibroblasts to reduce αSMA expression. Orwin and coworkers further showed that scaffold composition (collagen compared to tissue culture plates)[4] and structure (3D collagen sponge compared to 2D films)[5] reduce αSMA expression in myofibroblasts. In addition, Guillemette and coworkers demonstrated that aligned surface grooves (1 - 10 microns) stimulate corneal fibroblasts to deposit new collagen that is also oriented.[6] They found that the orientation of the first cell layer becomes a physical cue to induce other cell layers to orient and deposit collagen in a way that mimics the structure of the native cornea. These prior findings led us to hypothesize that nanofibers, reminiscent of those found in the native cornea both in dimension and

orientation, might promote orderly tissue repair. Therefore, we prepared nanofiber layers that could be used in a wound dressing and examined their influence on myofibroblast phenotype.

We chose to use electrospinning to fabricate the nanofibers, since electrospinning is a versatile method that allows for the formation of continuous fibers using virtually any material and does not require specialized equipment.[7,8] Pioneered by Dr. Darrell Reneker, during the electrospinning process (described in detail at the end of the chapter), high voltage is applied to the electrospinning solution (usually polymeric or protein-based), which leads to the formation of fibers that are deposited on a grounded collector.[9,10] The dimensions and morphology of the fibers can be varied by changing the properties of the molecule itself (molecular weight, solubility), the properties of the solution (concentration, solvent), processing conditions (needle diameter, field strength, needle to collector distance, collector geometry) and ambient conditions (temperature, relative humidity).[11-15] Here, we used gelatin as our material to fabricate nanofibers of different diameter (100 – 220 nm) and different orientation (isotropic, uniaxially aligned, radially aligned) that could be used in a wound dressing, and examined their influence on the native behavior of corneal cells.

Our results show that the effect of nanofiber diameter in the range of 100 – 220 nm is weak; whereas, nanofiber orientation strongly affects the migration rate of corneal cells and αSMA expression of myofibroblasts *in vitro*. Surprisingly, the mechanism of the myofibroblast response is essentially integrin independent; rather, it appears to involve

mechanotransduction. In relation to potential clinical translation, the electrospun nanofiber substrates are transparent when wet, non-cytotoxic, and easy to handle without breaking. Thus, protein nanofiber mats may prove valuable in wound dressings for corneal injury that can orchestrate an orderly wound healing response, preventing corneal blindness.

2.2 Methods

Fabrication of nanofiber mats.

Gelatin A (Sigma Aldrich, St. Louis, MO) was dissolved in a mixture of 5:3:2 acetic acid/ethyl acetate/distilled water at a concentration of 10-15% (w/w) and stirred overnight at 37^{o}C. Electrospun nanofibers were fabricated from the gelatin solution using a 22-gauge needle at a voltage of +15kV (Universal Voltronics high voltage supply) and a needle to collector distance of 8 cm. Different fiber orientations were achieved using different grounded collectors: isotropic nanofibers were obtained using a metal ring (stainless steel back ferrule, 0.95 cm in diameter) placed on a flat aluminum plate; radially aligned nanofibers were collected on a metal ring nested on a copper frame with a centered copper point electrode, and uniaxially aligned nanofibers were made using a pair of split electrodes (0.95 cm apart). Electrospun fibers were crosslinked with glutaraldehyde (vapor phase) overnight, and sterilized with 70% ethanol prior to use. Details on nanofiber characterization are found in Supplementary Information.

Characterization of fabricated scaffolds

To visualize the nanofiber mats, they were labeled with either NHS-rhodamine or NHS-fluorescein dye (Thermo Fisher, Rockford, IL). A stock solution was prepared by

dissolving the dye in dimethyl sulfoxide at a concentration of 10 mg/mL. The staining solution was made by diluting the stock solution with Dulbecco's phosphate buffered saline (DPBS, GIBCO, Grand Island, NY) to a final dye concentration of 0.1 mg/mL. The nanofiber mats were immersed in the staining solution for 1 hour (at room temperature) on a rocker. To remove any residue dye, the nanofibers were rinsed in deionized water for a total of 1.5 hours, during which the water was replaced twice. Nanofiber mats were air dried prior to use.

To characterize the morphology and diameter of the electrospun fibers, a field emission scanning electron microscope operating at an accelerating voltage of 5 kV was utilized (Zeiss 1550 VP). Samples were mounted onto aluminum SEM stubs using double-sided carbon tape and sputter-coated (Cressington 208HR) with a 10 nm layer of palladium prior to measurement to minimize electron charging effects. 3 pictures were taken for each scaffold, and 40 independent fibers were counted for each picture. Each scaffold was performed in triplicate, and the experiment was repeated three times on separate days.

To examine the transparency of the nanofiber mats, the optical transmittance of the scaffolds was measured with a UV-VIS spectrophotometer (Beckman DU640) at a spectral range of 400-700 nm. The reference sample was an explanted porcine cornea alone, and the experimental sample consisted of a nanofiber mat placed in front of the porcine cornea.

Rabbit corneal fibroblast isolation and culture.

Fibroblasts were isolated from young rabbit eyes (mixed gender, approximately 8-12 weeks old, Pel-Freez, Rogers, AR) as described elsewhere.[16] The isolated fibroblasts were passaged every 2-3 days when 95% confluence was reached. Cells from passages 5-8 were used in the present study.

Characterization of cell shape, orientation and viability.

To examine cell shape and orientation, fibroblasts seeded on the nanofiber surfaces were imaged under an inverted phase contrast microscope with a 10x objective, and 3 random pictures were taken of each surface. To visualize the intracellular cytoskeleton, cells were first fixed with 4% paraformaldehyde in DPBS for 10 minutes, washed 3x with DPBS, and permeabilized with 0.1% Triton X-100 in DPBS for 10 minutes. Blocking was then performed with 1% bovine serum albumin in DPBS for 30 minutes at room temperature. The cells were incubated with 1:1000 rhodamine phalloidin (Invitrogen, Grand Island, NY) in 1% BSA for 60 minutes at room temperature, followed by 3x washes in DPBS. Cell nuclei were stained with Hoescht 33342 (Invitrogen, Grand Island, NY) at 0.5 µg/mL for 10 minutes at room temperature in the dark. Cells were then imaged with a confocal microscope (Zeiss LSM 510) using a 40x objective. Five random images were taken for each scaffold. Cell viability on the scaffolds was assessed using a LIVE/DEAD® cell viability assay following the manufacturer's protocol using 10µM ethidium homodimer-1 and 2µM calcein AM (Invitrogen, Grand Island, NY).

***In vitro* study of cell migration.**

Nanofiber mats were detached from collectors and placed onto circular gelatin hydrogel disks (15% gelatin A in DPBS, 9.5 mm diameter, 700 µm thick, crosslinked with glutaraldehyde, liquid phase, and rinsed in deionized water). A circular polydimethylsiloxane (PDMS) disk (4 mm diameter, 100 µm thick, prepared following manufacturer's protocol, Dow Corning, Midland, MI) was placed at the center of the fiber mat, creating a three-layered structure. Cells were then seeded in each well ($1x10^5$ cells/mL) and cultured to confluence (typically 24 hours following cell seeding). The PDMS disks were lifted with sterile tweezers, thereby creating a circular wound site. A gelatin hydrogel with no nanofiber mat was used as a control. Cell migration was tracked and imaged at regular time intervals using an inverted phase contrast microscope. Images were analyzed using Autostitch and ImageJ software (NIH). Each scaffold parameter was repeated at least 5 times. Cells of the same passage were used for each independent experiment.

qPCR, Western blotting, immunocytochemistry.

Nanofiber mats were detached from collectors and placed onto glass slides coated with an N-hydroxsuccinimide ester functionalized polymer layer (Nexterion Slide H, Schott, Louisville, KY). Glass slides spin-coated with gelatin (50 µm) were used as the planar control. Glass slides were then exposed to glutaraldehyde (vapor phase, 2 hours), followed by washing 3x in deionized water (30 minutes each). Corneal fibroblasts were seeded onto nanofibers ($5x10^4$ cells/mL). Transforming growth factor-beta (TGF-β, 1 ng/mL) was added 24 hours post-seeding to induce the myofibroblast phenotype[16,18], and cells were grown for 72 hours.

Quantitative PCR (qPCR).

TGF-β induced myofibroblasts were lifted from the nanofiber surface and pelleted. RNA was extracted using the Qiagen RNeasy kit following the manufacturer's protocol (Qiagen, Valencia, CA). RNA yield was determined using a Nanodrop spectrophotometer (Thermo Sci., Wilmington, DE). Gene expression was evaluated using qPCR with an EXPRESS One-Step SYBR® GreenER™ Universal kit (Invitrogen, Grand Island, NY) in an Eco Real-Time PCR system (Illumina, San Diego, CA). qPCR was carried out using 50 ng RNA per sample and commercially available primers for αSMA, GAPDH and β-actin in a total reaction volume of 10 µL per sample. GAPDH and β-actin served as references. Products were evaluated by melt curve analysis and sizing on agarose gels. Gene expression was normalized relative to the expression of mRNA from control surfaces (no nanofibers present) under the same culture conditions using the ΔΔCt method as described elsewhere.[17] The mRNA from the control surface was given an arbitrary value of 1.0. qPCR reactions were run in triplicates per sample, and the experiment was repeated three times on separate days.

Western blotting.

TGF-β induced myofibroblasts were lifted from the nanofiber surface, pelleted and lysed with M-PER mammalian protein extraction reagent following the manufacturer's protocol (Thermo Sci., Rockford, IL). Insoluble cellular debris was removed by centrifugation at 10k rpm for 10 minutes, and the supernatant was collected into new tubes. A bicinchroninic acid (BCA) protein assay (Thermo Sci., Rockford, IL) was

performed to determine the concentration of the extracted protein. Equivalent amounts of protein (10 µg per sample) were mixed with loading buffer, denatured by boiling for 5 minutes and loaded onto a MINI-PROTEAN TGX precast gel (Bio-Rad, Hercules, CA). Gel electrophoresis was performed at 200V for 40 minutes. Protein bands were then transferred to a nitrocellulose membrane at 100V for 1 hour. The nitrocellulose membrane was blocked for 1 hour at room temperature in blocking solution (5% BSA, 0.1% Tween-20 in DPBS). The membrane was then incubated with mouse anti-GAPDH antibody (Invitrogen, Grand Island, NY) at 1:2500 dilution in blocking solution for 1 hour at room temperature. The blot was washed 3x (10 minutes each) in DPBS-T (DPBS + 0.1% Tween-20), followed by incubation with AlexaFluor 647 goat anti-mouse secondary antibody (Invitrogen, Grand Island, NY) in blocking solution at 1:2500 dilution for 1 hour in the dark. The blot was washed 3x (10 minutes each) in DPBS-T and incubated with FITC-conjugated mouse anti-αSMA antibody (Sigma Aldrich, St. Louis, MO) at 1:2500 dilution in blocking solution for 1 hour in the dark. After rinsing with DPBS-T, the blot was scanned using a Typhoon Trio Scanner (GE, Piscataway, NJ). Relative intensities of α-SMA bands were normalized with GAPDH bands. Immunoblotting was performed on samples from three independent experiments.

Immunocytochemistry.

TGF-β induced myofibroblasts were first washed 3 times with DPBS, and then fixed, permeabilized and blocked as detailed above. The cells were then incubated with 1:1000 FITC-conjugated mouse anti-αSMA antibody (Sigma Aldrich, St. Louis, MO) in 1% BSA for 60 minutes at room temperature. Cells were washed 3 times with DPBS, and

cell nuclei were stained with Hoescht 33342 (Invitrogen, Grand Island, NY) at 0.5 ug/mL for 10 minutes at room temperature in the dark. Cells were then stored in PBS until imaging with a Zeiss Axiovert 25CFL fluorescent microscope. For analysis of αSMA protein expression, 5 random images were taken of each scaffold using a 5x objective for both Hoescht and FITC fluorescence. Blue dots (Hoechst stained nuclei) were counted as total cells per image, while cells presenting a green signal (FITC) were counted as positive for αSMA. Immunocytochemistry was performed on samples from three independent experiments.

siRNA transfection of human corneal fibroblasts.

FAK, Raf-1, YAP and TAZ were knocked down in human corneal fibroblasts (ScienCell, Carlsbad, CA) using siRNAs targeted to the corresponding genes (all from Santa Cruz Biotechnology, Dallas, TX). Cells (P3, 60-70% confluent) were transfected with siRNA (60 nM) using siRNA transfection reagent (Santa Cruz Biotechnology, Dallas, TX) according to the manufacturer's instructions. Control cells were transfected with FITC-conjugated control siRNA (Santa Cruz Biotechnology, Dallas, TX). The cells were incubated for 72 hours before collection.

Statistical analysis.

All results are reported as mean ± standard deviation. Differences between groups were assessed by two-tailed t-tests. $P < 0.05$ was considered as significant.

2.3 Results

Nanofiber substrates of different diameter and orientation were fabricated

Gelatin nanofibers were fabricated using electrospinning. By varying the concentration of the starting gelatin solution, we created nanofibers of three different diameters (10% solution: 105 nm; 12% solution: 155 nm; 15% solution: 220 nm) (**Figure 1, Table S-1**). By varying the grounded collector, we created nanofibers of three different orientations (planar collector: isotropic; pair of electrodes: uniaxially aligned; metal ring with central point electrode: radially aligned) (**Figure 2**).

Corneal fibroblasts elongate and orient on radially and uniaxially aligned nanofibers

Rabbit corneal fibroblasts (RCF) were seeded on nanofiber mats of different orientation: planar, isotropic, radially aligned and uniaxially aligned (**Figure 3,** left to right, FITC stained, false colored to red). Using a fluorescently-labeled phalloidin probe to visualize the cytoskeleton of seeded cells (**Figure 3**), we observed that cells on radial and uniaxial nanofibers are elongated and oriented along the same axis of the underlying nanofibers. Cells that were seeded on isotropic nanofibers showed no preferred orientation, and cells that were seeded on a planar surface showed few focal adhesions and the associated fan-shaped morphology.

Corneal fibroblasts migrate faster on oriented nanofibers

To compare the rate of migration of corneal cells moving across nanofibers of different orientation, we carried out an *in vitro* mock wound-healing assay (**Figure 4A**). Relative to the sharp initial boundary (“wound edge”) between confluent cells and freshly exposed substrate, we observed that corneal fibroblasts migrated faster along the

direction of oriented nanofibers (**Figure 4B**). Relative to a planar surface, fibroblasts advanced less rapidly on isotropic nanofibers, more rapidly along radial nanofibers and along uniaxial nanofibers, and much slower orthogonal to the nanofibers. On radial nanofibers, the migration velocity increased as the surface concentration of nanofibers increased, leading to a faster overall migration velocity than along uniaxially-oriented nanofibers. Varying the nanofiber diameter did not significantly change the rate of fibroblast migration. In contrast to fibroblasts, when corneal epithelial cells were used, we observed that they migrated fastest on isotropic nanofibers, approximately twice as fast as on a planar substrate or migration along oriented nanofibers (radial or uniaxial) (**Figure 4C**). Migration orthogonal to nanofibers was slowest for both epithelial and fibroblast cells.

Reduced levels of αSMA are observed in cells seeded on oriented nanofibers

To study the response of myofibroblasts to nanofibers of different orientation, we transformed corneal fibroblasts into myofibroblasts by adding 1 ng/mL of TGF-β to the cell culture medium, and analyzed the αSMA expression of the transformed cells. Immunocytochemical staining indicated that the proportion of cells producing αSMA depends on the orientation distribution of nanofibers, with significantly fewer cells expressing αSMA on radial (20% decrease) and uniaxial (40% decrease) nanofibers compared with planar surfaces or randomly-oriented nanofibers (**Figure 5, Figure 6A**). Total mRNA was isolated from cells seeded on the four different substrates and analyzed using qPCR, which revealed a significant decrease in αSMA mRNA expression in cells grown on oriented nanofiber substrates (**Figure 6B**). Specifically, cells seeded on

uniaxially-aligned nanofibers (D_{fiber} = 155 nm) expressed the lowest levels of αSMA (40% decrease compared to cells on planar surfaces). For other nanofiber diameters, cells on uniaxially-oriented nanofibers consistently showed the lowest αSMA mRNA expression (approximately 40% reduction for D_{fiber} = 100 nm, 25% for D_{fiber} = 220 nm relative to planar control) (**Figure S-2**). Western blot analysis of αSMA protein content (normalized by GAPDH) in cells seeded on differently-oriented nanofibers showed that cells cultured on nanofiber surfaces have significantly lower αSMA protein expression (**Figure 6C**), with cells on uniaxial nanofibers showing the largest decrease (75%). A similar trend was observed at different nanofiber diameters (**Figure S-3**).

TAZ/YAP may play a much stronger role than FAK/Raf-1 in transducing topological cues into cellular signals that modulate αSMA expression

To investigate the molecular mechanism by which cells cultured on nanofiber surfaces demonstrate a reduced αSMA expression, we examined focal adhesion kinase (FAK), serine/threonine protein kinase Raf-1, transcription co-activator TAZ and Yes-associated protein (YAP) by generating the corresponding knocked-down cells (transfected human corneal fibroblasts with the corresponding siRNA). These cells were then seeded onto uniaxially-aligned nanofibers, transformed into myofibroblasts with 10 ng/mL TGF-β, and their αSMA protein expression was visualized using immunocytochemistry (**Figure 7**). Interestingly, knockdown of FAK or Raf-1 did not restore αSMA expression and cells looked similar to control cells on uniaxial nanofibers. In contrast, both TAZ and YAP knockdowns partially reversed nanofiber-dependent changes in αSMA expression: both siTAZ and siYAP cells express αSMA (labeled

green) at a level intermediate between control cells on planar surfaces and control cells on uniaxial nanofibers.

2.4 Discussion

Topological cues have emerged as important factors in affecting cellular behavior, attracting attention in the context of guided wound healing and tissue regeneration.[19-21] However, the role of length scale and biochemical functionality of the topological features is the subject of debate. In relation to the ocular cornea, Pot and colleagues studied the behavior of corneal keratocyte, fibroblast and myofibroblast cells cultured on uniaxial pitches (400 - 4000 nm), and found that while corneal stromal cells elongated and migrated favorably on large surface features (> 800 nm), cells failed to respond to topographic features close to the dimensions of their native environment.[1] In contrast, Wray and Orwin demonstrated that nanofiber substrates as small as 50 nm in diameter promoted elongated morphologies of corneal fibroblasts.[22] Both studies suggest that mechanical cues can induce significant changes in corneal cell behavior.

Our motivation for studying the effects of nanofiber diameter and orientation on corneal fibroblasts is to pave the way to using such nanofiber mats as building blocks in a wound dressing for corneal injury. An ideal wound healing material would be a transparent, acellular scaffold containing topological and biochemical cues that first encourage healthy cells near the wound to infiltrate into the scaffold, and then promote orderly tissue repair or replacement. The central challenge in treating corneal wounds is mitigating the myofibroblast phenotype that is responsible for the disordered and non-refractive-index-matched scar that leads to corneal blindness.[23,24] Therefore, we

deliberately provoked corneal fibroblasts into myofibroblasts using TGF-β,[5,18] and examined the effects of nanofiber diameter and orientation on the cellular phenotype.

In this study, we used electrospinning to fabricate nanofibers with diameter in the range 110 – 220 nm (**Figure S-4**). The upper limit was chosen to minimize light scattering of the material. The smallest diameter was the lowest for which we could fabricate fibers with a uniform diameter. In relation to potential clinical translation, we found that nanofiber mats with fiber diameter <100 nm were delicate, and tore during routine handling. By choice of the geometry of the collection electrode (**Figure 2**), we created radially-oriented nanofibers that might speed wound closure, and uniaxial nanofibers (reminiscent of collagen fibrils found in individual lamellae of the corneal stroma) that might promote orderly healing. Behavior of cultured cells on these two surfaces was compared to those on isotropic nanofibers with no preferred orientation and control substrates with no nanofibers.

For the fabricated nanofiber mats to be used in corneal applications, they must first satisfy two important prerequisites: transparency and non-cytotoxicity. When we placed the nanofiber mats on an excised fresh cornea and measured the transmittance through the material, there was no measurable change in light transmission compared to a control cornea without nanofibers (**Figure S-5**). Also, using a LIVE/DEAD fluorescent assay to test for cell viability, we found cells plated at the same density onto nanofiber substrates and a control substrate with no nanofibers had indistinguishable and very high

cell survival rates (**Figure S-6**). Having fulfilled these two requirements, the behavior of the corneal fibroblasts cultured on the different nanofiber surfaces was examined.

When corneal fibroblasts are seeded on oriented nanofibers (radial or uniaxial), they elongate in the direction of the axis of the underlying nanofibers. This observation is in agreement with Wray and Orwin's results that corneal fibroblasts are able to respond to topological and biochemical cues presented by electrospun collagen nanofibers in the 50-300 nm range.[22] Wray and Orwin's hypothesis that nanofibers in this size range affects cells in part through patterned cell binding ligands applies equally to the present study and may reconcile our observations with those of Pot and coworkers, who found that oriented topography with periodicity less than 400 nm did not alter cell morphology when the ligand distribution was uniform.[1] In addition, literature suggests that oriented corneal fibroblasts deposit newly-synthesized protein along the same direction of their orientation.[6,25] This is of interest, in the context of remodeling an injured cornea, because the layers of aligned, uniformly-spaced collagen fibrils are essential to maintaining the transparency of the cornea.

Toward the goal of recruiting cells into the scaffold, we examined the effects of nanofiber diameter and orientation on the rate of migration of corneal fibroblasts. The presence of oriented nanofibers enhances the rate of migration of corneal fibroblasts in the direction parallel to the fibers, and inhibits it in the direction orthogonal to the fibers. The migration velocity parallel to the fibers to that perpendicular to the fibers is approximately 3 (i.e. 35 μm/hour parallel, 12 μm/hour perpendicular, **Figure 2**) for

corneal fibroblasts independent of fiber diameter. The parallel/perpendicular velocity ratio here is similar to that observed by Pot *et al.* for >1200 nm pitch size (and contrasts with their finding that this ratio approaches 1 for pitch <800 nm).[1] Relative to the uniaxially aligned nanofiber substrate, one that has a radial pattern further enhances the rate of cell migration (~45 μm/h). We speculate that fibroblasts migrate faster on radial nanofibers than on uniaxial nanofibers because the surface concentration of fibers, and hence the density of cell binding domains available, increases as the cells move closer to the center of the radial pattern **(Figure S-7**).

Interestingly, corneal epithelial cells migrate more rapidly on randomly-oriented nanofibers than along aligned ones (radial or uniaxial) with the same fiber diameter and density (**Tables S3-4**). While there are prior studies that report epithelial cell migration being faster along uniaxial oriented nanofibers,[26,27] we did not find any studies that compared randomly-oriented nanofibers to oriented ones. While epithelial migration on aligned nanofibers is faster than on planar substrates, it is *not* faster than on randomly-oriented nanofibers (**Figure 2C**). This characteristic of epithelial cells is different from skin fibroblasts[28], glioma cells[29] and aggressive metastatic breast cancer cells[30]. To our knowledge, this is the first report of a cell type that migrates faster on randomly-oriented nanofibers than on aligned nanofibers.

We speculate that the unusual response of epithelial cells to nanofiber orientation may be due to the distinctive mode of wound closure used by epithelial cells when closing around small circular wounds: “cables of actin filaments appear to extend from cell to

cell forming a ring around the wound circumference… [perhaps] as a contractile 'purse string' to facilitate wound closure."[31] While fibroblasts move primarily by cell crawling, epithelial cells at the concave edges of migrating cell sheets exhibit purse-string healing in addition to cell crawling.[32] Indeed, purse-string healing is the predominant mode of closing small round wounds in the corneal epithelium. Perhaps purse-string healing is adversely affected by aligned nanofiber substrates, although further investigation would be required to test this hypothesis. In relation to corneal wound dressings, the different responses of epithelial cells and fibroblasts suggest that a top layer of isotropic nanofibers might promote epithelial wound closure, and uniaxial nanofibers in the bulk of the dressing might enhance fibroblast recruitment.

As alluded to previously, a key feature of a successful corneal scaffold is its ability to modulate the myofibroblast phenotype. Myofibroblasts lead to corneal haze and loss of transparency, both due to their refractive index mismatch with respect to the stroma (insufficient expression of corneal crystallins and expression of αSMA stress fibers) and due to the disordered extracellular matrix proteins they produce.[33-36] The present results show that nanofiber substrates are capable of mitigating the myofibroblast phenotype: compared to planar controls, there is a decreased expression of αSMA mRNA and protein in TGF-β-transformed myofibroblasts cultured on oriented nanofibers (**Figure 3** and **4**).

The molecular mechanism by which myofibroblasts perceive microenvironmental cues and relay information to initiate a cellular response is still unclear. Based on two

prevailing hypotheses regarding the mechanisms of cell response to the extracellular matrix, we designed siRNA experiments to discern whether myofibroblasts respond to nanofibers 1) through integrin-dependent signaling pathways, and/or 2) by direct mechanotransduction.

Integrin-dependent signaling is mediated by non-receptor tyrosine kinases, most notably focal adhesion kinase (FAK).[37,38] Integrin binding to underlying extracellular matrix components activates FAK, which subsequently influences cellular transcription events through phosphorylation of downstream signaling molecules. One of the most-studied pathways downstream of FAK is the extracellular signal-regulated kinase (ERK) cascade, which modulates cellular differentiation and directional migration.[39,40] One of the important gatekeepers in the ERK pathway is Raf-1.[41] Therefore, we chose FAK and Raf-1 as two targets for gene silencing that would reveal a possible role of integrin-dependent signaling (i.e., if silencing them blocks myofibroblast response to nanofibers).

Alternatively, direct mechanotransduction is initiated when cells pull on the extracellular matrix and develop cytoskeletal tension. This tension then leads to subsequent post-translational modifications of downstream targets that regulate gene transcription. Recently, YAP and TAZ have been suggested to play an important role in relaying to the nucleus cytoskeletal changes caused by substrate stiffness.[42,43] In relation to the cornea, Vijay and coworkers speculate that YAP and TAZ are involved in regulating contact guidance in corneal epithelial cells.[44] Therefore, we chose YAP and

TAZ as two targets for gene silencing that would reveal a possible role of mechano-transduction.

We generated knockdown cells by transfecting human corneal fibroblasts with one of the corresponding siRNAs (FAK, Raf-1, YAP or TAZ) (**Figure S-8**), and cultured them on uniaxially-aligned nanofiber substrates. We found that inhibition of myofibroblast character persisted despite knockdown of FAK or Raf-1, suggesting that integrin-dependent signaling does not seem to play a significant role in the present system. In contrast, knockdown of TAZ and YAP both partially restored αSMA expression, suggesting that mechanotransduction is involved in mitigating the myofibroblast phenotype in this system. We speculate that myofibroblasts cultured on aligned nanofibers orient their cytoskeleton in the direction of the underlying substrate, and develop greater cytoskeletal tension than they do on planar substrates or isotropically distributed nanofibers. In the view of the complexity of intracellular signaling, mechanotransduction may be one of a number of pathways modulating the myofibroblast phenotype.

To our knowledge, this is the first study which examines the role of TAZ and YAP in cellular protein expression in response to underlying substrate orientation. Previously, TAZ and YAP have only been studied as mediators of mechanical cues in the context of substrate stiffness. Since the composition, crosslinking and diameter of individual nanofibers, and the density of the fiber mats are almost identical for each mat of different orientation (isotropic, radial and uniaxial), we expect the stiffness of the fiber mats to

be similar. Thus, TAZ and YAP appear to be involved in transduction of information regarding anisotropic orientation distribution of fibrils (e.g., collagen) in the extracellular matrix.

Taken together, our results demonstrate that nanofiber substrates are well-suited for corneal wound healing scaffolds due to their transparency, non-cytotoxicity, ability to promote cell migration, and ability to modulate the myofibroblast phenotype. In particular, our findings suggest that an ideal scaffold would be composed of a top layer of isotropic nanofibers to expedite wound closure by epithelial cells, and aligned nanofibers in the bulk to mitigate the myofibroblast wound response.

2.5 Conclusions

Taken together, our results demonstrate that nanofiber substrates are well-suited for corneal wound healing scaffolds due to their transparency, non-cytotoxicity, ability to promote cell migration and ability to modulate the myofibroblast phenotype. In particular, our findings suggest that an ideal scaffold would be composed of a top layer of isotropic nanofibers to expedite wound closure by epithelial cells, and aligned nanofibers in the bulk to mitigate the myofibroblast wound response. Interestingly, integrin-dependent signaling plays a minor role (if any) in myofibroblast response to oriented nanofibers, while mechano-transduction plays a significant role.

2.6 References

1 Pot, S.A.; Liliensiek, S.J.; Myrna, K.E. *et al.* Nanoscale topography-induced modulation of fundamental cell behaviors of rabbit corneal keratocytes, fibroblasts and myofibroblasts. *Invest. Ophthalmol. Vis. Sci.* **2010**; 51:1373-1381.

2 Myrna, K.E.; Mendonsa, R.; Russell, P. *et al.* Substratum topography modulates corneal fibroblast to myofibroblast transformation. *Invest. Ophthalmol. Vis. Sci.* **2012**; 53:811-816.

3 Dreier, B.; Thomasy, S.M.; Mendonsa, R.; Raghunathan, V.K.; Russell, P.; Murphy, C.J. Substratum compliance modulates corneal fibroblast to myofibroblast transformation. *Invest. Ophthalmol. Vis. Sci.* **2013**; 54:5901-5901.

4 Phu, D.; Wray, L.S.; Warren, R.V.; Haskell, R.C.; Orwin, E.J. Effect of substrate composition and alignment on corneal cell phenotype. *Tissue Eng. Part A* **2011**; 17:799-807.

5 Thompson, R.E.; Boraas, L.C.; Sowder, M.; Bechtel, M.K.; Orwin, E.J. Three-dimensional cell culture environment promotes partial recovery of the native corneal keratocyte phenotype from a subcultured population. *Tissue Eng. Part A* **2013**; 19:1564-1572.

6 Guillemette, M.D.; Cui, B.; Roy, E. *et al.* Surface topography induces 3D self-orientation of cells and extracellular matrix resulting in improved tissue function. *Integr. Biol.* **2009**; 1:196-204.

7 Greiner, A.; Wendorff, J.H. Electrospinning: A Fascinating Method for the Preparation of Ultrathin Fibers. *Angew. Chem. Int. Ed.* **2007**; 46:5670-5703.

8 Li, D.; Xia, Y. Electrospinning of Nanofibers: Reinventing the Wheel? *Advanced Materials* **2004**; 16:1151-1170.

9 Reneker, D.H.; Chun, I. Nanometre diameter fibres of polymer, produced by electrospinning. *Nanotechnology* **1996**; 7:216-223.

10 Dosunmu, O.O.; Chase, G.G.; Kataphinan, W.; Reneker, D.H. Electrospinning of polymer nanofibers from multiple jets on a porous tubular surface. *Nanotechnology* **2006**; 17:1123-1127.

11 Meng, D.; Erol, M.; Boccaccini, A.R. Processing Technologies for 3D Nanostructured Tissue Engineering Scaffolds. *Adv. Eng. Mater.* **2010**; 12:467-487.

12 Boudriot, U.; Dersh, R.; Greiner, A.; Wendorff, J.H. Electrospinning approaches toward scaffold engineering – a brief overiew. *Artif. Organs*. **2006**; 30:785-792.

13 Sun, B.; Long, Y.Z.; Zhang, H.D.; Li, M.M.; Duvail, J.L.; Jiang, X.Y. *et al.* Advances in three-dimensional nanofibrous macrostructures via electrospinning. *Prog. Polym. Sci*. **2014**; 39:862-890.

14 He, J.; Qin, T.; Liu, Y.; Li, X.; Li, D.; Jin, Z. Electrospinning of nanofibrous scaffolds with continuous structure and material gradient. *Mater. Lett*. **2014**; 137:393-397.

15 Zheng, J.; Kontoveros, D.; Lin, H.; Hua, G.; Reneker, D.H.; Becker, M.L. *et al*. Enhanced Schwann cell attachment and alignment using one-pot "dual click" GRGDS and YIGSR derivatized nanofibers. *Biomarcomolecles* **2015**; 16:357-363.

16 Jester, J.V.; Barry-Lane, P.A.; Cavanagh, H.D.; Petroll, W.M. Induction of alpha-smooth muscle actin expression and myofibroblast transformation in cultured corneal keratocytes. *Cornea* **1996**; 15:505-516.

17 Livak, K.J.; Schmittgen, T.D. Analysis of relative gene expression data using real-time quantitative PCR and the $2^{-\Delta\Delta Ct}$ method. *Methods* **2001**; 25:402-408.

18 Singh, V.; Barbosa, F.L.; Torricelli, A.A.; Santhiago, M.R.; Wilson, S.E. Transforming growth factor β and platelet-derived growth factor modulation of myofibroblast development from corneal fibroblasts in vitro. *Exp. Eye Res.* **2014**; 120:152-160.

19 Chew, S.Y.; Mi, R.; Hoke, A.; Leong, K.W. Aligned protein-polymer composite fibers enhance nerve regeneration: a potential tissue-engineering platform. *Adv. Funct. Mater*. **2007**; 17:1288-1296.

20 Kim, H.N.; Hong, Y.; Kim, M.S.; Kim, S.M.; Suh, K.Y. Effect of orientation and density of nanotopography in dermal healing. *Biomaterials* **2012**; 33:8782-8792.

21 Londono, C.; Loureiro, M.J.; Slater, B. *et al*. Nonautonomous contact guidance signaling during collective cell migration. *Proc. Natl. Acad. Sci. U.S.A.* **2014**; 111:1807-1812.

22 Wray, L.S.; Owrin, E.J. Recreating the microenvironment of the native cornea for tissue engineering applications. *Tissue Eng. Part A.* **2009**; 15:1463-1472.

23 Netto, M.V.; Mohan, R.R.; Sinha, S.; Sharma, A.; Dupps, W.; Wilson, S.E. Stromal haze, myofibroblasts, and surface irregularity after PRK. *Exp. Eye Res*. **2006**; 82:788-797.

24 Jester, J.V.; Budge, A.; Fisher, S.; Huang, J. Corneal keratocytes: phenotypic and species differences in abundant protein expression and in vitro light-scattering. *Invest. Ophthalmol. Vis. Sci.* **2005**; 46:2369-2378.

25 Karamichos, D.; Lakshman, N.; Petroll, W.M. Regulation of corneal fibroblast morphology and collagen reorganization by extracellular matrix mechanical properties. *Invest. Ophthalmol. Vis. Sci* **2007**; 48:5030-5037.

26 Dalton, B.A.; Walboomersm X.F.; Dziegielewski, M. *et al.* Modulation of epithelial tissue and cell migration by microgrooves. *J. Biomed. Mater. Res. Part A.* **2001**; 56:195-207.

27 Diehl, K.A.; Foley, J.D.; Nealey, P.F.; Murphy, C.J. Nanoscale topography modulates corneal epithelial cell migration. *J. Biomed. Mater. Res. A.* **2005**; 75:603-611.

28 Huang, C.; Fu, X.; Liu, J.; Qi, Y.; Li,S.; Wang, H. The involvement of integrin β1 signaling in the migration and myofibroblastic differentiation of skin fibroblasts on anisotropic collagen-containing nanofibers. *Biomaterials* **2012**; 33:1791-1800.

29 Agudelo-Garcia, P.A.; De Jesus, J.K.; Williams, S.P. *et al.* Glioma cell migration on three-dimensional nanofiber scaffolds is regulated by substrate topography and abolished by inhibition of STAT3 signaling. *Neoplasia* **2011**; 13:831-840.

30 Nelson, M.T.; Short, A.; Cole, S.L. *et al.* Preferential enhanced breast cancer cell migration on biomimetic electrospun nanofiber 'cell highways'. *BMC Cancer* **2014**; 14:825

31 Danjo, Y.; Gipson, I.K. Actin 'purse string' filaments are anchored by E-cadherin-mediated adherens junctions at the leading edge of the epithelial wound, providing coordinated cell movement. *J. Cell Sci.* **1998**; 111:3323-3332.

32 Klarlund, J.K. Dual modes of motility at the leading edge of migrating epithelial cell sheets. *Proc. Natl. Acad. Sci. U.S.A.* **2012**; 109:15799-15804.

33 Jester JV, Petroll WM, Cavanagh HD. Corneal stromal wound healing in refractive surgery: the role of myofibroblasts. *Prog. Ret. Eye Res.* 1999;18:311-356.

34 Jester JV, Petroll WM, Barry PA, Cavanagh HD. Expression of alpha-smooth muscle (alpha-SM) actin during corneal wound healing. *Invest. Ophthalmol. Vis. Sci.* 1995;36:809-819.

35 Saika S, Yamanaka O, Sumioka T. *et al*. Fibrotic disorders in the eye: targets of gene therapy. *Prog. Retin. Eye. Res.* 2008;27:177-196.

36 Jester, J.V.; Ho-Chang, J. Modulation of cultured corneal keratocyte phenotype by growth factors/cytokines control in vitro contractility and extracellular matrix contraction. *Exp. Eye Res.* **2003**; 77:581-592.

37 Thannickal, V.J.; Lee, D.Y.; White, E.S. *et al.* Myofibroblast differentiation by transforming growth factor-β1 is dependent on cell adhesion and integrin signaling via focal adhesion kinase. *J. Biol. Chem.* **2003**; 278:12384-12389.

38 Hood, J.D.; Cheresh, D.A. Roles of integrins in cell invasion and migration. *Nature Reviews Cancer* **2002**; 2:91-100.

39 Lai, C-F.; Chauldhary, L.; Fausto, A. *et al.* ERK is essential for growth, differentiation, integrin expression and cell function in human osteoblastic cells. *J. Biol. Chem.* **2001**; 276:14443-14450.

40 Sieg, D.J.; Hauck, C.R.; Schlaepfer, D.D. Required role of focal adhesion kinase (FAK) for integrin-stimulated cell migration. *J. Cell Sci.* **1999**; 112:2677-2691.

41 Holderfield, M.; Deuker, M.M.; McCormick, F.; McMahon, M. Targeting RAF kinases for cancer therapy: BRAF-mutated melanoma and beyond. *Nature Reviews Cancer* **2014**; 14:455-467.

42 Dupont, S.; Morsut, L.; Aragona, M. *et al.* Role of YAP/TAZ in mechanotransduction. *Nature* **2011**; 474:179-183.

43 Thomasy, S.M.; Morgan, J.T.; Wood, J.A.; Murphy, C.J.; Russell, P. Substratum stiffness and latrunculin B modulate the gene expression of the mechanotransducers YAP and TAZ in human trabecular meshwork cells. *Exp. Eye Res.* **2013**; 113:66-73.

44 Raghunathan, V.K.; Dreier, B.; Morgan, J.T. *et al.* Involvement of YAP, TAZ and HSP90 in contact guidance and intercellular junction formation in corneal epithelial cells. *PLoS One* **2014**; 9:e109811.

45 Zhang, J.F.; Yang, D.Z.; Nie, J. Effect of electric potential and coulombic interactions on electrospinning nanofiber distribution. *Polymer International* **2008**; 57:1194-1197.

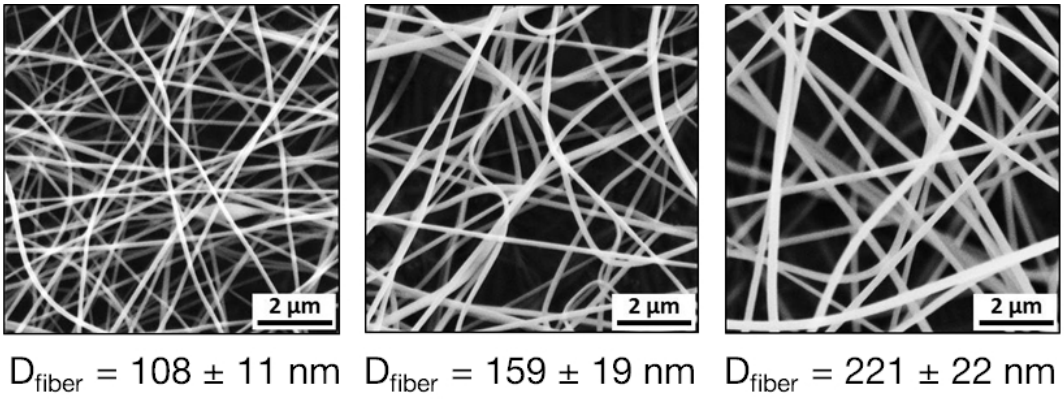

Figure 1. Scanning electron micrographs demonstrate ability to electrospin nanofibers of different diameter by choice of gelatin concentration in the electrospinning solution (for 15kV and 8cm needle to collector distance): 10% w/w gave 108 nm *(left)*, 12% w/w gave 159 nm *(middle)* and 15% w/w gave 221 nm *(right).*

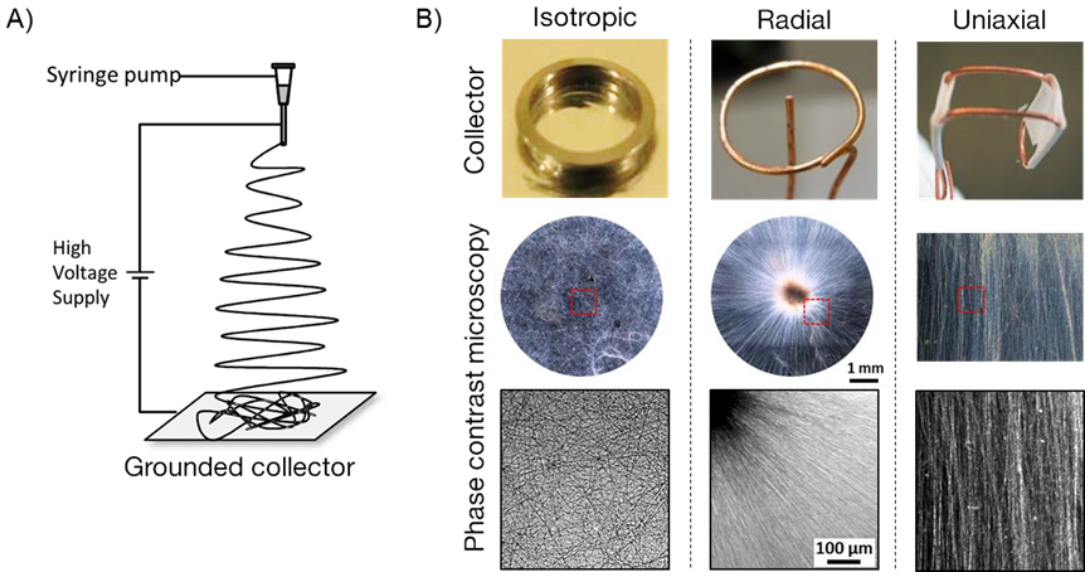

Figure 2. Nanofiber mats were fabricated by electrospinning. **(A)** Schematic of electrospinning apparatus. **(B)** Different grounded collectors used to electrospin isotropic *(B, left*, planar electrode with a ring used to recover the fiber mat*)*, radially aligned *(B, middle)* and uniaxially aligned *(B, right)* nanofibers.

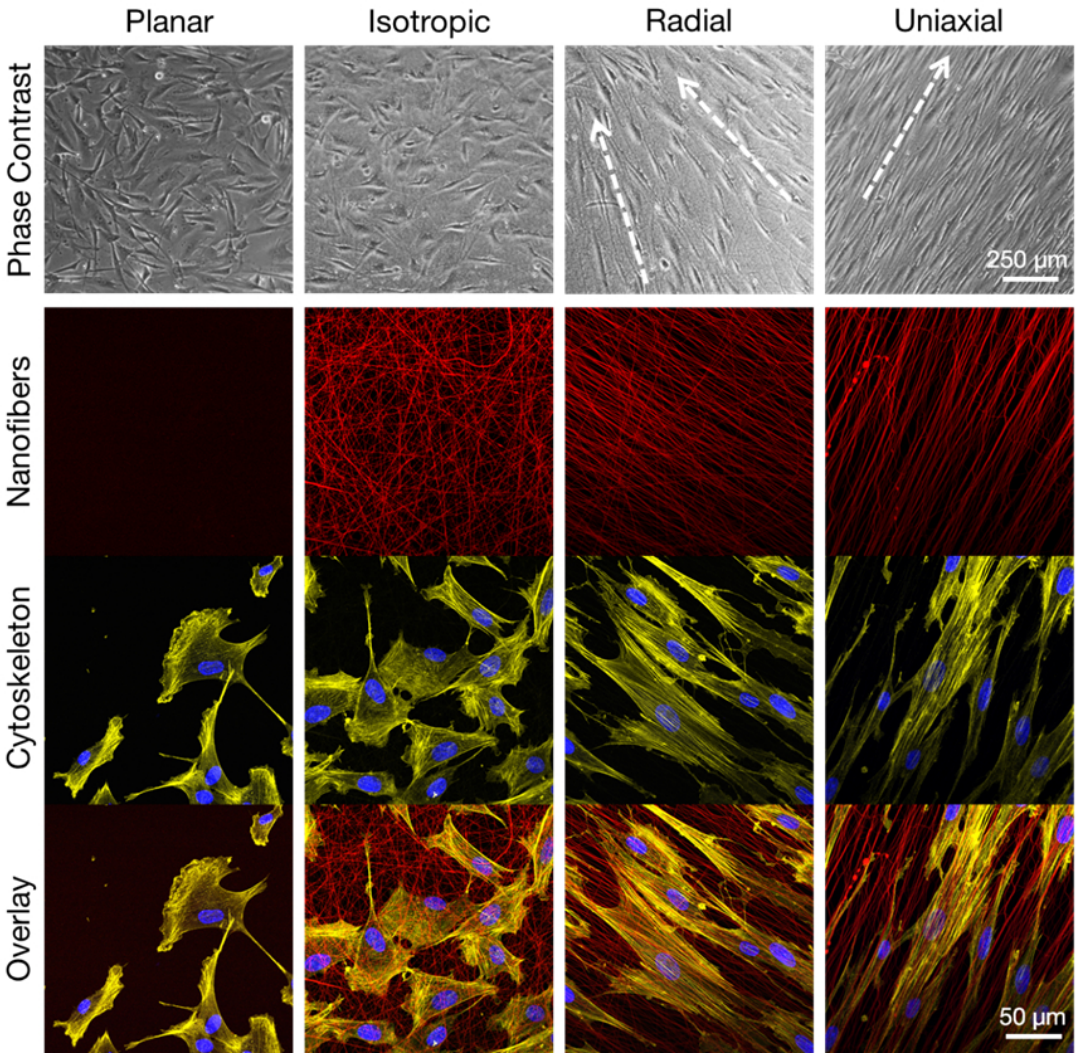

Figure 3. Nanofiber orientation influences cell shape and orientation. Phase contrast micrographs *(top row)* show that corneal fibroblasts (P5) are elongated when exposed to uniaxial and radial nanofibers compared to either a planar surface or isotropic nanofibers. Immunostaining *(second to bottom row)* demonstrates that cells orient along the same axis of the underlying nanofibers. Nanofibers were labeled using NHS-FITC (false color to red for consistency with Figure 3); cell nuclei, Hoescht stain (blue); F-actin cytoskeleton, phalloidin-Rhodamine (false color to yellow to avoid confusing with the αSMA in Figure 3). Nanofiber diameter = 155 nm.

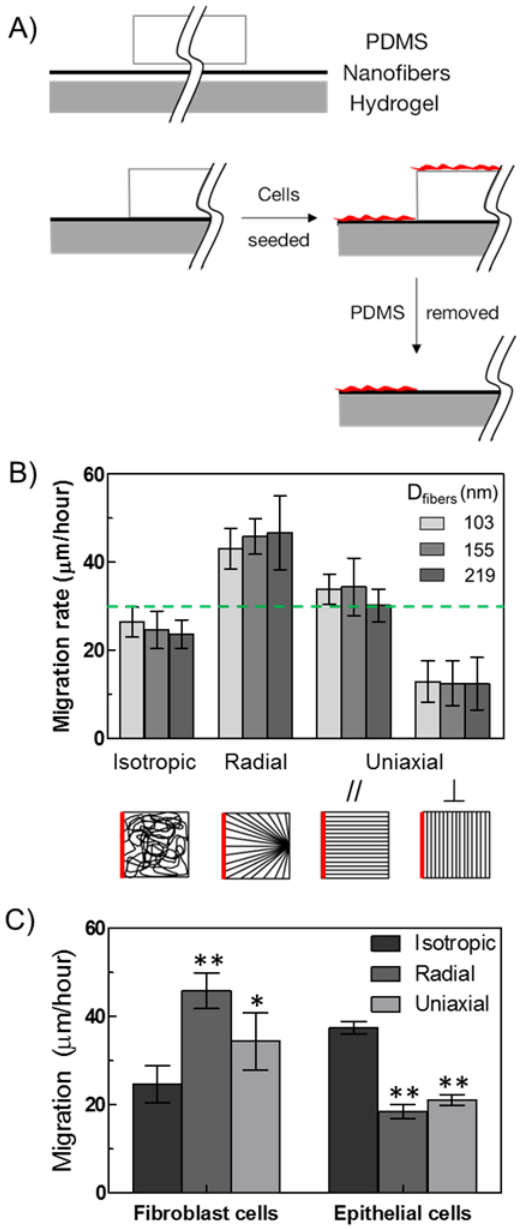

Figure 4. Nanofiber orientation affects the rate of cell migration. **(A)** Schematic of *in vitro* mock wound healing assay (after cells grow to confluency, a 4 mm dia. polydimelthylsiloxane, PDMS, mask is lifted to expose the substrate). **(B)** Corneal fibroblasts migrate faster along oriented nanofibers, both radial and uniaxial, compared with isotropic nanofibers. Green dashed line indicates fibroblast migration rate on a control planar surface. Solid red lines in schematic diagram below indicate initial cell boundary.

P-values are in Supplementary Tables 1-2. **(C)** Epithelial cells migrate faster on isotropic nanofibers than on oriented ones (radial or uniaxial). *: p-value < 0.05; **: p-value < 0.001 compared to isotropic nanofibers. Cells between passages 5-8 were used in these experiments.

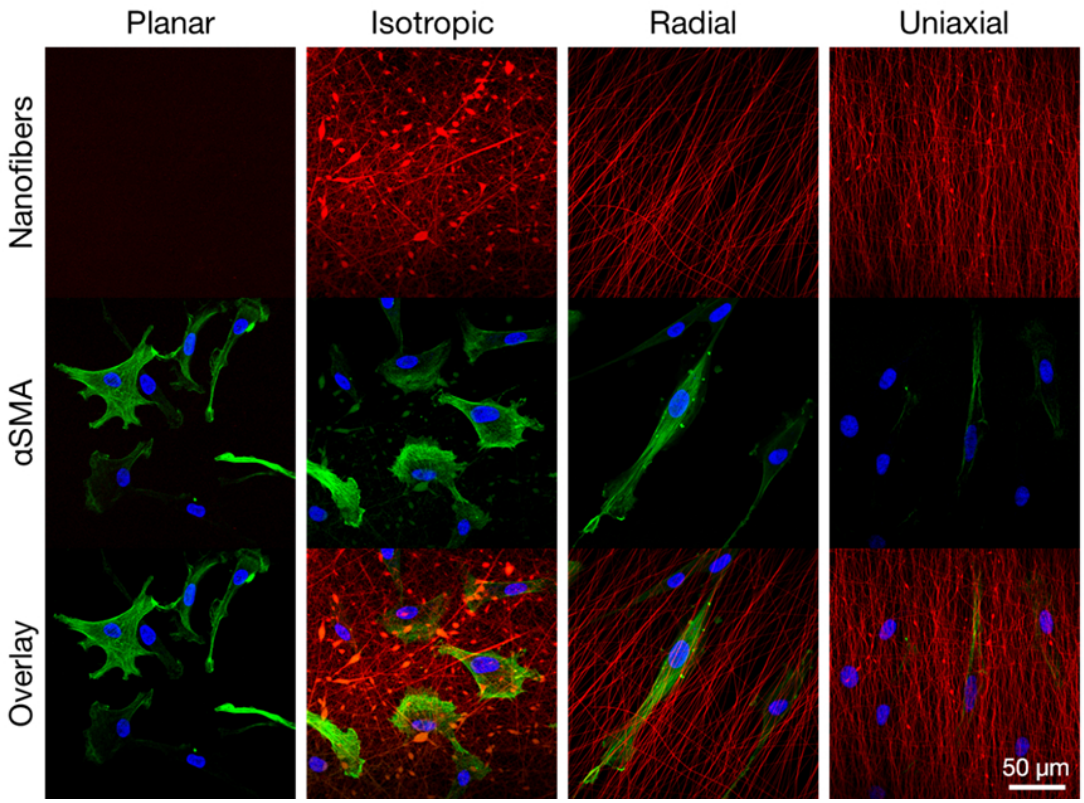

Figure 5. Representative images of corneal fibroblasts (P5) transformed to myofibroblasts with 1 ng/mL TGF-β on nanofibers of different orientation. Relative to planar control, there are fewer cells positive for αSMA on oriented nanofibers. Nanofibers were labeled using NHS-Rhodamine (red); cell nuclei, Hoechst stain (blue); αSMA, anti-αSMA-FITC (green). Nanofiber diameter = 155 nm.

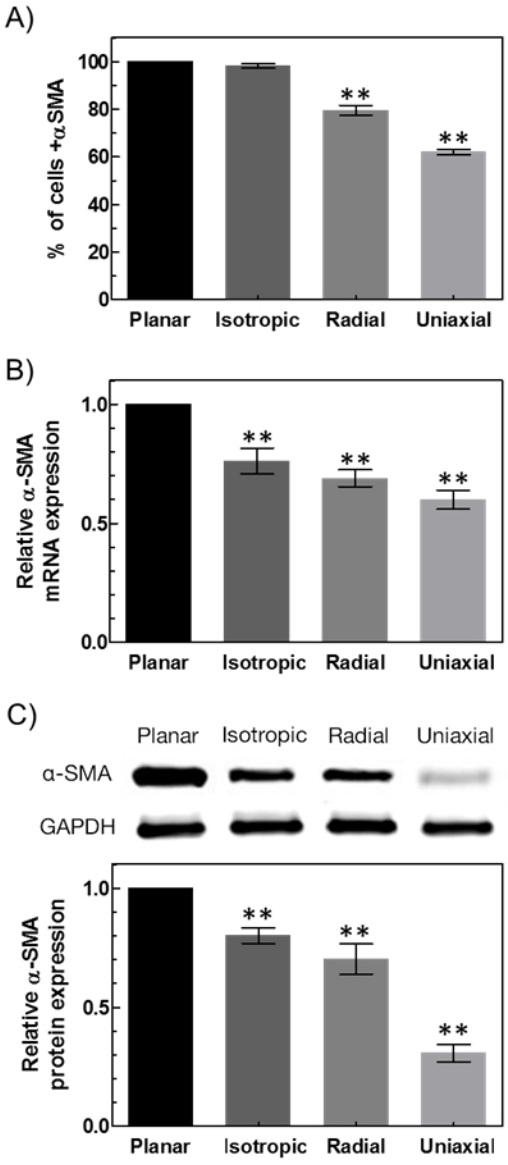

Figure 6. Relative to Planar control, TGF-β (1 ng/mL) induced myofibroblasts grown on nanofiber surfaces demonstrated **(A)** fewer α-SMA positive cells (analysis of images of Figure 3), (**B)** significantly lower levels of α-SMA mRNA, and (**C)** significantly lower α-SMA protein expression based on Western blot analysis of cell lysates, quantified by the ratio of α-SMA protein signals normalized by GAPDH. Passage 5 cells were used in all

experiments. Nanofiber diameter = 155 nm. **: p-value < 0.001 compared to planar controls.

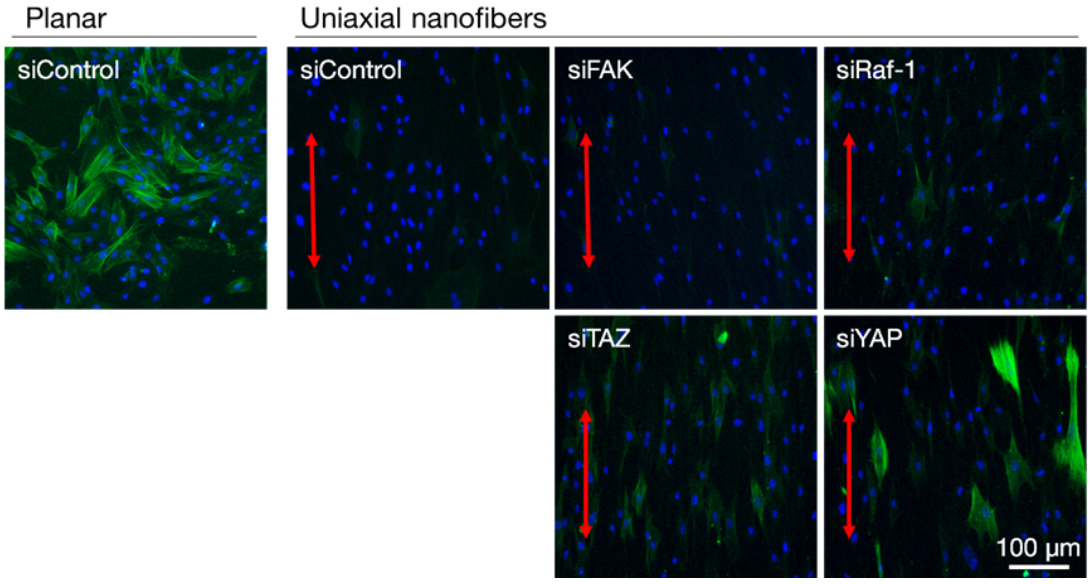

Figure 7. Human corneal fibroblasts (P5) were transfected with the indicated siRNA (control, FAK, Raf-1, TAZ, YAP), seeded on uniaxially-aligned nanofibers and transformed to myofibroblasts with 10 ng/mL TGF-β. (The greater concentration used for human cells compared to rabbit cells in Figures 3-4 was selected to provide visible αSMA expression in the control.) Cell nuclei, Hoechst stain (blue); αSMA, anti-αSMA-FITC (green). Red arrows indicate direction of the underlying nanofibers. Nanofiber diameter = 155 nm.

Additional information

Electrospinning

The basic setup of an electrospinning apparatus consists of three main components: a high-voltage supply, a syringe needle and a grounded collector (Figure). The electrospinning solution (usually polymeric or protein-based) is fed through the syringe needle. During the electrospinning process, a high voltage (usually in the range of 10 - 30 kV) is applied to the solution, and the droplet of fluid coming out from the needle becomes highly charged. The droplet experiences two major electrostatic forces: the electrostatic repulsion between surface charges in the droplet, and the Coulomb forces exerted by the external electric field. These interactions cause the droplet to deform into a conical shape, known as the Taylor cone. When the electrostatic forces pass a certain critical value and are able to overcome the surface tension of the droplet, a charged liquid jet is ejected from the tip of the Taylor cone, and the jet undergoes an unstable whipping process. The solvent evaporates as the liquid jet is accelerated towards the counterelectrode, leading to the formation of continuous thin fibers. The fibers are deposited onto the grounded collector as a randomly-oriented, non-woven mat. By changing the type of grounded collector, we can obtain nanofiber substrates of different orientation.

How aligned fibers are formed

To fabricate uniaxially-aligned nanofibers, we used a pair of split electrodes as the grounded collector. We can explain the formation of aligned fibers on split electrodes using Coulombic interactions and electrostatic forces.[45] When a fiber is deposited

across the gap between the split electrodes, it does not discharge immediately, and is affected by fibers already present. The Coulomb force generated by the newly-deposited fiber is

$$F = \frac{k\lambda^2}{r^2}$$

where k is the Coulomb's constant, λ is the linear charge density of the fiber, and r is the distance between two interacting fibers. In **Figure S-1**, when r1<r2 (as in the top region of the newly deposited fiber), F1 will be stronger than F2, and thus, the top of the fiber is pushed towards fiber 2. At the same time, the bottom region of the fiber experiences forces of the opposite effect, and therefore, the overall fiber is preferentially aligned with the other fibers. In addition, fibers also prefer to arrange perpendicularly to the split electrodes, because this configuration possesses the lowest electrostatic energy (Figure 19-B).

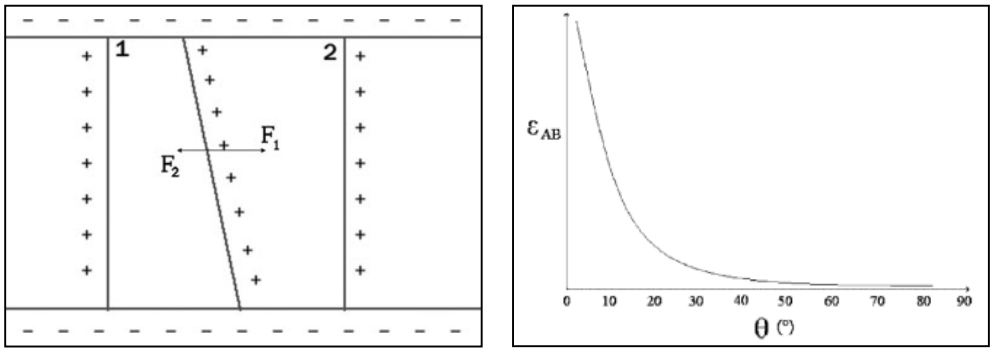

Figure S-1. (A) Coulombic interaction between electrospun fibers (B) Relationship between the electrostatic potential between the split electrodes (ε) and the angle between the fiber and the electrode (Θ).[45]

Isolation of corneal fibroblasts from rabbit eyes

10-15 eyeballs from young rabbits were purchased from Pel-Freez and used immediately upon delivery. Excess fat and connective tissue was trimmed from the eyeballs. Cold RPMI media was used to wash the surface of the eye. For each eyeball, the epithelium layer was scraped off using a scalpel. The cornea (with 5 mm scleral rim for handling) was cut from the eyeball. The cornea was then placed upside down on a sterile petri-dish. The iris was then removed and the endothelial layer was removed with a sterile cotton-tipped applicator. The middle portion of the cornea (now without the epithelium and endothelium) was punched out using a corneal punch (8 mm diameter). The stromal buttons were then placed in a cell culture dish filled with fresh RPMI media. This process was repeated until all the eyeballs were processed. All 10-15 stromal buttons were then placed in a 14 mL round-bottom tube with 10 mL digest media (0.5 mg/mL hyaluronidase, 2 mg/mL collagenase, 0.02% Pen/Strep/Fungizone in DMEM). The tube was then placed in the cell culture incubator (5% CO2, 37oC) overnight. The next day, the solution was pipetted up and down to make a homogeneous solution (debris will be observed at the bottom of the tube). The suspension was transferred to a 50 mL conical tube and was diluted with 20 mL culture medium. The mixture was centrifuged at 1,500 rpm for 5 minutes, and the supernatant was removed. The cell pellet was resuspended in 2 mL culture medium, and the cells were plated in 100 mm cell culture dishes at a density of 2.5 x 104 cells/cm2. The cell medium was replaced every 2 days until the cells were 90% confluent. The cells were then either passaged or frozen.

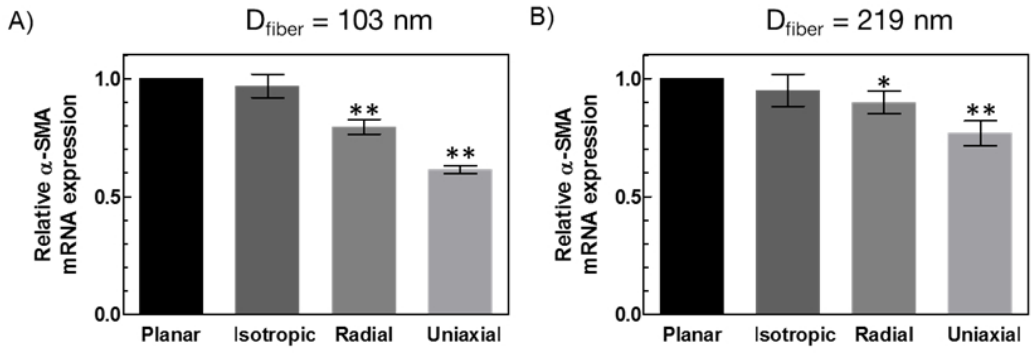

Figure S-2. TGF-β induced myofibroblasts grown on nanofiber surfaces of **(A)** 103 nm and **(B)** 219 nm show a similar trend in α-SMA mRNA expression to that of 155 nm **(Figure 4)**, with cells seeded on uniaxially-aligned nanofibers consistently expressing the lowest levels of α-SMA mRNA.

*: p-value < 0.01 compared to planar controls. **: p-value < 0.001 compared to planar controls.

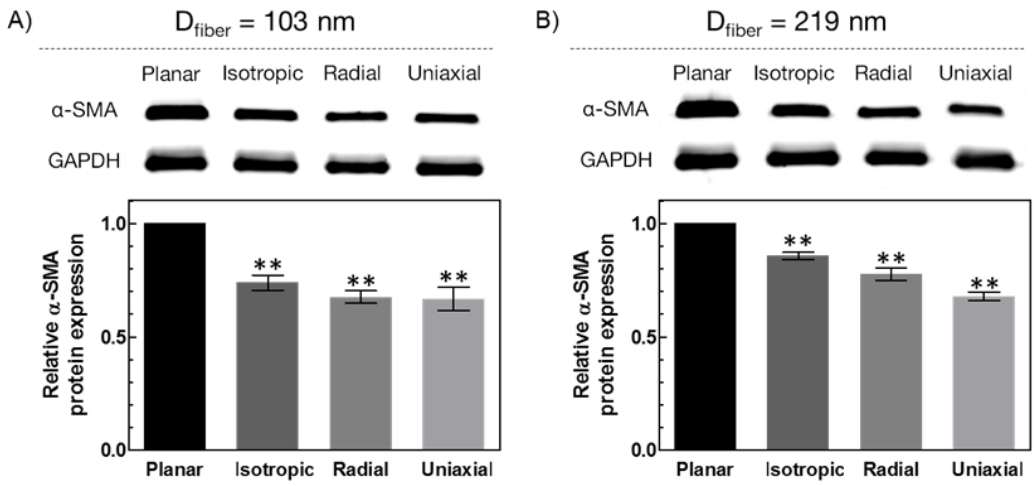

Figure S-3. TGF-β induced myofibroblasts grown on nanofiber surfaces of **(A)** 103 nm and **(B)** 219 nm show a similar αSMA protein expression trend to that of 155 nm **(Figure 4)**, with cells seeded on uniaxially-aligned nanofibers expressing the lowest levels of α-SMA when normalized to GAPDH. **: p-value < 0.001 compared to planar controls.

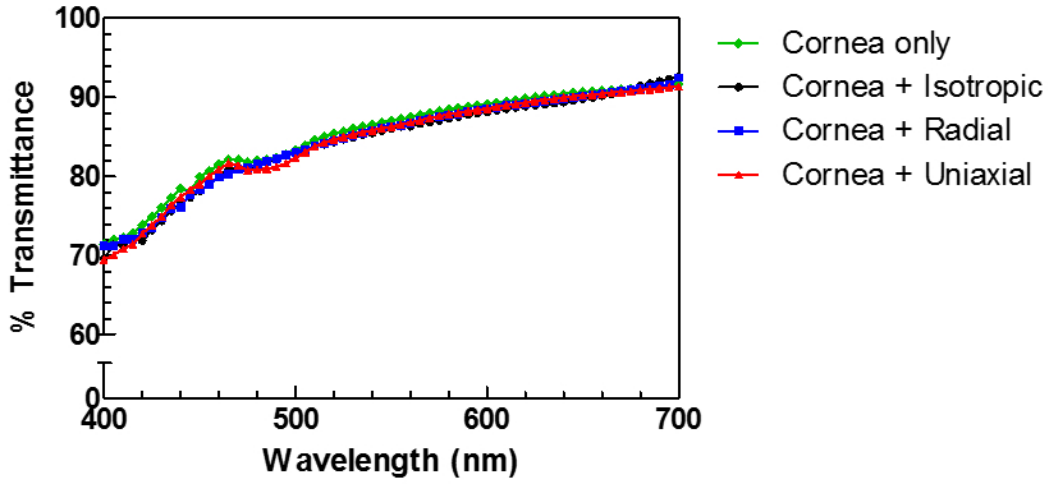

Figure S-4. Optical transmittance of various nanofiber mats placed on an explanted porcine cornea after application of PBS drops demonstrates that the nanofibers do not significantly reduce light transmission through the cornea.

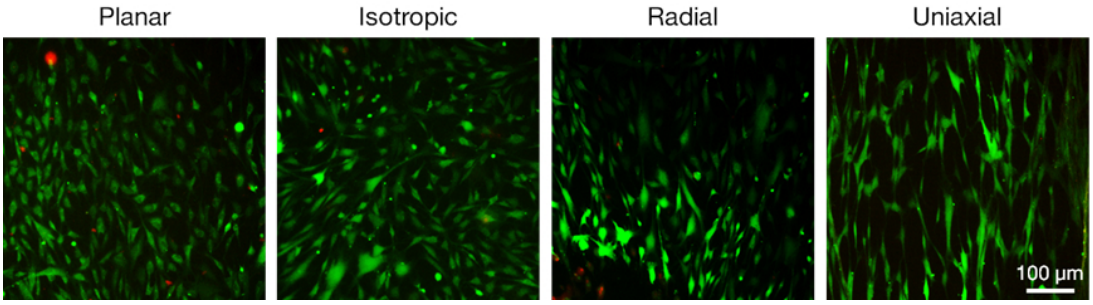

Figure S-5. LIVE/DEAD cell viability assay confirms that corneal fibroblasts seeded on nanofiber surfaces show no cytotoxicity issues. Green signal: live cells; Red signal: dead cells. Two days after seeding P5 cells. Scale bar is 100 µm.

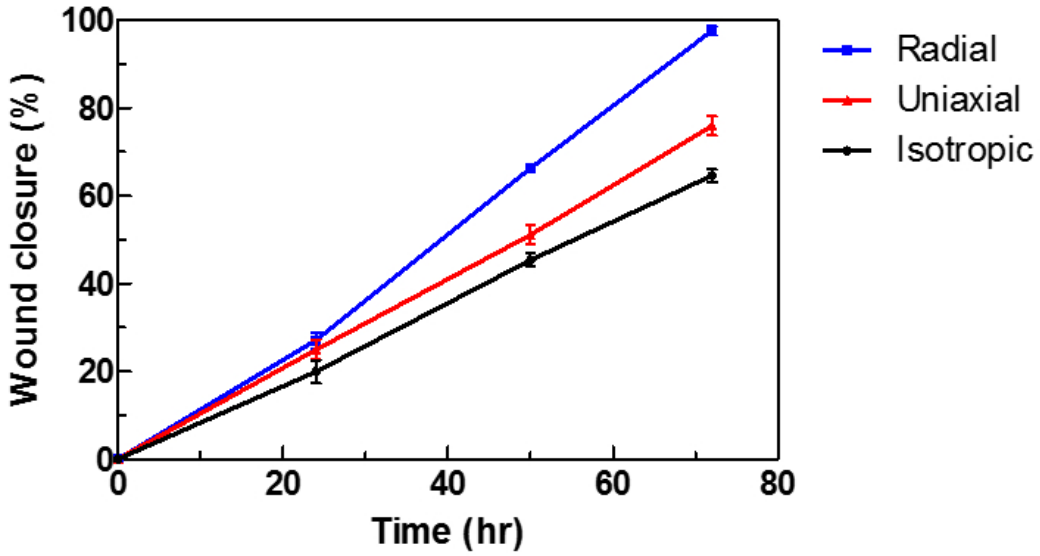

Figure S-6. In the mock wound-healing assay using a 4mm initial diameter 'wound,' the remaining wound area (i.e., not yet infiltrated with cells) is correlated with the rate of cell migration. Corneal fibroblasts that are cultured on radially-aligned nanofibers increase their rate of migration with time (i.e. as they move closer to the center of the radial pattern), while those that are on uniaxial and isotropic maintain a constant rate of migration.

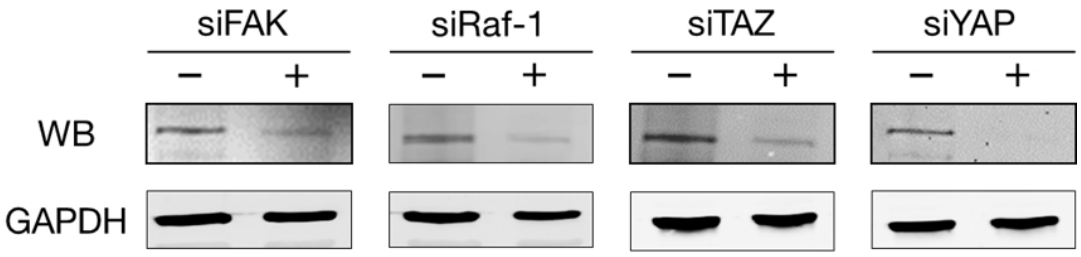

Figure S-7. Validation that silencing RNA did indeed reduce the expression of the corresponding protein. Top: Western Blot (WB) and antibody staining of the corresponding protein band for each case. Bottom: GAPDH band shows that gel loading was consistent.

Table S-1. Varying the nanofiber orientation by changing the grounded collector does not significantly influence the average fiber diameter at each protein concentration.

	10% gelatin	**12% gelatin**	**15% gelatin**
Isotropic	107.9 ± 10.7 nm	158.8 ± 18.7 nm	221.2 ± 22.2 nm
Radial	106.0 ± 14.1 nm	152.9 ± 16.1 nm	218.4 ± 27.3 nm
Uniaxial	103.2 ± 12.8 nm	155.3 ± 17.1 nm	219.3 ± 23.5 nm

Table S-2. P-values from two-tailed t-test show that nanofiber orientation (diameter fixed) significantly affects the rate of corneal fibroblast migration (**Figure 4**). Fields shaded in orange highlight results with relatively large p-values (0.01 or greater) that are still of significance ($p < 0.05$).

105 nm	Isotropic	Radial	Uniaxial //	Uniaxial ⊥
Isotropic		< 0.001	0.001	0.002
Radial	< 0.001		0.007	< 0.001
Uniaxial //	0.001	0.007		< 0.001
Uniaxial ⊥	0.002	< 0.001	< 0.001	

155 nm	Isotropic	Radial	Uniaxial //	Uniaxial ⊥
Isotropic		< 0.001	0.02	0.003
Radial	< 0.001		0.01	< 0.001
Uniaxial //	0.02	0.01		< 0.001
Uniaxial ⊥	0.003	< 0.001	< 0.001	

220 nm	Isotropic	Radial	Uniaxial //	Uniaxial ⊥
Isotropic		0.01	0.03	0.03
Radial	0.01		0.02	0.001
Uniaxial //	0.03	0.02		0.004
Uniaxial ⊥	0.03	0.001	0.004	

Table S-3. P-values from two-tailed t-test show that nanofiber diameter (orientation fixed) does not affect the rate of corneal fibroblast migration (**Figure 4**). Fields shaded in red show p values that exceed the threshold for significance (p> 0.05).

Isotropic	105 nm	155 nm	220 nm
105 nm		0.4	0.05
155 nm	0.4		0.6
220 nm	0.05	0.6	

Radial	105 nm	155 nm	220 nm
105 nm		0.4	0.5
155 nm	0.4		0.9
220 nm	0.5	0.9	

Uniaxial //	105 nm	155 nm	220 nm
105 nm		0.9	0.2
155 nm	0.9		0.3
220 nm	0.2	0.3	

Uniaxial ⊥	105 nm	155 nm	220 nm
105 nm		0.9	0.9
155 nm	0.9		1.0
220 nm	0.9	1.0	

Table S-4. Varying the nanofiber orientation by changing the grounded collector does not significantly influence the average fiber density.

	D_{fiber} = 155 nm
Isotropic	0.42 ± 0.06
Radial	0.41 ± 0.05
Uniaxial	0.41 ± 0.04

Chapter 3

Effects of growth factors on corneal myofibroblast phenotype

3.1 Introduction

The wound-healing cascade is complex, involving multiple processes such as cell proliferation, differentiation and migration.[1-3] These events act to repair and replace injured tissue, and are mediated by cytokines released from cells upon injury. In relation to the cornea, the repair response mainly involves epithelial regrowth, keratocyte-myofibroblast differentiation and new matrix deposition by myofibroblasts.[2,3] As described in Chapter 2, the central challenge to treating corneal wounds is mitigating the myofibroblast phenotype to reduce the production of α-smooth muscle actin (αSMA) that pulls on wound edges and disordered ECM proteins that lead to corneal blindness.[4,5] Identification of growth factors that modulate the myofibroblast phenotype may promote an orderly wound-healing response to recover the transparency of the cornea.

Growth factors influence cell decisions by binding to cell-surface receptors, which then become activated to initiate signaling cascades that affect gene transcription. Much progress has been made in identifying growth factors that influence corneal wound healing. For example, Yu and coworkers have shown that endogenous heparin-binding epidermal growth factor (HB-EGF) is essential for epithelial wound closure.[6] Also, epidermal growth factor (EGF) has been shown to increase migration and proliferation of keratocytes.[7] Jester and coworkers demonstrated that cells treated with fibroblast growth factor (FGF) exhibit a reduced expression of αSMA[8], a cell marker for myofibroblasts. In addition, Kim and coworkers found that the addition of platelet-

derived growth factor (PDGF) induces keratocyte elongation without the formation of stress fibers and promotes the deposition of ECM proteins that closely resemble those of the native cornea.[9,10]

Building on their findings, we chose to examine the role of EGF, FGF and PDGF on myofibroblast phenotype in the present study. Specifically, we systematically varied the concentration of each growth factor (0.1 - 100 ng/mL) in the cell culture medium of TGF-β transformed myofibroblasts and analyzed their αSMA expression. Our results show that each growth factor is capable of reducing αSMA expression in myofibroblasts, with a strong dependence in the growth factor concentration. Gene-silencing experiments suggest that one of the pathways in which growth factors regulate αSMA expression is through the ERK signaling cascade. In relation to potential clinical translation, the addition of growth factors (at their optimal concentrations) may prove valuable to orchestrate an orderly wound-healing response.

3.2 Methods

Rabbit corneal fibroblast isolation and culture. Fibroblasts were isolated from young rabbit eyes (mixed gender, approximately 8-12 weeks old, Pel-Freez, Rogers, AR) as described elsewhere.[11] The isolated fibroblasts were passaged every 2-3 days when 95% confluence was reached. Cells from passages 5-8 were used in the present study. Corneal fibroblasts were seeded in 6-well plates ($5x10^4$ cells/mL). Transforming growth factor-beta (TGF-β, 1 ng/mL) was added 24 hours post-seeding to induce the myofibroblast phenotype[11,12], and cells were grown for 72 hours. The cell culture medium was then

removed and replaced with fresh medium containing growth factors (EGF, FGF, PDGF at 0 – 100 ng/mL). Cells were grown in growth-factor-rich medium for 72 hours prior to assays.

Identification of αSMA producing cells using immunocytochemistry

Myofibroblasts treated with growth factors were first washed 3 times with DPBS, and fixed in 4% paraformaldehyde (in DPBS) for 10 minutes. Fixed cells were then washed 3x with DPBS and permeabilized with 0.1% Triton X-100 in DPBS for 10 minutes. Blocking was performed with 1% bovine serum albumin in DPBS for 30 minutes at room temperature. The cells were then incubated with 1:1000 FITC-conjugated mouse anti-αSMA antibody (Sigma Aldrich, St. Louis, MO) in 1% BSA for 60 minutes at room temperature. Cells were washed 3 times with DPBS, and cell nuclei were stained with Hoescht 33342 (Invitrogen, Grand Island, NY) at 0.5 ug/mL for 10 minutes at room temperature in the dark. Cells were then stored in PBS until imaging with a Zeiss Axiovert 25CFL fluorescent microscope. For analysis of αSMA protein expression, five randomly-selected locations on each scaffold were imaged using a 5x objective for both Hoescht and FITC fluorescence. Blue dots (Hoechst stained nuclei) were counted as total cells per image, while cells presenting a green signal (FITC) were counted as positive for αSMA. Immunocytochemistry was performed on samples from three independent experiments.

Quantitative PCR (qPCR)

Myofibroblasts treated with growth factors were lifted using 0.05% TRED and pelleted by centrifuging at 900 rpm for 3 minutes. RNA was extracted using the Qiagen RNeasy kit following the manufacturer's protocol (Qiagen, Valencia, CA). RNA yield was determined using a Nanodrop spectrophotometer (Thermo Sci., Wilmington, DE). Gene expression was evaluated using qPCR with an EXPRESS One-Step SYBR® GreenER™ Universal kit (Invitrogen, Grand Island, NY) in an Eco Real-Time PCR system (Illumina, San Diego, CA). qPCR was carried out using 50 ng RNA per sample and commercially-available primers for αSMA, GAPDH and β-actin in a total reaction volume of 10 μL per sample. GAPDH and β-actin served as references. Products were evaluated by melt curve analysis and sizing on agarose gels. Gene expression was normalized relative to the expression of mRNA from control cells (grown under the same culture conditions without added growth factors) using the ΔΔCt method as described elsewhere.[13] The mRNA from control untreated cells was given an arbitrary value of 1.0. qPCR reactions were run in triplicates per sample, and the experiment was repeated three times on separate days.

Western blotting

Myofibroblasts treated with growth factors were lifted, pelleted (as described above) and lysed with M-PER mammalian protein extraction reagent following the manufacturer's protocol (Thermo Sci., Rockford, IL). Insoluble cellular debris was removed by centrifugation at 10k rpm for 10 minutes and the supernatant was collected into new tubes. A bicinchroninic acid (BCA) protein assay (Thermo Sci., Rockford, IL) was performed to determine the concentration of the extracted protein. Equivalent

amounts of protein (10 µg per sample) were mixed with loading buffer (Laemmli sample buffer, Bio-Rad, Hercules, CA), denatured by boiling for 5 minutes, and loaded onto a MINI-PROTEAN TGX precast gel (Bio-Rad, Hercules, CA). Gel electrophoresis was performed at 200V for 40 minutes. Protein bands were then transferred to a nitrocellulose membrane at 100V for 1 hour. The nitrocellulose membrane was blocked for 1 hour at room temperature in blocking solution (5% BSA, 0.1% Tween-20 in DPBS). The membrane was then incubated with mouse anti-GAPDH antibody (Invitrogen, Grand Island, NY) at 1:2500 dilution in blocking solution for 1 hour at room temperature. The blot was washed 3x (10 minutes each) in DPBS-T (DPBS + 0.1% Tween-20), followed by incubation with AlexaFluor 647 goat anti-mouse secondary antibody (Invitrogen, Grand Island, NY) in blocking solution at 1:2500 dilution for 1 hour in the dark. The blot was washed 3x (10 minutes each) in DPBS-T and incubated with FITC-conjugated mouse anti-αSMA antibody (Sigma Aldrich, St. Louis, MO) at 1:2500 dilution in blocking solution for 1 hour in the dark. After rinsing with DPBS-T, the blot was scanned using a Typhoon Trio Scanner (GE, Piscataway, NJ). Relative intensities of α-SMA bands were normalized with GAPDH bands. Immunoblotting was performed on samples from three independent experiments.

siRNA transfection of human corneal fibroblasts. FAK, Raf-1, YAP and TAZ were knocked down in human corneal fibroblasts (ScienCell, Carlsbad, CA) using siRNAs targeted to the corresponding genes (all from Santa Cruz Biotechnology, Dallas, TX). Cells (P3, 60-70% confluent) were transfected with siRNA (60 nM) using siRNA transfection reagent (Santa Cruz Biotechnology, Dallas, TX) according to the

manufacturer's instructions. Control cells were transfected with FITC-conjugated control siRNA (Santa Cruz Biotechnology, Dallas, TX). The cells were incubated for 72 hours before collection.

Statistical analysis. All results are reported as mean ± standard deviation. Differences between groups were assessed by two-tailed t-tests. $P < 0.05$ was considered as significant.

3.3 Results

Growth factors can reduce the number of αSMA-expressing myofibroblasts

To study the response of myofibroblasts (induced from corneal fibroblasts using 72 hour exposure to medium with TGF-β at 1 ng/mL) to growth factors at different concentrations (0.1 - 100 ng/mL), we added growth factors to the cell culture medium and counted the number expressing αSMA.

Myofibroblasts treated with 0.1 ng/mL EGF showed a measurable reduction in the number of αSMA producing cells (15%, p-value < 0.001); the effect increased to 80% reduction upon increasing EGF concentration to 1 ng/mL, and the effect remained at that level for concentrations up to 100 ng/mL (**Figure 1**).

For FGF-treated cells, the number of cells producing αSMA was not significantly changed by concentrations of 0.1 and 1 ng/mL (>90% cells expressed αSMA), and

decreased similarly for concentrations of 10 ng/mL or more (65%, 70% and 85% reductions for 10, 50 and 100 ng/mL) (**Figure 2**).

For PDGF-treated cells, we observed a non-monotonic effect on the number of αSMA-producing cells (**Figure 3**). The lowest concentration (0.1 ng/mL) and the highest concentration (50 and 100 ng/mL) reduced the number of αSMA-producing cells by 80% or more. However 10 ng/mL PDGF had relatively little effect.

Growth factors can inhibit αSMA gene and protein expression

Total mRNA was isolated from cells treated with different growth factors at 50 or 100 ng/mL (based on largest decrease in αSMA-producing cells as described above) and analyzed using qPCR. Consistent with their effects on the number of αSMA-producing cells, 100 ng/mL concentrations strongly reduce αSMA-mRNA (**Figure 4**). Western blot analysis of αSMA protein content (normalized by GAPDH) in cells treated with different growth factors showed significantly lower αSMA protein expression compared to untreated cells (**Figure 5**), with cells treated with 100 ng/mL growth factor showing the largest decrease (30 - 40% in all cases).

Growth factors can mitigate myofibroblasts cultured on oriented nanofibers

In Chapter 2, we observed a reduction of αSMA expression in TGF-β myofibroblasts cultured on oriented nanofibers. To investigate whether the addition of growth factors could further mitigate the myofibroblast phenotype, we added EGF, FGF or PDGF (50 or 100 ng/mL) in the cell culture medium of myofibroblasts seeded on uniaxially-

aligned nanofibers and visualized the αSMA expression of the cells. The myofibroblasts were transformed from fibroblasts using 10 ng/mL TGF-β (a greater concentration was used here compared to Figures 1-5 to provide visible αSMA expression in the control). We confirmed that the addition of growth factors reduces αSMA expression in myofibroblasts cultured on oriented nanofibers (**Figure 6**).

FAK/Raf-1 play a role in modulating αSMA expression

To investigate the molecular mechanism by which cells treated with growth factors demonstrate a reduced αSMA expression, we examined focal adhesion kinase (FAK), serine/threonine protein kinase Raf-1, transcription co-activator TAZ and Yes-associated protein (YAP) by generating the corresponding knocked-down cells (transfected human corneal fibroblasts with the corresponding siRNA). These cells were then transformed into myofibroblasts with 10 ng/mL TGF-β, treated with EGF, FGF or PDGF at 100 ng/mL, and their αSMA expression was visualized using immunocytochemistry (**Figure 7**). Knockdown of FAK and Raf-1 partially reversed growth-factor-dependent changes in αSMA expression: both siFAK and siRaf-1 cells expressed αSMA (labeled green) at a level similar to control untreated cells. Interestingly, siTAZ and siYAP cells also expressed αSMA, but at a much lower intensity than control untreated cells.

3.4 Discussion

When the cornea encounters trauma, quiescent keratocytes transition into hyperactive myofibroblasts that proliferate and produce disordered intercellular and extracellular

proteins to repair the wound.[4,5] This repair response is a complex biological process, which involves many signaling cascades initiated by ligand-receptor binding. In particular, the use of peptide growth factors has emerged as an effective way to enhance corneal wound healing.[14-17] However, the type and concentration of growth factors that can produce such effects is still unclear. In the present study, we examined the effects of three growth factors (EGF, FGF and PDGF) on myofibroblast phenotype. The concentration range studied was between 0.1 to 100 ng/mL based on past literature.[16,18] The rationale for choosing each growth factor and a discussion on our experimental findings are detailed in separate sections below.

Effect of EGF on myofibroblast phenotype

EGF has been extensively studied for its effects on stimulating migration of both normal and cancer cells, including keratinocytes[19], prostate carcinoma cells[20], etc. In relation to the cornea, EGF has been shown to promote epithelial cell proliferation, fibroblast migration and endothelial cell mitosis *in vitro*[21,22], and accelerate reepithelialization of corneal surface injuries *in vivo*[23]. Based on these studies, we hypothesized that the addition of EGF to our wound-healing scaffold would encourage epithelial regrowth. Since EGF released from the scaffold may diffuse into other parts of the cornea, we were interested in examining effects of EGF on myofibroblast behavior as well.

We observed that EGF modulates the myofibroblast phenotype (**Figures 1, 4-5**). By adding 1 ng/mL of EGF to the cell culture medium of TGF-β transformed myofibroblasts, there were significantly fewer cells expressing αSMA compared to

untreated control cells. This effect was also observed at higher EGF concentrations of 10 - 100 ng/mL (highest tested). These results contrasts those of He and Bazan, who reported that EGF (5 - 200 ng/mL) synergizes with TGF-β to induce fibroblast-myofibroblast differentiation.[24] It may be possible to explain this discrepancy by the difference in the order in which EGF was added into the culture medium. In He's experiment, EGF was added simultaneously with TGF-β; whereas, in our experiment, we first induced myofibroblast transition with TGF-β, then replaced the culture medium with fresh medium containing EGF. Indeed, Kimura and coworkers observed that when cells were first cultured with TGF-β (3 days) and then cultured with EGF (3 days) after TGF-β removal, there was a decreased expression of αSMA compared to samples without EGF.[25] In the skin, it has been observed that there is a burst of active TGF-β immediately after wounding (9-fold increase 1 hour after wounding), which declines within 24 hours (to a level slightly above that of normal skin and surrounding tissue).[26] It is possible that TGF-β expression in corneal wound healing follows a similar trend; thus, sequential addition of TGF-β and EGF may be an accurate *in vitro* representation of the therapeutic situation.

Effect of FGF on myofibroblast phenotype

FGF has been widely studied for its effects on promoting proliferation in a broad range of cell types, including keratinocytes[27], osteoblasts[28] and endothelial cells[29]. In relation to the cornea, FGF has been shown to stimulate proliferation of epithelial cells and stromal fibroblasts, and to enhance healing after an epithelial scrape injury *in vivo*.[30,31] In addition, Maltseva and coworkers demonstrated that corneal myofibroblasts cultured

in the presence of FGF (20 ng/mL) and heparin (5 μg/mL) have reduced αSMA expression.[32] Although they found that the addition of FGF alone did not produce such effects, it has been suggested that raising the concentration of FGF (to 50 ng/mL) may eliminate the requirement of heparin.[33] Based on these findings, the present study examines the effects of FGF alone (0.1 - 100 ng/mL) on myofibroblast phenotype.

We observed that FGF reduces αSMA expression in myofibroblasts in a dose-dependent manner (**Figure 2, 4-5**). At low FGF concentrations (0.1 - 1 ng/mL), myofibroblasts express αSMA at levels that are indistinguishable from untreated control cells. We first see effects of FGF at a concentration of 10 ng/mL (65% fewer αSMA-expressing cells). Further increasing FGF concentration led to a larger decrease in αSMA-expressing cells (70% fewer at 50 ng/mL; 85% fewer at 100 ng/mL compared to untreated cells). Jester and Ho-Chang observed the addition of FGF did not induce αSMA expression in fibroblasts.[8] Here, we further proved that FGF can *decrease* αSMA expression in myofibroblasts after TGF-β induction. In addition, we confirmed that the presence of heparin is not required (for FGF concentrations >10 ng/mL) in modulating the myofibroblast phenotype.

Effect of PDGF on myofibroblast phenotype

Etheredge and coworkers found that PDGF stimulates corneal fibroblasts to synthesize collagen (type I) and proteoglycans (keratan sulfate and chondroitin sulfate) that closely resemble normal corneal composition.[34] This result suggests that PDGF is involved in the restoration of normal ECM following injury and that the addition of PDGF to a

corneal wound dressing can promote orderly tissue remodeling. Furthermore, Jester and Ho-Chang observed that PDGF (100 ng/mL) induced keratocytes to differentiate into fibroblasts that were negative for aSMA expression.[8] On the contrary, Wilson and coworkers reported that PDGF promotes the differentiation of αSMA-positive myofibroblasts from keratocytes, which contribute to the development of corneal haze.[35] To clarify this discrepancy, we cultured myofibroblasts with PDGF (0 - 100 ng/mL) and analyzed their αSMA expression.

We observed that PDGF was effective in reducing αSMA expression in myofibroblasts at very low concentrations (0.1 ng/mL) (**Figures 3-5**). However, the effects of PDGF diminished as PDGF concentration increased from 0.1 to 10 ng/mL. Interestingly, when PDGF concentration was further increased to 50 and 100 ng/mL, there was a drastic decrease in cells expressing αSMA. These results suggest that the effects of PDGF on αSMA expression is dose-dependent. Indeed, this dose-dependency in PDGF signaling has been observed in NIH3T3 fibroblasts, where cells switch from a migrating to a proliferating phenotype with increasing concentrations of PDGF.[36] The hypothesis by De Donatis and coworkers that different PDGF concentrations lead to different endocytotic routes of the PDGF receptors may also hold true for the present study, although further investigation would be required to test this hypothesis.

Different extent to which the number of αSMA-producing cells, αSMA mRNA and αSMA protein expression were affected by growth factors

It is noted that for each growth factor studied, they influence αSMA mRNA and protein levels, as well as the number of αSMA-producing cells, to different extents. For each growth factor at a given concentration, the number of αSMA-producing cells have a larger fold-change compared to that of αSMA mRNA changes, with the smallest fold-change observed in the αSMA protein levels (e.g. for EGF at 50 ng/mL, compared to cells that received no EGF, there was a 65% decrease in cells positive for αSMA, but only a 25% decrease in αSMA mRNA expression and a 20% decrease in αSMA protein expression).

It is possible that the number of αSMA-producing cells is underrepresented based on the method of quantitation. Here, we used immunostaining to label αSMA in growth factor treated and untreated myofibroblasts, and took photographs under the fluorescence microscope. The photographs were imported into ImageJ, and cells that showed fluorescence above a certain threshold were considered positive for αSMA expression. It is possible that additional cells are producing αSMA at levels that are either below the set threshold or not detectable by immunostaining. The αSMA protein in these cases would be detectable in our Western Blotting experiments (since protein is extracted from all cells in the culture dish), which may explain the discrepancy between the decrease in αSMA producing cells and the decrease in αSMA protein expression.

The different extent to which αSMA mRNA and protein levels are affected by growth factors may be explained in the differences between mRNA and protein turnover rates. It has been shown that TGF-β induced myofibroblasts have relatively long-lived αSMA

protein: the organization of SMA into stress fibers make αSMA more stable against degradation.[37] It is possible that growth factors affect downstream signaling molecules that decrease αSMA mRNA stability, which leads to a decrease in αSMA mRNA levels detected by qPCR experiments. However, since αSMA protein has a slow turnover rate, the decrease in αSMA protein levels is not as large as the decrease in αSMA mRNA levels. In addition, the regulation of αSMA expression has been shown to be controlled at multiple levels in transcription and translation[38], further complicating the relationship between αSMA mRNA and protein levels.

FAK and Raf-1 play a stronger role than TAZ and YAP in growth-factor-dependent signaling that modulates αSMA expression

We observed that EGF, FGF and PDGF are each able to mitigate the myofibroblast phenotype in a dose-dependent manner. The molecular mechanism by which these growth factors initiate signaling cascades that ultimately influence aSMA expression is still unclear.

The differentiation of myofibroblasts from keratocytes is initiated when TGF-β binds and activates TGF-β receptors, which then recruits and phosphorylates downstream regulatory Smad proteins.[39,40] Phosphorylated Smad proteins then translocate into the nucleus and regulate αSMA expression by targeting the Smad-binding sequence in its promoter region.

There are several hypotheses on the mechanism by which growth factors can inhibit αSMA expression (**Figure 8**). EGF, FGF and PDGF all activate the Raf/MEK/ERK signaling pathway[41-43], which has been shown to suppress Smad transcriptional activities and induce expression of TGIF (a known Smad repressor),[44] thereby negatively regulating levels of αSMA. In addition, it has been shown that focal adhesion kinase (FAK) is necessary for regulating the ERK pathway.[45] Activated FAK increases cell-surface expression of growth factor receptors, which in turn increases activation of the ERK pathway. Therefore, we chose FAK and Raf-1 as two gene-silencing targets to investigate the role of ERK signaling in αSMA expression.

Alternatively, it has been shown that TAZ and YAP promote the activity of TGFβ-activated Smad complexes.[46] In addition to being activated through substrate stiffness (as described in Chapter 2), TAZ and YAP can also be activated through other signaling pathways such as the Hippo cascade.[47] It is possible that growth factors can inhibit downstream signaling molecules in these pathways. Indeed, it has been demonstrated that there is crosstalk between growth factor receptors and G-protein coupled receptors activated in the Hippo pathway.[48] Therefore, we chose TAZ and YAP as two gene-silencing targets to investigate their role in αSMA expression.

We generated knockdown cells by transfecting human corneal fibroblasts with one of the corresponding siRNAs (FAK, Raf-1, TAZ or YAP) and cultured them in presence of a growth factor (EGF, FGF or PDGF at 100 ng/mL) (**Figure 7**). Knockdown of FAK and Raf-1 partially reversed αSMA expression to levels that were similar to control

untreated cells, suggesting that the ERK pathway plays a strong role in regulating αSMA expression. In contrast, siTAZ and siYAP cells expressed αSMA at a minimal level, suggesting that TAZ and YAP play a lesser role in the growth factor dependent reduction of αSMA expression. In the view of the complexity of intercellular signaling, it is possible that these are just two of the possible pathways with which growth factors influence αSMA expression.

3.5 Conclusions

We explored the use of growth factors in modulating the myofibroblast phenotype *in vitro*. Specifically, there were >80% fewer cells expressing αSMA (a cell marker of myofibroblasts) when treated with EGF, FGF or PDGF at a concentration of 100 ng/mL. Gene-silencing experiments suggest that the ERK signaling pathway plays an important role in propagating growth factor-receptor interactions into downstream molecular signals that affect αSMA expression.

3.6 References

1 Diegelmann, R.F.; Evans, M.C. Wound healing: an overview of acute, fibrotic and delayed healing. *Front. Biosci.* **2004**; 9:283-289.

2 Wilson, S.E.; Mohan, R.R.; Mohan, R.R.; Ambrosio Jr. R.; Hong, J.; Lee, J. The corneal wound healing response: cytokine mediated interaction of the epithelium, stroma and inflammatory cells. *Prof. Retin. Eye Res*. **2001**; 20:625-637.

3 Kuo, I.C. Corneal wound healing. *Curr. Opin. Ophthanol*. **2004**; 15:311-315.

4 Netto, M.V.; Mohan, R.R.; Sinha, S.; Sharma, A.; Dupps, W.; Wilson, S.E. Stromal haze, myofibroblasts, and surface irregularity after PRK. *Exp. Eye Res*. **2006**; 82:788-797.

5 Jester, J.V.; Budge, A.; Fisher, S.; Huang, J. Corneal keratocytes: phenotypic and species differences in abundant protein expression and in vitro light-scattering. *Invest. Ophthalmol. Vis. Sci.* **2005**; 46:2369-2378.

6 Yu, F.S.; Yin, J.; Xu, K.; Huang, J. Growth factors and corneal epithelial wound healing. *Brain Res. Bull.* **2010**; 81:229-235.

7 Grant, M.B.; Khaw, P.T.; Schultz, G.S.; Adams, J.L.; Shimizu, R.W. Effects of epidermal growth factor, fibroblast growth factor and transforming growth factor-β on corneal cell chemotaxis. *Invest. Ophthalmol. Vis. Sci.* **1992**; 33:3293-3301.

8 Jester, J.V.; Ho-Chang, J. Modulation of cultured corneal keratocyte phenotype by growth factors/cytokines control in vitro contractility and extracellular matrix contraction. *Exp. Eye Res.* **2003**; 77:581-592.

9 Kim, A.; Lakshman, N.; Karamichos, D.; Petroll, W.M. Growth factor regulation of corneal keratocyte differentiation and migration in compressed collagen matrices. *Invest. Ophthalmol. Vis. Sci.* **2010**; 51:864-875.

10 Lakshman, N.; Petroll, W.M. Growth factor regulation of corneal keratocyte mechanical phenotypes in 3-D collagen matrices. *Invest. Ophthalmol. Vis. Sci.* **2012**; 53:1077-1086.

11 Jester, J.V.; Barry-Lane, P.A.; Cavanagh, H.D.; Petroll, W.M. Induction of alpha-smooth muscle actin expression and myofibroblast transformation in cultured corneal keratocytes. *Cornea* **1996**; 15:505-516.

12 Singh, V.; Barbosa, F.L.; Torricelli, A.A.; Santhiago, M.R.; Wilson, S.E. Transforming growth factor β and platelet-derived growth factor modulation of myofibroblast development from corneal fibroblasts in vitro. *Exp. Eye Res.* **2014**; 120:152-160.

13 Livak, K.J.; Schmittgen, T.D. Analysis of relative gene expression data using real-time quantitative PCR and the $2^{-\Delta\Delta Ct}$ method. *Methods* **2001**; 25:402-408.

14 Schultz, G.; Kwaw, P.T.; Oxford, K.; Macauley, S.; Van Setten, G.; Chegini, N. Growth factors and ocular wound healing. *Eye* **1994**; 8:184-187.

15 Bennett, N.T.; Schultz, G.S. Growth factors and wound healing: Part II. Role in normal and chronic wound healing. *Am. J. Surg.* **1993**; 166:74-81.

16 Imanishi, J.; Kamiyama, J.; Iguchi, I.; Kita, M.; Sotozono, C.; Kinoshita, S. Growth factors: importance in wound healing and maintenance of transparency of the cornea. *Prog. Retin. Eye Res.* **2000**; 19:113-129.

17 Baldwin, H.C.; Marshall, J. Growth factors in corneal wound healing following refractive surgery: a review. *Acta Ophthalmol. Scand.* **2002**; 80:238-247.

18 Hauner, H.; Rohrig, K.; Petruschke, T. Effects of epidermal growth factor (EGF), platelet-derived growth factor (PDGF) and fibroblast growth factor (FGF) on human adipocyte development and function. *Eur. J. Clin. Invest.* **1995**; 25:90-96.

19 Shirakata, Y.; Kimura, R.; Nanba, D.; Iwamoto, R.; Tokumaru, S.; Morimoto, C. *et al.* Heparin-binding EGF-like growth factor accelerates keratinocyte migration and skin wound healing. *J. Cell Sci.* **2005**; 118:2363-2370.

20 Festuccia, C.; Angelucci, A.; Gravina, G.L.; Biordi, L.; Millimaggi, D.; Muzi, P. *et al.* Epidermal growth factor modulates prostate cancer cell invasiveness regulating urokinase-type plasminogen activator activity. EGF-receptor inhibition may prevent tumor cell dissemination. *Thromb. Haemost.* **2005**; 93:964-975.

21 Watanabe, K.; Nakagawa, S.; Nishida, T. Stimulatory effects of fibronectin and EGF on migration of corneal epithelial cells. *Invest. Ophthamol. Vis. Sci*. **1986**; 28:205-211.

22 Kruse, F.; Tseng, S.C.G. A serum-free clonal growth assay for limbal peripheral and central corneal epithelium. *Invest. Ophthamol. Vis. Sci.* **1991**; 32:2086-2095.

23 Fabricant, R.N.; Alpar, A.J.; Centifanto, Y.M.; Kaufman, H.E. Epidermal growth factor receptors on corneal endothelium. *Arch. Ophthamol*. **1981**; 99:305-308.

24 He, J.; Bazan, H.E.P. Epidermal growth factor (EGF) induces corneal keratocyte differentiation via PI-3 kinase activity. Synergism with TGF-β1. *Invest. Ophthalmol. Vis. Sci.* **2008**; 49:2936-2945.

25 Kimura, H.; Okubo, N.; Chosa, N.; Kyakumoto, S.; Kamo, M.; Miura, H. *et al*. EGF positively regulates the proliferation and migration, and negatively regulates the myofibroblast differentiation of periodontal ligament-derived endothelial progenitor cells through MEK/ERK-and JNK-dependent signals. *Cell. Physiol. Biochem.* **2013**; 32:899-914.

26 Yang, L.; Qiu, C.X.; Ludlow, A.; Ferguson, M.W.J.; Brunner, G. Active transforming growth factor-beta in wound repair. *Am. J. Pathol.* **1999**; 154:105-111.

27 Zhang, K.; Tian, Y.; Yin, L.; Zhang, M.; Beck, L.A.; Zhang, B. *et al.* FGF-P improves barrier function and proliferation in human keratinocytes after radiation. *Int. J. Radiat. Oncol. Biol. Phys.* **2012**; 81:248-254.

28 Raucci, A.; Bellosta, P.; Grassi, R.; Basilico, C.; Mansukhai, A. Osteoblast proliferation or differentiation is regulated by relative strengths of opposing signaling pathways. *J. Cell. Physiol.* **2008**; 215:442-451.

29 Gospodarowicz, D.; Mescher, A.L.; Birdwell, C.R. Stimulation of corneal endothelial cell proliferation in vitro by fibroblast and epidermal growth factors. *Exp. Eye Res.* **1977**; 25:75-89.

30 Hu, C.; Ding, Y.; Chen, J.; Liu, D.; Zhang, Y.; Ding, M. *et al.* Basic fibroblast growth factor stimulates epithelial cell growth and epithelial wound healing in canine corneas. *Vet. Ophatholmol*. **2009**; 12:170-175.

31 Fredj-Reygrobellet, D.; Plouet, J.; Delayre, T. Baudouin, C.; Bourret, F.; Lapalus, P. Effects of aFGF and bFGF on wound healing in rabbit corneas. *Curr. Eye Res.* **1987**; 6:1205-1209.

32 Maltseva, O.; Folger, P.; Zekaria, D.; Petridou, S.; Masur, S.K. Fibroblast growth factor reversal of the corneal myofibroblast phenotype. *Invest. Ophthalmol. Vis. Sci.* **2001**; 42:2490-2495.

33 Padera, R.; Venkataraman, G.; Berry, D.; Godavarti, R.; Sasisekharan, R. FGF-2/fibroblast growth factor receptor/heparin-like glycosaminoglycan interactions: a compensation model for FGF-2 signaling. *FASEB J.* **1999**; 13:1677-1687.

34 Etheredge, L.; Kane, B.P.; Hassell, J.R. The effect of growth factor signaling on keratocytes in vitro and its relationship to the phases of stromal wound repair. *Invest. Ophthalmol. Vis. Sci.* **2009**; 50:3128-3136.

35 Kaur, H.; Chaurasia, S.S.; de Mederios, F.W.; Agrawal, V.; Salomao, M.Q.; Singh, N. et al. Corneal stroma PDGF blockade and myofibroblast development. *Exp Eye Res*. **2009**; 88:960-965.

36 De Donatis, A.; Comito, G.; Buricchi, F.; Vinci, M.C.; Parenti, A.; Caselli, A. et al. Proliferation versus migration in platelet-derived growth factor signaling: the key role of endocytosis. *J. Bio. Chem.* **2008**; 18:19948-19956.

37 Arora, P.D.; McCulloch, C.A.G. The deletion of transforming growth factor-b-induced myofibroblasts depends on growth conditions and actin organization. *Am. J. Pathol.* **1999**; 155:2087-2099.

38 Gallucci, R.M.; Lee, E.G.; Tomasek, J.J. IL-6 modulates alpha-smooth muscle actin expression in dermal fibroblasts from IL-6-deficient mice. *J. Invest. Derm.* **2006**; 126:561-568.

39 Gu, L.; Zhu, Y.J.; Yang, X.; Guo, Z.J.; Xu, W.B.; Tian, X.L. Effect of TGF-beta/Smad signaling pathway on lung myofibroblast differentiation. *Acta. Pharmacol. Sin.* **2007**; 28:382-391.

40 Hu, B.; Wu, Z.; Phan, S.H. Smad3 mediates transforming growth factor-beta-induced alpha-smooth muscle actin expression. *Am. J. Respir. Cell. Mol. Biol.* **2003**; 29:397-404.

41 Liu, X.; Hubchak, S.C.; Browne, J.A.; Schnaper, H.W. Epidermal growth factor inhibits transforming growth factor-β-induced fibrogenic differentiation marker expression through ERK activation. *Cell. Signal.* **2014**; 26:2276-2283.

42 Nakayama, K.; Satoh, T.; Igari, A.; Kageyama, R.; Nishida, E. FGF induces oscillations of Hes1 expression and Ras/ERK activation. *Curr. Biol.* **2008**; 18:332-334.

43 Kolch, W. Meaningful relationships: the regulation of the Ras/Raf/MEK/ERK pathway by protein interactions. *Biochem. J.* **2000**; 351:289-305.

44 Liu, X.; Hubchak, S.C.; Browne, J.A.; Schnaper, H.W. Epidermal growth factor inhibits transforming growth factor-β-induced fibrogenic differentiation marker expression through ERK activation. *Cell. Signal.* **2014**; 26:2276-2283.

45 Greenberg, R.S.; Bernstein, A.M.; Benezra, M.; Gelman, I.H.; Taliana, L.; Masur, S.K. FAK-dependent regulation of myofibroblast differentiation. *FASEB J.* **2006**; 20:1006-1008.

46 Hiemer, S.E.; Szymaniak, A.D.; Varelas, X. The transcriptional regulators TAZ and YAP direct transforming growth factor β-induced tumorigenic phenotype in breast cancer cells. *J. Biol. Chem.* **2014**; 289:13461-13474.

47 Guo, X.; Zhao, B. Integration of mechanical and chemical signals by YAP and TAZ transcription coactivators. *Cell & Bioscience* **2013**; 3:33-42.

48 Yu, F-X.; Zhao, B.; Panupinthu, N.; Jewell, J.L.; Lian, I.; Wang, L.H. et al. Regulation of the Hippo-YAP pathway by G-protein coupled receptor signaling. *Cell* **2012**; 150:780-791.

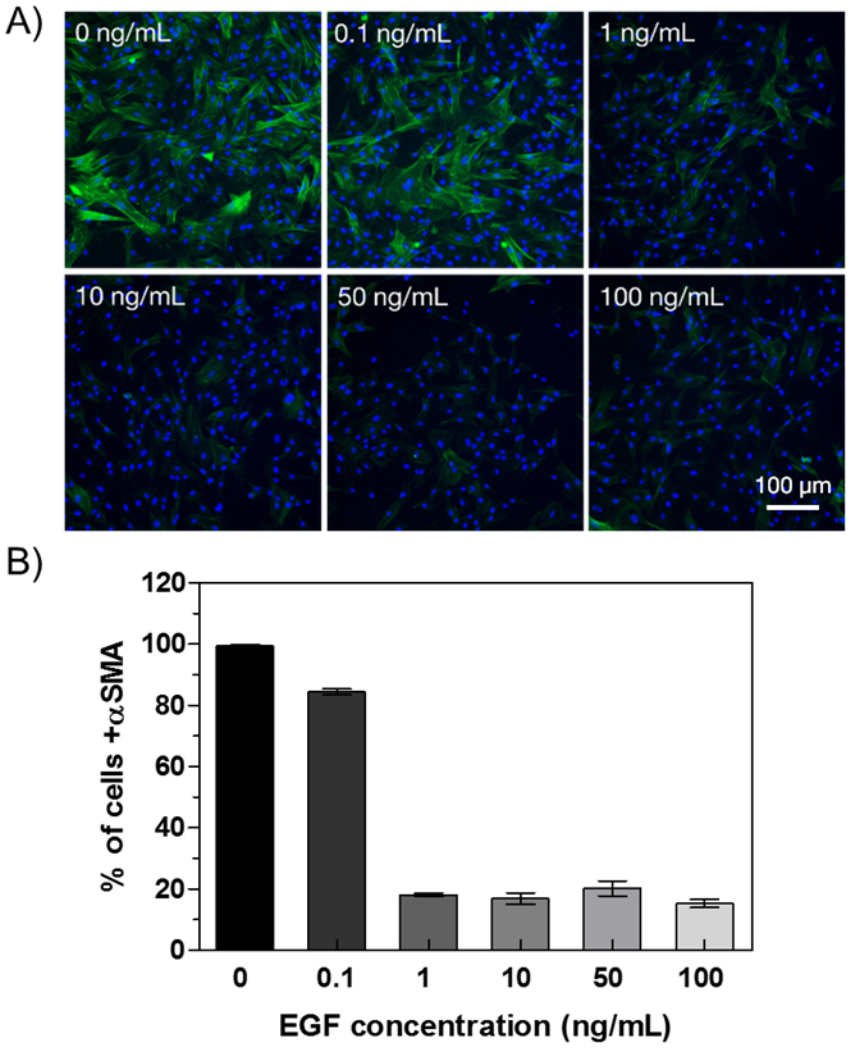

Figure 1. Myofibroblast response to epidermal growth factor (EGF). A) Representative images of TGF-β (1 ng/mL) transformed myofibroblasts (P5) treated with EGF at different concentrations. Cell nuclei, Hoescht stain (blue); αSMA, anti-αSMA-FITC (green). B) Relative to control untreated cells, EGF treatment (>1 ng/mL) led to fewer αSMA-positive cells (analysis of images in A).

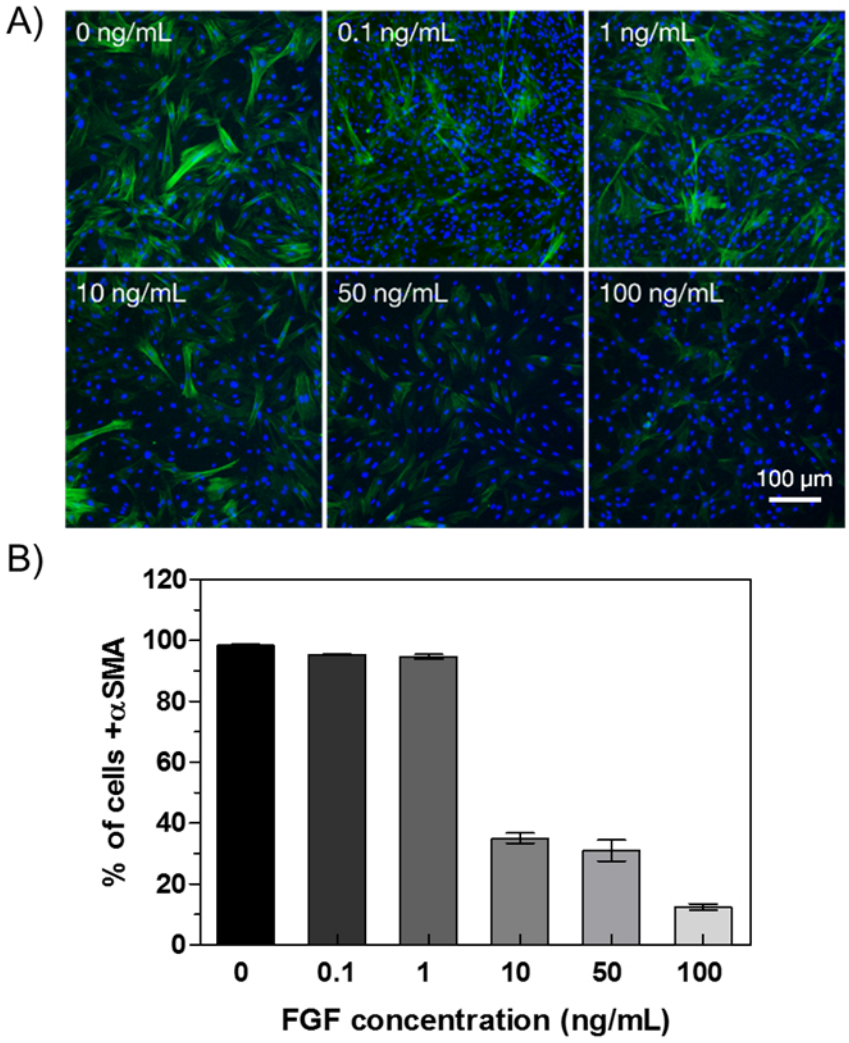

Figure 2. Myofibroblast response to fibroblast growth factor (FGF). A) Representative images of TGF-β (1 ng/mL) transformed myofibroblasts (P5) treated with FGF at different concentrations. Cell nuclei, Hoescht stain (blue); αSMA, anti-αSMA-FITC (green). B) Relative to control untreated cells, FGF treatment at high concentrations (10 – 100 ng/mL) led to fewer αSMA-positive cells (analysis of images in A).

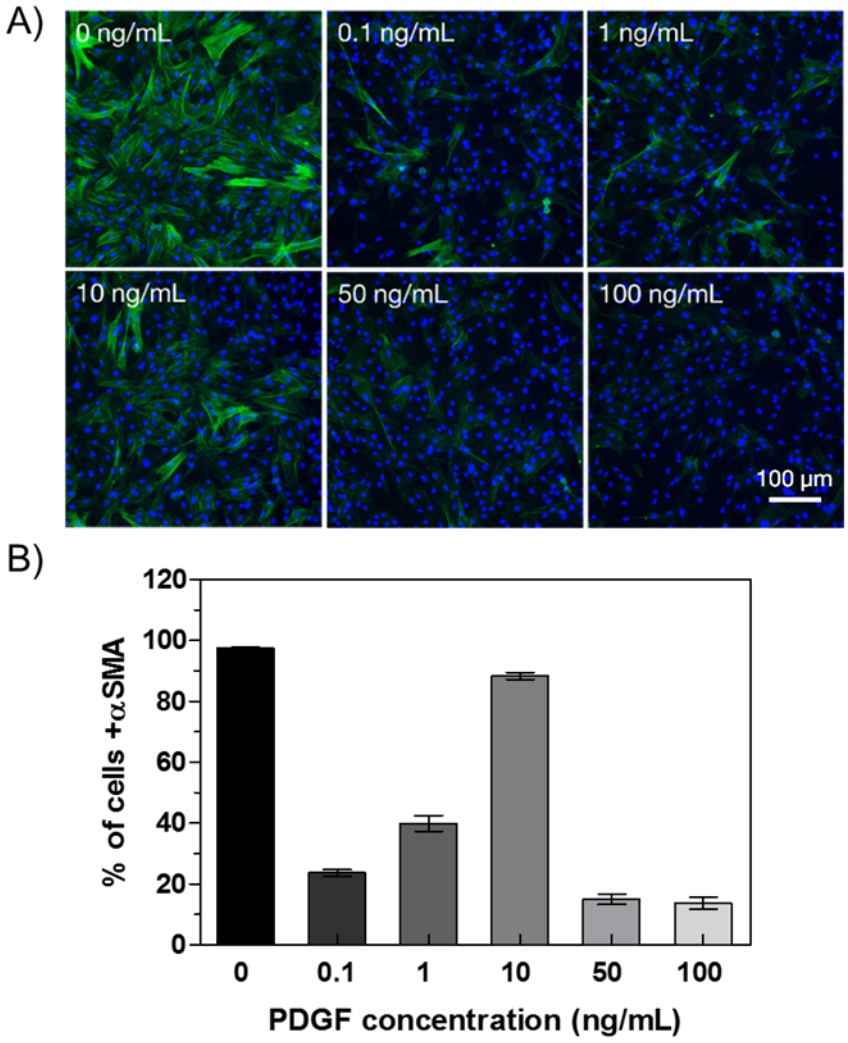

Figure 3. Myofibroblast response to platelet-derived growth factor (PDGF). A) Representative images of TGF-β (1 ng/mL) transformed myofibroblasts (P5) treated with PDGF at different concentrations. Cell nuclei, Hoescht stain (blue); αSMA, anti-αSMA-FITC (green). B) Relative to control untreated cells, PDGF treatment at high concentrations (50 – 100 ng/mL) led to fewer αSMA-positive cells (analysis of images in A).

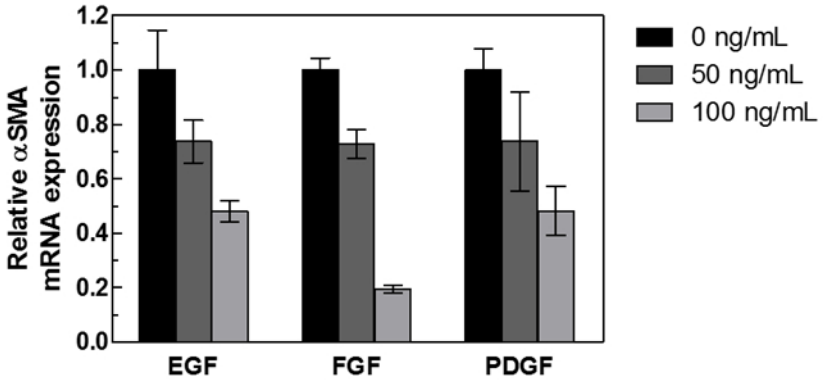

Figure 4. Relative to control untreated cells, TGF-β (1 ng/mL) transformed myofibroblasts (P5) treated with growth factors (EGF/FGF/PDGF at 50 or 100 ng/mL) demonstrated significantly lower levels of αSMA mRNA.

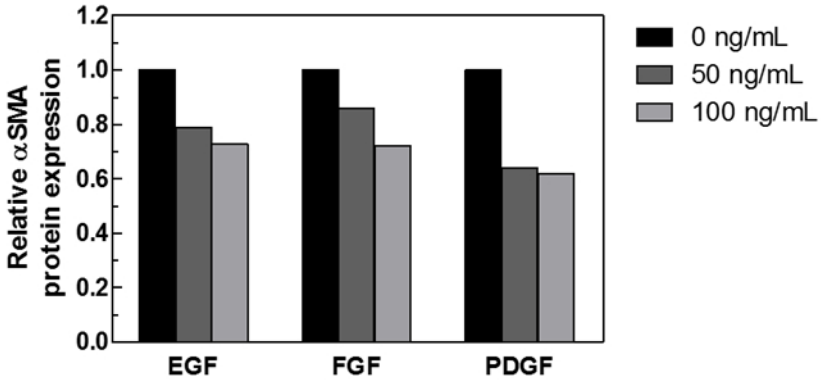

Figure 5. Relative to control untreated cells, TGF-β (1 ng/mL) transformed myofibroblasts (P5) treated with growth factors (EGF/FGF/PDGF at 50 or 100 ng/mL) demonstrated significantly lower αSMA protein expression. Results plotted here are based on Western blot analysis of cell lysates, quantified by the ratio of αSMA protein signals normalized by GAPDH.

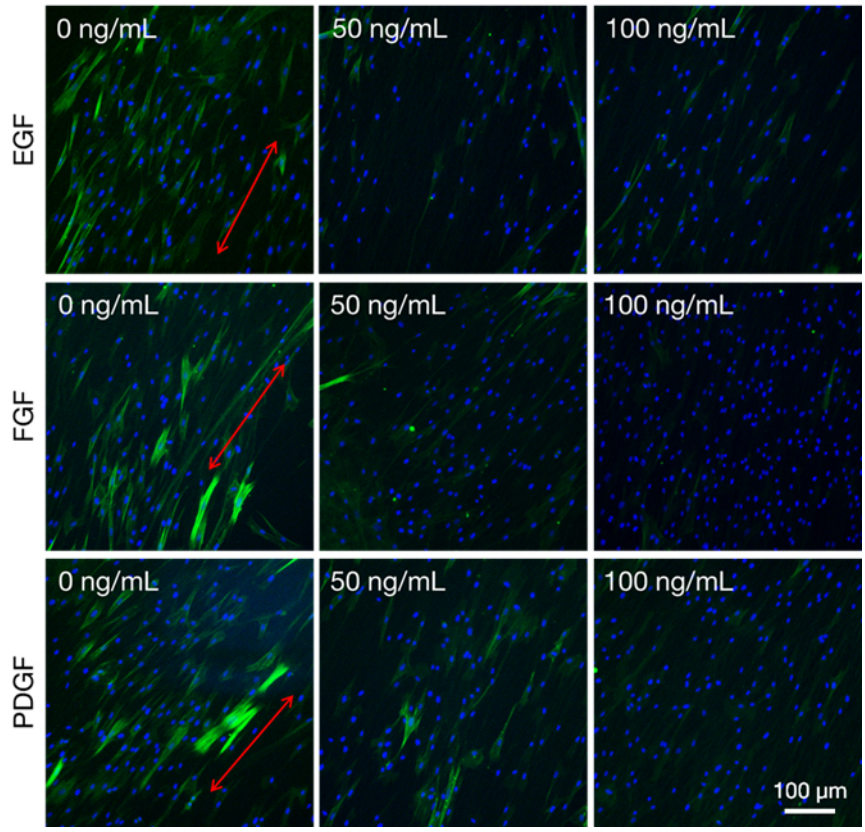

Figure 6. Representative images of TGF-β (1 ng/mL) transformed myofibroblasts (P5) cultured on uniaxially-aligned nanofibers. Cells were treated with EGF/FGF/PDGF (50 or 100 ng/mL) for 3 days, and their αSMA expression was visualized. Red arrows indicate direction of underlying nanofibers. Cell nuclei, Hoescht stain (blue); αSMA, anti-αSMA-FITC (green).

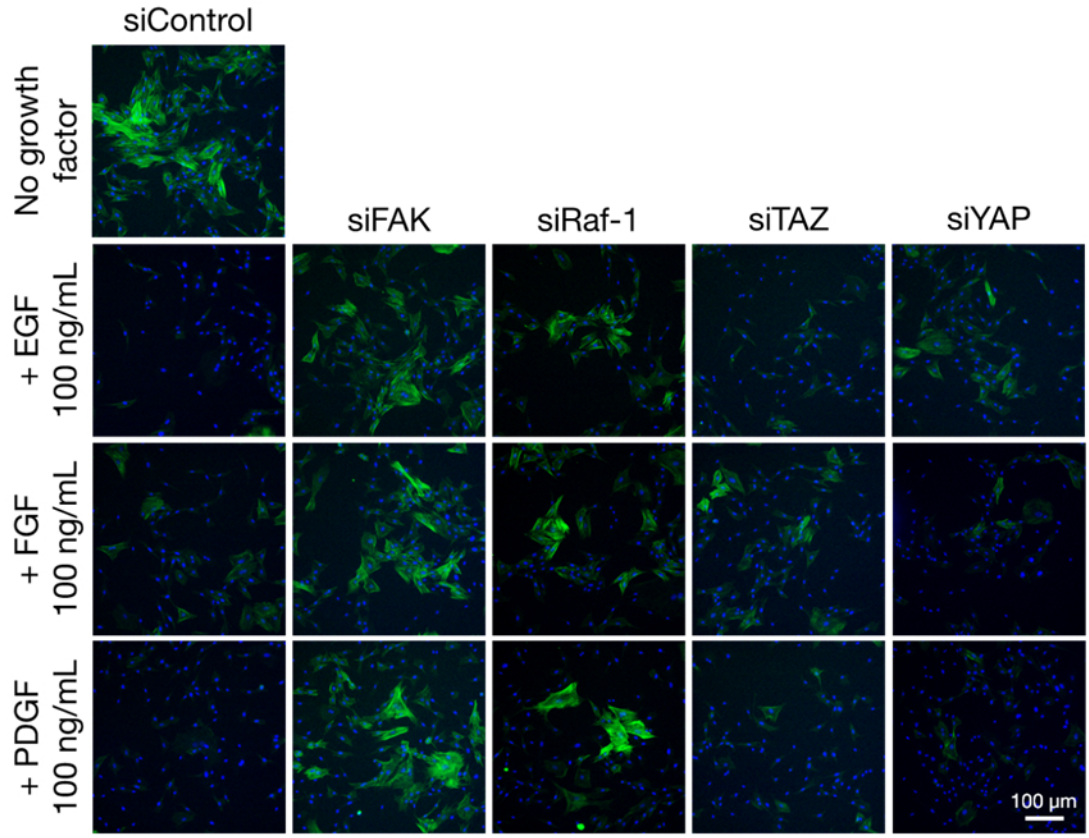

Figure 7. Human corneal fibroblasts (P5) were transfected with the indicated siRNA (control, FAK, Raf-1, TAZ, YAP) and transformed to myofibroblasts (10 ng/mL TGF-β; greater concentration was used for human cells compared to rabbit cells in Figures 1-7 to provide visible αSMA expression in the control). Cells were then treated with EGF/FGF/PDGF (100 ng/mL) for 3 days, and their αSMA expression was visualized. Cell nuclei, Hoescht stain (blue); αSMA, anti-αSMA-FITC (green).

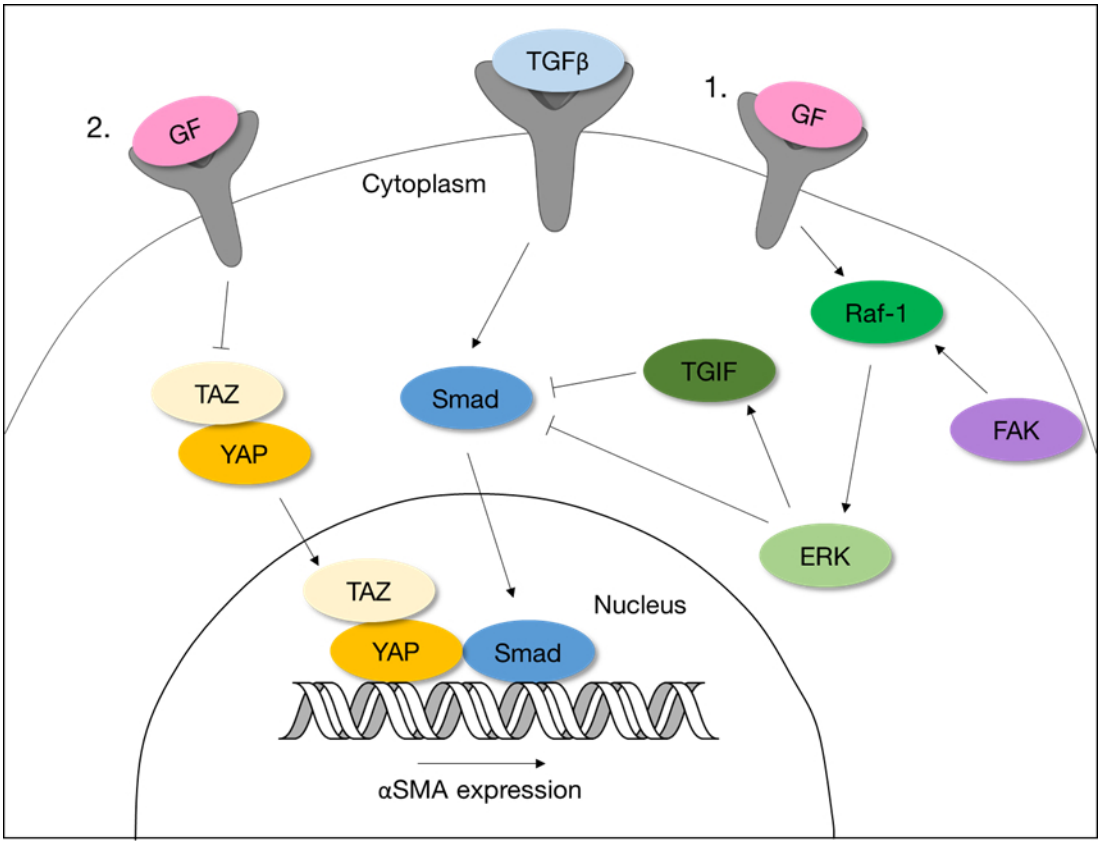

Figure 8. Possible mechanisms by which growth factors regulate αSMA expression: 1. through activation of the ERK pathway that inhibits Smad activity and/or 2. by inhibiting TAZ/YAP translocation to the nucleus. Intermediate signaling molecules have been omitted for simplicity.

Table 1. Summary of prior literature on using GFs to influence corneal cells

Growth factors	**Findings**	**Authors**	**Ref**
Epidermal growth factor (EGF)	Essential for epithelial wound closure	Yu *et al.*	6
	Promotes epithelial cell proliferation, fibroblast migration and endothelial cell mitosis	Watanabe *et al.* Kruse *et al.*	
	Accelerates reepithelialization of corneal surface injuries in vivo	Fabricant *et al.*	23
	Induces fibroblast-myofibroblast differentiation	He *et al.*	24
	Decreases expression of αSMA	Kimura *et al.*	25
Fibroblast growth factor (FGF)	Reduced expression of αSMA in fibroblasts	Jester *et al.*	8
	Stimulates proliferation of corneal cells	Hu *et al.*	30
	Reduced αSMA expression in myofibroblasts in conjunction with heparin	Maltseva *et al.*	32
Platelet-derived growth factor (PDGF)	Induces keratocyte elongation without formation of stress fibers	Kim *et al.* .	9
	Stimulates corneal fibroblasts to synthesize collagen and proteoglycans that closely resemble normal corneal composition	Etheredge *et al.*	34
	Induced keratocytes to differentiate into fibroblasts that were negative for αSMA	Jester *et al.*	8
	Promotes differentiation of αSMA – positive myofibroblasts from keratocytes	Wilson *et al.*	12

Chapter 4

Development of a heparin-based hydrogel for corneal injury

4.1 Introduction

Regenerative medicine aims to promote tissue regeneration and remodeling, which can be achieved through drug delivery or controlling the biological environment surrounding injured tissues, among others. This in turn influences cell decisions such as replication, differentiation, proliferation and migration.[1,2] Regenerative medicine provides an alternative to organ transplantation that relieves demand for transplant organs and avoids complications associated with immune responses against allografts. The use of hydrogels in regenerative medicine is appealing since they provide a three-dimensional framework that can present stimuli to promote and direct formation of new tissue.[3-5] Moreover, *in situ* forming hydrogels can be combined with living cells or bioactive molecules, such as growth factors, and be delivered to injured tissue in a minimally invasive manner.[6,7]

A variety of synthetic and naturally-derived materials have been used for hydrogel formation. Among the synthetic polymers, end-functionalized polyethylene glycol (PEG) is widely used to prepare hydrogels under mild conditions[8-9], and has progressed to the clinic as a component in a number of FDA-approved formulations for *in-situ* forming hydrogels (Matrix VSG™, ProGEL™, ReSure® to name a few). However, synthetic polymers do not present inherent biochemical cues or binding sites for bioactive molecules. Naturally-derived materials, such as collagen and hyaluronic acid,

have been used as a hydrogel because of their bioactivity and natural occurrence in the human body.[10-13] Naturally-derived materials present challenges in controlling and tuning their hydrogel properties due to the materials' heterogeneity. Hybrid hydrogels are promising because they take advantage of the benefits of each type of material and combine the tunable characteristic of synthetic material with the bioactivity of naturally-derived materials.[14,15]

Heparin is an anionic polysaccharide found naturally in the body, and is best known for its anticoagulant properties.[16] A variety of proteins, including many growth factors, have heparin-binding domains.[17] Incorporating heparin into hydrogels therefore provides an efficient way to sequester growth factors without loss of activity. Tae *et al.* have developed a heparin-based hydrogel that forms by reacting thiolated heparin (Hep-SH) and poly(ethylene glycol) diacrylate (PEG-DA) through a Michael-type addition.[18] The addition of PEG-DA allows for easy control of physical properties of the hydrogel by varying the concentration and architecture of the crosslinker. Tae has demonstrated that his heparin-based hydrogel is well-suited for the cultivation of hepatocytes[19] and chondrocytes[20], as well as the regeneration of cartilage *in vivo*[21]. More recently, *in situ* forming hydrogels based on heparin have been extended to maleimide functionalized heparin and thiolated PEG with glutathione–sensitive crosslinks[22]; peptide-heparin networks[23] and starPEG-heparin hydrogels.[24]

To increase the gelation rate and provide spatial and temporal control of gelation, photo-polymerization of hydrogels has been widely used, particularly with the photoinitiator

Irgacure 2959.[25-28] In the context of heparin-based hydrogels, Tae demonstrated gelation within minutes when the precursor solution was exposed to ultraviolet (UV) light (365 nm, 18 W/cm^2).[29,30] However, UV light can compromise cytocompatibility due to production of cytotoxic free radicals that damage cellular proteins and DNA.[31] Also, it has been shown that certain cell types (osteoblasts and corneal epithelial cells) are very sensitive to UV exposure.[32] Therefore, we have developed a variation of the heparin-based hydrogel that can be cured using visible light. Specifically, we replaced Irgacure 2959 with eosin Y (EY). The maximum absorbance of EY is at 524 nm, and therefore is activated by green light. Since the 1990s, EY with TEOA as a coinitiator has attracted interest because, even in direct contact with cells, it permits photopolymerization with very low toxicity,[33,34] and is used in an FDA-approved lung sealant (FocalSeal).[35] The ability to encapsulate cells in photopolymerized hydrogels using EY as the initiator has since been used by the Lin group to embed hepatocytes in thiol-acrylate PEG hydrogels[36,37] and by the West group to study endothelial morphogenesis in laminin functionalized PEGDA hydrogels.[38]

The present visible light initiated formulation permits gelation within minutes, comparable to the Irgacure-containing hydrogels, using a light dose that conforms with Group 1 eye safety threshold (no hazard). Thus, the current formulation opens the way to applications of heparin-based hydrogels on and in the eye. Relationships between gel formulation and irradiation conditions, and properties are described. The visible light photo-crosslinking is shown to be well-suited for use as a cell carrier, as well as a scaffold for growth-factor delivery.

4.2 Methods

Preparation of heparin-based hydrogels

Thiol-functionalized heparin (Hep-SH) was synthesized by modifying 40% of the carboxyl groups of heparin, following established protocols.[18] In heparin, each disaccharide repeat has one carboxylate group, so the functionalized polymer has one thiol group per 1500 g/mol of heparin at 40% modification. The amount of thiol groups in Hep-SH was determined using Ellman's reagent and measurement of molar absorptivity at 412 nm. In this study, 40 ± 2.5% thiolated heparin was used for all of the experiments. PEG macromers (PEG-DA or 4-arm PEG) and Hep-SH were sequentially dissolved in either PBS or DMEM (thiol:acrylate = 1:1 – 1:0.25 molar ratio). 0.005 – 0.01% (w/v) eosin Y as a photo-initiator and 0 – 0.5% (v/v) TEOA as an electron donor were added via stock solutions ($[EY_{stock}]$ = 0.5%; $[TEOA_{stock}]$ = 5%) to the precursor solution. The pH of the reaction mixture was adjusted to 7.0 – 8.0 with 1 N HCl and/or NaOH. Precursor solutions were used within 1 hour of preparation and stored in the dark at 4^{o}C prior to use. Prepared precursor solution was photo-polymerized under green LED light (5 – 100 mWcm^2) exposure. The LED emission wavelength is 525 ± 15 nm.

Micropatterning

1. Preparation of release layer on the glass slide.

In order to enable controlled retrieval of micropatterned heparin-based hydrogels from their substrate, one of the glass slides is treated to provide an initially-adhesive surface

that can be subsequently "switched" to release the gel in a stimuli-response manner.[30] Specifically, a layer by layer (LbL) technique was used to deposit a $(PLL\text{-}HA)_2$ multilayer, as described previously.[30] Finally, a capping layer of methacrylate-functionalized chitosan (GMA-Chi) (5 kDa) is adsorbed to provide sites for anchoring the hydrogel to the system. Additional experimental details can be found in the Supplementary Information. Glass substrates bearing this multilayer are denoted as $(PLL\text{-}HA)_2$-(GMA-Chi).

2. Micropatterning of heparin-based hydrogel on multilayer-adsorbed glass slide.

For each formulation investigated, 30 μL of the corresponding hydrogel precursor solution was pipetted on the $(PLL\text{-}HA)_2$-(GMA-Chi) glass slide and covered with a bare cover slip using a 320 μm spacer to provide a uniform thickness. A photomask was put on the cover slip prior to irradiation using green light. After irradiation, the photomask and coverslip were carefully removed. The coverslip and glass slide were rinsed with PBS and imaged. The presence of heparin in the micropatterned hydrogel structures was visualized by toluidine blue O staining, as previously reported.[30,39]

Cell culture and live-dead assay

To encapsulate 3T3 fibroblast (NIH 3T3) cells in the heparin-based hydrogel, cells were detached from standard cell culture plates and re-suspended in the prepared hydrogel precursor solution in DMEM. A gel precursor solution (30 μL) containing cells ($2x10^6$ cells/mL) was pipetted on a $(PLL\text{-}HA)_2$-(GMA-Chi) modified glass slide, and hydrogels

were formed following the same micropatterning procedure as described above. Cell-laden hydrogels were maintained in the DMEM containing 10% FBS, 200 U/mL penicillin, and 200 μg/mL streptomycin at 37°C in a humidified 5% CO2 incubator with a medium change every 2 days. The viability of fibroblasts inside the hydrogel was analyzed using a double-staining live-dead assay procedure. Briefly, cell-laden hydrogels were rinsed with PBS and then incubated in a medium with 0.67 μM AO and 7.5 μM PI for 30 minutes. After rinsing again with PBS, stained cells were imaged using a confocal microscope (FV1000, Olympus, Center Valley, PA). The percentage of viable cells was calculated by counting the number of green (live) cells and dividing by the total number of cells including red (dead) cells. The average viability was obtained from 4 independent preparations of precursor solutions.

Rheological measurements

Moduli of hydrogels were determined using oscillatory shear. For gelation studies, a rheometer (AR-1000, TA Instruments, New Castle, DE) fitted with a custom-built photo-crosslinking setup (**Figure S1**) was used to perform simultaneous irradiation and rheological measurements. Measurements were performed in the linear viscoelastic regime (**Figure S2**). 30 μL of gel precursor solution was pipetted onto the rheometer and the 8 mm parallel plate geometry was set to a gap of 500 μm. A 10-minute time sweep (an angular frequency of 1 rad/s and a stress of 50 Pa) was carried out for monitoring hydrogel gelation. The hydrogel precursor solution was irradiated with a 525 nm green light at 5 mW/cm^2 for the first 2.5 minutes of the time sweep, and the green light was then turned off for the remainder of the time. The experiment was repeated

four times for each precursor solution. To measure the modulus after swelling, hydrogels were separately prepared and swollen in PBS (pH 7.4) for 2 days at 37ºC. Swollen hydrogels were then cut to fit the 8 mm parallel plate geometry. An angular frequency of 1 rad/s and a strain of 2% was used in these studies (ARES-RFS, TA Instruments, New Castle, DE). The experiment was repeated four times for each precursor solution.

Swelling measurements

To measure the wet-to-dry mass ratio of the hydrogels, we first prepared the hydrogels and immersed them in PBS (pH 7.4) for 2 days at 37ºC. Fully-swollen hydrogels were dabbed gently with a Kimwipe to remove excess PBS and weighed immediately to obtain the wet-mass weight (W_s). The hydrogels were then lyophilized and weighed to obtain the dry-mass weight (W_d). The fully-swollen:dry-mass ratio was calculated by W_s/W_d (n = 4). The dry mass includes salts from PBS, which could represent 10-15% of the dry mass. None of the conclusions are affected by this uncertainty in the dry mass.

Heparin incorporation

A toluidine blue assay was used to quantify the amount of heparin retained in hydrogels after swelling.[40] The hydrogels were prepared as described above and placed in PBS for 2 days. 1 mL of 0.04% (w/v) toluidine blue in aqueous 0.01 N HCl/0.2% (w/v) NaCl was then added to each hydrogel. The mixture was gently shaken for 6 hours, during which heparin-toluidine blue complexes were formed. The mixture was then centrifuged at 1,000 x *g* for 10 minutes to remove excess toluidine blue solution. The amount of

toluidine blue in the heparin-toluidine blue complex (i.e. the amount of toluidine blue in the hydrogel) was determined by first rinsing the hydrogel with aqueous 0.01 N HCl/0.02% (w/v) NaCl and then adding a solution of 4:1 (v/v) mixture of ethanol and aqueous 0.1 N NaOH until all the heparin-toluidine blue complex was dissolved. The absorbance of the resulting solution was measured at 530 nm. A standard curve was carried out using the same procedure with solutions of heparin at known concentrations. To rule out the possibility that EY is responsible for some of the signal at 530 nm (attributed to heparin), the assay was performed on heparin-free hydrogels (replacing heparin with gelatin) photocured using EY. When the heparin-free hydrogels were subjected to the same heparin incorporation analysis, no significant reading was measured. The experiment was repeated 4 times for each precursor solution.

***In vitro* EGF release from hydrogels**

Loading of the hydrogels was achieved by adding EGF to the hydrogel precursor solution with a final EGF concentration of 100 ng/mL. 50 μL of gel precursor solution was pipetted into a well in a 96-well plate and irradiated for 2.5 minutes at 5 mW/cm^2 using a 525 nm green light. After gelation, 200 μL of PBS (pH 7.4) was added to the well as release buffer and samples were kept at 37ºC in a humidified 5% CO_2 incubator. The release buffer was collected and replaced with fresh buffer each day. Collected samples were stored frozen prior to analysis. The released EGF at different time points was analyzed with a human EGF ELISA kit (Life Technologies, Carlsbad, CA). Absorbance was measured using a microplate reader at 450 nm (Tecan, Männedorf, Switzerland). The experiment was repeated 4 times for each precursor solution.

Cell culture assay of EGF bioactivity

Bioactivity of EGF released from hydrogels was assayed using scratch wound assay.[41] 3T3 fibroblasts (NIH 3T3) were grown in a 24-well plate in a humidified incubator (5% CO_2) at 37^oC in DMEM containing 10% FBS, 200 U/mL penicillin, and 200 μg/mL streptomycin. When the cells were confluent, a sterile pipette tip was used to scrape the cell monolayer, thereby creating a 'mock wound.' The initial wound boundaries were imaged with an inverted phase contrast microscope (Zeiss Axiovert 25CFL). The cell medium was then replaced with fresh media containing either no growth factor (negative control), 20 ng/mL of as-received EGF (positive control) or 20 ng/mL released EGF. The mock wound area was imaged every 12 hours. The experiment was repeated 4 times.

4.3 Results

We have developed a visible-light photo-crosslinking formulation of a heparin-based hydrogel (**Figure 1**), using green light (525 nm) to photocrosslink thiolated-heparin and acrylate-ended poly(ethylene glycol) (PEG) in the presence of eosin Y as the photoinitiator and triethanolamine as the electron donor.

Effect of concentration on gelation kinetics and micropatterning gelation time

With a higher concentration of heparin and PEG, holding thiol:acrylate ratio fixed at 1:1, gelation occurred faster and a higher final modulus was achieved (**Figure 2A**). Doubling the heparin concentration from 1.66% to 3.33% while keeping the

thiol:acrylate ratio and all other solution conditions constant, increased the storage modulus more than an order of magnitude (from 550 ± 110 Pa to 6900 ± 800 Pa).

When placed in a large volume of PBS, the as-prepared gels swell, taking in an additional 50 to 75% of water (e.g. the solids content of the as prepared 1.67% heparin hydrogel is 5%, corresponding to an initial wet:dry mass ratio of 20, which increases to 30.5 after 2 days in PBS). The increase in water content is accompanied by a decrease in modulus by a factor of 2 to 3 (**Table 1**). A small fraction of heparin diffused out from the gel, particularly for the lowest crosslinking density (1.67% heparin gel loses 13% of its heparin to the bath).

In the micropatterning experiment, decreasing the heparin concentration led to an increase in the time required for spatially-resolved gelation from 4 minutes at 3.33% to 10 minutes at 1.67% (**Figure 2B**). In contexts in which higher intensity is acceptable, increasing the light intensity can be used to significantly decreased gelation time (e.g. from 10 minutes at 5 mW/cm^2 to 2.5 minutes at 100 mW/cm^2 for 1.67% heparin).

Effect of gel formulation on gelation kinetics and micropatterning gelation time

To investigate the effect of gel formulation on hydrogel formation, we varied the pH, TEOA concentration and EY concentration. Even small changes in pH strongly affect gelation kinetics and modulus. Increasing pH from 7.0 to 8.0 provided a 3-fold increase in the modulus (**Figure 3A**, *top*) and a 3-fold decrease in the micropatterning time (**Figure 3B**, *top*).

Increasing the TEOA concentration from 0.05% to 0.1% enhanced gelation rate (**Figure 3A**, *middle*) and shortened the time required for micropatterning (**Figure 3B**, *middle*). However, further increase of the TEOA concentration did not have a significant effect: both G'(t) and optimal photo-patterning exposure were virtually indistinguishable for 0.1% and 0.5% TEOA.

Increasing the photo-initiator (EY) concentration from 0.005% to 0.01% increased gelation rate (**Figure 3A**, *bottom*) and shortened the time required for micropatterning (**Figure 3B**, *bottom*). Interestingly, further increasing the EY concentration to 0.02% resulted in the incomplete formation of a hydrogel (the side that was irradiated formed a gel, but a liquid layer was observed on the dark side).

Equilibrium swelling correlates with as-prepared gel modulus (**Table 2**), in accord with trends observed as a function of heparin concentration (**Table 1**). All gels that had an as-prepared modulus of 1400 Pa or more had higher retention of heparin (93% or more). Gel formulations that gave low modulus (1150 Pa or less) exhibited relatively high equilibrium swelling (wet:dry mass ratio > 27), low modulus of equilibrium swollen gels (530 Pa or less) and low heparin retention (< 80%).

Effect of crosslinking stoichiometry for linear PEG and 4-arm PEG on gelation kinetics and micropatterning gelation time

To study the effects of the acrylate-containing crosslinker on hydrogel formation, we varied the molar ratio of thiol to acrylate groups in the gel formulation, as well as the crosslinker architecture. Increasing the thiol:acrylate ratio from 1:1 to 1:0.3 (effectively decreasing the amount of crosslinker) while keeping the heparin concentration and all other solution conditions fixed, slowed the gelation rate (**Figure 4A**, *top*) and increased micropatterning time (**Figure 4B**, *top*). The modulus of the resulting gel decreased from 1800 ± 80 Pa at 1:1 thiol:acrylate to 270 ± 50 Pa at 1:0.3 thiol:acrylate, which correlated the increase in both swelling ratio and extractables with decreased crosslinking of hydrogels (**Table 3**).

Replacing linear PEG-DA (6 kDa) with its 4-arm counterpart (13 kDa) led to faster gelation and higher moduli (**Figure 4A**), and a shorter irradiation dose for optimal patterning (**Figure 4B**). These effects could be systematically modulated by increasing the thiol:acrylate ratio from 1:1 to 1:0.25 (keeping the heparin concentration and all other solution conditions fixed) to slow the gelation rate (**Figure 4A**, *bottom*) and increase the micropatterning time (**Figure 4B**, *bottom*).

In vitro release of bioactive growth factors

Hydrogels with encapsulated EGF (100 ng/mL) were formed as described in Methods and 200 µL of PBS as release medium was collected daily. Over the first two days, ~30% of EGF was released from the heparin-based hydrogel (**Figure 5**). To validate the bioactivity of released EGF, we carried out a mock wound assay.[33] It has been well-established that EGF promotes cell migration in a variety of cell types.[42-44] We collected

EGF that had been released from hydrogels (EGF_{rel}) and compared it to native EGF by observing its effect on 3T3 fibroblasts at a concentration of 20 ng/mL. The migration rate of 3T3 fibroblasts into a 'mock wound' was indistinguishable for cells exposed to EGF_{rel} and cells exposed to native EGF, and both move much faster than control samples without EGF (**Figure 6**).

4.4 Discussion

To reduce phototoxicity *in vivo* during *in situ* photo-crosslinking of heparin-based hydrogels developed by Tae,[19-21] a visible-light activated formulation is demonstrated. Previously, photo-polymerization of the heparin-based hydrogels used Irgacure 2959 as the photoinitiator, activated by UV light (365 nm at 18 mW/cm^2). To enhance the biocompatibility of the photo-crosslinking procedure, we replaced Irgacure 2959 with eosin Y (EY), a photoinitiator that can be activated by visible light, and has been shown to be biocompatible in several biomedical applications.[33,34] EY is a type II photo-initiator, which requires a co-initiator to generate sufficient radicals for photo-polymerization. Hubbell *et al*. demonstrated hydrogel photocrosslinking using TEOA as the co-initiator with EY and found minimal toxicity.[45] More recently, Lin and coworkers have used EY and visible light in photo-polymerizable thiol-acrylate hydrogels.[36,37,46,47] They show that TEOA can be replaced by N-vinyl pyrrolidone (NVP), which becomes covalently incorporated during photo-polymerization and that cells encapsulated in the formulation remain viable. In the present study, we chose TEOA as the co-initiator because it has a higher median lethal dose (LD50) than NVP, e.g. LD50 (rabbit-dermal) for NVP is 560 mg/kg[48] while that for TEOA is >22.5 g/kg[49].

When a precursor solution of Hep-SH, PEG-DA, EY and TEOA is irradiated with green light (525 nm), a transparent hydrogel forms (**Figure 1**).

Two different methods were used to study the gelation process of the visible light activated heparin-based hydrogel: oscillatory photo-rheology and micropatterning. The former provides information on the parameters that control gelation kinetics and the modulus of the gel, and the latter provides a useful platform for creating 3-D cell-encapsulated hydrogel microstructures for cell therapy applications.[29,50,51] Indeed, the motivation for using $(PLL\text{-}HA)_2$-(GMA-Chi)-treated substrates is to pave the way to selectively retrieve cell-laden microgels, which can then be used as tissue building blocks in a bottom-up approach to assemble full tissue constructs.[52]

We monitored hydrogel formation using a custom optical rheometer with the ability to perform simultaneous irradiation and rheological measurements (**Figure S-1**). During oscillatory shear with a parallel plate geometry, the hydrogel precursor solution was irradiated with green light at 5 mW/cm^2 for 2.5 minutes. The light was then turned off for the remainder of the experiment. The gelation rate is characterized by the rate of increase of the storage modulus during irradiation. The short irradiation time was chosen because we intend to use this hydrogel for wound-healing applications where short gelation times are clinically desirable. Likewise, the modest light intensity was chosen based on clinical considerations (see **Table 4**).

In the micropatterning experiments, the observed outcomes fell into three groups (**Figure S-3**): “insufficient exposure” was associated with incomplete arrays of gel on the treated glass slides, “sufficient exposure” provided a complete array of uniform gel disks, and “excessive exposure” was manifested by the formation of gel in the dark regions that interconnected the microgel disks. The onset of “excessive exposure” occurred at approximately 2-3x the onset of “sufficient exposure.” Therefore, we simply show the latter when comparing the effect of material parameters and irradiation conditions on the “micropatterning gelation time.” In these micropatterning experiments, light intensities of up to 100 mW/cm^2 were tested. This relatively high light flux was chosen to test the feasibility of forming microgels using short light exposure times (< 1 minute) for high throughput applications (such as microfluidics).

Using these methods, we first studied the effect of heparin concentration on gelation time and gel stiffness. As expected, using a higher heparin concentration resulted in hydrogels that had a higher final modulus. Clinically, the gels will be in contact with an open system. Therefore, it is of interest to know the physical properties and heparin content of the hydrogels after equilibrating with a large bath (**Table 1**). We observed that the hydrogels swell when placed in PBS and a small fraction of heparin diffused out from the gels. A high swelling ratio and high level of extractables (water-soluble solids that can be readily extracted from a hydrogel when it is swollen in excess liquid) are both characteristic of a hydrogel system of low crosslinking density.[53,54] A relatively high fraction of heparin remained in the hydrogel, representing an efficient crosslinking reaction in our case.

We then studied the effects of gel formulation on gelation time and gel stiffness. We speculate that TEOA plays a role in the increase of gelation rate at higher pH, similar to observations of Valdebenito *et al.*[55], who attribute the effect of increase in pH near TEOA's pK_a of 7.74 to change the ionization of TEOA that facilitates electron transfer and, thus, increases the rate of polymerization. Interestingly, corresponding effects could not be achieved by increasing TEOA concentrations.

The effect of EY concentration shows the usual trade-off between availability of photo-initiator and penetration of light through the sample.[56] For each EY concentration, there is a specific optical penetration depth (L_p, also known as extinction length) for light of a particular wavelength, at which the light intensity has attenuated by 1/e.[57] The photoinitiator EY is the only species in the present formulation that absorbs light significantly; thus, the light intensity profile in the sample can be approximated by:

$$I(z) = I_o e^{-c\varepsilon z}$$

where I(z) is the light intensity at depth z, I_o is the incident light intensity, ε is the molar absorptivity of EY, and c is the concentration of EY in the sample (**Figure S-4**). Using UV-VIS spectroscopy to measure the absorbance of EY at different concentrations, we calculated ε for EY at 525 nm to be 1.09 x 10^5 $M^{-1}cm^{-1}$ from Beer's Law. For the EY concentrations considered here, the extinction lengths are approximately 1200 μm (0.005% EY), 600 μm (0.01% EY) and 300 μm (0.02% EY). For the first two, light penetrates through the entire sample thickness (500 μm on the rheometer and 320 μm for micropatterning); therefore, the increase in concentration of photo-initiator leads to

an increase in the rate of gelation (**Figure 3A**, *top*) and a shorter micropatterning gelation time (**Figure 3B**, *bottom*). However, for the highest of these concentrations, gelation occurs mainly on the irradiated side of the formulation. Due to the presence of a liquid layer on the dark side of the gap, the rheometer fails to detect an increase in modulus and the micropattern fails to adhere to the treated glass slide (it is observed on the cover slip instead, **Figure S-3**).

The well-known method of using 4-arm PEG instead of linear PEG to increase formation of elastically-effective junctions also works in the present system.[58] Replacing linear PEG-DA with its 4-arm counterpart resulted in faster gelation. In addition, the final moduli of hydrogels can be systematically modulated by varying the thiol:acrylate ratios (changing the ratio from 1:1 to 1:0.25 resulted in a softer gel).

Thiol-acrylate photo-polymerization occurs through a mixed-mode mechanism, *i.e.*, a combination of chain-growth and step-growth reactions.[59,60] When a thiol-acrylate system is photo-polymerized, a competition exists between the chain-growth homopolymerization of acrylate groups and the step-growth thiol-ene coupling. Bowman and Anseth *et al.* have demonstrated that the reaction of a thiyl radical with a carbon-carbon double bond is almost 10x faster than that of a carbon-based radical with the same double bond.[61,62] In accord with their findings, we observe a strong propensity to form SH – acrylate bonds (high levels of heparin incorporation) and negligible acrylate polymerization rates (as evidenced by failure to gel when Hep-SH was replaced

with heparin under matched concentration and irradiation conditions 5 mW/cm^2, 2.5 minutes).

Our motivation for developing a visible light photo-crosslinking formulation is for application of heparin gels in guided wound-healing of corneal injuries. In this context, the irradiation conditions are limited by damage thresholds for the cornea and retina. Therefore, we performed calculations for a computational eye model of the eye using ZEMAX ray-tracing software (geometry shown in **Figure S-5**).

In the EY/vis ZEMAX simulations, we allowed for a relatively long exposure (10 minutes) of visible light from a single LED (32^o viewing angle) placed 2 cm away from the cornea on axis. Under conditions that give a 5 mW/cm^2 flux at the apex of the cornea, the maximum retinal irradiance using these parameters was found to be ~6.9 mW/cm^2. Assuming that EY absorbs 50% of the incident light and using the retinal photochemical hazard-weighting function, the maximum flux of green light at the retina appears to be compatible with Group 1 and 2 Ophthalmic Instruments (ISO-15004-2:2007): 6.9 mW/cm^2 at 525 nm is approximately half the Group 1 threshold and is only 0.6% of the Group 2 threshold (**Table S-1**). In the Irgacure/UV case for heparin-based hydrogel formation, simulations were not required because the 18 W/cm^2 flux at 365 nm for photo-gelation is 5,000x over the threshold for corneal damage (which has a much greater damage threshold than the retina). In more common Irgacure/UV photopolymerization applications, the light flux used is between 5 and 20 mW/cm^2, with exposure times ranging from 1 to 30 minutes.[25-28] Taking a median value of 10 mW/cm2

flux and 10 minutes exposure time, the exposure level of the UV light is 2.75x over the threshold for corneal damage (far in excess of the threshold for retinal damage). The results for EY/vis suggest that the treatment might be compatible with a Group 1 device (no hazard), and indicate the treatment is well within the safety limit for the category of Group 2 devices (**Table S-1**).

The goal of using these heparin-based hydrogels as cell carriers or scaffolds is to display and deliver growth factors to nearby cells. Therefore, we confirm that they can be formed using EY/vis at physiological conditions without cytotoxicity and retain their ability to release growth factors. We tested the gelation time and final swollen moduli of hydrogels prepared at both 25ºC and 37ºC, and observed no significant differences between the two temperatures (**Figure S-6**). High levels of TEOA have been linked to cell toxicity.[63] To test cell viability, we encapsulated 3T3 fibroblasts in the hydrogels and subjected the samples to live/dead staining using acridine orange (AO) and propidium iodide (PI). We found that the addition of up to 0.1% w/v TEOA to the gel formulation did not measurably affect cell survival relative to TEOA-free controls (**Figure S-7**). Increasing the light intensity from 5 mW/cm^2 to 100 mW/cm^2, varying the crosslinking stoichiometry, and changing from linear PEG to 4-arm PEG also had no effect on 3T3 viability (**Table S-2, Figure S-7**). Encapsulated cells in all samples tested were over 96% viable.

To compare the present visible-light photocure system with the previously-reported UV cure with respect to growth factor delivery, we studied the release profile of epidermal

growth factor (EGF) from our hydrogel. We chose an EGF encapsulation concentration of 100 ng/mL based on studies that showed EGF to be effective in stimulating cell growth at concentrations of 0.1 – 100 ng/mL.[64,65]

The fraction of growth factor released (~30% in 2 days) is somewhat greater than that of hepatocyte growth factor (HGF) released from Tae and coworkers' original Michael-addition formulation over the same time period[19], and comparable to that of heparin-binding epidermal growth factor (HB-EGF) from a UV-activated chitosan hydrogel of Ishihara *et al.*[66], and that of encapsulated fibroblast growth factor (FGF) from a heparin-containing hydrogel reported by Nie *et al.*[58]. The time profile of release, with most of the release within the first day, is also similar to that of Ishihara *et al*.[66]. The *in vitro* EGF release profiles were not affected by the heparin content of the present gels, consistent with the small amount of EGF (~16 nM) loaded compared to the amount of heparin (~1 – 3 mM). The hydrogel has the capacity to carry a much greater amount of EGF, or to carry multiple growth factors in addition to EGF. To test the hypothesis that incomplete EGF release is due to a fraction of EGF becoming covalently bound to the hydrogel during photo-polymerization, we performed experiments in which EGF was loaded after photo-crosslinking. Approximately 60% of the EGF was released in that case. Thus, approximately half of the retained EGF may be covalently incorporated into the gel. EGF retained in the gel can act continuously on encapsulated cells or even promote the migration of external cells into the hydrogel.[67] To validate the bioactivity of released EGF, we carried out a mock wound-healing assay. Our results indicate that the EGF released from the heparin-based hydrogel has similar efficacy in promoting

fibroblast migration as native EGF, thereby confirming that its bioactivity is retained after hydrogel formation.

4.5 Conclusions

We have developed a visible-light photo-crosslinking formulation of a heparin-based hydrogel. Thiolated-heparin reacts with acrylate-ended poly(ethylene glycol) when green light (525 nm) is used to excite Eosin Y as a photoinitiator with triethanolamine as an electron donor. The hydrogel forms quickly (< 5 minutes), and is easily tunable in terms of both the mechanical properties and gelation kinetics by choice of the precursor concentration, crosslinker architecture and irradiation conditions (light intensity and exposure time). In addition, we successfully fabricated micropatterned cell-laden hydrogels, where the encapsulated fibroblasts remained viable after gelation. The incorporation of heparin in the hydrogel allows for the binding and release of a variety of growth factors. *In vitro* characterization of EGF as a model growth factor revealed that EGF retained its bioactivity after release from the hydrogel, indicating that our method of growth factor delivery protects the growth factors against damage. The irradiation conditions for gelation of the EY/vis formulation are compatible with safety standards for corneal and retinal exposure, opening the way to application of heparin-based hydrogels as cell or growth factor scaffolds for ocular tissue engineering.

4.6 References

1. Furth, M.E.; Atala, A.; Van Dyke, M.E. Smart biomaterials design for tissue engineering and regenerative medicine. *Biomaterials* **2007**; 28:5068-5073.
2. Daley, W.P.; Peters, S.B.; Larsen, M. Extracellular matrix dynamics in development and regenerative medicine. *J. Cell Sci.* **2008**; 121:255-264.

3. Bryant, S.J.; Anseth, K.S. Controlling the spatial distribution of ECM components in degradable PEG hydrogels for tissue engineering cartilage. *J. Biomed. Mater. Res., Part A* **2002**; 64A:70-79.

4. Brandl, F.; Sommer, F.; Goepferich, A. Rational design of hydrogels for tissue engineering: impact of physical factors on cell behavior. *Biomaterials* **2007**; 28:134-146.

5. Khademhosseini, A.; Langer, R. Microengineered hydrogels for tissue engineering. *Biomaterials* **2007**; 28:5087-5092.

6. Shu, X.Z.; Liu, Y.; Palumbo, F.S.; Luo, Y.; Prestwich, G.D. In situ crosslinkable hyaluronan hydrogels for tissue engineering. *Biomaterials* **2004**; 25:1339-1348.

7. Tan, H.; Chu, C.R.; Payne, K.A.; Marra, K.G. Injectable in situ forming biodegradable chitosan-hyaluronic acid based hydrogels for adipose tissue regeneration. *Biomaterials* **2009**; 30:2499-2506.

8. Lin, C-C.; Anseth, K.S. PEG hydrogels for the controlled release of biomolecules in regenerative medicine. *Pharmaceutical Research* **2009**; 26:631-643.

9. Raeber, G.P.; Lutolf, M.P.; Hubbell, J.A. Molecularly engineered PEG hydrogels: a novel model system for proteolytically mediated cell migration. *Biophysical Journal* **2005**; 89:1374-1388.

10. Tabata, Y.; Miyao, M.; Ozeki, M.; Ikada, Y. Controlled release of vascular endothelial growth factor by use of collagen hydrogels. *J. Biomater. Sci., Polym. Ed.* **2000**; 11:915-930.

11. Helary, C.; Bataille, I.; Abed, A.; Illoul, C.; Anglo, A.; Louedec, L.; Letourneur, D.; Meddahi-Pellé, A.; Giraud-Guille, M.M. Concentrated collagen hydrogels as dermal substitutes. *Biomaterials* **2010**; 31:481-490.

12. Gerecht, S.; Burdick, J.A.; Ferreira, L.S.; Townsend, S.A.; Langer R.; Vunjak-Novakovic, G. Hyaluronic acid hydrogel for controlled self-renewal and differentiation of human embryonic stem cells. *Proc. Natl. Acad. Sci. USA* **2007**; 104,11298-11303.

13. Segura, T.; Anderson, B.C.; Chung, P.H.; Webber, R.E.; Shull, K.R.; Shea, L.D. Crosslinked hyaluronic acid hydrogels: a strategy to functionalize and pattern. *Biomaterials* **2005**; 26:359-371.

14. Gonen-Wadmany, M.; Oss-Ronen, L.; Seliktar, D. Protein-polymer conjugates for forming photopolymerizable biomimetic hydrogels for tissue engineering. *Biomaterials* **2007**; 28:3876-3886.

15. Wang, C.; Stewart, R.J.; Kopeček, J. Hybrid hydrogels assembled from synthetic polymers and coiled-coil protein domains. *Nature* **1999**; 397:417-420.

16. Bjork, I.; Lindahl, U. Mechanism of the anticoagulant action of heparin. *Mol. Cell. Biochem.* **1982**; 48:161-182.

17. Burgess, W.H.; Maciag, T. The heparin-binding (fibroblast) growth factor family of heparin. *Annu. Rev. Biochem.* **1989**, 58:575-606.

18. Tae, G.; Kim, Y-J.; Choi, W-I.; Kim, M.; Stayton, P.S.; Hoffman, A.S. Formation of a novel heparin-based hydrogel in the presence of heparin-binding biomolecules. *Biomacromolecules* **2007**; 8:1979-1986.

19. Kim, M.; Lee, J.Y.; Jones, C.N.; Revzin, A.; Tae, G. Heparin-based hydrogel as a matrix for encapsulation and cultivation of primary hepatocytes. *Biomaterials* **2010**; 31:3596-3603.

20. Kim, M.; Shin, Y.; Hong, B.H.; Kim, Y.J.; Chun, J.S.; Tae, G.; Kim, Y.H. In vitro chondrocyte culture in a heparin-based hydrogel for cartilage regeneration. *Tissue Eng. Part C Methods* **2010**; 16:1-10.

21. Kim, M.; Kim, S.E.; Kang, S.S.; Kim, Y.H.; Tae, G. The use of de-differentiated chondrocytes delivered by a heparin-based hydrogel regenerate cartilage in partial-thickness defects. *Biomaterials* **2011**; 32:7883-7896.

22. Baldwin, A.D.; Kiick, K.L. Reversible maleimide-thiol adducts yield glutathione-sensitive poly(ethylene glycol)-heparin hydrogels. *Polym. Chem.* **2013**; 4:133-143.

23. Wieduwild, R.; Tsurkan, M.; Chwalek, K.; Murawala, P.; Nowak, M.; Freudenberg, U.; Neinhuis, C.; Werner, C.; Zhang, Y. Minimal peptide motif for non-covalent peptide-heparin hydrogels. *J. Am. Chem. Soc.* **2013**;135:2919-2922.

24. Chwalek, K.; Tsurkan, M.V.; Freudenberg, U.; Werner, C. Glycosaminoglycan-based hydrogels to modulate heterocellular communication in *in vitro* angiogenesis models. *Scientific Reports* **2014**; 4:4414.

25. DeForest, C.A.; Anseth, K.S. Photoreversible patterning of biomolecules within click-based hydrogels. *Angew. Chem. Int. Ed.* **2012**; 51:1816-1819.

26. Prado, S.S.; Weaver, J.M.; Love, B.J. Gelation of photopolymerized hyaluronic acid grafted with glycidyl methacrylate. *Mater. Sci. Eng., C* **2011**; 31:1767-1771.

27. Olofsson, K.; Malkoch, M.; Hult, A. Soft hydrogels from tetra-functional PEGs using UV-induced thiol-ene coupling chemistry: a structure-to-property study. *RSC Adv.* **2014**; 4:30118-30128.

28. Mironi-Harpaz, I.; Wang, D.Y.; Venkatraman, S.; Seliktar, D. Photopolymerization of cell-encapsulating hydrogels: crosslinking efficiency versus cytotoxicity. *Acta Biomaterialia* **2012**; 8:1838-1849.

29. Kim, M.; Kim, Y.H.; Tae, G. Human mesenchymal stem cell culture on heparin-based hydrogels and the modulation of interactions by gel elasticity and heparin amount. *Acta Biomaterialia* **2013**; 9:7833-7844.

30. Gwon, K.; Kim, M.; Tae, G. A biocompatible method of controlled retrieval of cell-encapsulating microgels from a culture plate. *Integr. Biol.* **2014**; 6:596-602.

31. Cerutti, P.A. Prooxidant states and tumor production. *Science* **1985**; 227:375-381.

32. Williams, C.G.; Malik, A.N.; Kim, T.K.; Manson, P.N.; Elisseeff, J.H. Variable cytocompatibility of six cell lines with photoinitiators used for polymerizing hydrogels and cell encapsulation. *Biomaterials* **2005**; 26:1211-1218.

33. Cruise, G.M.; Hegre, O.D.; Scharp, D.S.; Hubbell J.A. A sensitivity study of the key parameters in the interfacial photopolymerization of poly(ethylene glycol) diacrylate upon porcine islets. *Biotechnol. Bioeng.* **1998**; 57:655-665.

34. West, J.L.; Hubbell, J.A. Separation of the arterial wall from blood contact using hydrogel barriers reduces intimal thickening after balloon injury in the rat: the role of medial and luminal factors in arterial healing. *Proc. Natl. Acad. Sci. USA* **1996**; 93:13188-13193.

35. Torchiana, D.F. Polyethylene glycol based synthetic sealants. *J. Card. Surg.* **2003**; 18:504-506.

36. Hao, Y.; Shih, H.; Muňoz, Z.; Kemp, A.; Lin, C-C. Visible light cured thiol-vinyl hydrogels with tunable degradation for 3D cell culture. *Acta Biomaterialia* **2014**; 10:104-114.

37. Hao, Y.; Lin, C-C. Degradable thiol-acrylate hydrogels as tunable matrices for three-dimensional hepatic culture. *J. Biomed. Mater. Res. Part A* **2014**; 102A:3813-3827.

38. Ali, S.; Saik, J.E.; Gould, D.J.; Dickinson, M.E.; West, J.L. Immobilization of cell-adhesive laminin peptides in degradable PEGDA hydrogels influences endothelial cell tubulogenesis. *Biores. Open Access* **2013**; 2:241-249.

39. Shah, S.S.; Kim, M.; Tae, G.; Revzin, A. Micropatterning of bioactive heparin-based hydrogels. *Soft Matter* **2011**; 7:3133-3140.

40. Hinrichs, W.L.J.; ten Hoopen, H.W.M.; Wissink, M.J.B.; Engbers, G.H.M.; Feijen, J. Design of a new type of coating for the controlled release of heparin. *J. Control. Release* **1997**; 45:163-176.

41. Liang, C-C.; Park, A.Y.; Guan, J-L. In vitro scratch assay: a convenient and inexpensive method for analysis of cell migration in vitro. *Nature Protocols* **2007**; 2:329-333.

42. Ando, Y.; Jensen, P.J. Epidermal growth factor and insulin-like growth factor I enhance keratinocyte migration. *J. Invest. Dermatol.* **1993**; 100:633-639.

43. Blay, J.; Brown, K. D. Epidermal growth factor promotes the chemotactic migration of cultured rat intestinal epithelial cells. *J. Cell. Physio*. **1985**; 124:107-112.

44. Price, J.T.; Tiganis, T.; Agarwal, A.; Djakiew, D. Thompson E.W., Epidermal growth factor promotes MDA-MB-231 breast cancer cell migration through a phosphatidylinositol 3'-kinase and phospholipase C-dependent mechanism. *Cancer Res.* **1999**; 59:5475-5478.

45. Halstenberg, S.; Panitch, A.; Rizzi, S.; Hall, H.; Hubbell, J.A. Biologically engineered protein-graft-poly(ethylene glycol) hydrogels: a cell adhesive and plasmin-degradable biosynthetic material for tissue repair. *Biomacromolecules* **2002**; 3:710-723.

46. Shih, H.; Lin, C-C. Visible-light mediated thiol-ene hydrogelation using eosin-Y as the only photoinitiator. *Macromol. Rapid Comm.* **2013**; 34:269-273.

47. Shih, H.; Fraser, A.K.; Lin, C-C. Interfacial thiol-ene photoclick reactions for forming multilayer hydrogels. *ACS Appl. Mater. Interfaces* **2013**; 5:673-1680.

48. Lewis, R.J. Sax's Dangerous Properties of Industrial Materials, 9th ed. Volumes 1-3; Van Nostrand Reinhold: New York **1996**; pp 1500.

49. Gillner, M. and Loeper, I. Health effects of selected chemicals. 2. Triethanolamine. Nord 29; **1993**; pp 235-260.

50. Lee, S-H.; Moon, J.J.; West, J.L. Three-dimensional micropatterning of bioactive hydrogels via two-photon laser scanning photolithography for guided 3D cell migration. *Biomaterials* **2008**; 29:2962-2968.

51. Khademhosseini, A.; Eng, G.; Yeh, J.; Fukuda, J.; Blumling III, J.; Langer, R.; Burdick, J.A. Micromolding of photocrosslinkable hyaluronic acid for cell encapsulation and entrapoment. *J. Biomed. Mater. Res. Part A* **2006**; 79A:522-532.

52. Du, Y.; Ghodousi, M.; Lo, E.; Vidula, M.K.; Emiroglu, O. Surface-directed assembly of cell-laden microgels. *Biotechnol. Bioeng.* **2010**; 105:655-662.

53. Kao, Y.H.; Phillips, P.J. Crystallinity in chemically crosslinked low density polyethylenes: 1. Structural and fusion studies. *Polymer* **1986**; 27:1669-1678.

54. Davis, T.P.; Huglin, M.B.; Yip, D.C.F. Properties of poly(N-vinyl-2-pyrrolidone) hydrogels crosslinked with ethyleneglycol dimethacrylate. *Polymer* **1988**; 29:701-706.

55. Valdebenito, A.; Encinas, M.V. Photopolymerization of 2-hydroxylethyl methacrylate: effect of the medium properties on the polymerization rate. *J. Polym. Sci. A Polym. Chem.* **2003**; 41:2368-2373.

56. Terrones, G. and Pearlstein, A.J. Effects of optical attenuation and consumption of a photobleaching initiator on local initiation rates in photopolymerization. *Macromolecules* **2001**; 34:3195-3204.

57. Huynh, J. Factors governing photodynamic cross-linking of ocular coat. Ph.D. Dissertation [Online], California Institute of Technology, Pasadena CA, **2011**. http://resolver.caltech.edu/CaltechTHESIS:05202011-143758537

58. Nie, T.; Baldwin, A.; Yamaguchi, N.; Kiick, K.L. Production of heparin-functionalized hydrogels for the development of responsive and controlled growth factor delivery systems. *J. Control. Release* **2007**; 122:287-296.

59. Salinas, C.N. and Anseth, K.S. Mixed mode thiol-acrylate photopolymerizations for the synthesis of PEG-peptide hydrogels. *Macromolecules* **2008**; 41:6019-6026.

60. Reddy, S.K.; Okay, O.; Bowman, C.N. Network development in mixed step-chain growth thiol-vinyl photopolymerizations. *Macromolecules* **2006**; 39:8832-8843.

61. Cramer, N.B.; Bowman, C.N. Kinetics of thiol-ene and thiol-acrylate photopolymerizations with real-time fourier transform infrared. *J. Polym. Sci., Part A: Polym. Chem.* **2001**; 39:3311-3319.

62. Rydholm, A.E.; Bowman, C.N.; Anseth, K.S. Degradable thiol-acrylate photopolymers: polymerization and degradation behavior of an in situ forming biomaterial. *Biomaterials* **2005**; 26:4495-4506.

63. Maekawa, A.; Onodera, H.; Tanigawa, H.; Furuta, K.; Kanno, J.; Matsuoka, C.; Ogiu, T.; Hayashi, Y. Lack of carcinogenicity of triethanolamine in F344 rats. *J. Toxicol. Environ. Health* **1986**; 19:345-357.

64. Yan, F.; Hui, Y.N.; Li, Y.J.; Guo, C.M.; Meng, H. Epidermal growth factor receptor in cultured human retinal pigment epithelial cells. *Ophthalmologica* **2007**; 221:244-250.

65. Kawamoto, T.; Sato, J.D.; Le, A.; Polikoff, J.; Sato, G.H.; Mendelsohn, Growth stimulation of A431 cells by epidermal growth factor: identification of high-affinity receptors for epidermal growth factor by an anti-receptor monoclonal antibody. J. *Proc. Natl. Acad. Sci. USA* **1983**; 80:1337-1341.

66. Ishihara, M.; Obara, K.; Ishizuka, T.; Fujita, M.; Sato, M.; Masuoka, K.; Saito, Y.; Yura, H.; Matsui, T.; Hattori, H.; Kikuchi, M.; Kurita, A. Controlled release of fibroblast growth factors and heparin from photocrosslinked chitosan hydrogels and subsequent effect on in vivo vascularization. *J. Biomed. Mater. Res. Part A* **2003**; 64A:551-559.

67. Gobin, A.S.; West, J.L. Effects of epidermal growth factor on fibroblast migration through biomimetic hydrogels. *Biotechnology Progress* **2003**; 19:1781-1785.

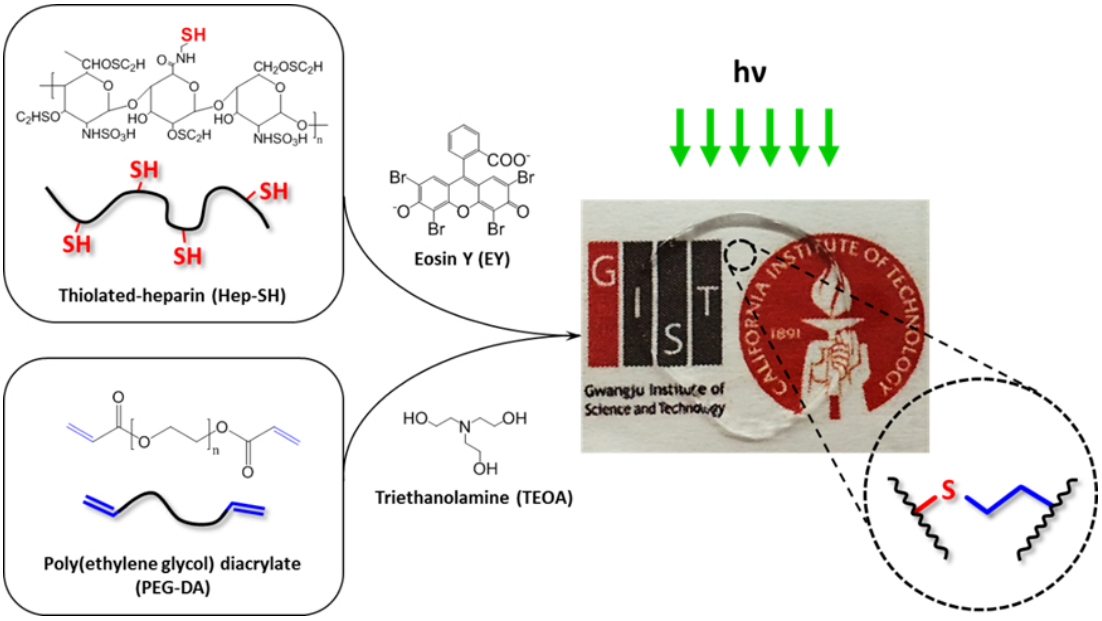

Figure 1. Schematic representation of visible-light activated heparin-based hydrogel formation. Thiol-functionalized heparin (Hep-SH) reacts with poly(ethylene glycol) diacrylate (PEG-DA) when green light (525 nm) is used to excite Eosin Y (EY) as a photoiniator with triethanolamine (TEOA) as an electron donor.

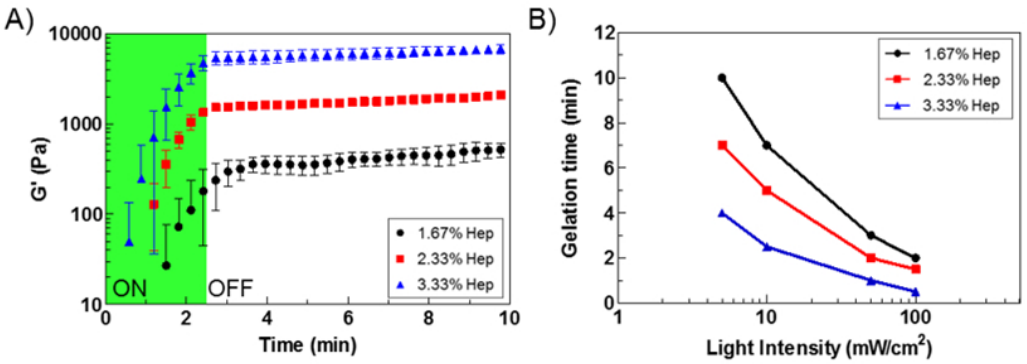

Figure 2. Effect of concentration on (A) gelation kinetics and (B) micropatterning gelation time for a fixed molar ratio of heparin to linear PEG (thiol:acrylate 1:1 mol, equivalent to Hep-SH:PEG-DA 1:2 mass ratio) in PBS (pH 7.8) with 0.01% EY and 0.1% TEOA. Concentrations are given in terms of heparin weight percent to emphasize the bioactive component. (A) Storage modulus of gel solution during irradiation with 525 nm green light at 5 mW/cm^2 for 2.5 minutes (shaded green area) and afterward for a total of 10 minutes. (B) Optimal irradiation time to achieve spatially-resolved gelation using 525 nm green light at 100 mW/cm^2.

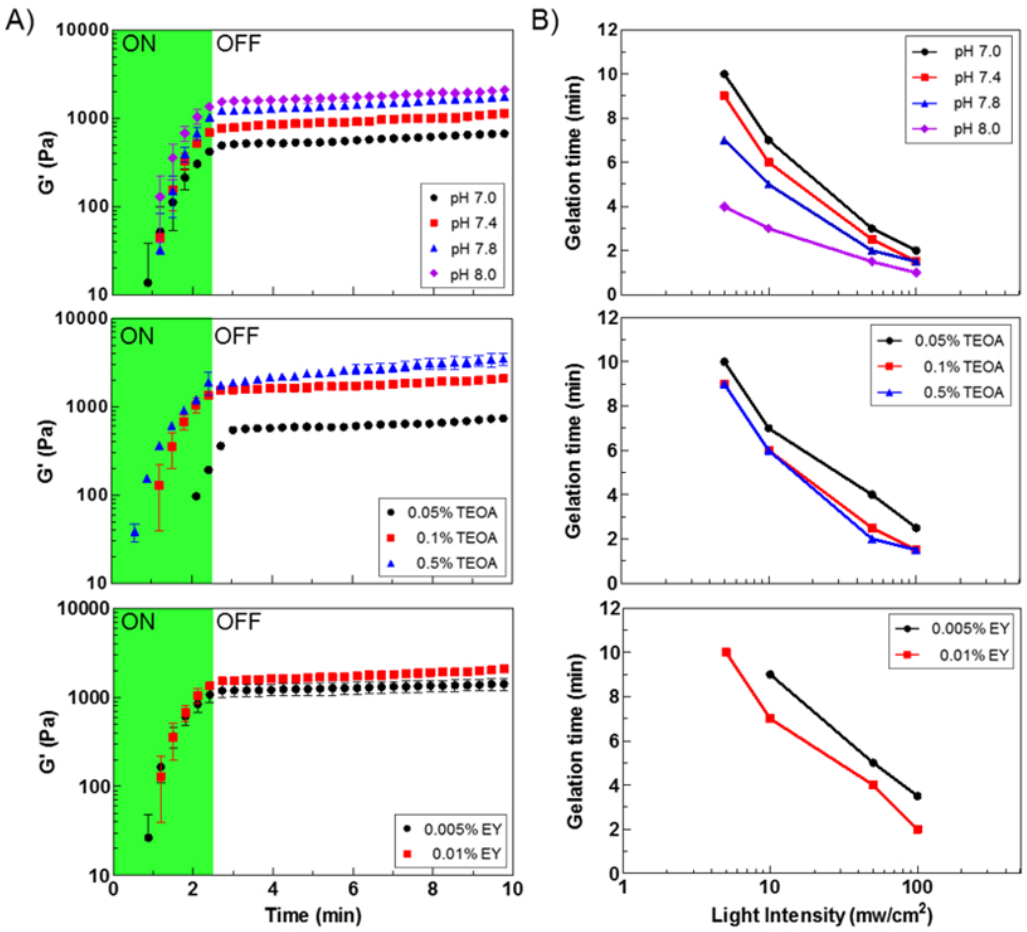

Figure 3. Effects of pH for [TEOA] = 0.1% and [EY] = 0.01% (*top*), TEOA concentration with pH = 8.0 and [EY] = 0.01% (*middle*), and EY concentration for pH 8.0 and [TEOA] = 0.1% (*bottom*) on (A) gelation kinetics and (B) micropatterning gelation time for fixed concentrations of heparin (2.33% w/v) and heparin-to-linear-PEG molar ratio thiol:acrylate 1:1, equivalent to Hep-SH:PEG-DA 1:2 mass ratio, in PBS (pH 7.8). Compositions listed in Table 2. (A) Storage modulus of gel solution during irradiation with 525 nm green light at 5 mW/cm^2 for 2.5 minutes (green shaded area) and afterward for a total of 10 minutes. (B) Optimal irradiation time to achieve spatially-resolved gelation using 525 nm green light at 100 mW/cm^2.

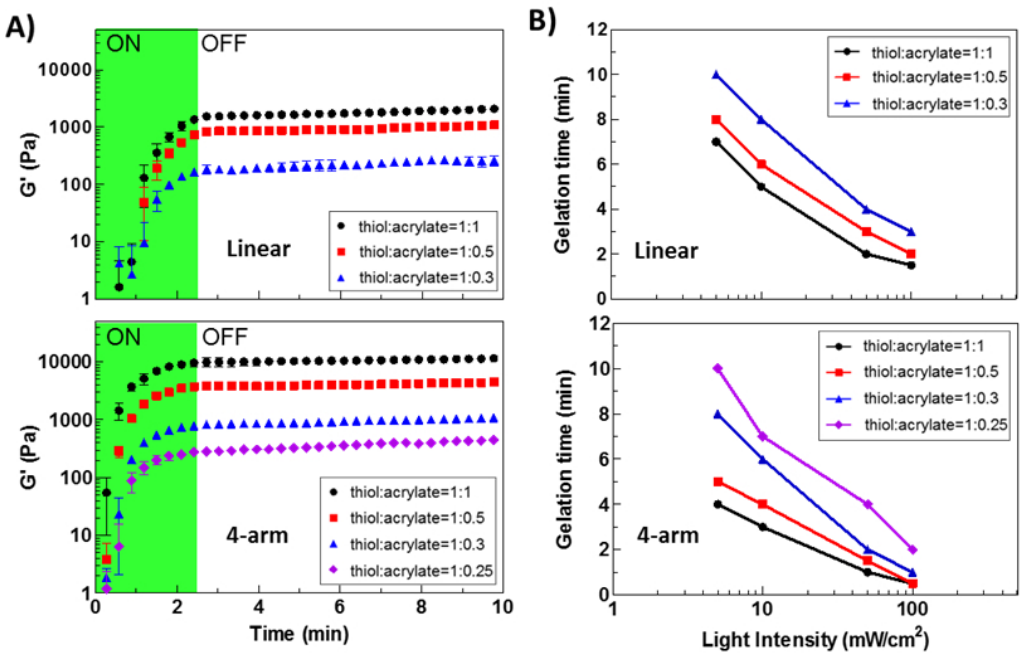

Figure 4. Effects of crosslinking stoichiometry for linear PEG (top) and 4-arm PEG (bottom) on (A) gelation kinetics and (B) micropatterning gelation time for fixed concentrations of heparin (2.33% w/v), EY (0.01%) and TEOA (0.1%) in PBS (pH 7.8). Compositions listed in Table 3. (A) Storage modulus of gel solution during irradiation with 525 nm green light at 5 mW/cm^2 for 2.5 minutes (green shaded area) and afterward for a total of 10 minutes. (B) Optimal irradiation time to achieve spatially-resolved gelation using 525 nm green light at 100 mW/cm^2. Note that thiol:acrylate = 1:0.25 was characterized for both linear and 4-arm PEG; it is not shown in (*top*) because it did not gel under any of the irradiation conditions shown.

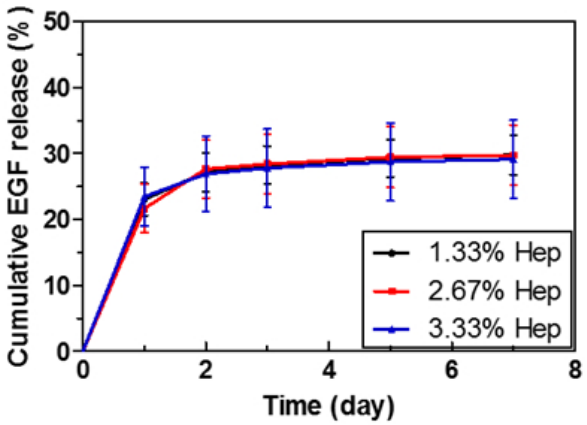

Figure 5. *In vitro* release profiles of epidermal growth factor (EGF) from heparin-based hydrogels at different heparin concentration. Hydrogels were prepared in PBS (pH 7.8) with 0.01% EY, 0.1% TEOA and 100 ng/mL EGF. [Heparin] = 2.33% w/v, [PEG-DA] = 4.67% w/v.

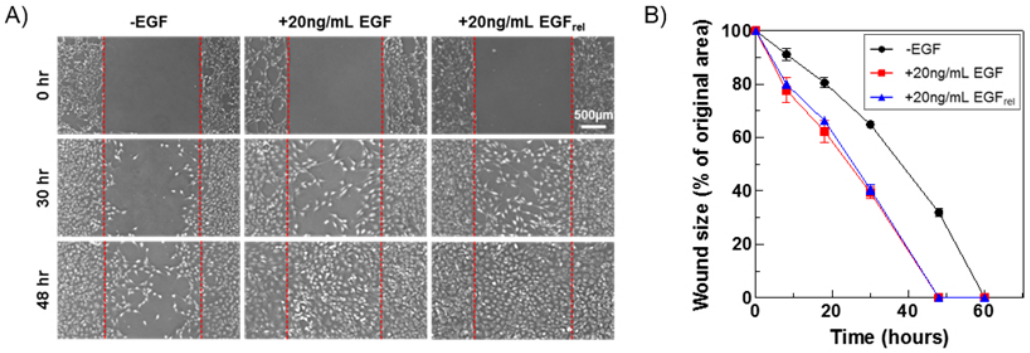

Figure 6. Effect of EGF on cell migration of 3T3 fibroblasts in a wound-healing assay: (A) representative pictures taken using phase contrast microscopy and (B) quantified results. EGF released from the heparin-based hydrogel (EGF_{rel}) promotes cell migration at a rate similar to native EGF. Cells exposed to EGF or EGF_{rel} migrate faster than control samples without EGF exposure.

Table 1. Effect of heparin concentration on gel properties.

Heparin (%)	PEG-DA (%)	G' (Pa) as prepared[(a)]	G' (Pa) after swelling	Wet : dry mass ratio[(b)]	Fraction of heparin retained
1.67%	3.33%	550 ± 110	200 ± 20	30.5 ± 1.6	0.87 ± 0.03
2.33%	4.67%	1800 ± 80	900 ± 120	25.2 ± 1.0	0.94 ± 0.03
3.33%	6.67%	6900 ± 800	4350 ± 240	17.5 ± 2.1	0.96 ± 0.02

[(a)] Hep-SH (12 kDa) and linear PEG-DA (6 kDa), thiol:acrylate mole ratio 1:1 (hence 1:2 mass ratio Hep-SH:PEG-DA), 25°C, pH 7.8, [EY] = 0.01%, [TEOA] = 0.1%, 5 mW/cm^2 at 525 nm for 2.5 minutes. [(b)] Note that the dry mass may contain 10-15% of salts introduced with the PBS buffer.

Table 2. Effect of gel formulation on gel properties.

pH	TEOA	EY	G' (Pa) as prepared[(a)]	G' (Pa) after swelling	Wet : dry mass ratio[(b)]	Fraction of heparin retained
7.0	0.1%	0.01%	680 ± 50	480 ± 80	30.1 ± 1.3	0.71 ± 0.10
7.4			1150 ± 120	530 ± 80	27.4 ± 0.6	0.77 ± 0.06
7.8			1800 ± 80	900 ± 120	25.2 ± 1.0	0.94 ± 0.03
8.0			2110 ± 140	980 ± 110	23.9 ± 1.0	0.96 ± 0.01
8.0	0.05%	0.01%	760 ± 60	340 ± 20	27.7 ± 0.7	0.66 ± 0.01
	0.1%		1800 ± 80	900 ± 120	25.2 ± 1.0	0.94 ± 0.03
	0.5%		3580 ± 580	1550 ± 190	17.2 ± 1.0	0.96 ± 0.02
8.0	0.1%	0.005%	1440 ± 220	860 ± 210	25.1 ± 0.6	0.93 ± 0.03
		0.01%	1800 ± 80	900 ± 120	25.2 ± 1.0	0.94 ± 0.03

[(a)] [Heparin (12 kDa)] = 2.33%, linear [PEG-DA (6 kDa)] = 4.67%, thiol:acrylate molar ratio 1:1 (equivalent to 1:2 mass ratio Hep-SH:PEG-DA), 25°C, 5 mW/cm^2 at 525 nm for 2.5 minutes. [(b)] Note that the dry mass may contain 10-15% of salts introduced with the PBS buffer.

Table 3. Effects of crosslinking stoichiometry and architecture on gel properties

Molar Ratio (thiol:acryl)	PEG	PEG (%)	G' (Pa) as prepared[(a)]	G' (Pa) after swelling	Wet : dry mass ratio[(b)]	Fraction of heparin retained
1:1	Linear	4.67%	1800 ± 80	900 ± 120	25.2 ± 1.0	0.94 ± 0.03
1:0.5	Linear	2.33%	1100 ± 60	310 ± 50	30.7 ± 0.9	0.80 ± 0.04
1:0.3	Linear	1.40%	270 ± 50	80 ± 10	34.0 ± 1.6	0.50 ± 0.07
1:1	4-arm	5.06%	11630 ± 520	4530 ± 170	13.4 ± 1.0	0.97 ± 0.01
1:0.5	4-arm	2.52%	4510 ± 350	1650 ± 200	19.7 ± 1.4	0.77 ± 0.02
1:0.3	4-arm	1.51%	1080 ± 70	320 ± 50	30.1 ± 1.2	0.69 ± 0.07
1:0.25	4-arm	1.26%	450 ± 40	160 ± 70	35.2 ± 0.8	0.61 ± 0.09

[(a)] Hep-SH (12 kDa), linear PEG-DA (6 kDa), 4-arm acrylate-terminated PEG (13 kDa), 25°C, [Heparin] = 2.33%, [EY] = 0.01%, [TEOA] = 0.1%, 5 mW/cm^2 at 525 nm for 2.5 minutes. [(b)] Note that the dry mass may contain 10-15% of salts introduced with the PBS buffer.

Additional Information

Preparation of release layer on the glass slide.

In order to enable controlled retrieval of micropatterned heparin-based hydrogels from their substrate, one of the glass slides is treated to provide an initially-adhesive surface that can be subsequently "switched" to release the gel in a stimuli-response manner.[1] Specifically, a layer-by-layer (LbL) technique was used to deposit a $(PLL\text{-}HA)_2$ multilayer followed by an adhesive-capping layer. First, the glass slides were cleaned by ultrasonication in isopropanol and deionized water for 10 minutes in each. The glass slides were dried with filtered nitrogen and exposed to an oxygen plasma (YES-R3, San Jose, CA, USA) for 5 minutes. The polyelectrolytes were adsorbed on the glass using the usual layer-by-layer technique immersing the substrate alternately in the polycation and the polyanion solutions with rinsing in between. Specifically, the glass slide is first placed in a PLL (0.5 mg/ml) solution for 5 minutes, followed by rinsing with PBS, then it is placed in a HA (0.5 mg/ml) solution, followed by rinsing with PBS. This procedure was repeated one more time to create a $(PLL\text{-}HA)_2$ multilayer. As the last adsorption step, acryl-functionalized chitosan (GMA-Chi, 30% acrylation) (5 kDa) was adsorbed by immersing in a GMA-Chi (30% acrylation, 2 mg/ml) solution for 30 minutes, followed by rinsing with PBS. GMA-Chi was synthesized as previously reported.[2] Modified glass slides were placed in a desiccator until further use. The glass substrates bearing this multilayer are denoted as $(PLL\text{-}HA)_2$-(GMA-Chi).

[1] Gwon, K.; Kim, M.; Tae, G. *Integr. Biol*. **2014**, *6*, 596-602.

[2] Kim, J. Y.; Choi, W. I.; Kim, Y. H.; Tae, G.; Lee, S. Y.; Kim, K.; Kwon, I. C. *J. Controlled Release* **2010**, *147*, 109-117.

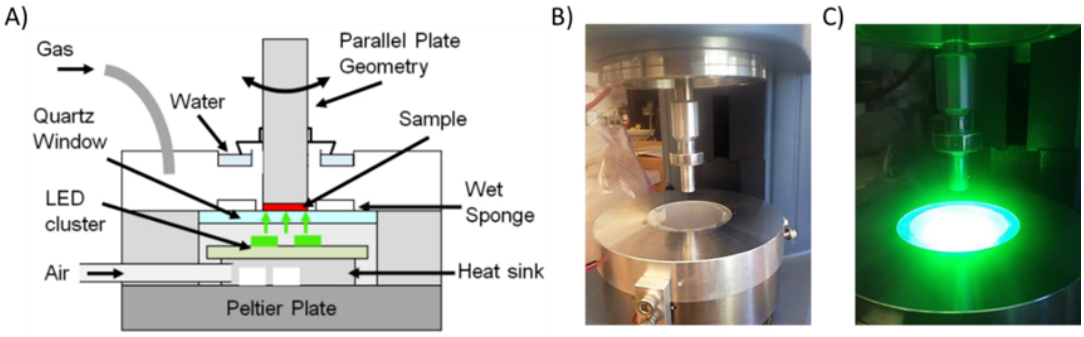

Figure S-1. A) Diagram of photo-rheology apparatus. The green LED cluster is mounted on a ventilated heat sink that removes heat generated from the LED to prevent the sample from heating when the LED is on. The LED assembly is mounted beneath the transparent bottom plate of the rheometer, used in a parallel plate geometry The hydrogel ("Sample," shown in red) is prevented from drying by surrounding the sample with a wet sponge during the experiment. Photographs of the rheometer (without sample and environmental control) when the LEDs are turned off (B) and turned on (C).

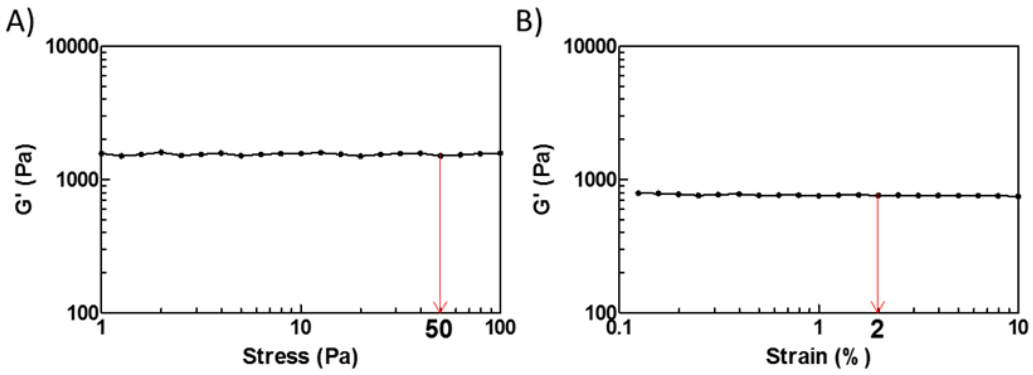

Figure S-2. Results of A) a stress sweep from 1 to 100 Pa in oscillatory rheology at 1 rad/s on the photorheometry apparatus based on a stress-controlled rheometer (AR 1000) and B) a strain sweep from 0.1 to 10% on the strain-controlled rheometer that was used to measure the storage modulus of swollen hydrogels (ARES RFS). The results confirm that all of the oscillatory conditions used in this study are in the linear viscoelastic range: The red arrows show the stress amplitude used during photorheometry experiments and the strain amplitude used for subsequent analysis after cure.

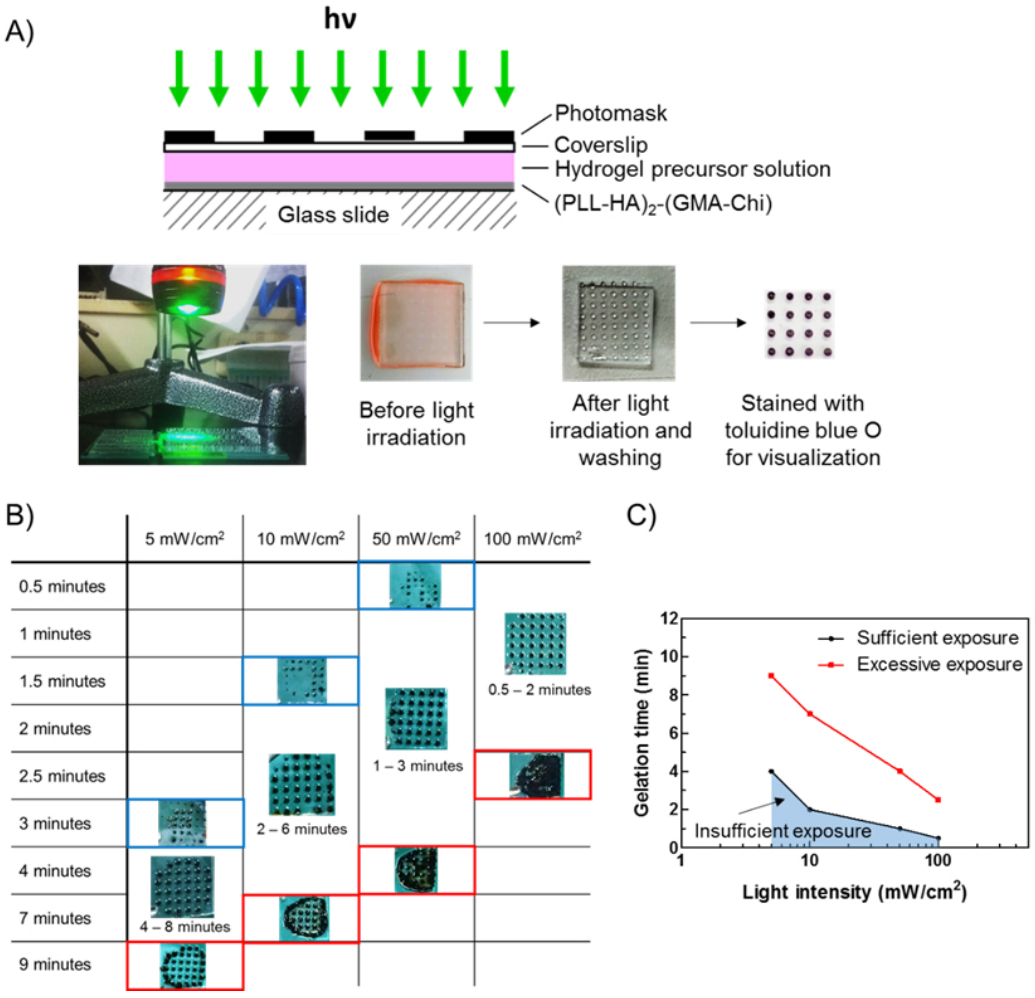

Figure S-3. A) Schematic representation of the micropatterning process. The hydrogel precursor solution is applied onto the $(PLL\text{-}HA)_2$-(GMA-Chi)-modified glass slide, bounded by a 320micron thick Teflon spacer. A cover slip is placed over the gel, and a photomask is placed on top of it. Thus, irradiation is performed from the side in contact with an untreated glass surface. The LED source is placed over the sample and turned on for the desired irradiation time. Then, the mask and coverslip are removed (in cases of insufficient exposure, small islands of gel are on the coverslip). The $(PLL\text{-}HA)_2$-(GMA-Chi)-modified glass slide is rinsed with PBS, and then stained. B) Representative photographs of microgels formed using different light intensities and exposure times.

Images indicative of insufficient exposure are outlined in blue; images indicating that gels had undergone “excessive exposure” are outlined in red. C) Graphical representation of the minimum exposure that produces a well-defined pattern on the $(PLL\text{-}HA)_2$-(GMA-Chi)-modified glass slide (black curve), corresponding to “sufficient exposure” in the body of the manuscript and the upper bound on exposure time so that disks of gel are separate (red curve). [Heparin] = 3.33%, linear [PEG-DA] = 6.67%, [EY] = 0.01%, [TEOA] = 0.1%, in PBS (pH 7.8).

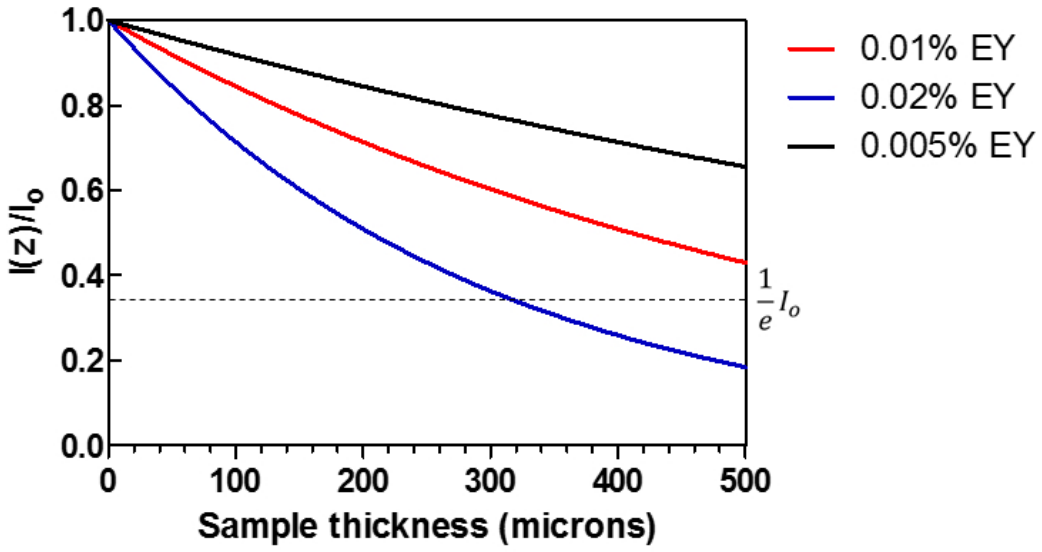

Figure S-4. Intensity profiles calculated using the molar absorptivity of EY (1.09 10^5 $M^{-1}cm^{-1}$) for thickness up to that of the thickest samples used in this study (rheometry samples were 500 microns thick, while the micropatterning samples were 320 microns thick). The fraction of incident light that reaches the back of the sample depends on the concentration of the photo-initiator EY. The optical penetration depth, Lp, defined as the depth at which the initial light intensity is attenuated by 1/e (dotted line), which decreases from 1200 microns for 0.005% EY to 300 microns for 0.02% EY.

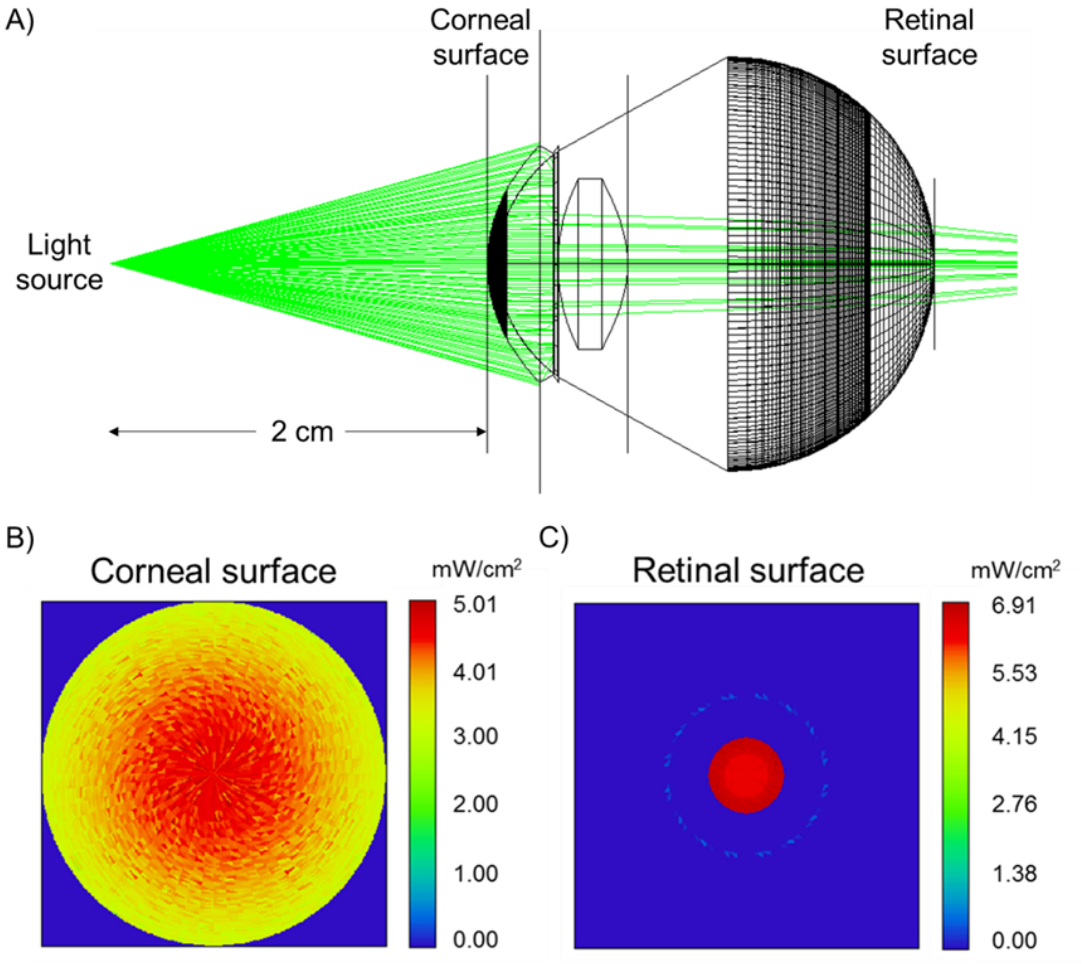

Figure S-5. Computational eye model using ZEMAX ray-tracing software. (A) A single LED (32^{o} viewing angle, 525 nm) was placed 2 cm away from the cornea on axis. The number of rays from the light source was set at 10 million. A corneal irradiance of 5 mW/cm^2 (B) corresponds to a retinal irradiance of 6.9 mW/cm^2 (C).

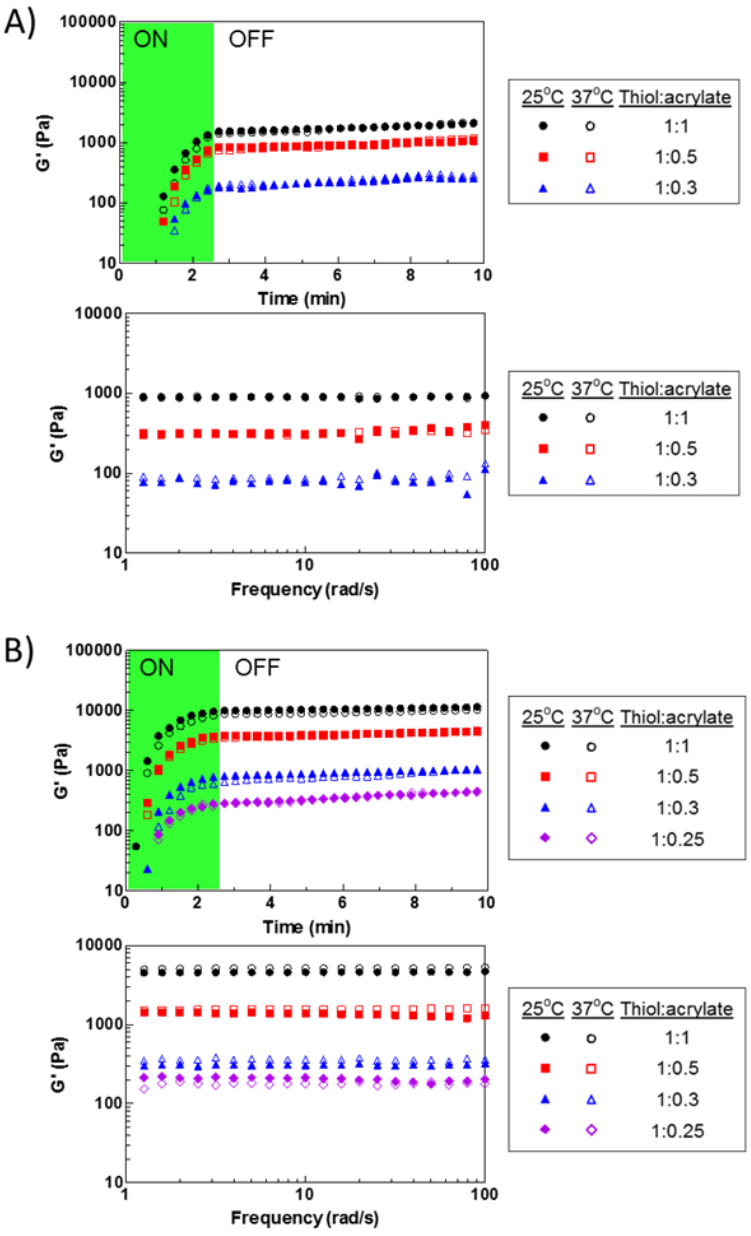

Figure S-6. Gelation kinetics and final gel moduli of hydrogels prepared at different crosslinking conditions using linear PEG (A) and 4-arm PEG (B), other parameters held fixed in PBS (pH 7.8). There is no significant difference in gelation time or final swollen modulus between hydrogels prepared at 25°C and 37°C. Gel solution was irradiated with a 525nm green light at 5 mW/cm^2 for 2.5 minutes.

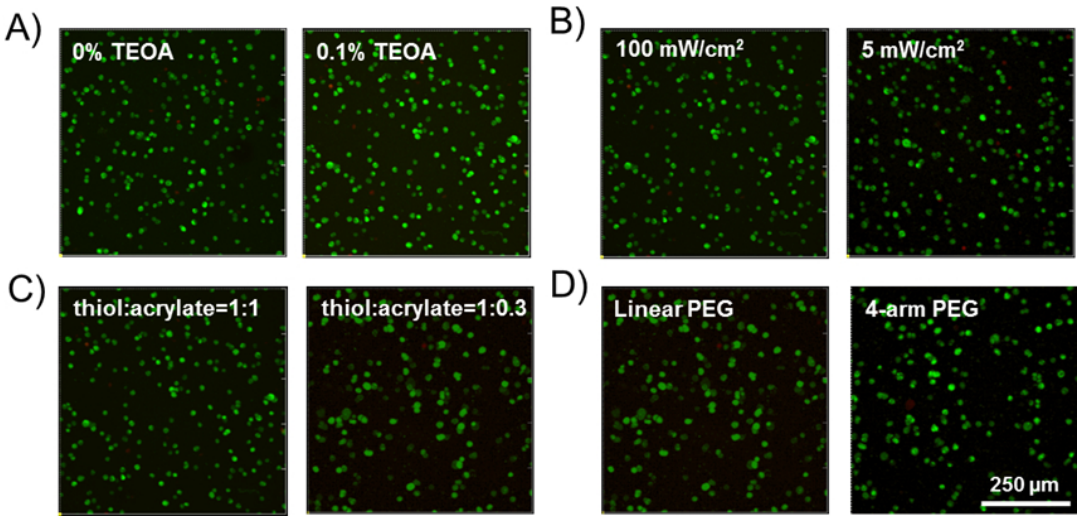

Figure S-7. Cell viability of 3T3 fibroblasts (2 x 10^6 cells/mL) encapsulated inside heparin-based hydrogels at different (A) TEOA concentration, (B) light intensities, (C) crosslinking densities and (D) PEG architecture. Live cells are stained green, and dead cells are stained red. Cell viability in all cases was ≥ 96%. Unless otherwise noted, hydrogels were prepared with 2.33% heparin (w/v), thiol:acrylate 1:1, 0.01% EY and 0.1% TEOA in PBS (pH 7.8) with linear PEG and 5 mW/cm^2 irradiation.

Table S-1. Comparison of visible and UV photo-gelation conditions to eye safety thresholds

	EY/vis	**Irgacure/UV**
Wavelength	525 nm	365 nm
Flux	5 mW/cm^2	10 mW/cm^2
Exposure time	10 minutes	10 minutes[(d)]
Hazard weighting function[(a)]	A(λ:525 nm) = 0.031	S(λ:365 nm) = 1.1 x 10^{-4}
Group 1[(b)] safety limit	220 μW/cm^2	0.4 μW/cm^2
Calculated irradiance	110 μW/cm^2	1.1 μW/cm^2
% of threshold for Group 1	**50% (**ret.)	**275%** (cor.)
Group 2[(c)] safety limit	10,000 mJ/cm^2	3 mJ/cm^2
Calculated exposure	64 mJ/cm^2	0.66 mJ/cm^2
% of threshold for Group 2	**0.6%** (ret.)	**22%** (cor.)

[(a)] Hazard weighting functions represent the relative spectral sensitivity of the human eye to light hazards. For visible light the *retinal* photochemical hazard weighting function A(λ) is used because the light dose is far below the threshold for corneal damage. For UV light, the *corneal* UV radiation hazard weighting function S(λ) is used. The UV conditions are far in excess of the safety threshold of the retina.
[(b)] Group 1 devices are those for which no potential light hazard exists. See text for description of ZEMAX calculations. For visible light, Group 1 limit refers to weighted *retinal* irradiance. For UV light, *corneal* threshold is reached for UV (far in excess of retinal damage threshold).
[(c)] Group 2 devices are those for which a potential light hazard exists. For visible light, Group 2 limit refers to the weighted *retinal* radiant exposure. For UV light, Group 2 limit refers to the weighted *corneal* UV radiant exposure (much greater than the threshold for retina damage).
[(d)] The lower the light intensity, the longer the exposure time.
(ret.) indicates retinal photochemical threshold, see (a); (cor.) indicates corneal UV radiation threshold, see (a).

Table S-2. Cell viability of 3T3 fibroblasts encapsulated inside heparin-based hydrogels (2×10^6 cells/mL) at different conditions.

Condition	**Cell viability**			
[TEOA][a]	0% TEOA	96.2 ± 1.1%	0.1% TEOA	97.2 ± 1.0%
Light intensity[b]	5 mW/cm^2	97.6 ± 0.4%	100 mW/cm^2	97.2 ± 1.0%
Thiol:acrylate ratio[c]	1:1	97.2 ± 1.0%	1:0.3	99.6 ± 0.2%
PEG architecture[d]	Linear	99.6 ± 0.2%	4-arm	99.4 ± 0.7%

[a] [Hep-SH (12 kDa)] = 2.33%, linear [PEG-DA (6 kDa)] = 4.67%, thiol:acrylate = 1:1, 25ºC, pH 7.8, [EY] = 0.01%, 100 mW/cm^2 for 2 minutes for 0% TEOA and 1.5 minutes for 0.1% TEOA.

[b] [Hep-SH (12 kDa)] = 2.33%, linear [PEG-DA (6 kDa)] = 4.67%, thiol:acrylate = 1:1, 25ºC, pH 7.8, [EY] = 0.01%, [TEOA] = 0.1%. Irradiation time was 7 minutes at 5mW/cm^2, and 1.5 minutes at 100 mW/cm^2.

[c] Hep-SH (12 kDa), linear PEG-DA (6 kDa), 25ºC, [Heparin] = 2.33%, [EY] = 0.01%, [TEOA] = 0.1%, 100 mW/cm^2 for 1.5 minutes for 1:1 ratio and 3 minutes for 1:0.3 ratio.

[d] Hep-SH (12 kDa), PEG-DA (6 kDa) thiol:acrylate 1:0.3, Hep-SH:4-arm acrylate-terminated PEG (13 kDa) thiol:acrylate 1:0.25, 25ºC, [Heparin] = 2.33%, [EY] = 0.01%, [TEOA] = 0.1%, 100 mW/cm^2 for 3 minutes for linear PEG, and 2 minutes for 4-arm PEG.

Chapter 5

In vivo study of corneal scaffold in a mouse epithelial defect model

5.1 Introduction

In Chapter 2, we demonstrated that nanofiber substrates show great potential to be used in a scaffold for promoting orderly corneal wound healing. They are easy to fabricate and handle, transparent, and non-cytotoxic. In addition, we have shown that isotropic nanofibers (with no preferred orientation) can promote epithelial cell migration and that uniaxially aligned nanofibers can enhance fibroblast cell migration and modulate the myofibroblast phenotype by decreasing αSMA expression.

In Chapter 4, we developed a visible-light photo-crosslinking formulation of a heparin-based hydrogel. We showed that these hydrogels are suitable for corneal applications due to their transparency and non-cytotoxicity, and that the irradiation conditions for gelation (5 mW/cm^2 for 5 minutes) are compatible with safety standards for corneal and retinal exposure. In addition, these hydrogels form quickly (< 5 minutes), are easily tunable (by choice of precursor concentration, crosslinker architecture or irradiation conditions), and allow the binding and release of bioactive growth factors.

Taken together, we envision that an ideal corneal scaffold would consist of layers of nanofibers inside a transparent hydrogel, thereby containing the necessary topological and biochemical cues for orderly wound repair. Here, in addition to the heparin-based hydrogel described above, we also investigated the use of artificial extracellular matrix (aECM) protein-based hydrogels as an alternative.

Developed by Professor David Tirrell at Caltech, aECM proteins allow for systematic control of biochemical cues, as well as easily tunable degradation rates by proteolytic processes.[1,2] The Tirrell group have demonstrated that aECM proteins can be chemically crosslinked to form transparent films[3] or can be formed into injectable hydrogels through physical interactions of leucine zippers[4]. Furthermore, they showed that aECM proteins are favorable for collective cell migration[5], and promote endothelial cell adhesion and spreading[6-8]. The aECM protein chosen for this study was derived from elements of fibronectin and elastin, and can be crosslinked with four-armed poly(ethylene glycol) with end-terminated succinimidyl glutarate groups to form a transparent hydrogel. We hypothesize that the RGD cell-binding sites present in aECM are favorable for promoting cell infiltration.

Although live/dead staining results show that the nanofibers and hydrogel do not affect cell viability *in vitro,* it is important to validate the safety and biocompatibility of our scaffold *in vivo.* For clinical translation, we are also interested in testing the feasibility of our treatment protocol (e.g. how much time is needed to treat each eyeball? Is it easy to apply the treatment? etc.)

Mice corneas are very thin (~ 170 microns)[9], so it is not possible to create reproducible deep wounds without the risk of puncturing through the cornea. However, the mouse model is good for testing the biocompatibility of our scaffold. Indeed, studies have used alkali burns or sutures to induce corneal neovascularization and examined the efficacy

of different treatments in alleviating ocular damage.[10-13] Here, we use a less harsh method (by debriding the corneal epithelium with a corneal knife) to test our scaffold in treating epithelial defects.

The goal of this *in vivo* study is to answer the following questions:

1. Is the treatment transparent when placed on the mouse cornea?
2. Does the treatment remain in the wound following the procedure?
3. Does the treatment induce inflammation?
4. Does the treatment hinder re-epithelialization over the wounded area?

This study will yield significant insights regarding the biocompatibility of our scaffold. Observations made will allow us to optimize (and re-examine, if necessary) the properties of our scaffold with respect to corneal healing, prior to carry out experiments in rabbits where deeper wounds are possible.

5.2 Methods

Fabrication of scaffold

Fabrication of nanofibers

Gelatin (type A, porcine, Sigma Aldrich, St. Louis, MO) was dissolved in a mixture of 2:3:5 distilled water/ethyl acetate/acetic acid at 12% w/w and stirred overnight at 37^{o}C. Electrospun nanofibers were fabricated from the gelatin solution using a 22-gauge needle, +15 kV voltage and 8 cm needle to collector distance. Isotropic nanofibers were collected on a metal ring (6 mm diameter) placed on a planar electrode.

Characterization of nanofibers

To visualize the nanofibers, they were labeled with NHS-fluorescein (Thermo Fisher, Rockford, IL). The nanofiber mats were immersed in the staining solution (0.1 mg/mL NHS-fluorescein, 1% DMSO, PBS) for one hour at room temperature. Residual dye was removed by rinsing the nanofibers with deionized water three times (15 mins each). Nanofiber mats were air-dried prior to use. To characterize the fiber diameter, samples were mounted onto aluminum stubs using double-sided carbon tape and sputter-coated (Cressington 208HR) with a 10 nm layer of palladium. Prepared samples were then observed in a field emission scanning electron microscope (SEM, Zeiss 1550 VP) at an accelerating voltage of 5 kV.

Fabrication of aECM-PEG hydrogels

Artificial extracellular matrix proteins (aECM, 34.6 kDa) were synthesized and characterized using established protocols described elsewhere. To fluorescently label aECM proteins (aECM-f), aECM protein (2.5 mg/mL in PBS) was mixed with NHS-rhodamine (7 molar excess) for one hour at room temperature. Excess dye was removed by fluorescent dye removal columns (Thermo Scientific). aECM-f proteins were then lyophilized for storage until use. aECM protein solutions were prepared by dissolving aECM in PBS (34% aECM, 2% aECM-f w/v) overnight at 4^{o}C. Four-arm poly(ethylene oxide) terminated with succinimidyl glutarate groups (PEG-S, Polymer Source, Montreal, Canada) was dissolved in PBS (25% w/v) just prior to hydrogel fabrication. The aECM solution and PEG-S solution were mixed together in a 1:1 ratio to prepare

the aECM-PEG precursor solution (final concentration: 18% aECM, 12.5% PEG-S). The precursor solution was used immediately after preparation.

Characterization of aECM-PEG hydrogels

Moduli of aECM-PEG hydrogels were determined using oscillatory shear. Measurements were performed in the linear regime (**Figure S-5**). 30 uL of gel precursor solution was pipetted onto the rheometer (ARES-RFS, TA Instruments, New Castle, DE), and the 8 mm parallel plate geometry was set to 500 μm. A 60-minute time sweep (angular frequency of 1 rad/s and a strain of 2%) was carried out to monitor hydrogel gelation. Hydrogels were separately prepared and swollen in PBS (pH 7.4) for 2 days at 37^{o}C. Swollen hydrogels were cut to fit the 8 mm parallel plate geometry, and a frequency sweep (2% strain) was used to measure their moduli after swelling. A temperature sweep (angular frequency 1 rad/s, 2% strain) was carried out to examine the stability of hydrogels between 25 - 37^{o}C.

Preparation of heparin-based hydrogels

Thiol-functionalized heparin (Hep-SH) was synthesized by modifying 40% of the carboxyl groups of heparin, following established protocols.[14] In heparin, each disaccharide repeat has one carboxylate group, so the functionalized polymer has one thiol group per 1500 g/mol of heparin at 40% modification. The amount of thiol groups in Hep-SH was determined using Ellman's reagent and measurement of molar absorptivity at 412 nm. In this study, 40 ± 2.5% thiolated heparin was used for all of the experiments. Poly(ethylene glycol)-diacrylate (PEG-DA) and Hep-SH were

sequentially dissolved in either PBS or DMEM (thiol:acrylate = 1:1 molar ratio). 0.01% (w/v) eosin Y as a photo-initiator and 0.1% (v/v) TEOA as an electron donor were added via stock solutions ($[EY_{stock}] = 0.5\%$; $[TEOA_{stock}] = 5\%$) to the precursor solution. The pH of the reaction mixture was adjusted to 8.0 with 1 N HCl. Precursor solutions were used within 1 hour of preparation and stored in the dark at 4°C prior to use. Prepared precursor solution was photo-polymerized under green LED light (5 $mWcm^2$) exposure. The LED emission wavelength is 525 ± 15 nm.

Animal experiments

The experiments in a mouse model were performed according to the Association for Research in Vision and Ophthalmology Statement of Use for Animals, and were approved by the Institutional Animal Care and Use Committee of the University of Utah (aECM-PEG hydrogels) or the California Institute of Technology (heparin-based hydrogels). All drugs used were pharmaceutical-grade ophthalmic solutions. All scaffold components were sterilized as follows prior to use. Nanofiber mats were first immersed in 70% ethanol (twice, 10 minutes each) and then placed under UV light for 30 minutes (sufficient for all ethanol to evaporate from the present mats, which are less than 50 microns thick). Hydrogel precursor solutions were sterile filtered through a 0.2 micron filter. All mouse procedures were carried out in a sterile laminar flow hood, equipped with a dissecting microscope.

Epithelial debridement in mice

Mice (BALB/c, female, 20 - 30 g) were anesthetized with ketamine (100 mg/kg) and xylazine (10 mg/kg) through intraperitoneal injection. One drop of Proparacaine (0.5% solution, topical anesthetic) and one drop of Tropicamide (1% solution, pupil dilator) were applied to each eye. An alcohol pad (80% ethanol, 1.5 mm diameter) was placed on the cornea for 60 seconds to weaken the epithelium. The weakened epithelium was then removed by scraping with a sterile Tooke corneal knife, and the initial wound area was imaged. For each mouse, the left eye was untreated to serve as a control while the right eye was treated with our scaffold. For treated eyes, 1 µL of hydrogel solution (either aECM-PEG or heparin-based hydrogel) was pipetted onto the wound area, and a layer of nanofibers was placed on top; for control eyes, 1 µL of phosphate-buffered saline (PBS) was pipetted onto the wound area. The mice were allowed to recover from surgery, and their eyes were observed daily for signs of inflammation. Six mice were used in each experimental group.

Tracking epithelium regrowth following procedure

The surface area of the epithelial defect was assessed daily. For mice experiments, treated mice were anesthetized with 2% isoflurane (in oxygen), and one drop of proparacaine was applied to each eye. To observe the wound boundary, 1 µL of fluorescein solution (0.25% in PBS) was pipetted onto the surface of each eye. Excess fluorescein solution was rinsed with 0.9% sodium chloride solution and removed by gently touching a sterile cotton swab to the side of the eye. The wound area was then imaged under blue LED lights, and the extent of wound closure was analyzed using ImageJ.

Staining and immunolabeling of corneal sections

Mice were euthanized following wound closure, and their corneas were harvested. Frozen sections were prepared by first fixing the excised corneas with 4% paraformaldehyde for 2 hours, and then placing in two sucrose solutions (10% for 2 hours, 30% overnight). The corneas were then embedded in OCT medium and sectioned using a cryotome to 7 micron thick sections. The presence of the nanofibers and hydrogel were confirmed in treated animals by observing the sections using a fluorescence microscope. Paraffin sections were prepared by fixing excised corneas with 4% paraformaldehyde for 2 hours, dehydrating them through a graded ethanol series, and finally embedding them in paraffin. Sections were cut (7 microns) and processed for hematoxylin-eosin (H&E).

Hematoxylin & eosin staining

The tissue sections were deparaffinized in xylene (20 minutes) and rehydrated in a graded series of ethanol (100% to 70%, 5 minutes each). The slides were then rinsed with distilled water (5 minutes) and placed in hemotoxylin (3 minutes). The slides were rinsed with distilled water (5 minutes) and placed in acid alcohol (1 minute, Thermo Scientific Anatom Path Clarifier 1). They were then placed in 100% ethanol (1 minute), then in bluing reagent (1 minute, Thermo Scientific Richard-Allen Scientific Bluing Reagent) and eosin (3 minutes). The samples were then dehydrated in a graded series of ethanol (70% to 100%, 2 minutes each) and placed in xylene (two washes of 5 minutes

each). The slides were then mounted with Cytoseal (Fisher Scientific), cover-slipped and left to dry for 24 hours prior to imaging.

5.3 Results

The safety and biocompatibility of our scaffold were evaluated using a mouse model for epithelial debridement (**Figure 1**). Two types of materials were investigated. Nanofiber mats were tested in conjunction with a hydrogel that has already been proven to be compatible with the cornea (aECM-PEG). A heparin-based hydrogel that had not been tested for corneal compatibility was investigated separately.

Nanofiber scaffolds are well-tolerated in treating mice epithelial defects

In conjunction with experiments in which we used aECM-PEG hydrogel at pH 7.0 to support nanofiber attachment on the debrided area of the cornea, a control experiment was performed using only the aECM-PEG hydrogel at pH 7.0, and the effect of pH on the ease of handling the hydrogel was examined by including aECM-PEG hydrogel at pH 8.0. Five animals were used in each of these three groups, and the fellow eye served as the untreated control.

All three treatments were transparent after application. (**Figure 2A**). When observed immediately after and approximately 15 – 18 hours after the procedure, the mice (in all three experimental groups) showed no inflammation (free of conjunctival redness and swelling) (**Figure 2B**). The following day after the procedure, mice showed no signs of distress (they moved about the environment, ate and drank normally). Our treatment

also supported epithelial regrowth at rates comparable to control eyes (**Figure 3**): the rate of wound closure in treated eyes was not statistically different from that in untreated control eyes. Corneal epithelial defects usually heal quickly and without incident[15-17]; thus, our results show that our treatment did not hinder the re-epithelialization process.

Four days after the procedure, the mice were sacrificed, and their corneas were harvested and sectioned. To determine whether our treatment remained in the wound during the healing process, tissue sections were viewed under a fluorescence microscope, and both the fluorescein-labeled nanofibers (**Figure S-1**) and rhodamine-labeled aECM-PEG hydrogel (**Figure S-2**) were seen in the wound bed (**Figures 4** and **S-3**). To observe the corneal morphology following wound closure, the tissue sections were stained with hematoxylin and eosin (H&E) using standard protocols (**Figures 3** and **S-4**). H&E staining showed that the regenerated epithelium in untreated eyes was thicker than the epithelium of unwounded eyes (wounded but untreated cornea: 85.4 ± 2.4 μm thick; unwounded cornea: 50.5 ± 3.1 μm thick). Corneas that were treated with nanofibers and the hydrogel had an epithelial thickness (48.4 ± 1.6 μm) similar to that of a healthy cornea while the two experimental groups that received only the hydrogel treatment had an epithelial thickness similar to that of an untreated cornea (pH 7.0: 81.7 ± 4.0 μm; pH 8.0: 81.8 ± 3.6 μm).

Heparin-based treatment supports epithelial regrowth

To evaluate compatibility of heparin-based hydrogels with the cornea, we examined four groups (six mice per group) with successively more components of the envisioned

treatment (**Table 1**): Group 1: irradiated with green light only; Group 2: heparin-based hydrogel photo-polymerized with green light; Group 3: addition of a layer of isotropic nanofibers on top of hydrogel and photo-polymerized; Group 4: addition of epidermal growth factor (EGF) to the Group 3 treatment.

As was observed for aECM-PEG treated mice, the mice (in all four experimental groups) showed no inflammation, and the cornea and hydrogel were transparent 15 minutes after the procedure (**Figure 5A**). (In contrast to the aECM-PEG case, the cornea briefly exhibited haze that was visible at the time that the mice were placed on the heating pad after surgery, and it resolved itself within 15 minutes.) The following day, no inflammation was found, and the mice showed no signs of distress. Using fluorescein staining to visualize wound closure, we observed that heparin-based hydrogel treatment supported epithelial regrowth at rates that were not distinguishable from control eyes (**Figure 6**). The application of green light, hydrogel, nanofibers or epidermal growth factor did not hinder the ability of the injured cornea to regrow its epithelial layer.

Two weeks after the procedure, the mice were sacrificed, and their corneas were harvested, sectioned and stained with hematoxylin and eosin (H&E) using standard protocols. The pronounced increase in epithelial layer thickness after wound healing (wounded but untreated cornea: 83.4 ± 4.0 μm thick; unwounded cornea: 53.0 ± 4.2 μm thick) is also observed for mice that received only green light or green light and hydrogel as treatment (Group 1: 84.6 ± 7.6 μm; Group 2: 74.4 ± 5.0 μm). Interestingly, both treatment groups that received nanofibers on top of the hydrogel recovered with an

epithelial thickness closer to corneas that had never been injured (Group 3: 62.9 ± 3.3 μm; Group 4: 66.2 ± 5.2 μm). Fluorescence micrographs confirmed that the treatment remained in the wound during the healing process; fluorescein-labeled nanofibers (Groups 3-4) and rhodamine-labeled heparin-based hydrogel (Groups 2-4) were observed in the wound bed 14 days after the procedure (**Figure 5B**).

5.4 Discussion

Here, we developed two different corneal scaffolds (made of protein nanofibers and either an aECM-PEG based hydrogel or a heparin-based hydrogel) and confirmed their safety and biocompatibility *in vivo* using a mouse model for corneal epithelial defects. Furthermore, we observed that the regenerated epithelium of mice treated with nanofibers (on both types of hydrogel) had a thickness and morphology that was more similar to an unperturbed corneal epithelium than those that did not receive any nanofibers.

The motivation for using nanofibers in our corneal scaffold stems from our observations that gelatin nanofibers can enhance cell migration and influence cell phenotype *in vitro* (Chapter 2). In this study, we use isotropic nanofibers because they promote wound closure by epithelial cells *in vitro* relative to uniaxial or radially-oriented nanofibers. In addition, nanofibers (mean diameter 155 nm) were used because they are transparent upon wetting, easy to handle, and non-cytotoxic. Gelatin (as opposed to synthetic polymers) was our material of choice since it contains integrin binding sites that support cell migration.[18,19]

The hydrogel component of both scaffolds match the properties (mechanical and optical) of the native cornea. Thomasy and colleagues measured the elastic modulus of the anterior stroma of a rabbit cornea to be 1.1 ± 0.6 kPa.[20] Here, the two hydrogel formulations used have moduli in the range of 1 – 2 kPa. It is noted that the rabbit cornea and the human cornea have different stiffness (elastic modulus of the anterior stroma of a human cornea: 33.1 ± 6.1 kPa[21]). Here, we chose to use the rabbit cornea as a starting point, in preparation for *in vivo* experiments in rabbit models to validate the efficacy of our scaffold (Chapter 7). The two hydrogel formulations are tunable (by varying either the composition or gelation conditions), so stiffer gels can easily be made if needed for future studies. Both types of hydrogel are transparent upon gelation and adhere the nanofibers to the wound bed.

aECM-PEG-based treatment

The motivation for using an aECM-PEG hydrogel is that it presents cell-binding sites in addition to those on the nanofibers. The modular protein design of aECM affords systematic control of biochemical and proteolytic degradation. The particular aECM protein that we have chosen to use in this study (**Figure S-2**) is derived from elements of natural ECM proteins (fibronectin and elastin), which supports collective cell migration *in vitro* and reepithelialization when an inlay is implanted in the cornea of a rabbit model *in vivo*.

For gelation *in situ*, we use 4-armed NHS-functionalized poly(ethylene glycol) (PEG-S) as the crosslinker, which couples to lysine amino groups in aECM proteins. The

crosslinking kinetics are pH-dependent (optimal range pH 7 – 9), with slow kinetics at low pH due to protonation of amino groups.[22] At high pH, NHS-esters are quickly hydrolyzed, which competes with crosslinking. Constrained to pH ≤ 8 for corneal safety, we studied the gelation kinetics of aECM-PEG at pH 7.0, 7.6 and 8.0 using oscillatory rheology (**Figure S-5**). The gelation rate and final modulus of hydrogels formed at pH 7.6 were indistinguishable from those formed at pH 7.0. At pH 8.0, gelation was faster and the resulting gel was softer than those formed at lower pH values, as expected due to hydrolysis. In view of these results, we selected pH 7.0 and 8.0 aECM-PEG formulations for *in vivo* studies.

The epithelium closed equally well over aECM-PEG for both pH 7.0 and pH 8.0 formulations. The main difference between them was that during surgery, it was much harder to handle the pH 8.0 hydrogel due to the relatively short gelation time. Application of unoriented nanofibers over the aECM-PEG (and over heparin-based gels, below) led to reepithelialization with a thickness and number of cell layers that was closer to that of an unwounded cornea.

Heparin-based treatment

To our knowledge, this is the first *in vivo* test of heparin-based gels in the cornea and the primary objective is to assess inflammatory reactions and possible opacification. Because photo-crosslinking is used, *in vivo* experiments are needed to determine whether or not the dose of visible-light is well-tolerated. Using eosin Y (EY) as the photoinitiator and triethanolamine (TEOA) as a co-initiator, thiolated heparin reacts

with poly(ethylene glycol) diacrylate under green light (525 nm, 5 mW/cm^2) to form a transparent gel within a few minutes of irradiation (Chapter 4). *In vitro*, we have shown that encapsulated fibroblasts remain viable following gelation (Chapter 4). Furthermore, our calculations show that the irradiation conditions for gelation of the EY/vis formulation (2.33% heparin, 1:1 thiol: acrylate molar ratio, 0.01% EY, 0.1% TEOA in PBS pH 8.0, 5 mW/cm^2 irradiation for 5 minutes) are compatible with safety standards for corneal and retinal exposure (Chapter 4). These favorable *in vitro* results provided the basis for the present experiments on the ability of epithelium to close over the heparin-based gel in a mouse model.

Using a Teflon cylinder to give a consistent distance from the LED to the cornea provided a readily-sterilizable tool to easily align the light source over the mouse cornea and ensure a consistent light flux at the cornea. The present results demonstrate that a 5-minute exposure to green light (525 nm) at 5 mW/cm^2 did not cause any cytotoxicity: normal epithelial regrowth was observed in all four experimental groups. Corneas treated with nanofibers (Groups 3 and 4) had a regenerated epithelium where the thickness and the layer of cells were more similar to an unwounded cornea compared to those that did not receive any nanofibers, as also observed for aECM-PEG-treated mice.

Building on the observation that heparin-based hydrogel and the irradiation conditions were well-tolerated by the eye, we proceeded to examine the possibility of using heparin's natural binding sites as a reservoir for growth factors. We demonstrated *in vitro* that epidermal growth factor (EGF) can be loaded into the heparin-based hydrogel

and retains its bioactivity after release (Chapter 4). The incorporation of EGF (100 ng/mL) in the heparin gel formulation had no adverse effect on the response of the eye (no inflammatory response and no turbidity). Due to the very rapid closure of the mouse epithelium (all had closed within 18 hours), the present experiments cannot speak to the possibility that the addition of EGF might increase the rate of epithelial wound closure[23] (comparing Groups 3 and 4).

In the current study, H&E staining provided information on the overall morphology of the regenerated epithelium (i.e. thickness and approximate number of cell layers). The observed differences in epithelial thickness and number of cell layers when the epithelium closes over an unoriented fiber mat suggest that further investigation would be worthwhile. Specifically, the observation of epithelial characteristics that are closer to those of an unperturbed epithelium motivate higher resolution imaging with antibody staining (e.g., against tight junction proteins claudin-1, ZO1 or occludin) and membrane staining (e.g., CellTracker from Life Technologies).

5.5 Conclusions

We developed two different corneal scaffolds: both made of protein nanofibers and either an aECM-PEG hydrogel or a heparin-based hydrogel. Both scaffolds are transparent and able to support re-epithelialization of epithelial defects in mice corneas. Furthermore, we observed that the regenerated epithelium of mice treated with nanofibers (on both types of hydrogel) have a thickness and morphology that was more similar to an wounded corneal epithelium than those that did not receive any nanofibers.

In relation to clinical translation, we found that aECM-PEG hydrogels at pH 7.0 were much easier to handle than those at pH 8.0. For the heparin-based treatment, we confirmed that the green light used for photo-crosslinking did not induce any adverse effects in epithelial regrowth.

5.6 References

1. Shen, W.; Zhang, K.; Kornfield, J.A.; Tirrell, D.A. Tuning the erosion rate of artificial protein hydrogels through control of network topology. *Nature Materials* **2006**; 5:153-158.

2. Di Zio, K.; Tirrell, D.A. Mechanical properties of artificial protein matrices engineered for control of cell and tissue behavior. *Macromolecules* **2003**; 36:1553-1558.

3. Nowatzki, P.J.; Tirrell, D.A. Physical properties of artificial extracellular matrix protein films prepared by isocyanate crosslinking. *Biomaterials* **2004**; 25:1261-1267.

4. Olsen, B.D.; Kornfield, J.A.; Tirrell, D.A. Yielding behavior in injectable hydrogels from telechelic proteins. *Macromolecules* **2010**; 43:9094-9099.

5. Fong, E.; Tirrell, D.A. Collective cell migration on artificial extracellular matrix proteins containing full-length fibronectin domains. *Adv. Mater.* **2010**; 7:5271-5275.

6. Liu, J.C.; Heilshorn, S.C.; Tirrell, D.A. Comparative cell response to artificial extracellular matrix proteins containing the RGD and CS5 cell-binding domains. *Biomacromolecules* **2004**; 5:497-504.

7. Liu, J.C.; Tirrell, D.A. Cell response to RGD density in cross-linked artificial extracellular matrix protein films. *Biomacromolecules* **2009**; 9:2984-2988.

8. Heilshorn, S.C.; Liu, J.C.; Tirrell, D.A. Cell-binding domain context affects cell behavior on engineered proteins. *Biomacromolecules* **2005**; 6:318-323.

9. Zhang, E.P.; Schrunder, S.; Hoffmann, F. Orthotopic corneal transplantation in the mouse – a new surgical technique with minimal endothelial cell loss. *Graefes. Arch. Clin. Exp. Ophthalmol.* **1996**; 234:714-719.

10. Zhou, S.Y.; Xie, Z.L.; Xiao, O.; Yang, X.R.; Heng, B.C.; Sato, Y. Inhibition of mouse alkali burn induced-corneal neovascularization by recombinant adenovirus encoding human vasohibin-1. *Mol. Vis.* **2010**; 16:1389-1398.

11. Giacomini, C.; Ferrari, G.; Bignami, F.; Rama, P. Alkali burn versus suture-induced corneal neovascularization in C57BL/6 mice: an overview of two common animal models of corneal neovascularization. *Exp. Eye Res.* **2015**; 121:1-4.

12. Anderson, C.; Zhou, Q.; Wang, S. An alkali-burn injury model of corneal neovascularization in the mouse. *J. Vis. Exp.* **2014**; 86.

13. Xiao, O.; Xie, Z-L.; Liu, B-W.; Yin, X-F.' Pi, R-B.; Zhou, S-Y. Minocycline inhibits alkali burn-induced corneal neovascularization in mice. *PLoS ONE* **2012**; 7:e41858.

14. Tae, G.; Kim, Y-J.; Choi, W-I..; Kim, M.; Stayton, P.S.; Hoffman, A.S. Formation of a novel heparin-based hydrogel in the presence of heparin-binding biomolecules. *Biomacromolecules* **2007**; 8:1979-1986.

15. Kiazawa, T.; Kinoshita, S.; Fujita, K.; Araki, K.; Wantanbe, H.; Ohashi, Y. *et al.* The mechanism of accelerated corneal epithelial healing by human epidermal growth factor. *Invest. Ophthamol. Vis. Sci.* **1990**; 31:1773-1778.

16. Dua, H.S.; Gomes, J.A.; Singh, A. Corneal epithelial wound healing. *Br. J. Ophthalmol.* **1994**; 78:401-408.

17. Lu, L.; Reinach, P.S.; Kao, W. Corneal epithelial wound healing. *Exp. Biol. Med.* **2001**; 226:653-664.

18. Xu, Y.; Gurusiddappa, S.; Rich, R.L.; Owens, R.T.; Keene, D.R.; Mayne, R. *et al.* Multiple binding sites in collagen type I for the integrins α1β1 and α2β1. *J. Biol. Chem.* **2000**; 275:38981-38989.

19. Brett, D. A review of collagen and collagen-based wound dressings. *Wounds* **2008**; 20:12

20. Thomasy, S.M.; Raghunathan, V.K.; Winkler, M.; Reilly, C.M.; Sadeli, A.R.; Russell, P. et al. Elastic modulus and collagen organization of the rabbit cornea: epithelium to endothelium. *Acta Biomaterialia* **2014**; 10:785-791.

21. Last, J.A.; Thomasy, S.M.; Croasdale, C.R.; Russell, P.; Murphy, C.J. Compliance profile of the human cornea as measured by atomic force microscopy. *Micron* **2012**; 43:1293-1298.

22. Hermanson, G.T. Bioconjugate Techniques, 3rd Edition (2013) Elsevier Inc.

23. Carrier, P.; Deschambeault, A.; Talbot, M.; Giasson, C.J.; Auger, F.A.; Guerin, S.L. et al. Characterization of wound re-epithelialization using a new human tissue-engineered corneal wound healing model. *Invest. Ophthalmol. Vis. Sci.* **2008**; 49:1376-1385.

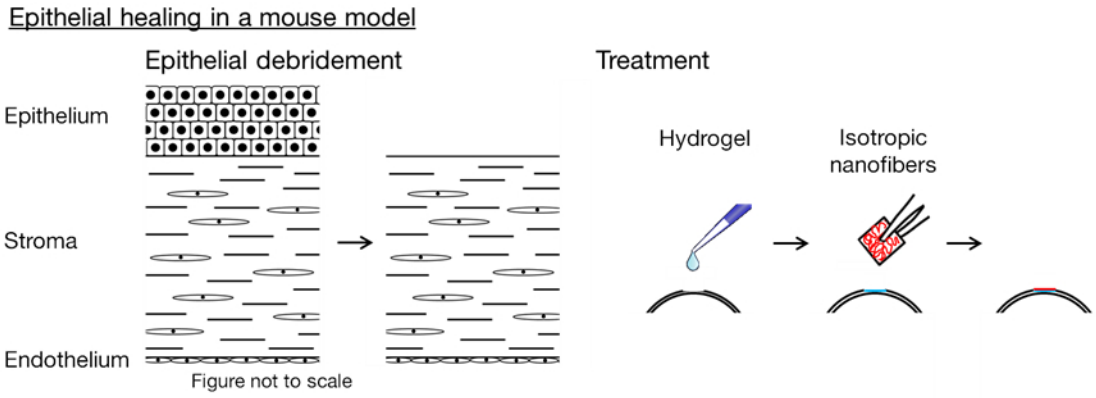

Figure 1. Schematic of *in vivo* mouse epithelial defect model. For each mouse, the epithelium is debrided using a corneal Tooke knife to create a surface wound. For treated eyes, 1 µL of hydrogel was pipetted onto the wound bed (followed by a layer of isotropic nanofibers for the nanofiber-treated group). For control eyes, 1 µL of PBS was pipetted onto the wound bed.

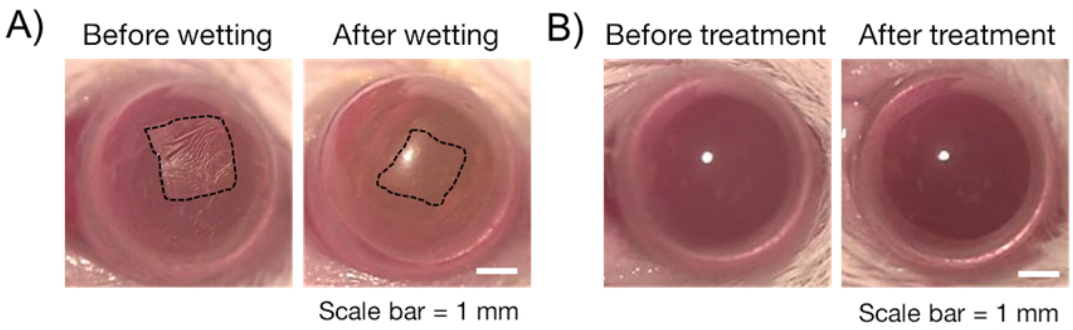

Figure 2. Treatment application to the wound bed. A) The nanofibers become transparent upon addition of PBS, and B) no signs of inflammation are observed 30 minutes after treatment or the following day (approximately 15 – 18 hours after treatment, not shown).

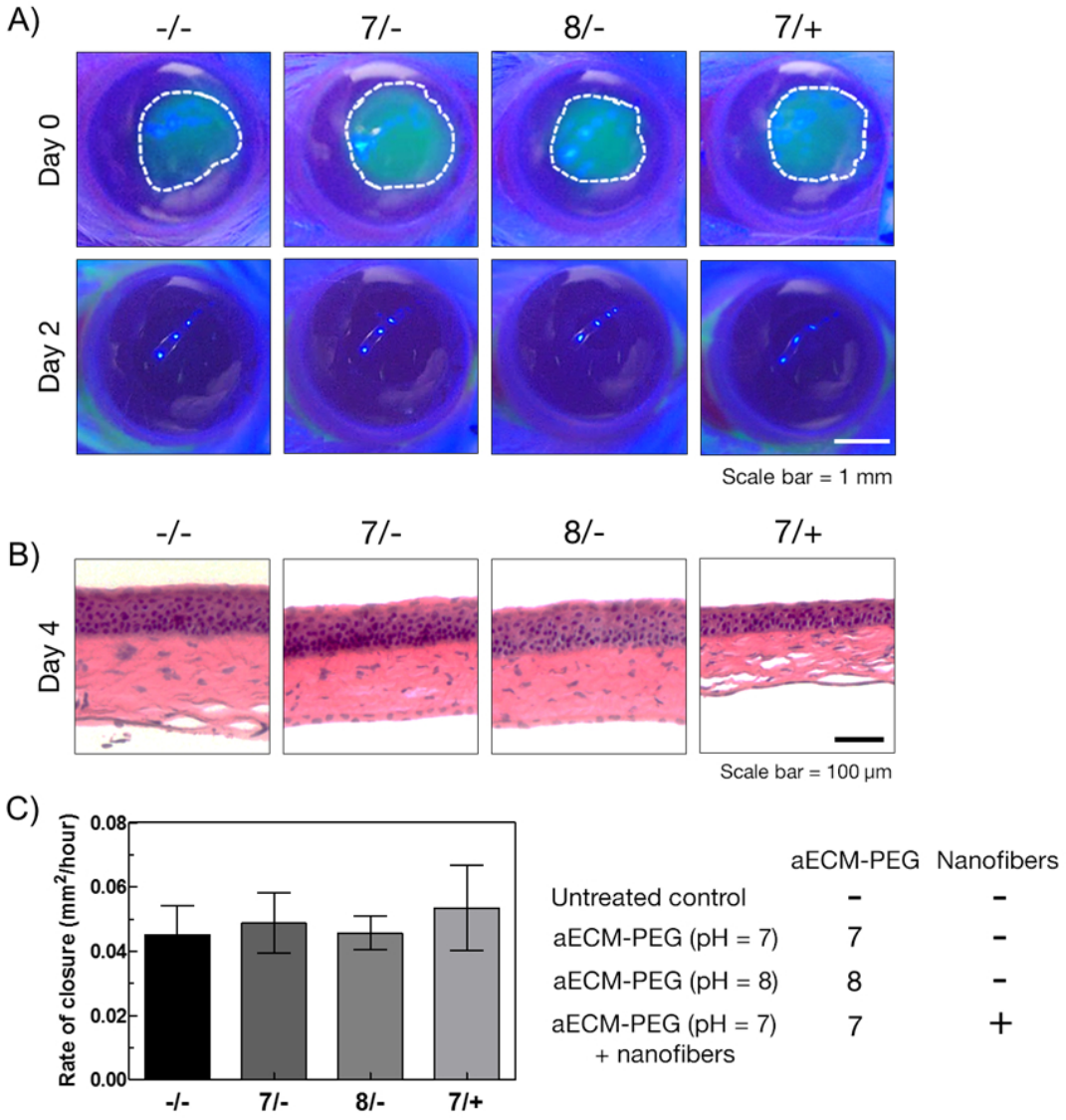

Figure 3. A) Representative images of fluorescein staining to visualize wound closure. The initial wound area was imaged on day 0. By day 2, re-epithelialization was observed in all experimental groups. B) H&E staining of tissue sections from corneas harvested on day 4 following the procedure show that the regenerated epithelium show normal morphology compared to that of the untreated cornea. C) Quantification of wound area observed in A). The rate of re-epithelialization of treated groups are comparable to that of untreated controls.

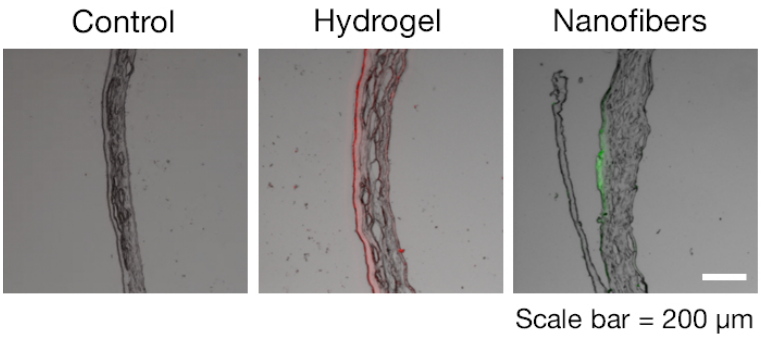

Figure 4. The treatment remains in the wound 4 days after the procedure. The aECM-PEG hydrogel was labeled with NHS-Rhodamine; the nanofibers were labeled with NHS-fluorescein.

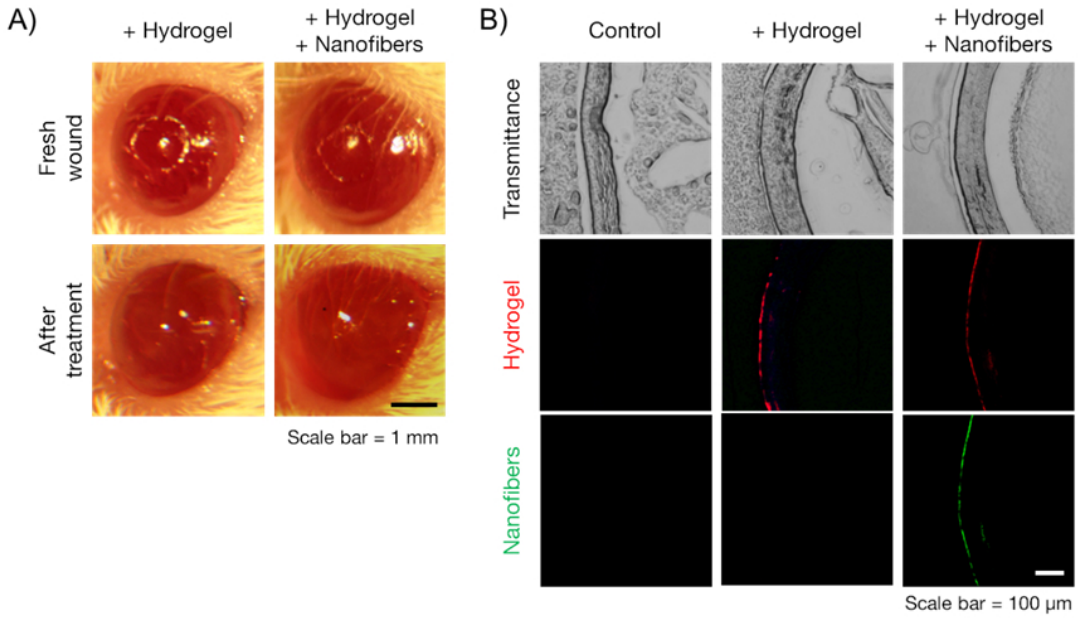

Figure 5. Treatment application to the wound bed. A) The hydrogel and nanofibers are transparent upon addition of PBS, and B) the treatment remains in the wound 14 days after the procedure. The haprin-based hydrogel was labeled with NHS-Rhodamine; the nanofibers were labeled with NHS-fluorescein.

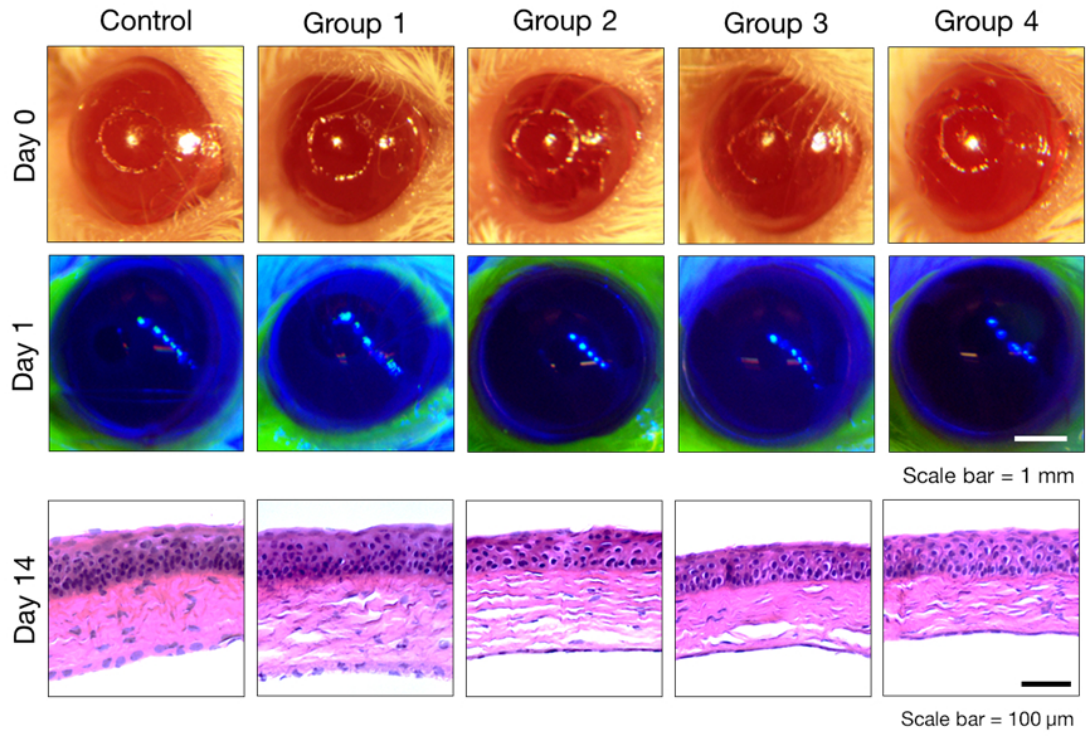

	Control	Group 1	Group 2	Group 3	Group 4
Light	-	+	+	+	+
Hydrogel	-	-	+	+	+
Nanofibers	-	-	-	+	+
EGF	-	-	-	-	+

Figure 6. Representative images of fluorescein staining to visualize wound closure. The initial wound area was imaged on day 0 without fluorescein staining. By day 1, re-epithelialization was observed in all experimental groups. H&E staining of tissue sections from corneas harvested on day 14 following the procedure show that the regenerated epithelium show normal morphology compared to that of the untreated cornea.

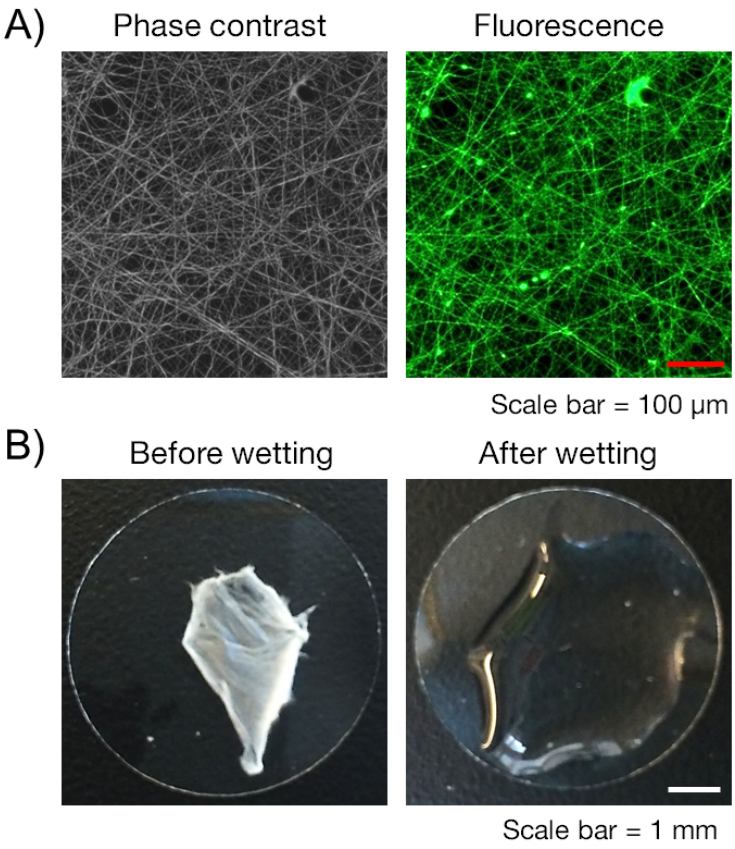

Figure S-1. A) Nanofiber substrates are fluorescently labeled with NHS-fluorescein. B) Nanofiber substrates become transparent upon wetting.

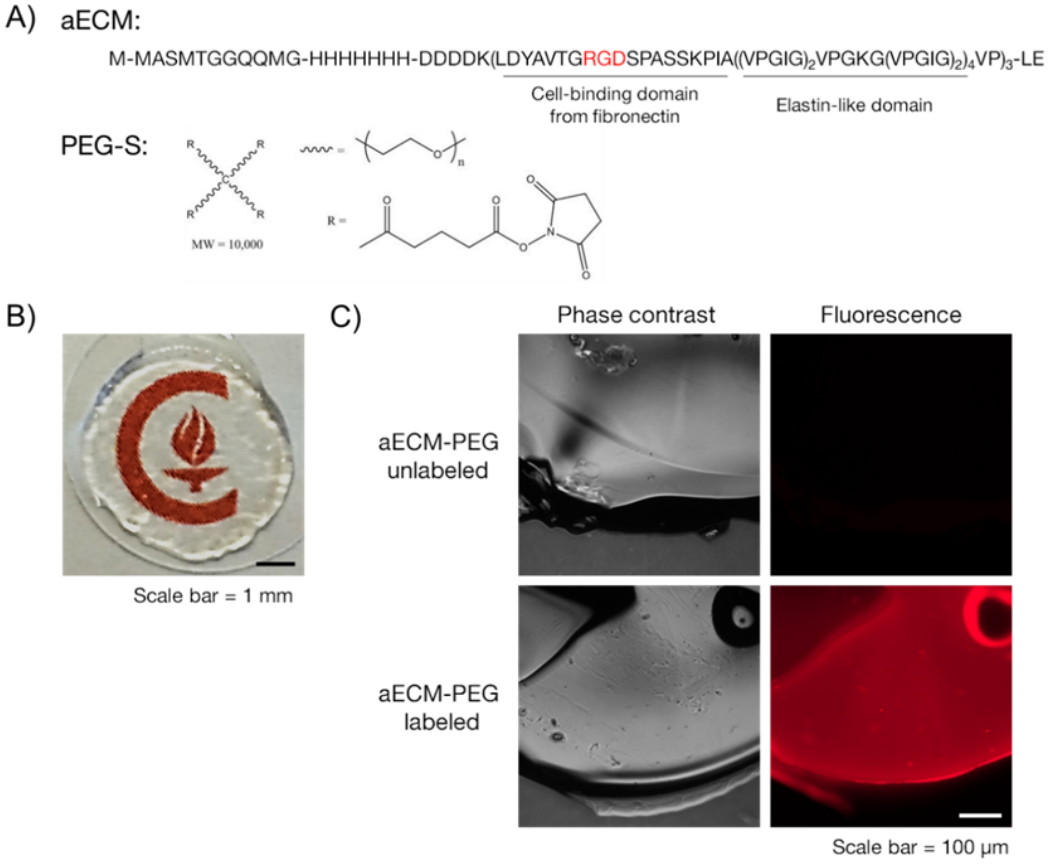

Figure S-2. A) Amino acid sequence of the artificial extracellular matrix (aECM) protein and the structure of 4-armed poly(ethylene glycol) with end-terminated succinimidyl glutarate groups used in this study. The aECM protein contains an RGD binding domain derived from fibronectin and an elastin-like domain. B) The hydrogel formed by crosslinking aECM and PEG-S is transparent, and C) is fluorescently labeled using NHS-Rhodamine.

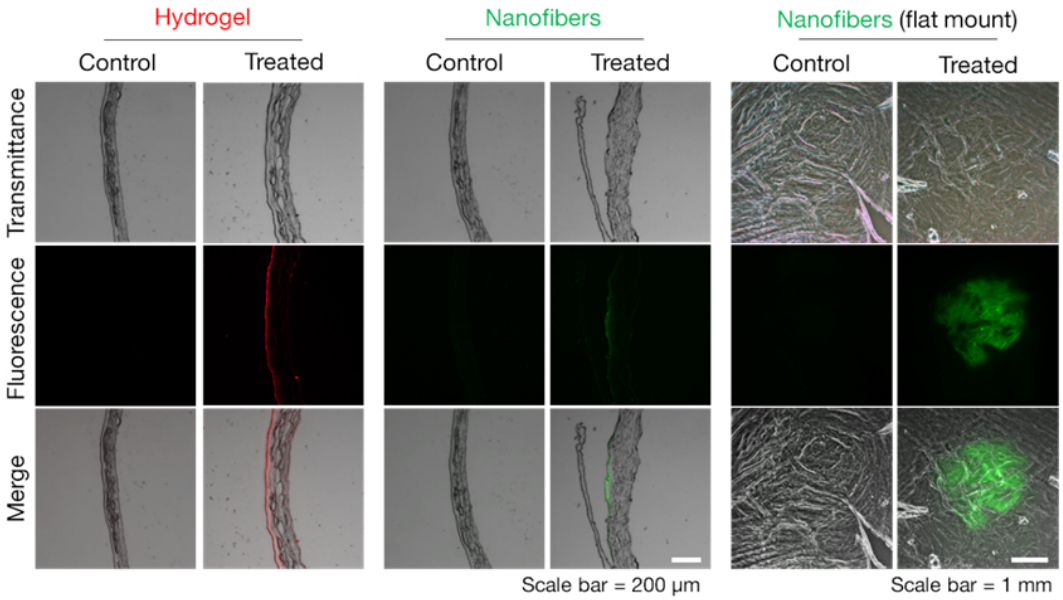

Figure S-3. The aECM-PEG treatment remains in the wound 4 days after the procedure. The aECM-PEG hydrogel was labeled with NHS-Rhodamine; the nanofibers were labeled with NHS-fluroescein. The nanofibers can be seen both in the tissue section (cross-section of cornea) and in the flat mount (top-down view of cornea).

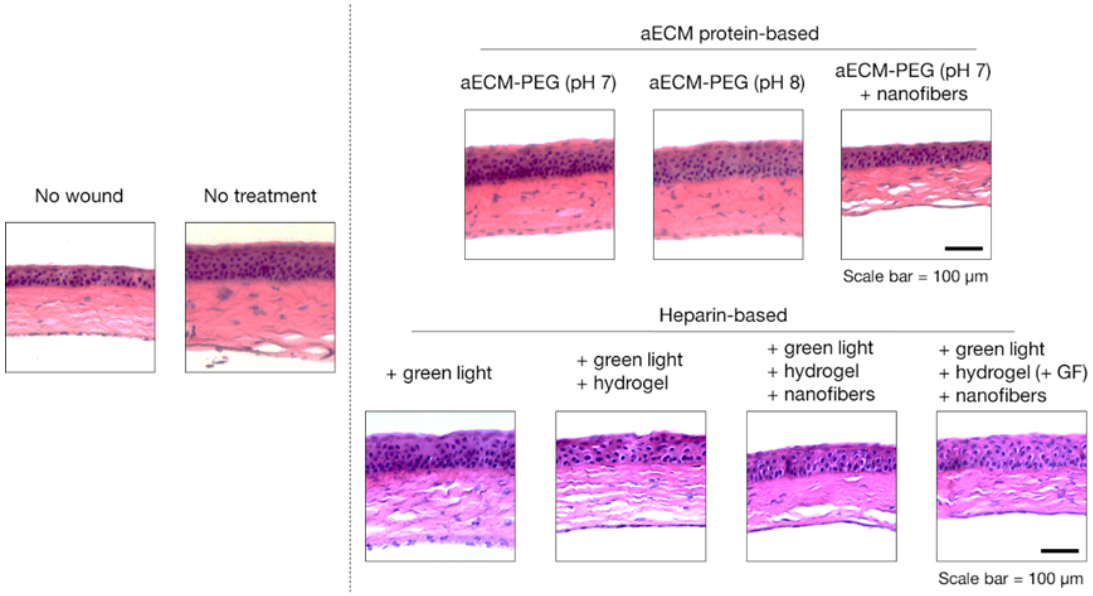

Figure S-4. H&E staining of tissue sections. The corneas from the aECM protein-based treatment were harvested on day 4 following the procedure, and those from the heparin-based treatment were harvested on day 14. Treated corneas that did not receive any nanofibers had a corneal morphology similar to that of untreated corneas. Treated corneas that received nanofibers (*top row, last; bottom row, last two*) had a corneal morphology similar to that of an unwounded cornea.

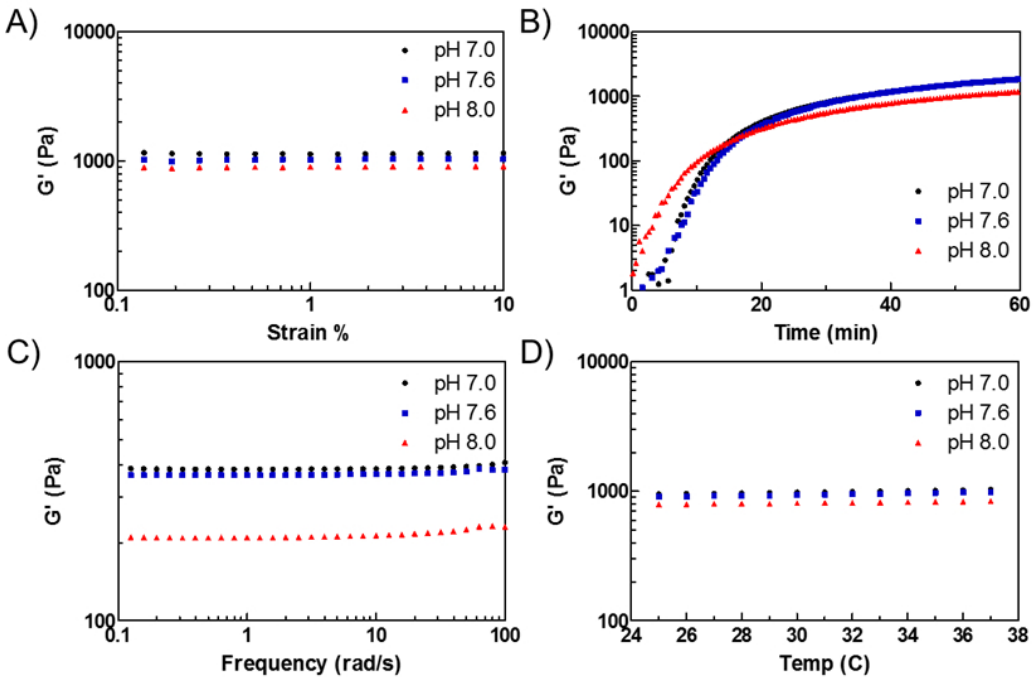

Figure S-5. The storage modulus of aECM-PEG hydrogels was examined using oscillatory rheology. Results of A) a strain sweep from 0.1 to 10% at 1 rad/s on a strain-controlled rheometer (ARES RFS) confirm that oscillatory conditions used are in the linear viscoelasticity range. A strain of 2% was used for subsequent analysis. B-C) aECM-PEG hydrogels prepared at pH 8.0 have a faster gelation time and a lower overall modulus (both freshly prepared and swollen) compared to hydrogels prepared at pH 7.0 and 7.6 (which were indistinguishable from each other). D) The storage modulus of aECM-PEG hydrogels did not change with temperature in the range 25 – 37°C.

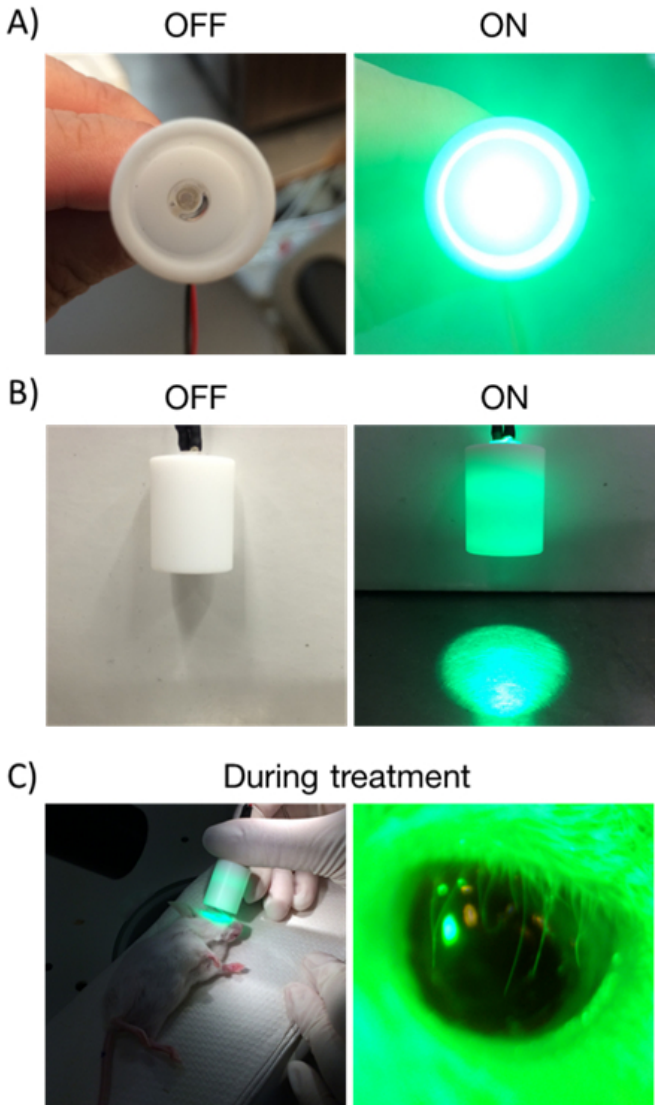

Figure S-6. The light device used for photo-crosslinking heparin-based hydrogels *in vivo*. A single green LED light (525 nm) was placed inside a Teflon holder (1 cm diameter, 2 cm height). This specific height was chosen such that when the light is turned on, the irradiation intensity at the base of the holder is 5 mW/cm^2. A) Top down view of light, off and on; B) side view of light device, off and on, and C) light device in use during *in vivo* experiments.

Table 1. Experimental groups for mice receiving heparin-based treatment.

	Group 1	**Group 2**	**Group 3**	**Group 4**
Green light	✓	✓	✓	✓
Nanofibers	×	✓	✓	✓
Hydrogel	×	×	✓	✓
Epidermal growth factor	×	×	×	✓

Chapter 6

Development of an *ex vivo* tissue culture model system

6.1 Introduction

In Chapter 5, the safety and biocompatibility of our composite scaffold was examined in a mouse model for epithelial debridement. We demonstrated that the scaffolds were well-tolerated in mice, and supported epithelial regrowth over the wounded area. However, most corneal epithelial defects heal quickly and without incident even in the absence of any treatment.[1-3] Corneal wounds that penetrate into the stromal layer are injuries which eventually lead to corneal haze and blindness. Unfortunately, mice corneas are thin (~170 microns)[4], and we are unable to create reproducible deep wounds without the risk of puncture. In order to test the efficacy of our scaffold in treating stromal wounds, studies must be carried out in larger animal species (e.g. rabbits).

According to the United States Department of Agriculture, there were approximately 890,000 animals (excluding mice, rats, birds and fish) used in scientific studies in 2013, of which ~169,000 (19%) were rabbits.[5] The National Institutes of Health spends ~30 billion dollars annually on research projects[6], where ~40% of them have an animal experiment component[7]. To reduce both the number of animals used and the amount of funding spent on animal studies, researchers have been actively finding alternatives to animal testing.

In recent years, *ex vivo* organ cultures have proven to be promising substitutes for animal experiments. Schmook and coworkers demonstrated that pig skin can be cultured *in vitro* and is a suitable model for human skin.[8] Nunes and colleagues showed that trachea explanted from a pig can be effectively maintained in organ culture, and can be used to study influenza infection.[9] Dyer and Patterson have further showed that an excised mouse heart can be cultured in a semi-solid, dilute Matrigel, where it remains viable for days (evidenced by continued contractions).[10]

Much work has also been carried out in relation to the cornea. One of the challenges in developing an *ex vivo* corneal culture model is to maintain the curvature of the cornea while still being able to deliver nutrients to the endothelial side to keep corneal cells alive. Sriram *et al.* and Castro-Combs *et al.* separately developed an *ex vivo* protocol in which excised corneas were cultured on dome-shaped supports made from the bottom of 50 mL laboratory test-tubes.[11,12] In their studies, nutrients from the culture medium could not be transported to the corneas; therefore, although they were able to culture the corneas for 14 days, results are likely not good representations of what would be observed *in vivo*. Xu and coworkers cultured excised corneas on top of an agarose/collagen gel to study epithelial responses to surfactants.[13] However, the corneas in their study were only cultured for a short period of time (< 1 hour). Janin-Manificat and coworkers were able to keep excised corneas alive for 31 days by placing a sterile blotting paper (soaked in culture medium) on the endothelial face of the cornea and culturing them on top of a conformer.[14] However, it is unclear whether the corneas maintained their curvature during the culture period.

Here, we describe an *ex vivo* corneal culture model in which excised animal corneas are cultured on an agar-gel to maintain the curvature of the cornea. We show that epithelial defects or deeper stromal wounds can be created in the corneas, and that the corneas retain their ability to heal and repair wounds. Using this method, corneas can be kept alive in a 37^{o}C incubator for up to 21 days with daily culture medium changes. We used this *ex vivo* culture model to test the efficacy of our composite scaffold in treating stromal wounds. Results from these studies guided our scaffold selection for subsequent *in vivo* rabbit studies.

6.2 Methods

Creating wounds on the cornea

Fresh animal eyes were purchased from vendors (bovine, porcine from Sierra Biomedical; rabbit from Pel Freez). Once received, the intact globes were immersed in tissue culture medium for 1 hour at 4^{o}C for disinfection. The tissue culture medium used here and throughout this study was Dulbecco's Modification of Eagles Medium/Ham's F-12 (DMEM/F-12) containing 2.5 mM L-glutamine, 120 ug/mL Penicillin, 200 ug/mL Streptomycin sulfate and 5 ug/mL Amphotericin B. Excess fat and connective tissue was trimmed from the eyeball, and 1 mL of air was injected into the posterior of the eye using a 30-gauge needle to provide a firm corneal surface.

To create an epithelial defect, an alcohol pad (80% ethanol, 3 mm diameter) was placed on the cornea for 60 seconds to weaken the epithelium. The weakened epithelium was

then removed by scraping with a sterile Tooke corneal knife. To create a stromal wound, a lamellar keratectomy was performed on the cornea. A corneal trephine (6 mm diameter) was used to create a circular wound to a depth of 100 microns. Colibri forceps were used to lift edge of the cut tissue such that a crescent knife could be used to remove the corneal tissue.

Ex vivo organ culture

The *ex vivo* model used here was modified from that of Evans and coworkers.[15] After creating wounds on the corneal surface, the corneas were excised from the eyeballs while keeping part of the scleral rim intact (~ 5mm). The corneas were then placed upside down (with the endothelial side up) and filled with an agar-gel to provide support and maintain the curvature of the cornea. The agar gel was prepared by mixing the tissue culture medium and a 1% agar solution (in PBS) in a 1:1 volume ratio. The corneas (with the agar gel support) were then placed (epithelial side up) in a 12-well plate (6-well plate for bovine corneas). Tissue culture medium was added to the wells such that the scleral rim was just immersed in the medium. The corneas were cultured in the 37^{o}C incubator (at 5% CO_2) with daily medium changes.

Application of corneal scaffold to wound bed

The nanofiber substrates and hydrogel precursor solutions were prepared and characterized as described in Chapter 5. For treated eyes, a layer of nanofibers was first placed onto the wound bed, 10 uL of hydrogel solution (either aECM-PEG or heparin-based) was then pipetted onto the nanofibers, and finally, a second layer of nanofibers

was placed on top of the hydrogel. In the case of the heparin-based hydrogels, the cornea was then irradiated with a green LED light (525 nm) at 5 mW/cm^2 for 5 minutes to initiate photo-polymerization of the hydrogel. For untreated eyes, 10 uL of sterile PBS was pipetted onto the wound bed.

Fluorescein staining to visualize wound closure

The area of the epithelial defect was assessed daily using fluorescein staining. Tissue culture medium was first removed, and the corneas were then washed twice by pipetting PBS over the corneal surface. 15 uL of fluorescein solution (0.25% in PBS, sterile-filtered) was pipetted onto the surface of each cornea. Excess fluorescein solution was removed by pipetting PBS over the corneal surface. The wound area was then imaged under blue LED lights, and the extent of wound closure was analyzed using ImageJ.

Transmission electron microscopy to examine corneal nanostructure

A 2 mm x 5 mm block was cut from the central region of the cornea where the wound was originally created. The corneal blocks were fixed with 2.5% glutaraldehyde (in PBS) at 4^oC overnight and post-fixed with 1% osmium tetroxide (in PBS) for 60 minutes. Samples were then dehydrated in a graded series of ethanol (30% to 95%) and embedded in epoxy resin medium. 100-nm-thick sections were cut with a diamond knife on an ultramicrotome (Leica Ultracut UCT) and mounted on standard TEM grids. Samples were stained with 5% uranyl acetate and lead citrate prior to imaging (Tecnai Transmission Electron Microscope).

Histological analysis of corneal sections

The central region of the corneas (including the wounded area) were cut using a 9.5-mm-diameter corneal punch. These corneal 'buttons' were fixed in 4% paraformaldehyde (in distilled water) overnight at 4^{o}C and dehydrated using a graded series of sucrose solution (10% for 4 hours, 30% overnight at 4^{o}C). The corneal buttons were then embedded in OCT medium (Sakura Finetek, Torrance, CA) and sectioned using a cryotome to 7 micron-thick sections. The tissue sections were then processed for hematoxylin-eosin staining (H&E staining, described in Chapter 5).

6.3 Results

Developing *ex vivo* organ culture for corneal wounds

In our *ex vivo* model, corneal wounds were created on fresh animal eyeballs, treated with our scaffold and cultured in a standard cell culture incubator (**Figures 1 – 2**). Using this model, we created either a surface wound (where the epithelial layer is debrided) or a deeper wound (where part of the stroma is also removed) (**Figure 3**). After creating the wound, we excised the cornea (with a 5 mm scleral rim intact) and cultured the cornea on top of an agar gel as described in the Methods section. The agar gel provided support for the cornea and helped maintain its curvature. The corneas were then placed in tissue culture plates and cultured in a 37^{o}C incubator. Using this method, we were able to keep the corneas alive (with no signs of tissue deterioration) for up to 21 days.

To validate that the corneas are indeed alive and retain their ability to heal and repair, we created a wound on a bovine cornea that penetrated into the stromal layer (**Figure**

4). Fluorescein staining was used to visualize wound closure. By day 2, the epithelial layer had completely regrown over the wound area. We then re-wounded the same cornea on day 3 by removing the epithelial layer and tracked epithelial regrowth. By day 5, we did not see any fluorescein stained areas on the cornea, indicating that the epithelial layer was successfully regenerated. In addition to bovine corneas, we also validated the *ex vivo* organ culture model in porcine and rabbit eyes (**Figure 5**).

Testing composite scaffold with *ex vivo* organ culture

We used the *ex vivo* corneal culture model to test the efficacy of our scaffold in healing stromal wounds. For treated eyes, a layer of uniaxially-aligned nanofibers was placed onto the wound, followed by a hydrogel layer, and finally a second layer of nanofibers (of different orientation) was placed on top of the hydrogel. For untreated eyes, PBS was pipetted onto the wound bed as control.

When aECM-PEG was used as the hydrogel layer, we observed that eyes treated with isotropic nanofibers had the fastest rate of wound closure (**Figure 6**). This confirms our results *in vitro* that epithelial cells migrate faster on isotropic nanofibers than on aligned ones. We then processed the isotropic nanofiber-treated corneas, along with control corneas, for transmission electron microscopy. Results showed that treated corneas had a more organized nanostructure compared to untreated eyes (**Figure 7**).

When heparin-based hydrogels were used as the hydrogel layer, we observed that eyes treated with isotropic nanofibers had the fastest rate of wound closure (**Figure 8**), similar

to what we observed for aECM-PEG-hydrogel-treated ones. In a separate experiment, we examined the effects of growth factors on the rate of wound closure. In this experiment, we added either epidermal growth factor (EGF), fibroblast growth factor (FGF) or platelet-derived growth factor (PDGF) at 100 ng/mL to the heparin-based hydrogel formulation before application to the wound. We observed that the addition of growth factors slightly increased the rate of wound closure compared to those without growth factors. There were no observable differences between eyes treated with the different growth factors (**Figure 9**).

To observe the morphology of the corneal tissue during the course of wound repair, we processed the corneas for histological analysis at certain time points. Untreated control corneas, aECM-PEG treated corneas and heparin-based hydrogel treated corneas were fixed with 4% paraformaldehyde on days 1, 3 and 5 following the procedure, dehydrated with a graded series of sucrose, and processed for frozen sectioning. H&E staining of the tissue sections showed that on day 1, re-epithelialization was not complete on any of the corneas (neither untreated or treated) (**Figure 10 - 11**). By day 3, a regenerated epithelial layer was observed in both untreated and treated corneas. There were signs of inflammation on corneas treated with the heparin-based hydrogels. On day 5, the epithelial layer was completely regrown in the aECM-PEG treated corneas. The regenerated epithelium appeared slightly leaky in the untreated control cornea and there was further inflammation observed in the heparin-based hydrogel treated corneas.

6.4 Discussion

Developing *ex vivo* organ culture for corneal wounds

In this study, we developed an *ex vivo* organ culture model for corneal wounds. We demonstrated that both epithelial defects and stromal wounds can be created in the corneas, and that the corneas retain their ability to heal and repair themselves. Furthermore, the corneas can be cultured in a 37ºC incubator for up to 21 days, providing a good method to screen for suitable therapeutics prior to animal studies.

Our system (modified from that developed from Evans *et al.*[15]) improves on existing models for *ex vivo* corneal culture in that the explanted cornea is supported by a soft, permeable agar gel, which allows the diffusion of nutrients from the culture medium to the endothelium of the cornea. This allows the endothelial cells to stay vital and retain their ability to pump water from the cornea to avoid swelling.

We have also shown that the *ex vivo* model can be carried out in eyeballs obtained from various animal species (bovine, porcine or rabbits). Each species has their distinct advantages: bovine eyes are larger than porcine and rabbit eyes, and are thus easier to process and handle; porcine eyes share many structural similarities to human eyes and are the closest in dimension[16,17]; rabbit eyes have the smallest size out of the three species, but provide a good representation of results that would be expected in live rabbits (which is usually the next step in animal testing after mice).

During the development of our *ex vivo* model, we observed that the success of the experiments highly depended on the freshness of the tissue. Fresh eyeballs are firm due to their intraocular pressure, while eyeballs that are not fresh are soft and do not retain their shape when light pressure is applied. This is a sign that the tissue has started deteriorating and connective layers are starting to break down. When these eyeballs are used in the *ex vivo* model, there is a high probability that the cornea will begin rotting in the incubator after a few days. In our experiments, for bovine and porcine eyes, the eyeballs are harvested locally and shipped on ice for same day delivery. *Ex vivo* experiments are usually carried out within hours upon delivery. Rabbit eyes are harder to obtain, and are harvested and shipped from an out-of-state vendor. They are usually received the next day, and used immediately upon delivery.

Despite our success in developing the *ex vivo* model, there is room for improvement. In our model, the corneas are cultured in a 37^{o}C incubator with daily changes of media. To better simulate the blinking motion of the eye that aids in keeping the outer corneal layer moist, the corneas can be placed on a rocker such that the media in the tissue culture plate can routinely wash over the eye. Also, to improve nutrient diffusion from the culture media to the cornea, microchannels can be introduced in the agar gel base to create a perfusion culture system.

Testing composite scaffold with *ex vivo* organ culture

We used the *ex vivo* model to test the efficacy of our corneal scaffold. For both types of hydrogels (aECM-PEG and heparin-based), we observed that the rate of re-

epithelialization was fastest over isotropic nanofibers than aligned ones, thereby confirming our *in vitro* results that epithelial cells migrate faster on isotropic nanofibers (Chapter 2).

H&E staining showed that the epithelial layer in corneas treated with aECM-PEG hydrogel and nanofibers was completely regenerated, while corneas treated with the heparin-based hydrogel and nanofibers were incomplete and showed signs of infection. We also note that there was a higher percentage of eyeballs showing signs of rotting in the heparin-based hydrogel treatment group compared to the aECM-PEG treated ones during the course of the experiments (0-1 out of 10 eyes would show signs of rotting in aECM-PEG treated group, with the number increasing to 2-3 out of 10 eyes in the heparin-based hydrogel treated group). One possibility is that the eye tissue was already starting to deteriorate prior to the experiments; another explanation would be that the application of heparin to the wound area elicited an adverse effect that eventually led to infection. Although heparin has been associated with rapid endothelial cell repair, it has been suggested that heparin may not be beneficial to certain patients.[18] Indeed, studies have shown that heparin may interfere with wound healing by activating collagenase and accelerating collagen degradation, thereby affecting the formation of normal collagen.[19] It is possible that the application of heparin led to the activation of cytokines that are detrimental to corneal wound repair. Further experiments are needed to examine effects of heparin in corneal wounds.

In view of these results, we chose to test only the aECM-PEG hydrogel formulation in subsequent *in vivo* rabbit studies (Chapter 7). Though the *ex vivo* model is not a perfect model, it was an effective method to screen for potential scaffolds prior to rabbit experiments. By our conservative estimation, we were able to greatly reduce the number of rabbits needed for *in vivo* experiments (by over 100 animals).

6.5 Conclusions

An *ex vivo* corneal tissue culture is described: a mock wound (either an epithelial debridement or a deeper stromal wound) can be created in the cornea of an excised animal eyeball, treated with a candidate drug/scaffold, and cultured in a humidified incubator (37^{o}C, 5% CO_2). Our system improves on existing models for *ex vivo* corneal culture in that the endothelial layer is kept vital by allowing nutrients to diffuse from the culture medium through a permeable agar support gel to the endothelium. By allowing the endothelium to retain its ability to pump water from the cornea to avoid swelling, we can culture the corneas for up to 21 days to observe the effects of the treatment on corneal wound healing. We used the *ex vivo* model to study the efficacy of our two corneal scaffolds (nanofibers with either an aECM-PEG hydrogel or a heparin-based hydrogel) in treating stromal wounds. We determined that the aECM-PEG hydrogel treatment is preferred over the heparin-based treatment, since signs of infection were observed in those corneas treated with the heparin-based hydrogel. Using this model, we were able to screen for promising scaffolds (and eliminate those that had adverse effects) prior to carrying out further *in vivo* experiments, thereby greatly reducing the number of animals that would be needed otherwise.

6.6 References

1. Zhang, E.P.; Schrunder, S.; Hoffmann, F. Orthotopic corneal transplantation in the mouse – a new surgical technique with minimal endothelial cell loss. *Graefes. Arch. Clin. Exp. Ophthalmol.* **1996**; 234:714-719.

2. Kiazawa, T.; Kinoshita, S.; Fujita, K.; Araki, K.; Wantanbe, H.; Ohashi, Y. *et al.* The mechanism of accelerated corneal epithelial healing by human epidermal growth factor. *Invest. Ophthamol. Vis. Sci.* **1990**; 31:1773-1778.

3. Dua, H.S.; Gomes, J.A.; Singh, A. Corneal epithelial wound healing. *Br. J. Ophthalmol.* **1994**; 78:401-408.

4. Lu, L.; Reinach, P.S.; Kao, W. Corneal epithelial wound healing. *Exp. Biol. Med*. **2001**; 226:653-664.

5. United States Department of Agriculture, Animal and Plant Health Inspection Service, Annual Report Animal Usage 2013

   (http://www.aphis.usda.gov/animal_welfare/downloads/7023/Animals%20Used%20In%20Research%202013.pdf) (Accessed April 20th 2015).

6. National Institutes of Health Budget (http://www.nih.gov/about/budget.htm) (Accessed April 20th, 2015).

7. Gomez, L.M.; Conlee, K.; Stephens, M. Noncompliance with public health service (PHS) policy on humane care and use of laboratory animals: an exploratory analysis. *J. Appl. Anim. Welf. Sci.* **2010**; 13:123-136.

8. Schmook, F.P.; Meingassner, J.G.; Billich, A. Comparison of human skin or epidermis models with human and animal skin in in-vitro percutaneous absorption. *Int. J. Pharm*. **2001**; 215:51-56.

9. Nunes, S.F.; Murcia, P.R.; Tiley, L.S.; Brown, I.H. Tucker, A.W.; Maskell D.J. et al. An ex vivo swine tracheal organ culture for the study of influenza infection. *Influenza Other Respir. Viruses.* **2010**; 4:7-15.

10. Dyer, L.A.; Patterson, C.A. A novel ex vivo culture model for the embryonic mouse heart. *J. Vis. Exp*. **2013**; 75:e50359.

11. Sriram, S.; Gibson, D.J.; Robinson, P.; Pi, L.; Tuli, S.; Lewin, A.S. Assessment of anti-scarring therapies in ex vivo organ cultured rabbit corneas. *Exp. Eye Res.* **2014**; 125:173-182.

12. Castro-Combs, J.; Noguera, G.; Cano, M.; Yew, M.; Gehlbach, P.L.; Palmer, J. et al. Corneal wound healing is modulated by topical application of amniotic fluid in an ex vivo organ culture model. *Exp. Eye Res.* **2008**; 87:56-63.

13. Xu, K-P.; Li, X-F.; Yu, F-S. Corneal organ culture model for assessing epithelial responses to surfactants. *Toxicol. Sci.* **2000**; 58:306-314

14. Janin-Manificat, H.; Rovere, M-R.; Galiacy, S.D.; Malecaze, F.; Hulmes, D.J.S.; Moali, C. et al. Development of ex vivo organ culture models to mimic human corneal scarring. *Mol. Vis.* **2012**; 18:2896-2908.

15. Evans, M.D.M.; McFarland, G.A.; Xie, R.Z.; Taylor, S.; Wilkie, J.S.; Chaouk, H. The use of corneal organ culture in biocompatibility studies. *Biomaterials* **2002**; 23:1359-1367.

16. Ruiz-Ederra, J.; Garcia, M.; Hernandez, M.; Urcola, H.; Hernandez-Barbachano, E.; Araiz, J. *et al*. The pig eye as a novel model of glaucoma. *Exp. Eye Res.* **2005**; 8:561-569.

17. Sanchez, I.; Martin, R.; Ussa, F.; Fernandez-Bueno, I. The parameters of the porcine eyeball. *Graefes. Arch. Clin. Exp. Ophthalmol.* **2011**; 349:475-482.

18. Galvin, L. Effects of heparin on wound healing. *J. Wound Ostomy. Continence Nurs.* **1996**; 23:224-226.

19. Tarvady, S.; Anguli, V.C.; Pichappa, C.V. Effect of heparin on wound healing. *J. Biosci.* **1987**; 12: 33-40.

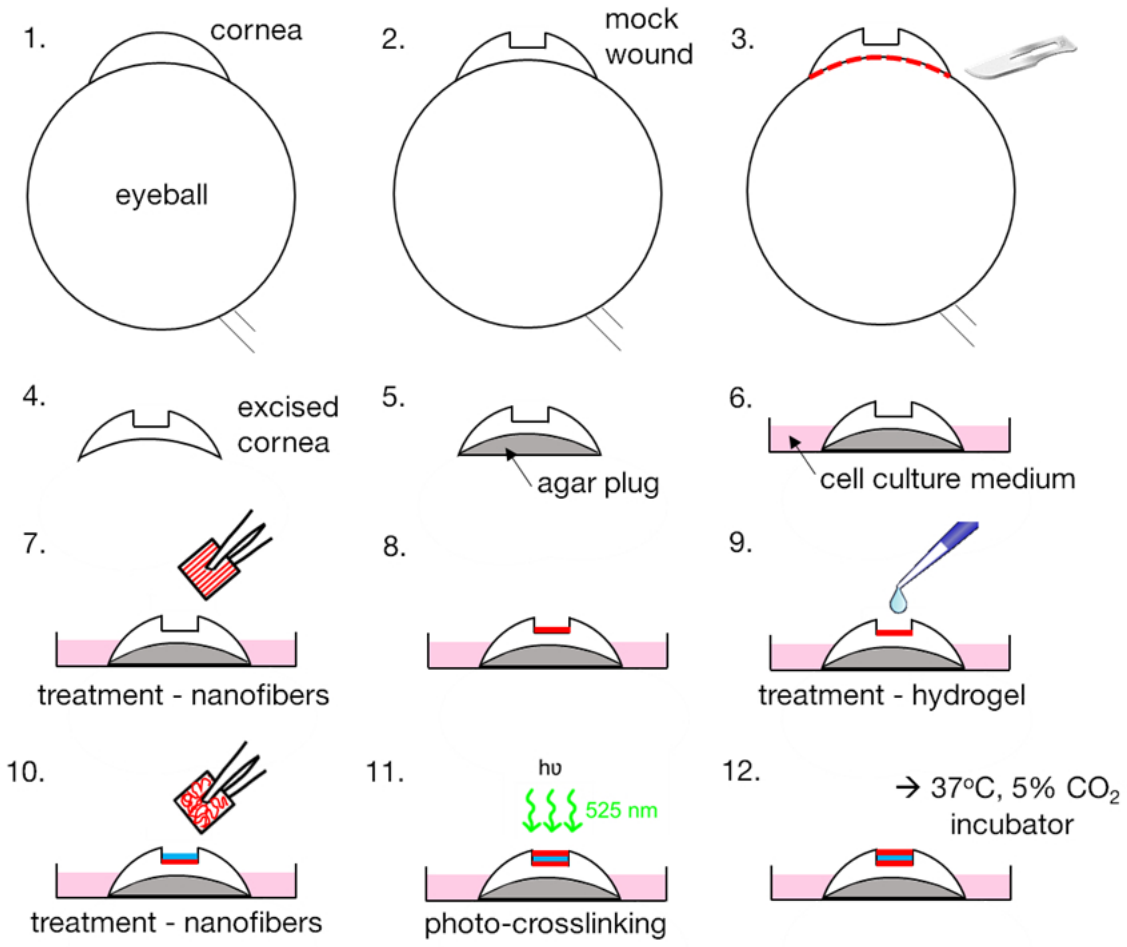

Figure 1. Schematic of *ex vivo* corneal tissue culture. 1) Fresh animal eyeballs are purchased. 2) A wound (either epithelial defect or stromal wound) is created in the cornea. 3-4) The cornea (with a 5-mm scleral rim intact) is excised from the eyeball. 5) The cornea is placed on an agar gel for support and 6) cultured in a tissue culture plate with medium at a level just above the scleral rim. 7-11) Corneas in the experimental group are treated with our composite scaffold with a layer of uniaxially-aligned nanofibers, followed by a layer of hydrogel, and finally a layer of isotropic nanofibers. Corneas treated with heparin-based hydrogels are then irradiated with green light (525 nm) for 5 minutes for photo-

polymerization. 12) Corneas are then placed in a 37^{o}C incubator and monitored daily. Steps 7-11 are skipped for untreated corneas.

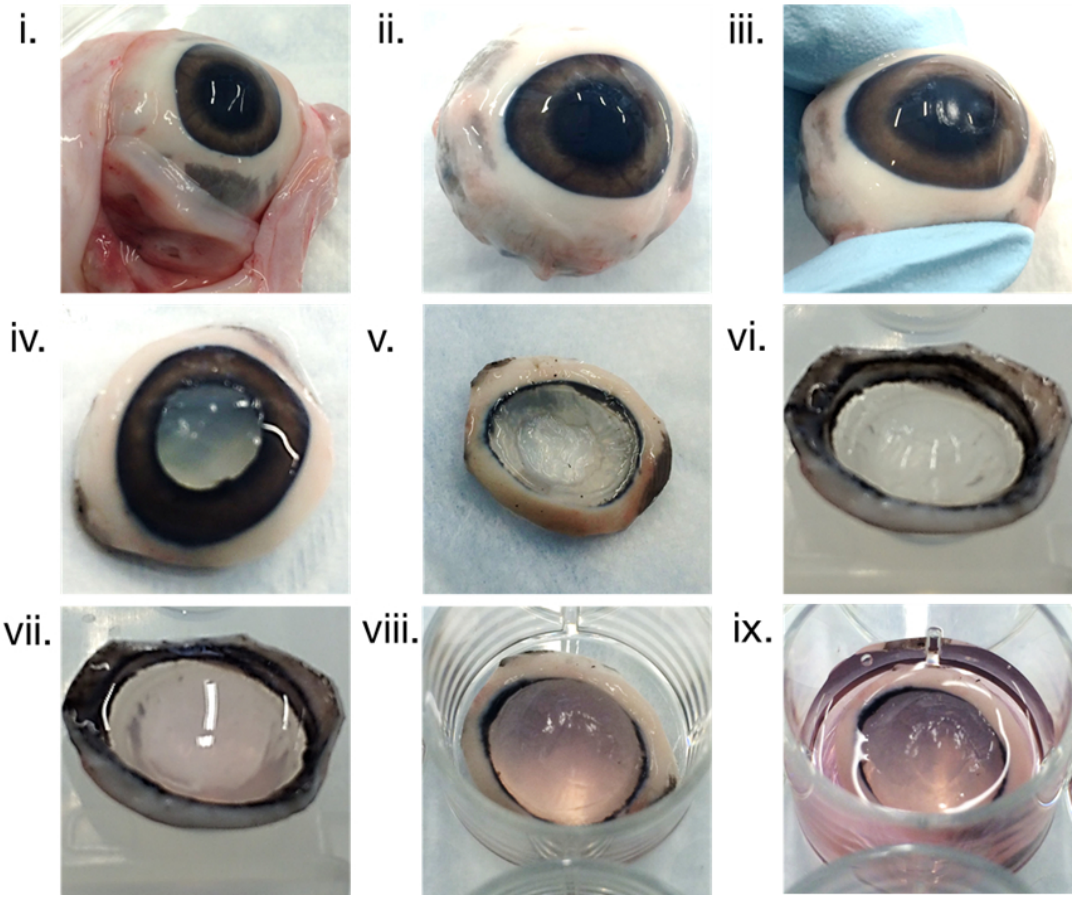

Figure 2. Photographs of preparing a porcine cornea for *ex vivo* culture. i) Fresh eyeballs are purchased and ii) the fat and connecting tissue are trimmed from the eyeball. iii) A wound is created on the cornea and iv) the cornea is excised from the eyeball with 5-mm scleral rim intact. v) The iris is removed. vi) The cornea is placed upside down (endothelial side up) and vii) filled with the agar gel support. viii) The cornea is then placed right-side up into a tissue culture dish (here 12-well plate) and ix) culture medium is filled until the level is just above the scleral rim.

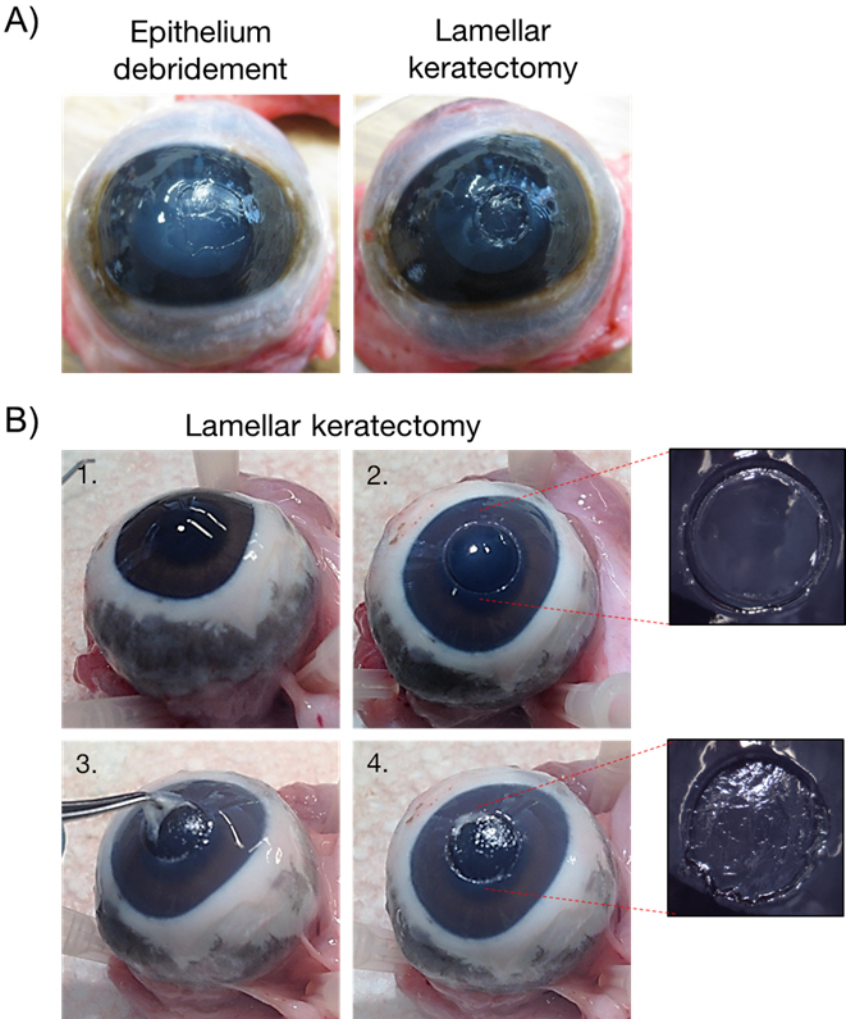

Figure 3. A) Two types of wounds can be created: an epithelial defect (which is a surface wound where only the epithelial layer is removed) or a stromal wound (where a lamellar keratectomy is performed such that part of the stroma, in addition to the epithelium, is also removed). B) To perform a lamellar keratectomy, a fresh eyeball is first secured onto a stable surface. A vacuum corneal trephine (6-mm diameter) is used to cut a circular wound of 100 microns deep. A pair of colibri forceps is used to lift edge of the cut tissue such that a crescent knife can be used to remove the corneal tissue.

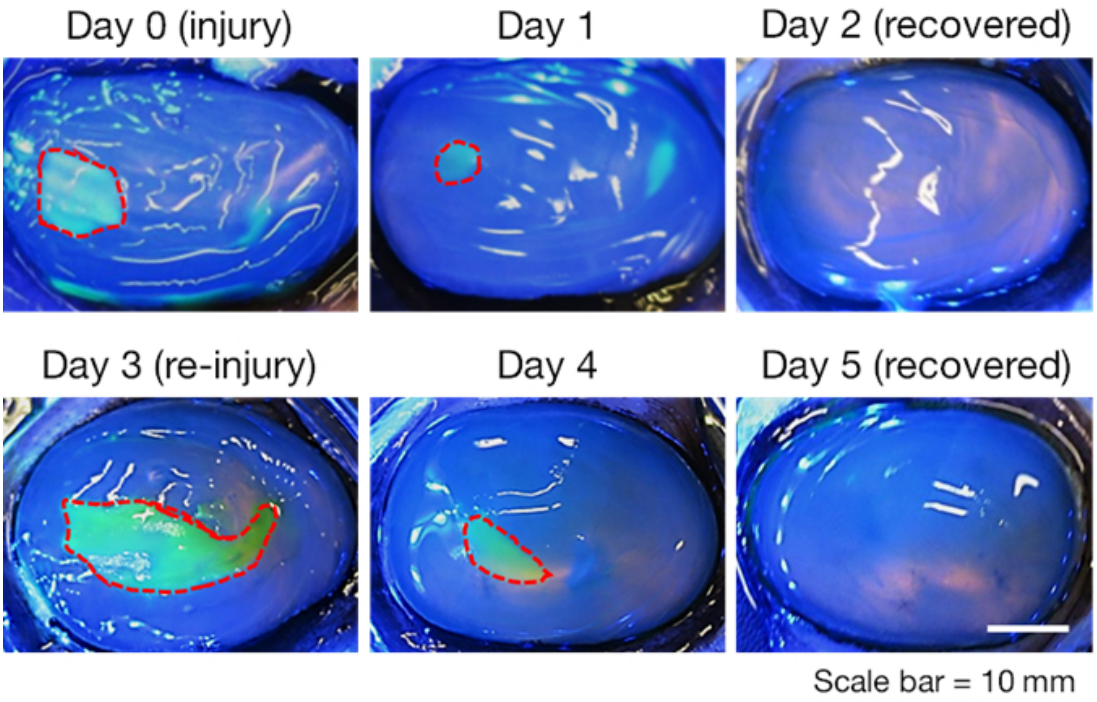

Figure 4. Representative images showing the ability of a bovine cornea to repair itself in *ex vivo* culture. On Day 0, a stromal wound was created on the cornea. By Day 2, the epithelial layer had regrown over the wounded area. On Day 3, an epithelial defect was created on the same cornea, and by Day 5, the epithelial layer was regenerated once again.

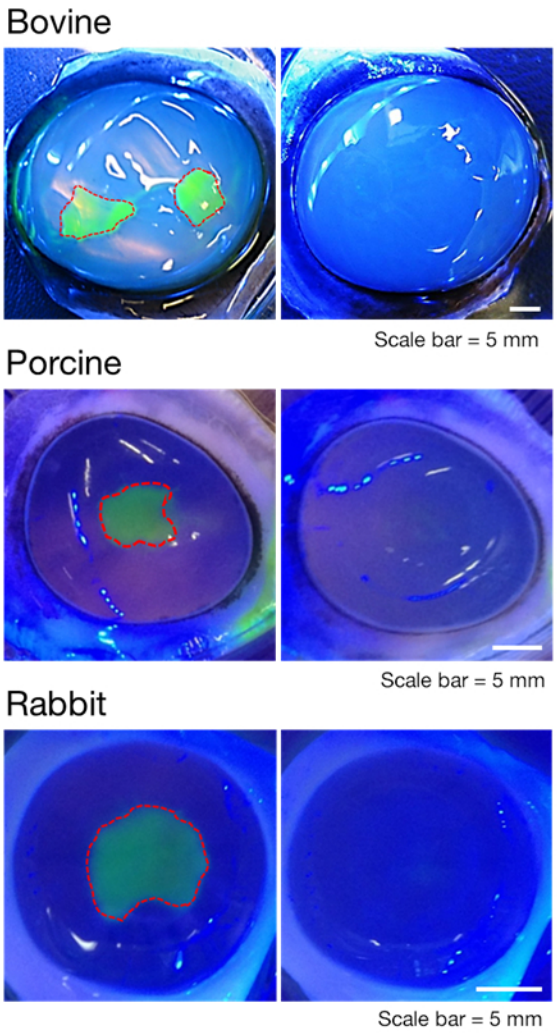

Figure 5. Representative images demonstrating that our *ex vivo* corneal culture model can be carried out in several different animal species (bovine, *top*; porcine, *middle*; rabbit, *bottom*).

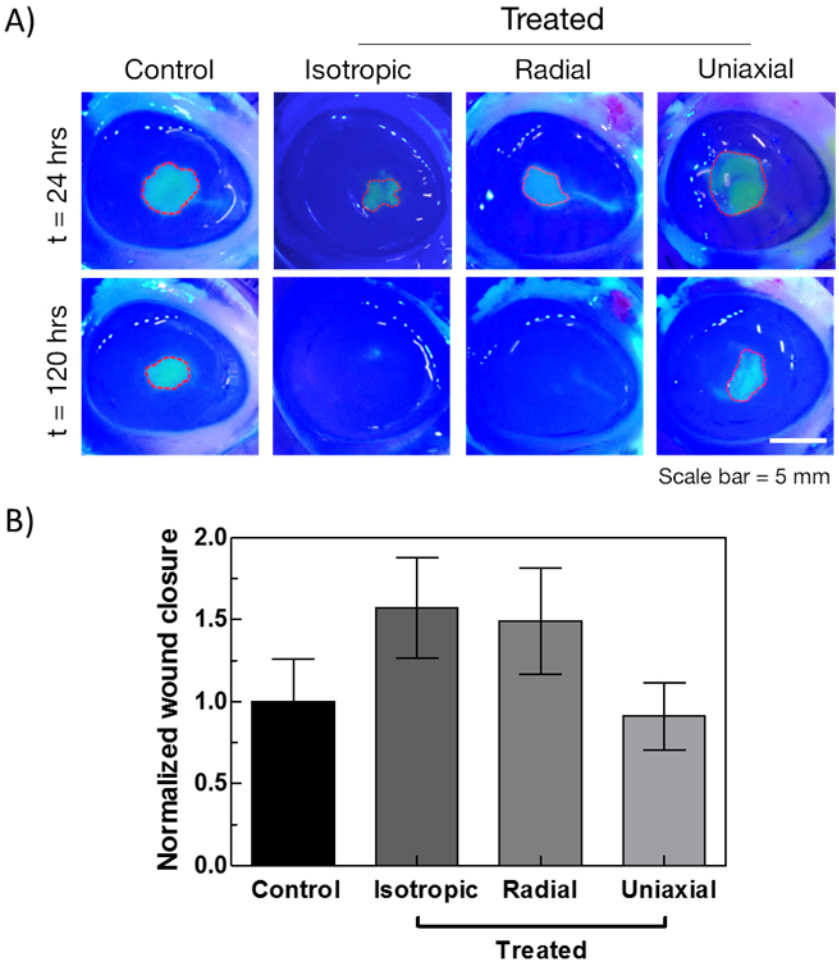

Figure 6. A) Representative images of wound closure for aECM-PEG treated and untreated corneas using fluorescein staining and B) Quantification of results in A). The initial wound was 6-mm diameter, 100 microns deep, created using a vacuum corneal trephine. Treated eyes were given a layer of uniaxially-aligned nanofibers, followed by a layer of aECM-PEG hydrogel, and finally, a second layer of nanofibers was placed on top (either isotropic, radial or uniaxial). Control eyes were left untreated. Corneas treated with isotropic and radial nanofibers had a faster rate of epithelial regrowth compared to those treated with uniaxial nanofibers and untreated controls.

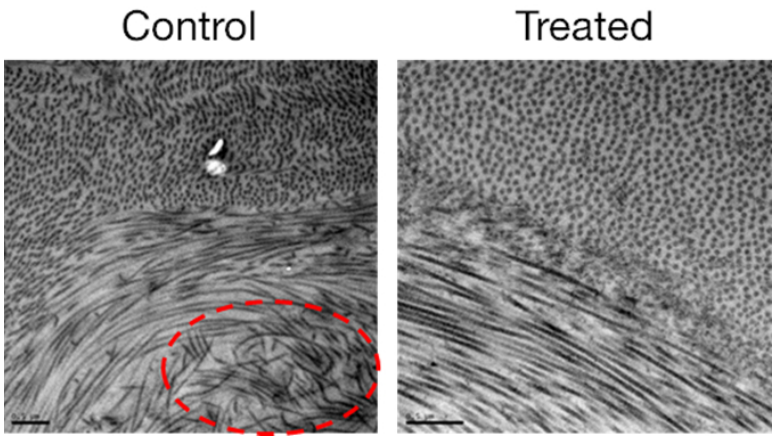

Figure 7. Transmission electron micrographs of an untreated cornea and a cornea treated with our scaffold made of aECM-PEG hydrogel and nanofibers. Results show that the collagen nanostructure is more disorganized in untreated corneas compared to those that were treated.

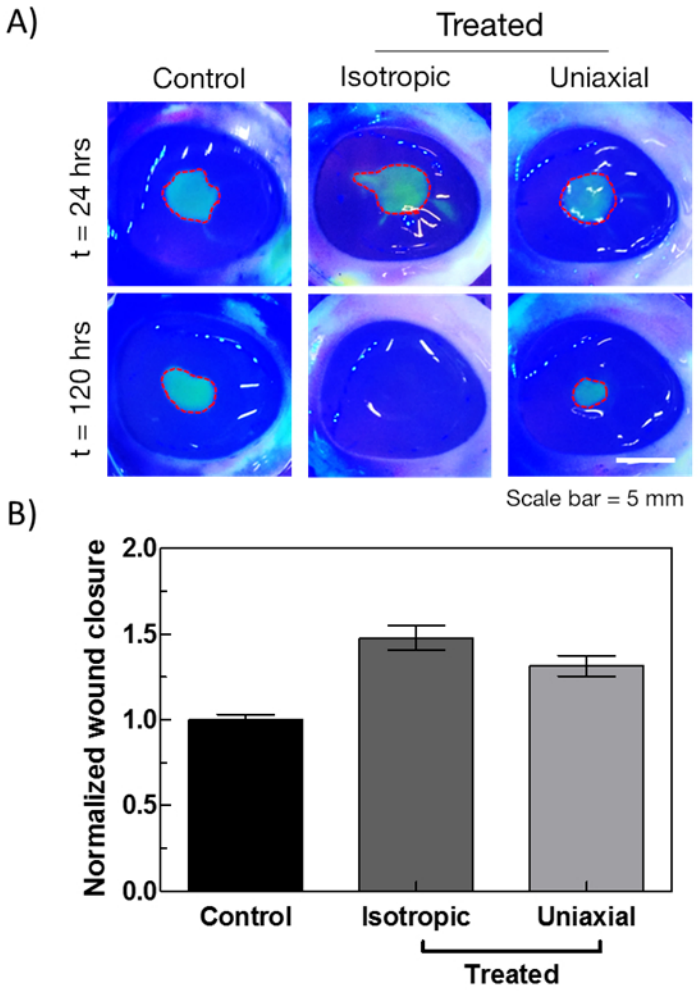

Figure 8. A) Representative images of wound closure for heparin-based hydrogel treated and untreated corneas using fluorescein staining and B) Quantification of results in A). The initial wound was 6-mm diameter, 100 microns deep, created using a vacuum corneal trephine. Treated eyes were given a layer of uniaxially-aligned nanofibers, followed by a layer of heparin-based hydrogel, and finally, a second layer of nanofibers was placed on top (either isotropic or uniaxial). Control eyes were left untreated. Corneas treated with isotropic nanofibers had a faster rate of epithelial regrowth compared to those treated with uniaxial nanofibers and untreated controls.

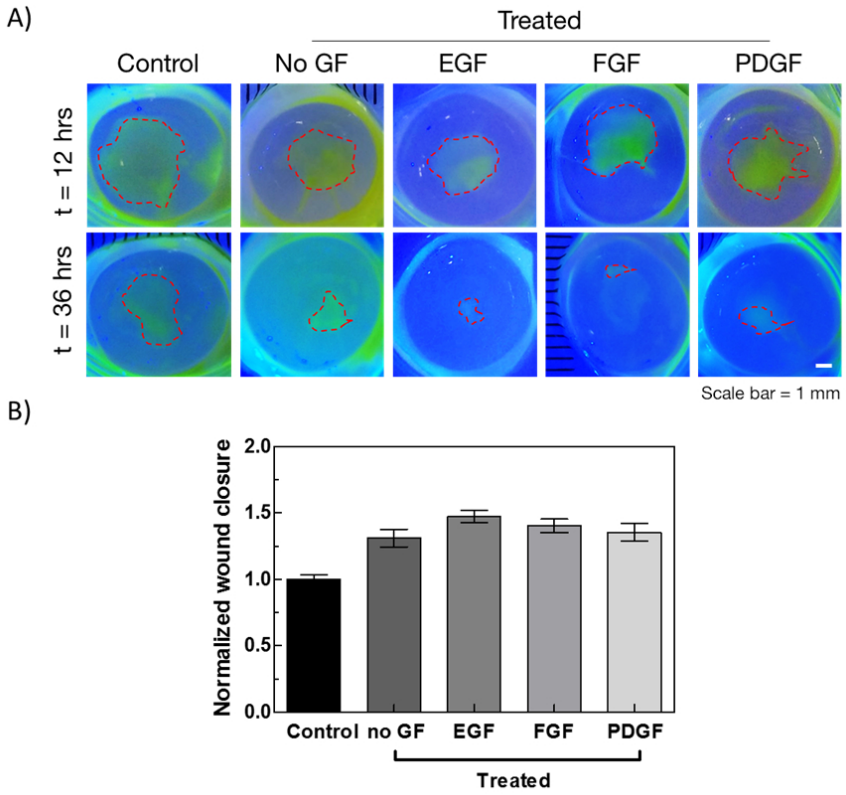

Figure 9. A) Representative images of wound closure for heparin-based hydrogel (loaded with growth factors) treated and untreated corneas using fluorescein staining and B) Quantification of results in A). The initial wound was 6-mm diameter, 100 microns deep, created using a vacuum corneal trephine. Treated eyes were given a layer of uniaxially-aligned nanofibers, followed by a layer of heparin-based hydrogel, and finally, a second layer of isotropic nanofibers. The heparin-based hydrogel was loaded with either epidermal growth factor (EGF), fibroblast growth factor (FGF) or platelet-derived growth factor (PDGF) at 100 ng/mL. Control eyes were left untreated. Corneas treated with growth factors had slightly faster rate of epithelial regrowth compared to those without.

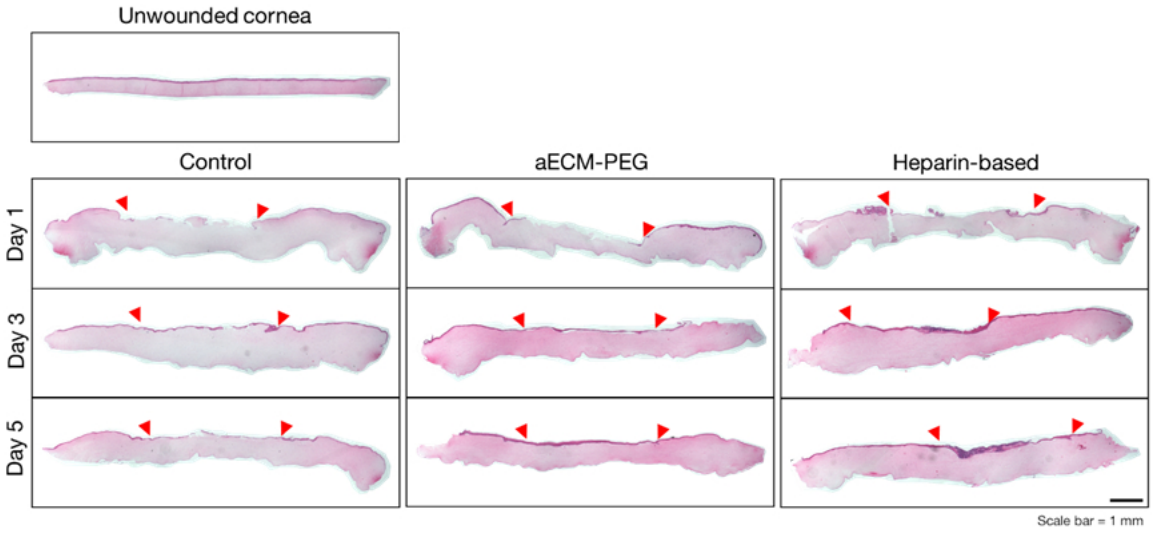

Figure 10. Hematoxylin and eosin (H&E) staining of tissue sections from treated and untreated corneas on day 1, 3 and 5 after the procedure. Red arrows denote the initial wound sites. On day 1, the epithelial layer has not regrown in any of the corneas. On day 3, the epithelial layer has regrown in the aECM-PEG-hydrogel treated cornea, while the heparin-based hydrogel-treated cornea showed signs of infection. On day 5, the epithelial layer of the control corneas has mostly regrown.

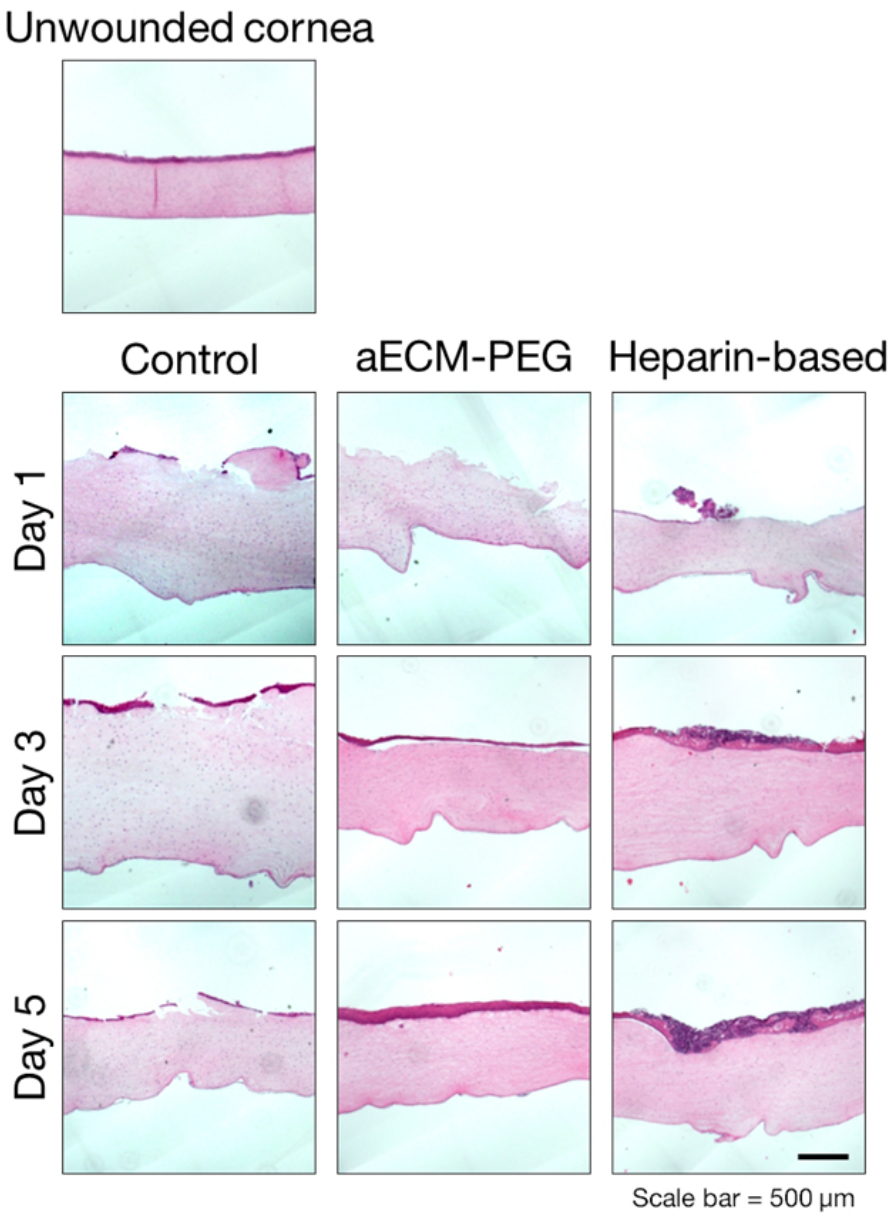

Figure 11. Higher magnification pictures of those shown in Figure 10 of hematoxylin and eosin (H&E) staining of tissue sections from treated and untreated corneas on day 1, 3 and 5 after the procedure.

Chapter 7

In vivo study of corneal scaffold in a rabbit model

7.1 Introduction

In the first two chapters, we studied the effects of topological and biochemical cues on corneal epithelial cells, fibroblasts and myofibroblasts. We identified that gelatin nanofibers of isotropic orientation can promote epithelial cell migration, while those that are uniaxially aligned increase fibroblast migration and modulate the myofibroblast phenotype. We also demonstrated that growth factors (EGF, FGF and PDGF at 50 - 100 ng/mL) can further decrease α-SMA expression. In Chapter 4, we developed a visible-light photo-crosslinkable heparin-based hydrogel that can bind and release bioactive growth factors.

We confirmed that our corneal scaffold, comprised of nanofibers and the heparin-based hydrogel, as well as the photo-crosslinking light dosage, are well-tolerated in a mouse model for epithelial defects (Chapter 5). In addition, we also fabricated and tested a different hydrogel material that is made of artificial extracellular matrix (aECM) proteins. To test the cellular response to our scaffold in corneal stromal wounds, we developed an *ex vivo* corneal tissue culture where the corneas can be kept alive for up to 21 days and retain their ability to heal and repair wounds (Chapter 6). In these studies, we observed that a scaffold that contains the aECM-based hydrogel is more favorable than one with the heparin-based hydrogel in treating corneal wounds.

Here, in collaboration with Dr. Bala Ambati at the University of Utah Moran Eye Center, we tested these scaffolds in stromal wounds created on rabbit corneas *in vivo*. Although the anatomy of rabbit eyes is slightly different from that of human eyes (in particular, rabbit eyes do not have Bowman's layer)[1,2], rabbit experiments have been the "gold standard" in testing candidate treatments for corneal wound repair[3-6].

For a given eye, a lamellar keratectomy was performed to make a 6-mm diameter, 100 micron deep corneal wound, which was then treated with our aECM-based scaffold or left untreated as control. The rate of epithelial regrowth was compared between experimental and control groups. The number of myofibroblasts and immune cells were analyzed by immunostaining of tissue sections from harvested corneas. Results show that our aECM-based scaffold shows promise in promoting a more orderly corneal wound response.

7.2 Methods

Fabrication of scaffold

Fabrication of nanofibers

Gelatin (type A, porcine, Sigma Aldrich, St. Louis, MO) was dissolved in a mixture of 2:3:5 distilled water/ethyl acetate/acetic acid at 12% w/w and stirred overnight at 37^{o}C. Electrospun nanofibers were fabricated from the gelatin solution using a 22-gauge needle, +15 kV voltage and 8 cm needle-to-collector distance. Isotropic nanofibers were collected on a metal ring (6 mm diameter) placed on a planar electrode, and uniaxially-aligned nanofibers were made using a pair of split electrodes (6 mm apart).

Fabrication of aECM-PEG hydrogels

Artificial extracellular matrix proteins (aECM, 34.6 kDa) were synthesized and characterized using established protocols described elsewhere. To fluorescently label aECM proteins (aECM-f), aECM protein (2.5 mg/mL in PBS) was mixed with NHS-rhodamine (7 molar excess) for one hour at room temperature. Excess dye was removed by fluorescent dye removal columns (Thermo Scientific). aECM-f proteins were then lyophilized for storage until use. aECM protein solutions were prepared by dissolving aECM in PBS (34% aECM, 2% aECM-f w/v) overnight at 4^{o}C. Four-arm poly(ethylene oxide) terminated with succinimidyl glutarate groups (PEG-S, Polymer Source, Montreal, Canada) was dissolved in PBS (25% w/v) just prior to hydrogel fabrication. The aECM solution and PEG-S solution were mixed together in a 1:1 ratio to prepare the aECM-PEG precursor solution (final concentration: 18% aECM, 12.5% PEG-S). The precursor solution was used immediately after preparation.

Characterization of aECM-PEG hydrogels

To determine the pore characteristics of fabricated aECM-PEG hydrogels, the hydrogels were first swollen in PBS for 2 days at 37^{o}C, and then flash-frozen in liquid nitrogen for 10 minutes. The frozen hydrogels were then lyophilized for 2 days. Cross-sections of the hydrogels were prepared by cutting with a cold razor blade, and mounted onto aluminum stubs. Samples were sputter-coated with 10 nm palladium and observed in a field emission scanning electron microscope (SEM, Zeiss 1550 VP) at an accelerating voltage of 5 kV.

Animal experiments

The experiments in a rabbit model were performed in the Moran Eye Center according to the Association for Research in Vision and Ophthalmology Statement of Use for Animals, and were approved by the Institutional Animal Care and Use Committee of the University of Utah. All drugs used were pharmaceutical-grade ophthalmic solutions. All scaffold components were sterilized as follows prior to use. Nanofiber mats were first immersed in 70% ethanol (twice, 10 minutes each) and then placed under UV light for 30 minutes. Hydrogel precursor solutions were sterile filtered through a 0.2 micron filter. All procedures were carried out in a sterile operating room following standard aseptic techniques: all personnel wore sterile surgical gown, mask and gloves. Between consecutive rabbits all personnel changed gloves. Each rabbit was covered with a sterile drape (with an opening for access to the animal's eye) during the procedure. All supplies needed (e.g., forceps, trephines, etc) were autoclaved under high temperature and pressure in between procedures.

Lamellar keratectomy in rabbits

Rabbits (New Zealand white, female, ~3.5 kg) were anesthetized with ketamine (35 mg/kg) and xylazine (5 mg/kg). Betadyne was applied to the rabbit eyes prior to surgery. Droplets of proparacaine (0.5%, Bausch & Lomb), tropicamide (1%, Bausch & Lomb), cyclopentolate (1%, Akorn) and phenylephrine hydrochloride (2.5%, Falcon) were then applied to the rabbit eyes. A corneal trephine (6 mm diameter) was used to create a circular wound to a depth of 100 microns. A crescent knife was then used to remove the

corneal tissue. For each rabbit, the left eye was untreated to serve as a control and the right eye was treated with our scaffold. Our treatment involved placing a layer of nanofibers gently onto the wound bed, applying a layer of aECM-PEG hydrogel (10 µL), followed by placing an additional layer of nanofibers on top of the hydrogel. Following surgery, erythromycin ointment was applied to both treated and untreated eyes. The rabbits were allowed to recover from surgery, and their eyes were observed daily for signs of inflammation. Six rabbits were used in each experimental group. A surgical error occurred in one eye of the aECM-PEG treated experimental group (the trephine was not properly zeroed and the resulting incisions were too deep) and the rabbit was euthanized. No data was recorded for that animal.

Tracking epithelium regrowth following procedure

The surface area of the epithelial defect was assessed on days 6 and 13 after surgery. To observe the wound boundary, 1 µL of fluorescein solution (0.25% in PBS) was pipetted onto the surface of each eye. Excess fluorescein solution was rinsed with 0.9% sodium chloride solution and removed by gently touching a sterile cotton swab to the side of the eye. The wound area was then imaged under blue LED lights, and the extent of wound closure was analyzed using ImageJ.

Staining and immunolabeling of corneal sections

Rabbits were euthanized (3 from each group on day 6 and remaining 3 on day 13), and their corneas were harvested. Frozen sections were prepared by first fixing the excised corneas with 4% paraformaldehyde for 2 hours, and then placing in two sucrose

solutions (10% for 2 hours, 30% overnight). The corneas were then embedded in OCT medium and sectioned using a cryotome to 7-micron-thick sections. For immunofluorescence, frozen sections were blocked with 5% (w/v) fetal bovine serum (FBS) in phosphate-buffered saline with 0.2% tween. The sections were probed with mouse anti-αSMA conjugated to FITC (1:400 dilution, Sigma Aldrich, St. Louis, MO) or mouse anti-neutrophil (1:200 dilution, Hycult Biotech) or mouse anti-macrophage (1:200 dilution, Abcam) antibodies overnight at 4^{o}C. The secondary antibody Alexa-Fluor 647 goat anti-mouse IgG (Life Technologies) was used at 1:1000 dilution for 1 hour. Nuclei was stained with DAPI.

Paraffin sections were prepared by fixing excised corneas with 4% paraformaldehyde for 2 hours, dehydrating them through a graded ethanol series, and finally embedding them in paraffin. Sections were cut (7 microns) and processed for hematoxylin-eosin (H&E) and Masson's trichrome staining. In Masson's trichrome, blue staining represents collagen. To quantify fibrosis, ImageJ software was used to calculate the number of highest-intensity blue pixels, which was then divided by the total number of pixels per corneal section.

7.3 Results

To study the efficacy of our scaffold in treating corneal wounds that penetrate into the stroma, we chose a rabbit model and performed a lamellar keratectomy to create a 6-mm diameter, 100 micron deep wound (**Figure 1**). As in the mouse experiments in Chapter 5, the wound in the left eye was treated with PBS followed by topical antibiotic

("untreated") to serve as a control, while the right eye was "treated" with our scaffold: a layer of uniaxially-aligned nanofibers at the base of the wound bed (**Figure S-1**), a hydrogel to fill the wound, and a top layer of unoriented nanofibers. Two hydrogels were compared: (i) aECM-PEG hydrogel and (ii) aECM-PEG hydrogel with 3.5% pluronic F-127 added as a porogen ("aECM-PEG-F127").

The rabbits showed no signs of distress during the recovery period after surgery. The cornea was observed to be transparent post-op and in the daily examinations thereafter. No differences in inflammation were observed between treated and control, indicating that our treatment was well-tolerated in rabbits.

The extent of epithelial closure was visualized on Days 1, 6 and 13 with fluorescein staining (**Figure 2**). We observed that treated rabbit eyes (in both aECM-PEG and aECM-PEG-F127 experimental groups) had similar rates of epithelial regrowth compared to untreated control eyes: Day 1, the epithelial defects had decreased in size; Day 6, treated eyes had slightly smaller epithelial defects than the untreated controls; and Day 13, treated eyes showed very small epithelial defects (point-like) and untreated control eyes showed diffuse update of fluorescein over an area similar to that of the initial wound.

Three rabbits from the aECM-PEG-F127 group and two from the aECM-PEG group (one animal was lost, see Methods) were sacrificed on Day 6; and the remaining three from each group were sacrificed on Day 13. Their corneas were harvested and processed

for histological examination. In accord with observations of epithelial closure by fluorescein staining, H&E staining of tissue sections showed that the epithelial layer had not fully regrown in either treated or untreated corneas on Day 6 (**Figure 2, S-2 to S-4**). Interestingly, epithelial defects could not be found in H&E stained sections of specimens taken on Day 13, despite the fact that some fluorescein stain penetrated the epithelium (**Figure 2, S-2 to S-4**). The regenerated epithelium of corneas treated with aECM-PEG had a morphology closest to that of a healthy unwounded cornea (based on prior literature and tissue sections from the corneas of fresh rabbit eyes purchased from vendor, **Figure S-5**).

Immunolabeling of αSMA protein (a cell marker for the hyperactive myofibroblast repair phenotype) in the tissue sections showed that there were less myofibroblast cells in treated corneas compared to controls that received no treatment (**Figure 3, S-6**). There were no measurable differences in the number of myofibroblasts between the two treated groups.

In addition, there were also fewer macrophages and neutrophils in treated corneas compared to controls (**Figure 4, S-7, S-8**), with the largest decrease in corneas treated with aECM-PEG-F127. Masson's trichrome staining showed a decrease of blue color in the repaired stroma of treated corneas compared to controls (**Figure 5**), indicating that there was less collagen formation in the scaffold-treated corneas.

7.4 Discussion

In these studies, we tested the aECM-PEG hydrogel treatment, since we observed more favorable results using this treatment than the heparin-based hydrogels in the *ex vivo* corneal culture experiments (Chapter 6). In particular, we chose to use aECM-PEG hydrogel at pH 7, since we observed no measurable differences between the effects of the pH 7 and 8 formulations in the mice experiments. In addition, NHS-groups hydrolyze at a slower rate at pH 7, thus allowing more time between preparing the precursor solution and applying it to the wound (the half-life of hydrolysis for NHS-groups is ~4 hours at pH 7 and 0^{o}C, while the half-life is only 10 minutes at pH 8.6 and 4^{o}C[7]).

A key concern in using our scaffold to treat deeper corneal wounds is whether the aECM-PEG hydrogel layer would allow cell infiltration. To address this concern, pluronic F-127 was added to the formulation as a porogen to induce the formation of larger pores. This strategy has been employed in PLLA porous foams to enhance pore size and improve the interconnectivity among pores.[8,9] Indeed, the addition of pluronic F-127 into our aECM-PEG hydrogels (aECM-PEG-F127) resulted in the formation of larger pores compared to those without (**Figure S-9**). Live/dead staining of corneal fibroblasts encapsulated in the aECM-PEG hydrogels showed that the addition of pluronic F-127 did not affect cell viability *in vitro* (**Figure S-10**). Using a scratch wound assay *in vitro*, we observed that the migration rate of fibroblasts into the 'mock wound' containing aECM-PEG-F127 was slightly faster than that with aECM-PEG (**Figure S-11**).

The rabbit studies were divided into two experimental groups: one treated with aECM-PEG, and the other with aECM-PEG-F127. In both groups, a layer of uniaxially-aligned nanofibers was first placed onto the wound bed, followed by the addition of a hydrogel layer, and finally, a layer of isotropic nanofibers was placed on top of the hydrogel.

Rabbit study results confirm observations from mice experiments that our scaffold is well-tolerated in animals, and supports epithelial regrowth. There were no measurable differences in the rate of epithelial closure between the two treatments. Interestingly, the epithelium in most control eyes were not fully restored after 13 days, evidenced by the large area stained with fluorescein. H&E staining of tissue sections showed the area that stains is not de-epithelialized, but rather, the epithelium is leaky. Elevated cytokines associated with inflammatory response tend to make epithelia and endothelia leaky[10-12]; perhaps the restoration of the epithelial barrier in treated eyes results from reduced cytokine levels evident in the decreased production of αSMA and fewer numbers of macrophages and neutrophils.

Immunostaining of tissue sections showed that the population of myofibroblasts and inflammatory cells (macrophages and neutrophils) were greatly reduced in the wound bed treated with our scaffolds relative to untreated controls, indicating that our treatment was effective in promoting a calmer wound response. This confirms our observations *in vitro* that fewer myofibroblasts are observed on oriented nanofibers than on planar surfaces. In addition, Masson's trichrome staining of tissue sections showed that there

is less collagen formation in treated corneas than in untreated ones, indicating our treatment is effective in reducing fibrosis.

There were no significant differences in cellular response to the scaffolds between the two experimental groups, suggesting that the addition of pluronic F-127 and thus size of pores in the scaffold is not a major factor in orchestrating orderly wound repair. Rather, we speculate that both hydrogel formulations allow repair myofibroblasts to infiltrate and migrate onto the uniaxially-aligned nanofibers. The topographical and biochemical cues from the nanofibers induce the myofibroblasts to express lower levels of αSMA and initiate a calmer wound response, which results in fewer activated immune cells and less formation of disorganized collagen. Guillemette and coworkers' hypothesis that cells which respond to physical cues on an underlying substrate can induce other cell layers to behave in a similar fashion may also hold true in the present study[13]: myofibroblasts on the oriented nanofibers may influence myofibroblasts throughout the scaffold to reduce their αSMA expression levels.

In the current study, the rabbits were only kept alive for 14 days after surgery. Jester and colleagues have shown that after full thickness stromal wounds, αSMA expression in myofibroblasts can be detected as early as 3 days in the anterior stroma and at 7 days throughout the thickness of the stroma. Thus, a time scale of 14 days is sufficiently long to observe effects of our scaffold treatment in modulating αSMA expression.[14] However, a longer duration rabbit study is still needed evaluate effects of the scaffold on the morphology of regenerated tissue (e.g., collagen fiber diameter, collagen

orientation, ratio of proteoglycans to collagen, lamellar superstructure). Indeed, Wang and colleagues have shown that a study of 3 months is required to evaluate corneal haze development, and confirm morphology and transparency of a healed stroma.[15]

Here, based on the results from the *ex vivo* corneal tissue cultures, both of the treated groups in the present rabbit studies received nanofibers. In view of the favorable response to nanofiber/aECM-PEG/nanofiber scaffolds, future work evaluating the role of each of the three layers is warranted. Specifically, experimental groups that are treated with the aECM-PEG hydrogel alone, aECM-PEG and an underlayer of oriented nanofibers, and aECM-PEG hydrogel with an overlayer of unoriented nanofibers should be compared. It is possible that the aECM-PEG hydrogel acts as a buffer for cytokines released upon corneal injury and is sufficient to mediate a calmer wound response in the stroma without the use of nanofibers. The incremental benefit of the nanofibers might be greater for the unoriented overlayer than for the underlayer. Simplifying the treatment to hydrogel alone or hydrogel with only an overlayer of nanofibers would greatly simplify the treatment.

7.5 Conclusion

We tested the efficacy of our corneal scaffold (nanofibers with an aECM-PEG hydrogel) *in vivo* using a rabbit model for stromal wounds. As expected from observations made in the *in vivo* mice and *ex vivo* culture experiments, our treatment supported epithelial regrowth over the scaffold. Immunostaining of tissue sections revealed that there was a decreased expression of αSMA protein in treated corneas than in untreated ones. To our

knowledge, this is the first study which has demonstrated *in vivo* that the expression of αSMA can be modulated by topological and biochemical cues presented on nanofibers. In addition, we found that there were fewer immune cells (macrophages and neutrophils) in treated corneas than untreated corneas. Further experiments are needed to fully examine whether the repaired cornea remains transparent in the long term, but in this short-term study, our corneal scaffold shows promise in promoting a calmer wound response.

7.6 References

1. Gwon, A. Chapter 13: The rabbit in cataract/IOL surgery in Animal models in eye research; Tsonis, P. Ed.; Elsevier Ltd. **2008**; 184-204.
2. Davis, F. A. The anatomy and histology of the eye and orbit of the rabbit. *Trans. Am. Ophthalmol. Soc.* **1929**; 27:401-441.
3. Choi, Y.S.; Kim, J.Y.; Wee, W.R.; Lee, J.H. Effect of the application of human amniotic membrane on rabbit corneal wound healing after excimer laser photorefractive keratectomy. *Cornea* **1998**; 17:389-395.
4. Huang, A.J.; Tseng, S.C. Corneal epithelial wound healing in the absence of limbal epithelium. *Invest. Ophthalmol. Vis. Sci.* **1991**; 32:96-105.
5. Mencucci, R.; Favuzza, E.; Boccalini, C.; Lapucci, A.; Felici, R.; Resta, F. *et al.* CoQ10-containing eye drops prevent UVB-induced cornea cell damage and increase cornea wound healing by preserving mitochondrial function. *Invest. Ophthalmol. Vis. Sci.* **2014**; 55:7266-7271.
6. Crooke, A.; Guzman-Aranguez, A.; Mediero, A.; Alarma-Estrany, P.; Carracedo, G.; Pelaez, T. *et al.* Effect of melatonin and analogues on corneal wound healing: involvement of Mt2 melatonin receptor. *Curr. Eye Res.* **2015**; 40:56-65.
7. Hermanson, G.T. Bioconjugate Techniques, 3rd ed.; Academic Press **2013**
8. Nam, Y.S.; Park, T.G. Biodegradable polymeric microcellular foams by modified thermally induced phase separation method. *Biomaterials* **1999**; 20:1783-1790.
9. Zhang, R.; Weng, W.; Du, P.; Zhao, G.; Shen, G.; Han, G. Effect of Pluronic F127 on the pore structure of macrocellular biodegradable polylactide foams. *Polymer. Adv. Tech.* **2004**; 15:425-430.

10. Capaldo, C.T.; Nusrat, A. Cytokine regulation of tight junctions. *Biochim. Biophys. Acta.* **2009**; 1788:864-871.

11. Srinivas, S.P. Dynamic regulation of barrier integrity of the corneal endothelium. *Optom. Vis. Sci.* **2010**; 87:E239-E254.

12. Ivanov, A.I.; Parkos, C.A.; Nusrat, A. Cytoskeletal regulation of epithelial barrier function during inflammation. *Am. J. Pathol.* **2010**; 177:512-524.

13. Guillemette, M.D.; Cui, B.; Roy, E. *et al.* Surface topography induces 3D self-orientation of cells and extracellular matrix resulting in improved tissue function. *Integr. Biol.* **2009**; 1:196-204.

14. Jester, J.V.; Petroll, W.M.; Barry, P.A.; Cavanagh, H.D. Expression of alpha-smooth muscle (alpha-SM) actin during corneal stromal wound healing. *IOVS* **1995**; 36:809-819.

15. Wing, M.X.; Gray, T.B.; Park, W.C.; Prabhasawat, P.; Culbertson, W.; Forster, R. *et al.* Reduction in corneal haze and apoptosis by amniotic membrane matrix in excimer laser photoablation in rabbits. *J. Cataract Refract. Surg.* **1997**; 27:310-319.

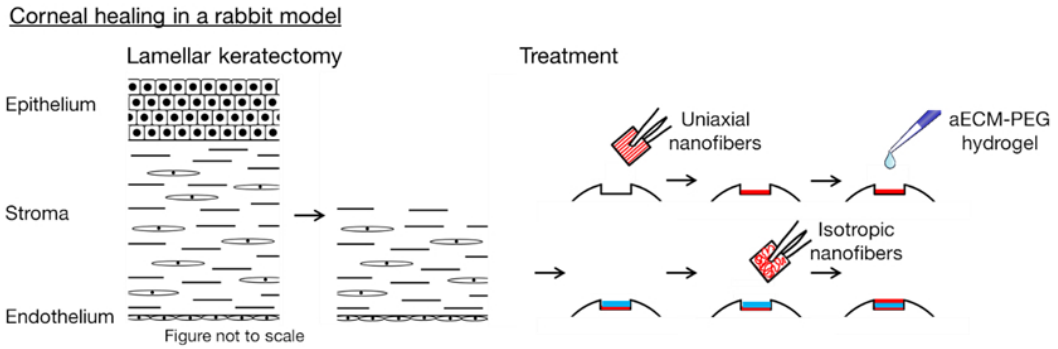

Figure 1. Schematic of *in vivo* rabbit model for stromal wounds. For each rabbit eye, a lamellar keratectomy was performed to create a 6-mm diameter, 100 micron deep wound. For treated eyes, a layer of uniaxially-aligned nanofibers were placed in the wound bed, followed by a layer of aECM-PEG hydrogel, and finally, a layer of isotropic nanofibers was placed on top of the hydrogel. For control eyes, 15 µL of PBS was pipetted onto the wound bed.

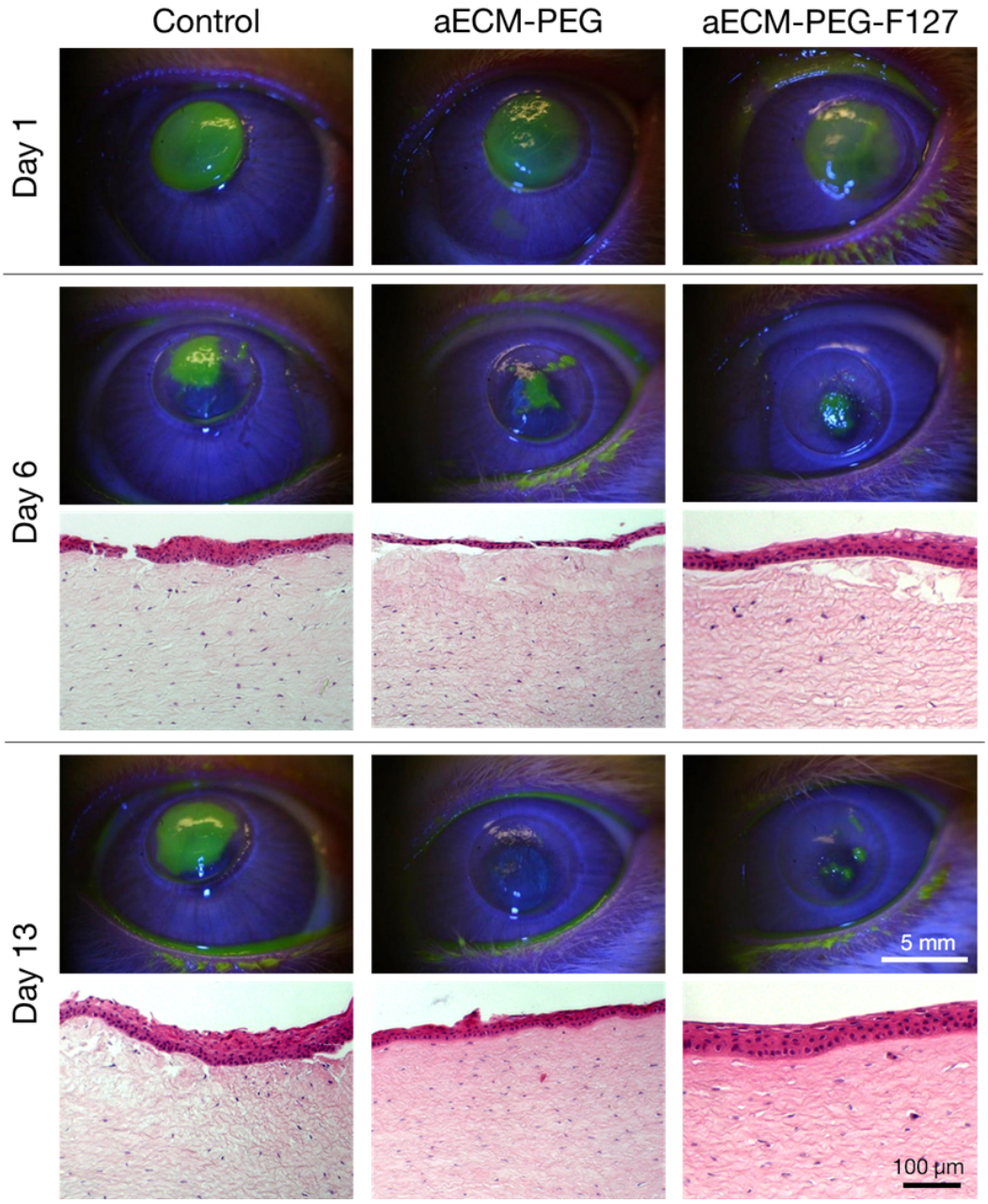

Figure 2. Representative images of fluorescein staining to visualize wound closure. The wound area was imaged on day 1, 6 and 13. Tissue sections from corneas harvested on day 6 and 13 were also subjected to H&E staining. Epithelial regrowth was faster in treated corneas than untreated ones. The corneal morphology for treated corneas also appeared more normal and organized than untreated controls.

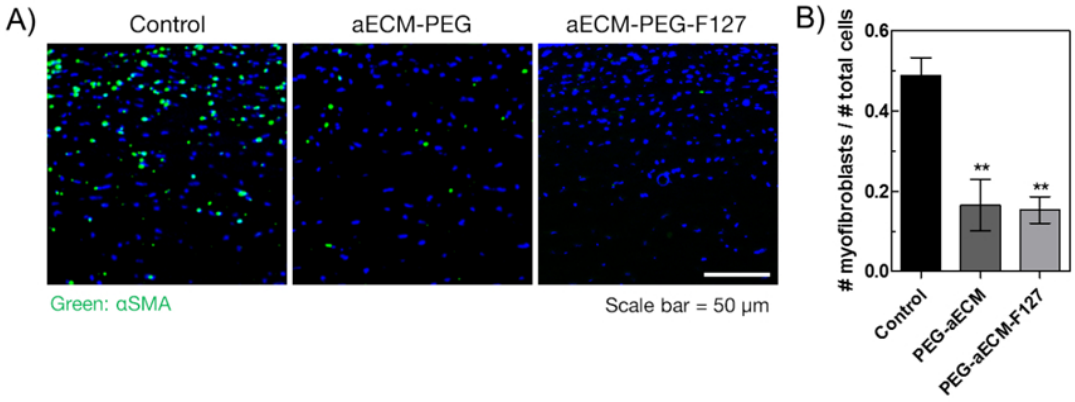

Figure 3. A) Representative images of immunolabeling of myofibroblasts and B) quantification of results. Corneas were harvested on day 14, fixed, dehydrated and embedded in optimum cutting temperature (O.C.T. compound). The samples were then sectioned using a cryotome. The 7-micron-thick tissue sections were labeled with FITC-conjugated anti-αSMA. Treated corneas had significantly fewer αSMA-positive myofibroblasts than untreated ones. There were no measurable differences between the two treated groups.

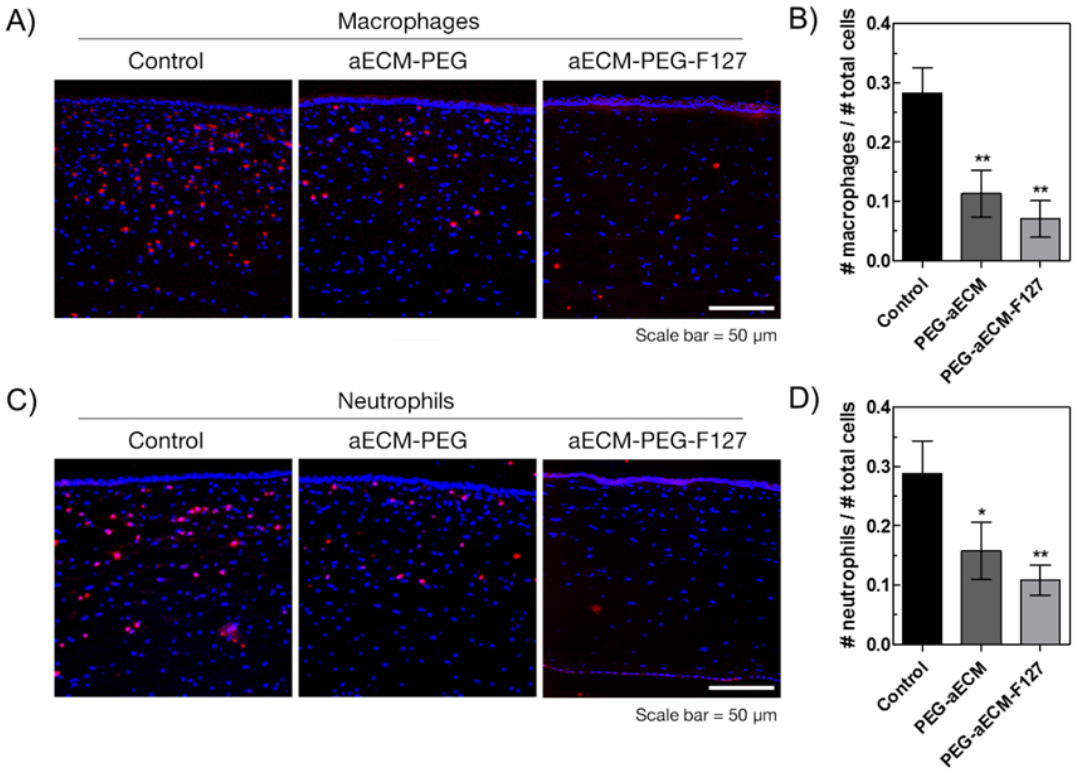

Figure 4. Representative images of immunolabeling of immune cells and quantification of results. Corneas were harvested on day 14, fixed, dehydrated and embedded in optimum cutting temperature (O.C.T. compound). The samples were then sectioned using a cryotome. The 7-micron-thick tissue sections were labeled with antibodies against macrophages (A) and neutrophils (B). Alexa-Fluor 647 goat anti-mouse antibodies were used as the secondary antibodies. Treated corneas had significantly fewer macrophages and neutrophils than untreated ones, with the most significant decrease in the aECM-PEG-F127-treated eyes.

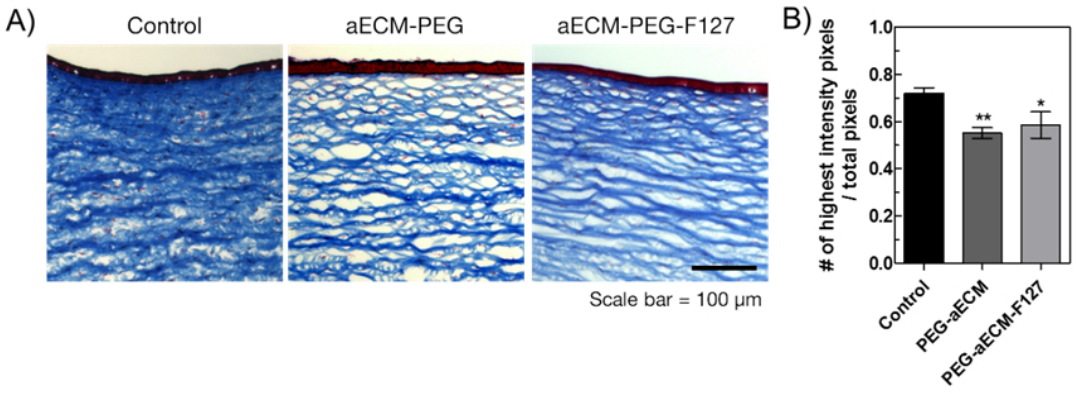

Figure 5. A) Representative images of Masson's Trichrome staining of tissue sections and B) quantification of results. Corneas were harvested on day 14, fixed and processed for paraffin embedding. The samples were then sectioned into 7-micron-thick sections and subjected to Masson's Trichrome staining. Treated corneas had less collagen formation than untreated ones.

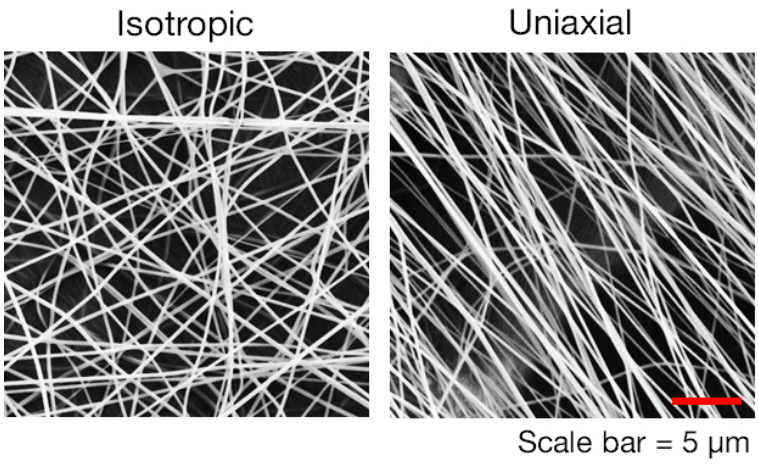

Figure S-1. Scanning electron micrographs showing the isotropic and uniaxially-aligned nanofibers used in this study.

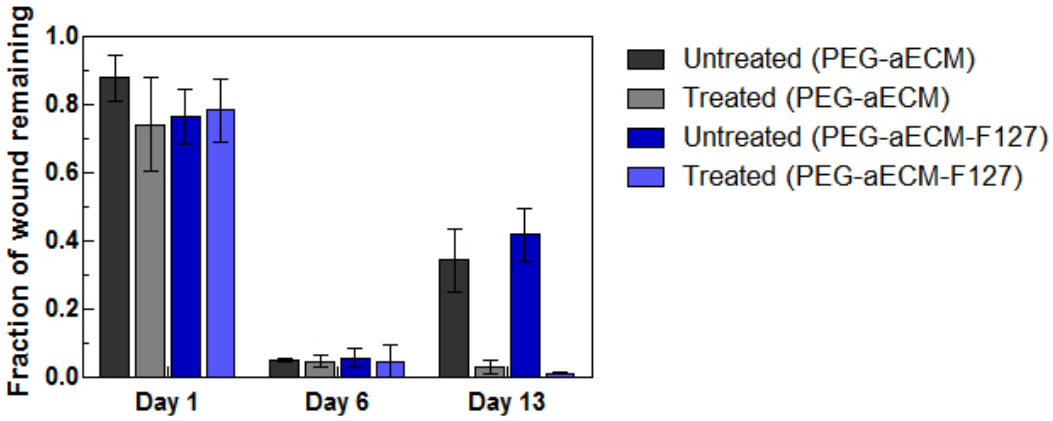

Figure S-2. Quantification of epithelial closure as observed from fluorescein staining.

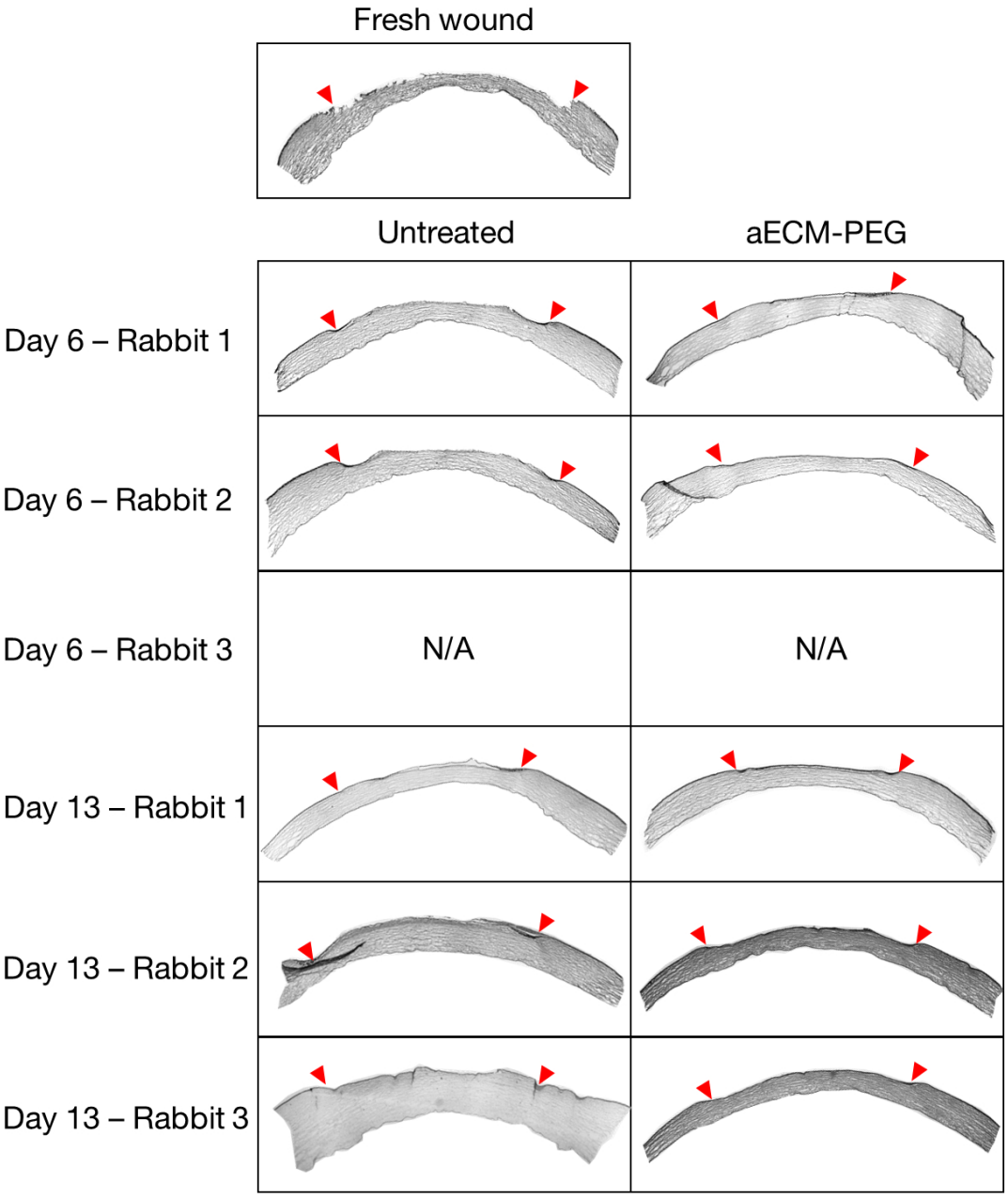

Figure S-3. H&E staining of tissue sections from all rabbits used in the aECM-PEG experimental group. For each rabbit, their left eye was left untreated, and their right eye was treated with our composite scaffold. Three rabbits were sacrificed on Day 6, and the remaining three were sacrificed on Day 13. Red arrows denote the initial wound site.

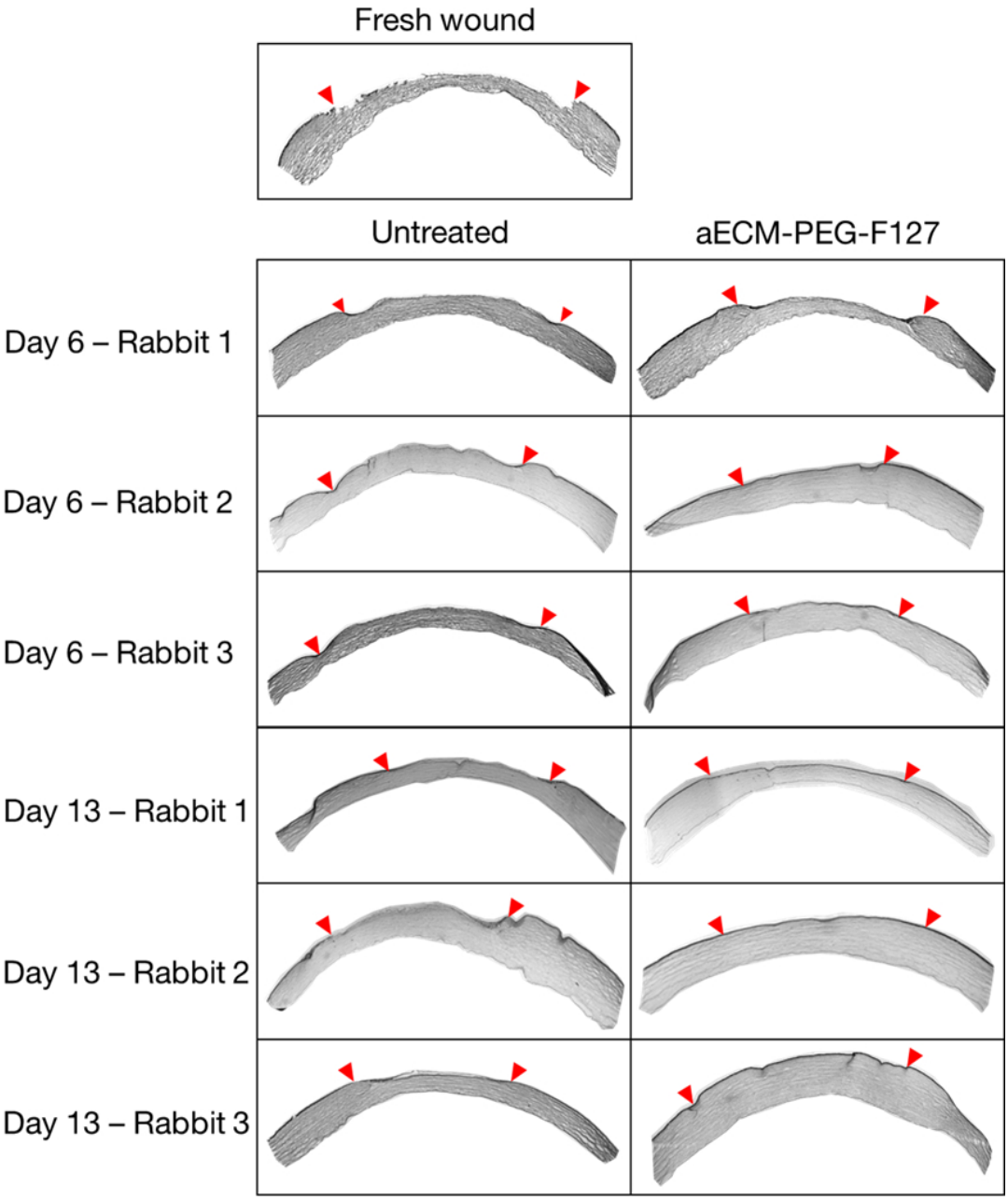

Figure S-4. H&E staining of tissue sections from all rabbits used in the aECM-PEG-F127 experimental group. For each rabbit, their left eye was left untreated, and their right eye was treated with our composite scaffold. Three rabbits were sacrificed on Day 6, and the remaining three were sacrificed on Day 13. Red arrows denote the initial wound site.

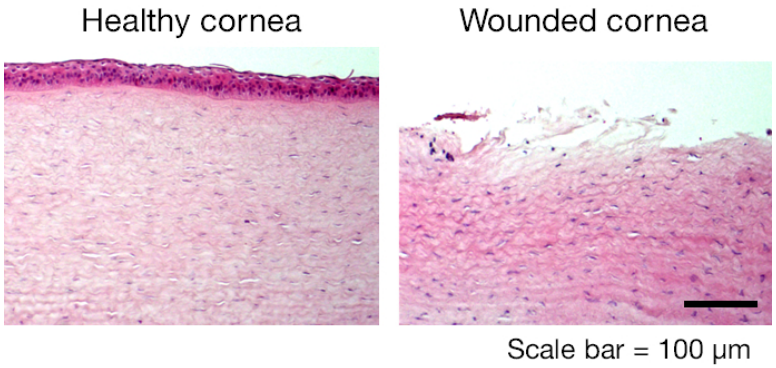

Figure S-5. For comparison purposes, we also prepared tissue sections from rabbit corneas (using fresh rabbit eyeballs purchased from Pel Freez). Corneas were either left unwounded (to show the morphology of a healthy cornea) or wounded using the same protocol as the *in vivo* studies (these corneas were processed immediately after creation of the wound to show the morphology of a freshly-wounded cornea).

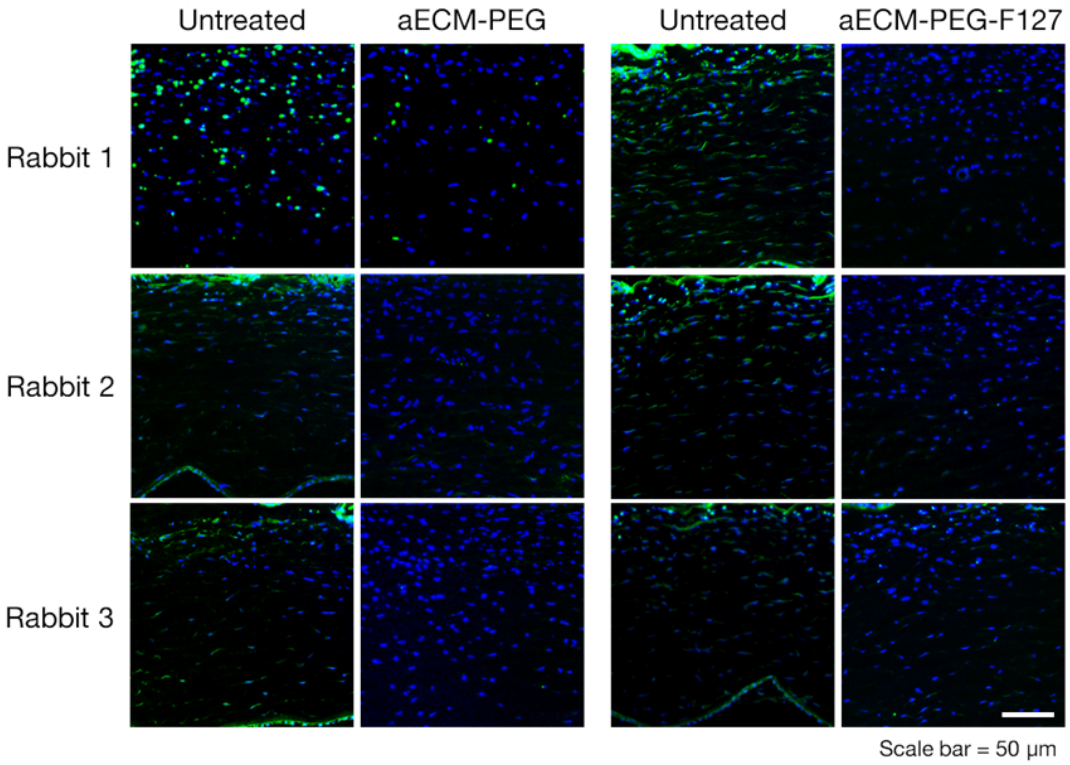

Figure S-6. Immunolabeling of myofibroblasts in tissue sections of corneas harvested on day 13 (all three rabbits represented here, extension of Figure 3). Treated corneas had significantly fewer αSMA-positive myofibroblasts (*green*) than untreated ones. There were no measurable differences between the two treated groups.

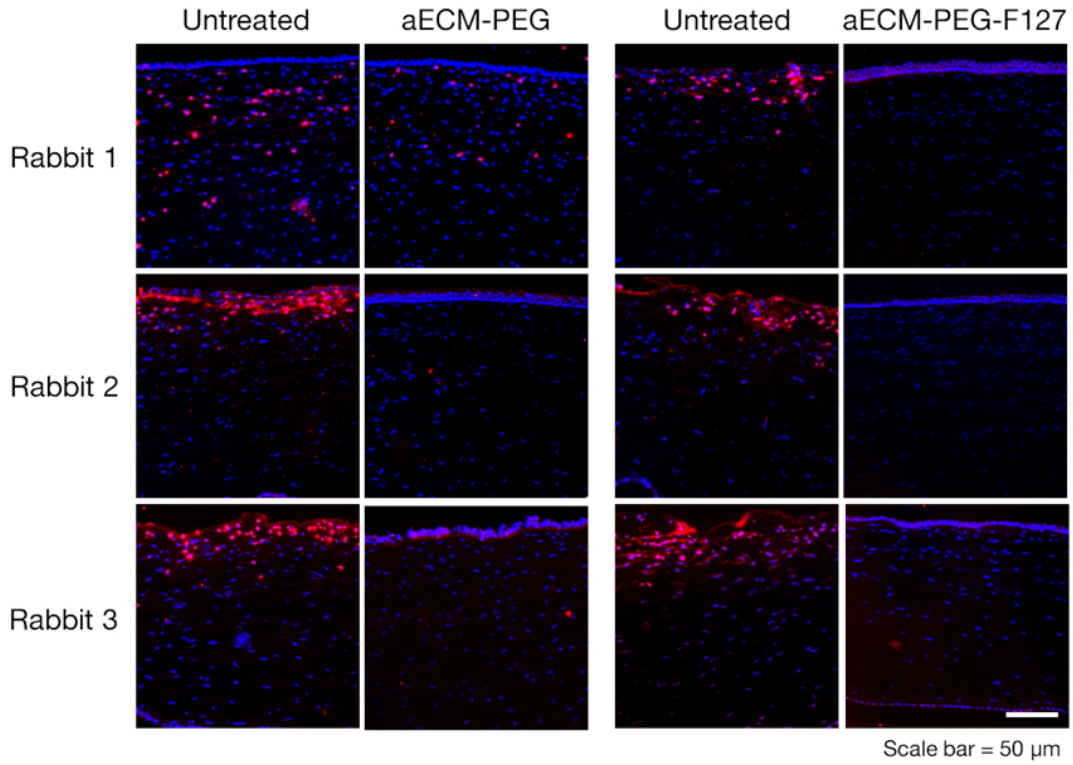

Figure S-7. Immunolabeling of macrophages in tissue sections of corneas harvested on day 13 (all three rabbits represented here, extension of Figure 4A-B). Treated corneas had significantly fewer macrophages (*red*) than untreated ones. There were no measurable differences between the two treated groups.

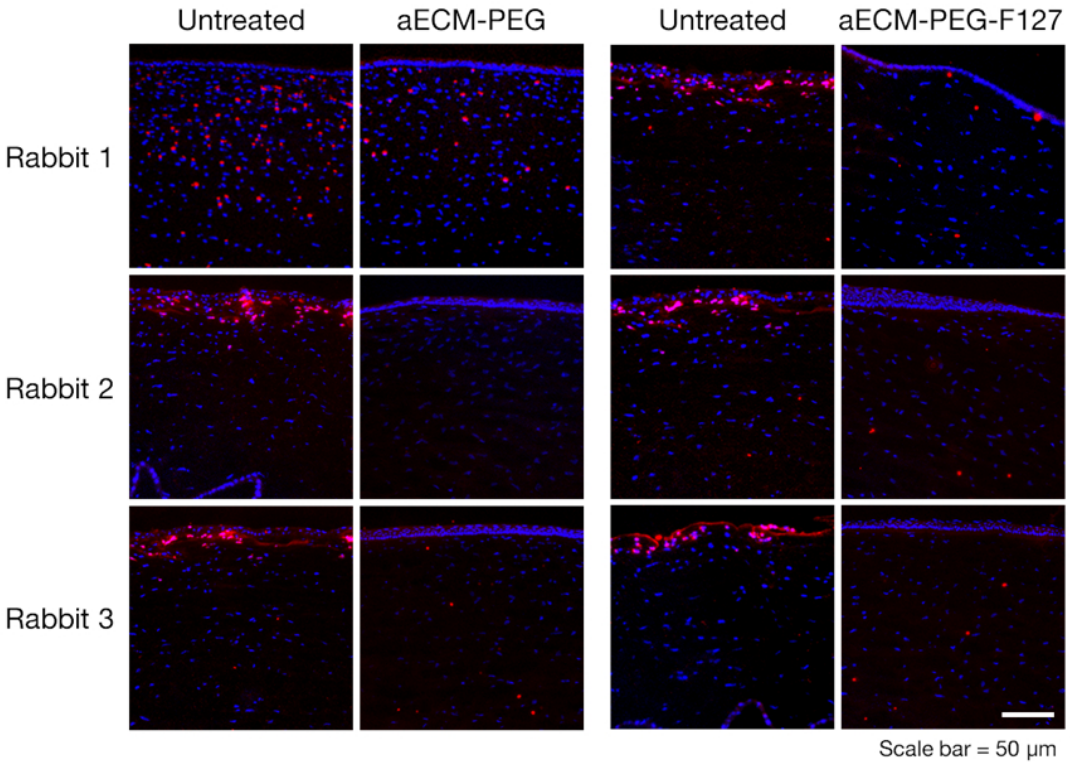

Figure S-8. Immunolabeling of neutrophils in tissue sections of corneas harvested on day 13 (all three rabbits represented here, extension of Figure 4C-D). Treated corneas had significantly fewer neutrophils (*red*) than untreated ones. There were no measurable differences between the two treated groups.

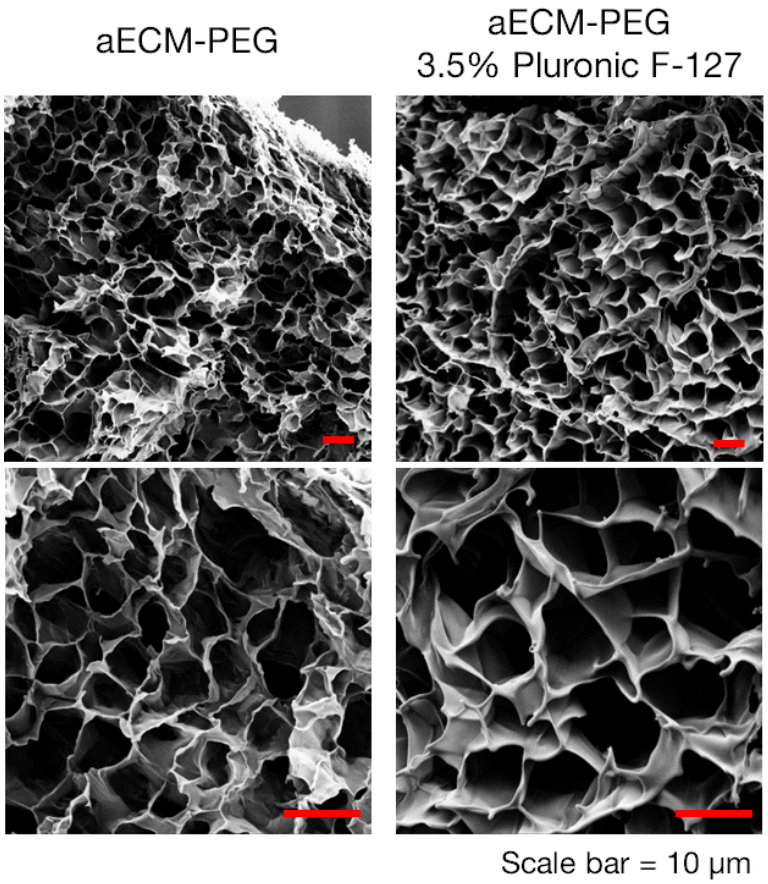

Figure S-9. Scanning electron micrographs of the cross-sections of aECM-PEG (left column) and aECM-PEG-F127 (right column) hydrogels. Hydrogels were swollen for 2 days in PBS at 37^{o}C, lyophilized and processed for SEM imaging. Results show that the addition of 3.5% Pluronic F-127 increased the pore size of the hydrogel.

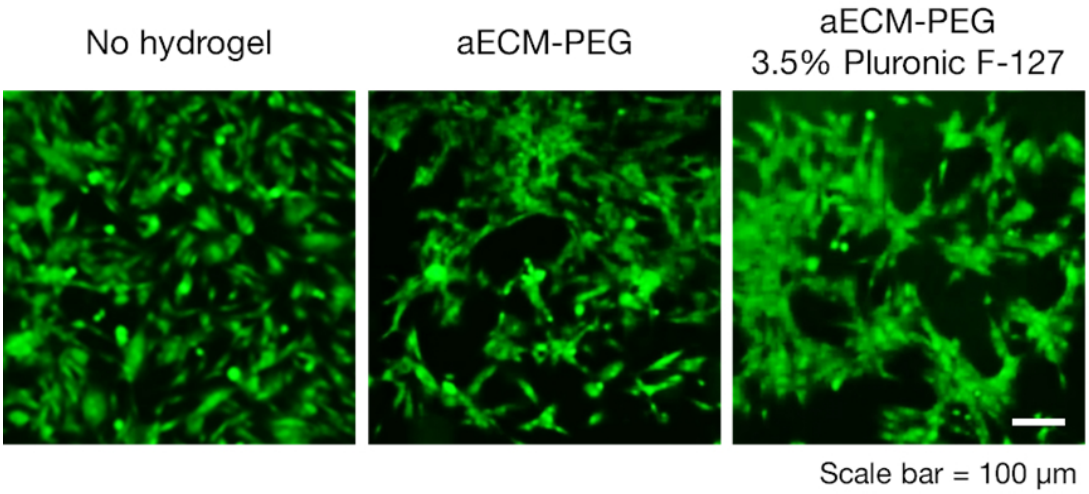

Figure S-10. Live/dead staining of encapsulated corneal fibroblasts in aECM-PEG and aECM-PEG-F127 hydrogels show that cells are viable. Live cells are stained green.

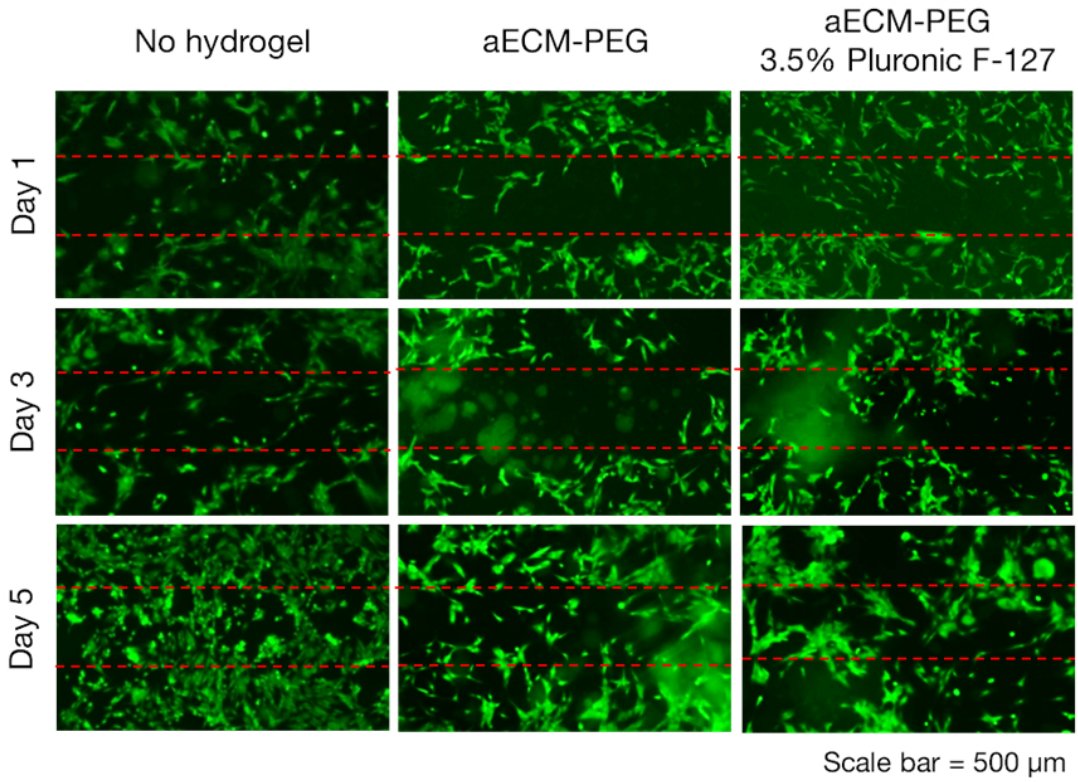

Figure S-11. Using a scratch wound assay *in vitro*, we observed that corneal fibroblasts were able to migrate into the 'mock wound,' which was filled with either the aECM-PEG or the aECM-PEG-F127 hydrogel. There were slightly more infiltrated cells in the hydrogel with added Pluronic F-127 than that without. Corneal fibroblasts are stained green using acridine orange.